THE INFLUENCE OF BLADE STACKING ON TURBINE LOSSES

by

Stephen Harrison

Trinity Hall

A dissertation submitted for the degree of Doctor of Philosophy

Department of Engineering
University of Cambridge

October 1989

PREFACE

The research described in this dissertation was carried out at the Whittle Laboratory, Cambridge University Engineering Department between October 1985 and October 1989. Except where specifically stated to the contrary, this dissertation is the original work of the author and contains nothing which is the result of work done in collaboration. No part of the work contained herein has been submitted to any other university or place of learning.

The author is indebted to many for their help and encouragement. First and foremost among these is his supervisor, Dr. J. D. Denton, whose apt and timely guidance has been invaluable. Many informal discussions with other members of staff and students at the Whittle Laboratory have also been greatly appreciated. In particular, thanks are due to Dr. J-J. Camus for permission to report results of his oil-dot shear stress measurements on the endwall of the unleaned cascade.

The test rig was manufactured in the Cambridge University Engineering Department workshops and considerable help in setting up, modifying and adding to it has been received throughout the project from the Whittle Laboratory technicians. Many thanks are due to the staff of both workshops, particularly Mr. R. A. Julian at the main department and Mr. K. A. Bryant at the Whittle Laboratory.

The author was supported by a Science and Engineering Research Council grant for the first three years. His support costs for the final year, and all other project costs for the entire four year period, were met by the Procurement Executive of the Ministry of Defence via the Royal Aircraft Establishment, Pyestock. Thanks are due to these organisations and to Dr. R. Kingcombe at Pyestock.

Stephen Harrison

October 1989

SUMMARY

Three linear cascades of highly loaded, low aspect ratio turbine blades have been tested in detail to investigate the mechanisms of secondary loss and the influence of non-radial stacking (lean) on these mechanisms. The blades in all three cascades had the same section but they were stacked perpendicular to the endwall in the first cascade, on a straight line inclined at 20° from perpendicular in the second and on a circular arc inclined at 30° from perpendicular at each end in the third cascade.

The boundary layer over much of the endwall within the blade passage was found to be laminar. Despite this, skin friction coefficients and rates of loss generation are still very high because this boundary layer is extremely thin.

Downstream mixing losses comprised a significant proportion of the overall loss. They arise mainly as a result of the dissipation of the kinetic energy of the secondary flow. If mixing is not complete before the subsequent bladerow is reached, acceleration in that bladerow is likely to increase the mixing loss.

Lean has a marked effect upon blade loading and the state of boundary layers on the blade suction surfaces and the endwalls. The distribution of loss generation is therefore changed but the effect upon overall loss coefficient is minimal for this blade.

The major benefit of compound lean is a reduction in the strength of secondary flows. The reasons for this are discussed. This reduces the downstream mixing losses and would also substantially reduce unsteadiness and spanwise variations of mean incidence at entry to the subsequent bladerow. In a turbine this would be likely to reduce losses in the downstream bladerow as well as making matching easier and improving off-design performance.

It seems that the details of the separation of the inlet endwall boundary layer and formation of the horseshoe vortex have a strong influence on the subsequent development of the secondary flow. Numerical calculations must model this correctly in order to obtain good overall predictions.

CONTENTS

NOMENCLATURE

A	Area
c or C	Blade chord
C_D	Dissipation integral $D/\rho U^3$
C_F	Skin friction coefficient $\tau_w/\frac{1}{2}\rho U^2$
D	Shear work in boundary layer per unit surface area
h	Specific enthalpy or blade height
H	Boundary layer shape factor δ^*/θ
p	Pressure
Re	Reynolds' number
s	Specific entropy or blade pitch
T	Temperature
u	Primary component of velocity
U	Free stream velocity
v	Velocity
w	Secondary component of velocity
x, y	Cascade co-ordinates (see fig.2.2)
Y	Loss coefficient (see p.10 and appendix 4.1)
z	Cascade co-ordinate (see fig.2.1)
δ^*	Boundary layer displacement thickness $\int_0^\infty \left(1 - \frac{u}{U}\right) dz$
δ_e	Boundary layer kinetic energy thickness $\int_0^\infty \frac{u}{U}\left(1 - \left(\frac{u}{U}\right)^2\right) dz$
θ	Boundary layer momentum thickness $\int_0^\infty \frac{u}{U}\left(1 - \frac{u}{U}\right) dz$
μ	Dynamic viscosity
ν	Kinematic viscosity
ρ	Density
ϕ	Flow angle (see fig.2.2)

Subscripts

0	Stagnation
1	Inlet
2	Exit
a	Atmospheric (N.B. $p_2 = p_a$)
BL	Boundary layer. See p.64 for definition of Y_{BL}.
M	Mean or mixed-out
MIX	Mixing
SKE	Secondary kinetic energy. See p.14 for definition of Y_{MIX} and Y_{SKE}.
W	Solid surface
x	Axial

CHAPTER 1

INTRODUCTION AND LITERATURE REVIEW

1.1 Introduction

The use of compound lean (i.e. a non-linear spanwise variation of dihedral) of turbine blades dates back further than one might expect, to the work of John Smeaton published in 1759. The method of windmill construction at that time dictated that the vane stagger (or "weathering") fixed the dihedral. Smeaton set out to determine the optimum variation of weathering from heel to tip of a windmill vane but found that it was important to obtain the correct variation of dihedral even if this resulted in non-optimum stagger at some radii. In his own words:

> "It appears that when the wind falls upon a concave surface, it is an advantage to the power of the whole, tho' every part, taken separately, should not be disposed to the best advantage."

Blade design has come a long way since 1759 but it is still far from straightforward. Modern turbine flows, particularly at low aspect ratio and high hub/tip ratio, tend to be dominated by secondary flow and so a fully three-dimensional approach to design is vital, but it is only in recent years that the understanding of secondary flows and the ability to predict them have made such an approach possible. Non-radial stacking (lean) is one "three-dimensional" feature which is now employed by a number of gas turbine manufacturers (see, for example, Williams, 1984, Woollatt et. al., 1989).

As a result of many theoretical and experimental studies over the past thirty years the basic structure of turbine secondary flows is now well known but deficiencies remain, particularly in the areas of secondary losses and the design of blades to reduce these losses. This project is concerned with the mechanisms of secondary loss generation in turbines and the influence of blade lean on losses.

A thorough understanding of turbine loss generation is necessary in order to design to minimise it. The present chapter will review the work published to date in four areas: secondary flows; secondary losses; loss prediction techniques; three-dimensional design, particularly blade lean. The project objectives will then be outlined.

1.2 "Classical" Secondary Flow

It was Hawthorne (1955) and Squire & Winter (1951) who developed the first detailed analyses of idealized, inviscid flows. Hawthorne identified three components of streamwise vorticity at exit from a bladerow, for which Came & Marsh (1974) later developed simplified derivations. These three "classical" components are often identifiable at exit from a real bladerow:

- Distributed secondary vorticity. This component results from the turning of the inlet vortex filaments (i.e. wall boundary layer) so that they have a streamwise component (see fig.1.1);

- Trailing filament vorticity. The fact that fluid passes more quickly over the blade surface than the pressure surface causes the inlet vortex filaments to be stretched (fig.1.1b), giving rise to this vortex sheet at the trailing edge. An alternative explanation of this component is that the passage vortex causes an upwash (i.e. flow away from the endwall) along the suction surface and a downwash, or more likely no spanwise flow at all, along the pressure surface. These different spanwise flows cause a net circulation in the wake which is in the opposite direction to the passage vortex.

- Trailing shed vorticity. This is also a vortex sheet appearing at the trailing edge but it arises from a spanwise variation of blade circulation. In a truly two-dimensional flow it would appear concentrated at the endwall but in practice the secondary flow and endwall boundary layer cause the blade loading to reduce near the endwall so the trailing shed vorticity spreads away from the endwall into the wake. If the blade circulation is designed to vary along the span, e.g. as a result of departure from free vortex design, then the trailing shed vorticity will also be spread right across the span.

This idealized approach provides an insight into the origins of secondary flow but has limited analytical value because of the sweeping assumptions necessary. As well as inviscid flow, it is usual to assume that either the inlet flow non-uniformity or the flow turning is small so that Bernoulli surfaces (i.e. surfaces of constant stagnation pressure) remain undistorted. Since none of these assumptions is applicable to turbines, Horlock (1977), in his review of developments in secondary flow, concludes that numerical methods are essential for predicting turbine flows.

Nevertheless, Gregory-Smith (1982) has incorporated an inviscid calculation based upon the work of Came & Marsh (1974) and Glynn & Marsh (1980) into his loss prediction program because the very small amounts of computer time needed for the solution make it suitable for use in the early stages of blade design. This calculation will be discussed more fully later.

1.3 Actual Secondary Flow Structure

There have been numerous experimental studies of secondary flows in turbomachines. Among the earliest was that of Herzig & Hansen (1955) who demonstrated the existence of the passage vortex and investigated the effect of tip clearance, relative endwall movement, Mach number and annular geometry on the secondary flow. Langston et al. (1977), working on a large scale, linear turbine cascade, identified most of the principal secondary flow features and Sieverding (1985) has reviewed the work published up to 1984.

1.3.1 The Horseshoe Vortex

As the inlet flow approaches a blade it must diverge in order to flow around the leading edge. This turning of the endwall boundary layer gives rise to streamwise vorticity of opposite sign on each side of the leading edge: the horseshoe vortex. In practice the horseshoe vortex originates at the "saddle point", the point on the endwall ahead of the blade where the inlet boundary layer separates (see fig.1.2a&b, based on Langston et al., 1977 and Sjolander, 1975). Note that, except near the saddle point, the

3D separation associated with the vortex is quite unlike a conventional 2D boundary layer separation, so to avoid confusion the term "lift-off line" will usually be used.

There is some evidence (Sjolander, 1975, Marchal & Sieverding, 1977) that the horseshoe vortex formation might be more complicated (fig.1.2c&d) with subsidiary vortices and an extra endwall lift-off line. The fact that oil flow visualization often only reveals a single lift-off line (Hodson & Dominy, 1987a, Moore, 1983, Langston et al., 1977 etc.) suggests that if these extra vortices do form then they are very small, highly unsteady or both. Ishii & Honami (1986), using smoke flow visualization near a wall placed perpendicular to an incoming flow, found clear evidence for these subsidiary vortices. Eckerle & Langston (1987), however, made detailed measurements of the (more realistic) flow around a 298mm diameter cylinder and showed that there can be two separate endwall lift-off lines even when there are no subsidiary vortices. They observed only one vortex but found that the saddle point was some way upstream of the point where the vortex began to form, with a very shallow separation angle (fig.1.2e). Oil flow visualization on the endwall therefore showed two separation lines: one associated with the separation at the saddle point; and a "local" lift-off line, closer to the cylinder, associated with the horseshoe vortex.

1.3.2 The Passage Vortex

The passage vortex is the dominant secondary flow feature, resulting from the action of the cross-passage pressure gradient on the low-momentum fluid in the inlet endwall boundary layer and corresponding to the distributed secondary vorticity of classical theory. The pressure side leg of the horseshoe vortex and the passage vortex rotate in the same direction, since they both form in the same way, i.e. by turning of the inlet boundary layer. They may develop separately (the model of Klein, 1966) or as a single vortex (the model of Langston, 1980). Marchal & Sieverding (1977), Sieverding et al. (1984) and Sharma et al. (1989) found a single horseshoe/passage vortex, so it seems that the latter model is more likely to be correct.

Moore & Ransmayr (1984) performed experiments on a linear turbine cascade with two different leading edge shapes (circular arc and wedge). Since the overall loss and its distribution were the same in each case (within experimental certainty) they concluded that the horseshoe vortex has little effect on loss. In the discussion on Moore & Ransmayr's paper Langston suggests instead that it may be that the leading edge geometry has little effect on the horseshoe vortex.

1.3.3 The Corner Vortex

The endwall boundary layer fluid is swept across the passage ahead of the main lift-off line and when it reaches the blade suction surface it separates and forms a corner vortex in much the same way as the horseshoe vortex forms at the leading edge. The corner vortex is small and remains in the suction surface/endwall corner, preventing the passage vortex lift-off line from reaching the blade suction surface (fig.1.2b). Evidence for its existence has been found by Marchal & Sieverding (1977), Gregory-Smith and Graves (1983), Jilek (1986) and Hodson & Dominy (1987a).

1.3.4 The Exit Flowfield

Most researchers into turbine secondary flows find broadly the same flow pattern at the bladerow exit. An example, from Hodson & Dominy (1987b) is shown in fig.1.3. The passage vortex is clearly visible, but so is another vortex close to it in the wake, rotating in the opposite direction. This vortex is observed by many workers but referred to variously as the trailing shed vortex (Hodson & Dominy, 1987a, Armstrong, 1955, Perdichizzi, 1989) the suction side leg of the horseshoe vortex (Jilek, 1986, Sharma et al., 1989) or the trailing shed/trailing filament vortex (Gregory-Smith et al., 1983).

The mechanism of formation of the additional vortex is shown particularly clearly in the flow visualization of Sonoda (1985) (see fig.1.4). Although this work should be treated with caution because it was carried out at low Reynolds' number (1.6×10^4 inlet, 4.8×10^4 exit, based on axial chord) it shows the two legs of the horseshoe vortex

winding around one another in the passage vortex (in agreement with the model of Sieverding and van den Bosche, 1983) and the "extra" vortex (labelled IV in fig.1.4) developing separately as a result of the interaction between the passage vortex and the suction surface boundary layer. (There is also a fourth, much smaller vortex which becomes entrained into the passage vortex.) This interaction is as follows. The passage vortex causes a spanwise component of flow along the suction surface which introduces a skew (i.e. streamwise component of vorticity) into the suction surface boundary layer. It also causes boundary layer fluid to accumulate near the lift-off line on the suction surface, so a discrete vortex forms here.

If the flow had been inviscid there would have been no blade boundary layer so the vortex could not have formed in this way, but there would still have been different spanwise flows on either side of the wake, so this component of vorticity would still exist in the wake. The additional vortex labelled "trailing shed vortex" in fig.1.3 is therefore most closely associated with the trailing filament circulation of classical theory but modified, of course, by the effects of viscosity.

Although Sonoda (1985) and Sieverding & van den Bosche (1983) report that the suction side leg of the horseshoe vortex becomes entrained into the passage vortex other workers, such as Sharma et al. (1989) show it merging into the suction surface boundary layer and therefore either being dissipated before the trailing edge or reinforcing the trailing filament vortex.

Trailing shed vorticity normally contributes very little to the trailing filament vortex for an unleaned blade with constant section in a linear cascade: although there is some spanwise variation of blade loading in the vicinity of the passage and trailing filament vortices (Jilek, 1986), most of the variation in blade loading occurs much nearer to the endwalls. Most of the trailing shed vorticity therefore appears in the corner vortex or as skew in the endwall boundary layer where it is intersected by the blade wake (fig.1.3).

It should be noted that these secondary flow features, particularly the passage vortex, are not insignificant. Maximum secondary velocities can be a large fraction of

the free stream velocity and the effect on pitchwise average exit flow direction, i.e. overturning near the endwall and underturning nearer to midspan, can be several degrees (e.g. Gregory-Smith & Graves, 1983).

1.3.5 Migration of Loss

In an inviscid turbine flow all vorticity and stagnation pressure deficit at the bladerow exit would have originated in the upstream endwall boundary layer and been convected by the secondary flows. Since maximum vorticity and maximum loss in the upstream boundary layer generally occur together at the endwall, vortex cores and loss cores at exit would be likely to coincide. Flow visualization by Gaugler & Russell (1982) shows that indeed it is the high-loss fluid nearest the wall in the inlet boundary layer which forms the horseshoe/passage vortex core and that fluid from further out in the boundary layer is then entrained into this vortex. Eckerle & Langston (1987) also found that the loss and vortex cores associated with the horseshoe vortex around a cylinder were coincident.

In a real flow, of course, there is generation and diffusion of entropy (loss) and vorticity, and vorticity can also be destroyed or cancelled. Most entropy generation occurs near solid surfaces, i.e. near the edges of vortices rather than their cores, so the effect of viscosity is to separate peak vorticity from peak stagnation pressure loss. The extent to which this separation occurs depends on the precise flow. If the bladerow acceleration is large then the inlet stagnation pressure deficit is small in terms of the exit dynamic pressure. In other words the high velocities within and downstream of the bladerow generate losses which are high compared with the inlet loss and so tend to move the loss peak away from the vortex core. This will be less true of bladerows with low overall acceleration. This is shown clearly by experiments on linear cascades (table 1.1).

Author(s)	Contraction ratio CR (see text)	δ^*/h (%)	Number of distinct loss cores per $^1/_2$ span	Loss and vortex cores coincident ?
Hodson & Dominy (1987a)	1.3	0.6	2	Yes
Jilek (1986) (impulse cascade)	1.4	0.9	2	Yes
Moore & Adhye (1985)	1.6	2.1	2	Yes
Yamamoto (1987b) (impulse cascade)	1.6	1.3 / 2.7	1 (distorted)	Nearly
Zunino et al. (1987)	1.7	1.6	2	Exit velocity field not shown
Gregory-Smith & Graves (1983)	1.9	3.9	1 (distorted)	Nearly
Perdichizzi (1989)	2.4	3.4 - 4.2	1	No
Marchal & Sieverding (1977)	2.6	1.1	1	No
Yamamoto (1987a) (nozzle cascade)	2.7	1.7 / 3.0	1	No
Jilek (1986) (nozzle cascade)	3.9	0.6	1	Unclear

Table 1.1 Linear turbine cascade tests: coincidence of loss and vortex cores.

In table 1.1 the contraction ratio CR is defined as $(h_1\cos\phi_1)/(h_2\cos\phi_2)$ where h_1 and h_2 are the inlet and exit blade heights ($h_1=h_2$ except for Hodson & Dominy, 1987a) and ϕ_1 and ϕ_2 are the inlet and exit flow angles (from axial). The contraction ratio is approximately equal to the ratio of exit to inlet free stream velocities. δ^*/h is the ratio of inlet wall boundary layer displacement thickness to inlet blade height (two values of this ratio are given in table 1.1 for each of the Yamamoto references because there were different boundary layers on the two walls of his cascade).

Table 1.1 shows clearly that an impulse cascade is more likely to produce two loss cores at exit, coincident with the principal secondary vortices, whereas an accelerating cascade generally produces a single core which is not coincident with either of the vortices. The inlet boundary layer thickness appears to have no bearing on this.

Yamamoto (1987 a & b) and Jilek (1986) each demonstrate the striking effect of acceleration ratio on secondary flow and loss distribution. The flow at exit from an impulse bladerow is dominated by the vortices and loss cores but flow from an accelerating bladerow is influenced much less by secondary flow. Indeed, the flow at exit from Jilek's nozzle (area ratio 3.9) is almost entirely two-dimensional, with a secondary loss core so small that it is difficult to say whether it is coincident with the passage vortex or not.

The other common feature of the exit loss distribution is a "gap" between the wake and the endwall boundary layer. This is caused by the passage vortex, which sweeps high-loss fluid away from the endwall, leaving a small accumulation of endwall boundary layer fluid on the endwall behind the trailing edge.

If there are any boundary layer separations, either on the blade surface or in the suction surface/endwall corner where secondary flow causes an accumulation of low-momentum fluid, then these can affect both the generation and redistribution of loss by allowing much stronger secondary flows to develop. For instance, Hunter (1982) noted a reduction in radial migration of loss when a laminar separation bubble was removed by tripping the suction surface boundary layer.

1.3.6 Effect of Annular Geometry

Most of the experimental work considered so far in this chapter was done on linear cascades. This simplifies both measurement and interpretation of results but neglects the radial pressure gradient present in annular bladerows.

Generally speaking, the secondary flow in an annular cascade is the same as in a linear one except for a radially inward migration of low-momentum fluid along the latter

part of the suction surface and in the wake. Thus Herzig & Hansen (1955), Hunter (1982) and Yamamoto & Yanagi (1985), working on accelerating nozzle bladerows with axial inlet flow, exit flow 65°-70° from axial and hub/tip ratios around 0.7, all observed a much greater accumulation of high loss fluid near the hub than near the casing. Sieverding et al. (1984), working on a similar cascade, found in addition that the passage vortices at hub and casing within the blade passage were in different positions and had different strengths. The radial flows in the cascades tested by Herzig & Hansen and Yamamoto & Yanagi were so strong that the hub passage vortex was eliminated and a vortex rotating in the opposite direction was observed downstream.

It has already been shown that the amount of acceleration in the bladerow determines the impact which the secondary flow has on the exit flowfield. It is perhaps not surprising, then, that Moustapha et al. (1985), working on a part-annular impulse cascade with midspan inlet and exit angles 64° and 64.5° from axial respectively, found that the exit flowfield was hardly affected by radial migration of boundary layer fluid. Instead, they found two loss cores of roughly equal size, as in the equivalent linear cascade but slightly closer together. The authors point out that the effects of annular geometry will be due to a combination of radial pressure gradient and radial variations of pitch/chord ratio and blade orientation.

1.4 Secondary Loss

1.4.1 Definition and Components of Secondary Loss

There are several definitions of dimensionless loss coefficient (see Horlock, 1973a) but this dissertation will use:

$$Y = \frac{p_{01} - p_0}{p_{01} - p_2} \qquad (1,1)$$

where p_{01} is the inlet free stream stagnation pressure, p_0 is the local stagnation pressure and $(p_{01}-p_2)$ is the exit free stream dynamic pressure. A mass-average Y over

the entire exit plane may be obtained using the formula given in Appendix 4.1. In incompressible, isenthalpic flow Y is a direct measure of the entropy of the flow, since

$$T_0 ds = dh_0 - \frac{1}{\rho_0} dp_0$$

$$dh_0 = 0$$

T_0, ρ_0 constant

$$\therefore s - s_1 = \frac{p_{01} - p_0}{\rho_0 T_0}$$

The overall loss coefficient at exit from a bladerow may be thought of as comprising three components: inlet boundary layer loss; profile loss, which may be defined as the midspan loss or as the predicted or measured loss coefficient of an equivalent 2D cascade; and the remainder, termed "secondary loss". Actual mechanisms of entropy generation are highly complex and interdependent but this arbitrary division into three components provides a convenient starting point for understanding loss generation processes.

A number of factors contribute to secondary loss:

- The endwall boundary layer within the cascade;
- The influence of secondary flows on the blade boundary layers. This may include "free stream" velocities different from a 2D cascade, a change in the position of transition and possibly separation triggered in some way by the secondary flow;
- Dissipation of the useless kinetic energy of the secondary flow. Part of this occurs within the cascade due to high levels of turbulence in the vortex cores (Gregory-Smith & Graves, 1983, measured peak turbulence levels about 30% of local velocity) and part will occur downstream.

Several investigators have concluded that the main loss mechanism is "corner stall", i.e. boundary layer separation caused by accumulation of low-momentum fluid in the suction surface / endwall corner. Belik (1972) observed by surface flow

visualization that there was an "intense mass transport from the region of the inlet boundary layer" towards the suction surface / endwall corner and assumed that this was "unquestionably associated with an intense separation in the corner region". In the light of more recent research this assumption is clearly false. Belik also found that the magnitude of the secondary loss could not be explained by his simple model of dissipation of the horseshoe vortex, and so concluded that the corner separation was responsible for the majority of the secondary loss.

Five years later Marchal & Sieverding (1977) made more detailed cascade measurements and again concluded that severe local separation in the corner was likely to be a major source of loss. They admitted to not having firm evidence of such a separation but based their conclusion on an apparent increase in the rate of loss generation downstream of the throat and the appearance of a loss core adjacent to the suction surface near the endwall. However, since their measurements did not include the blade boundary layers it is possible that both of these effects are attributable to the accumulation of low-energy fluid on the suction surface (due to the action of the passage vortex) becoming large enough to encroach into the five-hole probe traverse area. Yamamoto (1987a) comes to similar conclusions for similar reasons, and with the same shortcoming.

1.4.2 Calculation of Mixing Loss

Graves (1985) attributed 85% of secondary loss to dissipation of secondary kinetic energy. Other researchers (e.g. Langston et al., 1977, Moore & Adhye, 1985) have found that a large proportion (typically over $1/3$) of the overall loss appears downstream of the trailing edge so clearly downstream mixing of secondary flows is a major component of secondary loss. It is not one which can be directly measured in a cascade, however, except by traversing very far downstream, in which case new loss arising in the endwall boundary layers would have to be taken into account. In a full stage even this is not possible, since much of the mixing takes place in the following

bladerow. It is therefore necessary to calculate mixing loss from measurements using a control volume analysis as follows:

The measured flow has velocities v_x, v_y and v_z and flow area A perpendicular to the x direction. Assume that it mixes out to a uniform flow with static and stagnation pressures p_M and p_{0M} and velocities v_{xM} and v_{yM} ($v_{zM}=0$). The mixed-out flow area is A_M and external forces F_x and F_y are applied during the mixing process. If incompressible flow is assumed then the following equations may be written, where all integrals are evaluated over the inlet area A:

Continuity:

$$\rho\int v_x dA = \rho v_{xM} A_M \qquad (1,2)$$

x momentum:

$$F_x + \int(p + \rho v_x^2)dA = (p_M + \rho v_{xM})A_M \qquad (1,3)$$

y momentum

$$F_y + \int \rho v_x v_y dA = \rho v_x v_{yM} A_M \qquad (1,4)$$

Stagnation pressure:

$$p_{0M} = p_M + \tfrac{1}{2}\rho(v_{xM}^2 + v_{yM}^2) \qquad (1,5)$$

Combining (1,2-5) we obtain:

$$p_{0M} = \frac{1}{A_M}\left\{ F_x + \int(p+\rho v_x^2)dA \right\} + \frac{\rho}{2}\left\{ \left(\frac{F_y + \rho\int v_x v_y dA}{\rho \int v_x dA} \right)^2 - \left(\frac{\int v_x dA}{A_M} \right)^2 \right\} \qquad (1,6)$$

and subtracting this from the mass-average total pressure at the measurement plane

$$\bar{p}_0 = \frac{\int p_0 v_x dA}{\int v_x dA} \tag{1,7}$$

gives the mixing loss. The mixing loss coefficient is defined as

$$Y_{MIX} = \frac{\bar{p}_0 - p_{0M}}{p_{01} - p_2} \tag{1,8}$$

If F_x and F_y can be assumed to be zero, for instance when considering mixing at constant area downstream of the bladerow in question with no following bladerow and neglecting endwall shear stresses, then eq.(1,6) is easily applied. However, if there is a bladerow downstream or if a measurement plane within the bladerow is to be considered, then F_x/A_M and F_y/A_M are of the same order of magnitude as the dynamic head. Since the mixing loss is one or two orders of magnitude smaller than this then F_x and F_y must be known very accurately. In practice this means that mixing loss cannot be calculated reliably in this way except for constant area mixing outside of bladerows, so in practice eq.(1,6) can only been applied to planes downstream of the bladerows and with $A_M=A$ and $F_x=F_y=0$. The validity of this calculation in practice will be discussed in §1.4.3.

As an alternative to mixing loss some workers (e.g. Gregory-Smith, 1982 and Belik, 1968) assume that all of the "secondary kinetic energy" is dissipated . A secondary kinetic energy coefficient may be defined as

$$Y_{SKE} = \frac{\int \frac{1}{2}\rho w^2 u \, dA}{(p_{01} - p_2) \int u \, dA} \tag{1,9}$$

where u is the component of velocity in the primary (mean) direction and |w| is the secondary velocity, i.e. the component perpendicular to the primary direction. Note that it is very important to define the primary direction correctly as the direction of the

fully mixed-out flow, otherwise the primary flow may make a large contribution to the calculated secondary kinetic energy.

Kinetic energy is a scalar and cannot strictly be resolved into components so Y_{SKE} does not necessarily have any physical significance. However, it is easy to evaluate and Moore & Adhye (1985) showed that under certain circumstances it may be approximately equal to the mixing loss. They rearranged the equation for mixing loss as follows (notation has been changed to match the current work):

$$Y_{MIX} \approx Y_{SKE} - \frac{p_M - \bar{p}}{p_{01} - p_2} + \frac{\frac{1}{2}\rho\,(\overline{u^2} - u_M{}^2)}{p_{01} - p_2} \qquad (1,10)$$

$\bar{p}$ is the mass-average static pressure at the measurement plane. u is the component of velocity in the primary direction (Moore & Adhye defined the nominal blade exit angle rather than the mean flow direction as the primary direction but for this approximate analysis the distinction should not be significant). $\overline{u^2}$ and $u_M{}^2$ are therefore the primary kinetic energy at the measurement plane and the mixed-out plane respectively. Downstream of Moore & Adhye's cascade the primary flow terms (i.e. the second and third terms on the right of equation 1,10) roughly cancelled one another out. This lent weight to the rule-of-thumb that secondary kinetic energy and mixing loss are equal. Moore et al. (1987) measured Reynolds' stresses downstream of the same cascade and showed that they were compatible with the observed dissipation rates. They also showed how transfer of mean kinetic energy between the three co-ordinate directions via pressure terms and turbulence could account for the observation that secondary kinetic energy is dissipated while the primary flow appears to be reversible.

1.4.3 Validity of Mixing Calculation

Mixing loss can usually only be calculated from eq.(1,6) by assuming that mixing assumes at constant flow area with no externally applied forces, and the approximate

equality of Y_{MIX} and Y_{SKE} has only been verified for such a flow. (Moore & Adhye calculated mixing loss based on the flow just upstream of the trailing edge by including external forces due to blade surface pressures, but the measurement plane was so near to the trailing edge that these forces, and hence the possibility for error, were small). Such assumptions are clearly invalid when considering a full stage, so it is necessary to consider how and where mixing occurs in reality. Hodson & Dominy (1987a) found that the remaining mixing loss 0.42 axial chords downstream of the trailing edge was 10% of the measured loss at the same location. Moore & Adhye (1985) found that losses were still increasing, but slowly, 1.4 axial chords downstream. Kawai et al. (1985) did not measure losses but noted that secondary flow vortices were much reduced in strength, although still present, 2.0 axial chords downstream. Binder & Romey (1983) noted that the flow was almost completely mixed-out by 1.7 axial chords from the trailing edge.

These distances are greater than the typical spacing between bladerows so some mixing of secondary flow from one bladerow is bound to occur within, or even downstream of, the following bladerow. Sharma et al. (1988) measured the interaction between the flow in one bladerow and the exit flow from the previous bladerow. Since they did this on a $1^1/_2$ stage turbine they could look at a rotor with a following stator and a stator with a following rotor. The flow at exit from the second stator exhibited underturning near the walls and overturning near midspan. This is the opposite of the effect normally expected from secondary flow so it was suggested that the rotor passage vortices were persisting through the following stator and, furthermore, dominated over the stator passage vortices in the time-averaged flow. This explanation is plausible but a little surprising since the axes of rotation of the rotor passage vortices have a very different orientation from those of the stator passage vortices and there was little evidence of the passage vortex from the first stator persisting through the first rotor. Contour plots of unsteady total pressure loss downstream of the second stator appear to show rotor loss cores passing but since velocity vectors are not presented it is not possible to tell to what extent the rotor vortices persist at stator exit. There are other

mechanisms which might cancel the stator passage vortices. For instance, Yamamoto & Yanagi (1985) found that radially inward flow in the later part of the stator suction surface boundary layer and in the wake cancelled the stator hub passage vortex and set up a vortex rotating in the opposite direction. This effect is likely to be more pronounced in a stator wake than a rotor, since the "centrifuging" of a rotor wake tends to counteract the effect of the radial pressure gradient. Hebert & Tiederman (1989) looked at the effect of wakes from moving bars on the secondary flow in a linear cascade and noted that, even though the bars generated no streamwise vortices, the wakes caused a circulation to be set up in the cascade passage which was opposed to the cascade passage vortices. In reality this effect may be even stronger, since blade wakes, unlike the wakes from bars, are not uniform along the span but are concentrated towards midspan by secondary flow and might therefore lead to overturning at midspan in the following bladerow.

Binder (1985) carried out an investigation into turbulence production and mixing of a stator wake and passage vortex within the following rotor passage. Without the rotor present (Binder & Romey, 1983) mixing occupied at least 1.7 axial chord lengths downstream of the trailing edge (3.34 true chord lengths in the flow direction) but when the rotor was fitted rapid dissipation of the vortex took place very early in the rotor passage. A more detailed investigation (Binder et al., 1986) showed that the breakdown probably starts when the passage vortex is cut by a rotor blade and then propagates along the vortex very quickly (at the speed of sound) so that there is a very high rate of turbulence generation right across the passage immediately behind the leading edge plane. This suggests that in a turbine most mixing loss is generated before or just inside the following bladerow, so it may be acceptable to use eq.(1,6) after all. The effect of downstream bladerows on mixing loss will be considered further in chapter 4.

1.5 Prediction of Turbine Loss

1.5.1 Empirical Correlations

The oldest way to predict turbine losses, and still the most convenient, is by using correlations based on empirical data. Many correlations have been proposed, taking into account such factors as blade inlet angle, incidence, blade exit angle, maximum thickness, trailing edge thickness, pitch, chord, aspect ratio and tip clearance. Profile loss correlations (e.g. Ainley and Mathieson (see Horlock, 1973a) and Baljé and Binsley, 1968) are based on 2D cascade measurements and are generally presented graphically.

The secondary loss, i.e. the total loss less the profile loss, may be correlated against geometrical parameters in a similar manner. Dunham (1970) reviews such correlations and proposes one himself:

$$Y_S = \frac{c}{h}\left(\frac{\cos\phi_2}{\cos\phi_{B1}}\right)\left(\frac{C_L}{s/c}\right)^2 \frac{\cos^2\phi_2}{\cos^3\phi_M}\left(0.0055 + 0.078\sqrt{\frac{\delta_1^*}{c}}\right) \qquad (1,11)$$

where ϕ_{B1} is the inlet blade angle,

$$\tan\phi_M = \frac{1}{2}(\tan\phi_1 + \tan\phi_2)$$

and

$$C_L = 2\frac{s}{c}(\tan\phi_1 - \tan\phi_2)\cos\phi_M$$

An alternative, and simpler way, to estimate secondary losses is to assume that the mean rate of loss generation in the endwall boundary layer is the same as in the blade boundary layers, i.e.

$$\frac{\text{secondary loss}}{\text{profile loss}} = \frac{\text{annulus wall area}}{\text{blade surface area}}$$

This is the procedure proposed by Stewart et al. (1960) and Heurteux & Price (see Dunham, 1970) but for accurate predictions it is found to be necessary to increase the secondary loss artificially. Sharma & Butler (1987) argued that this increase is to account for the skew in the endwall boundary layer and, furthermore, that this skew is a function of the distance by which the horseshoe vortex lift-off line has move up the blade suction surface by the trailing edge (distance Z_{TE} in fig.1.5). They correlated this distance against blade turning (ε, radians) and contraction ratio (CR) and used throat/span (O/h) rather than annulus area/blade area to obtain a simple correlation:

$$\text{Secondary loss} \quad = \quad \text{2D (profile) loss} \times \left(1 + 4\frac{\varepsilon}{\sqrt{CR}}\right)\frac{O}{h} \qquad (1,12)$$

Empirical correlations have the advantage that they are quick and easy to apply and require only basic input information. This makes them particularly suitable for preliminary design, when detailed blade shapes etc. are not yet known. They suffer from a number of disadvantages, though:

- The implicit assumption is made that, provided blades are designed competently, the detailed profile shape has no effect on loss. In practice this means that, as designs improve, profile loss correlations become more pessimistic;
- Three-dimensional features, such as non-radial stacking, are not considered;
- The empirical data from which the correlations were derived were obtained at various distances downstream of the bladerows in question, so mixing losses are not consistently dealt with;
- The inlet endwall boundary layer is not dealt with consistently.

The last of these shortcomings is a particular problem since many correlations, e.g. eq.(1,11), include inlet boundary layer loss as part of the loss of the current bladerow and consider that the exit boundary layer belongs to the subsequent bladerow. This

probably originated out of convenience, since it meant that the exit boundary layer (which is very thin, skewed and non-axisymmetric) did not have to be measured accurately, but it has meant that most correlations are fairly heavily dependent upon the inlet boundary layer displacement thickness. Several investigators have found that the "new" loss in the cascade (i.e. including the exit wall boundary layer but not the inlet one) is independent of the boundary layer thickness. These include Atkins (1987), Chen & Dixon (1986), Marchal & Sieverding (1977), Gregory-Smith & Graves (1983), Richards & Johnson (1986) and Govardhan et al. (1986). It therefore seems reasonable to exclude the inlet boundary layer but include the exit boundary layer when formulating a loss correlation.

1.5.2 Numerical Predictions

Because empirical correlations ignore blade shape and because secondary flows, particularly in turbines, are highly complex it is often argued (e.g. Marchal & Sieverding, 1977; Carrick, 1977; Denton, 1973) that only fully-three-dimensional flow prediction programs have a long-term future for turbine design. A number of such programs are available (e.g. Moore & Moore, 1985; Denton, 1985; Dawes, 1986) which have been used successfully for a variety of blade shapes.

The principal disadvantage of such methods is obvious: expense. They tend to consume large amounts of computer memory and processing time, particularly if they are to resolve boundary layers sufficiently accurately, and it is no simple matter to prepare input data and obtain a good solution. As yet, it is generally agreed that such programs do not predict absolute loss levels reliably. Nevertheless, advances in the programs themselves and rapid improvements in computer hardware continue to make these predictions more promising for routine design.

1.5.3 Simple Loss Calculations

Empirical loss correlations provide too little information and fully three-dimensional numerical predictions, because of their cost and stringent input data

requirements, are only useful for the later stages of design, once the blade shape is defined precisely. There is therefore a need for simpler predictions which can nevertheless model the effect of design changes moderately well.

Since calculation of the endwall boundary layer is crucial to secondary loss predictions this will be considered first, followed by Gregory-Smith's simple method based on classical secondary flow theory, and finally boundary layer loss predictions based on the assumption of constant dissipation integral.

(i) The Endwall Boundary Layer

Senoo (1958) investigated the endwall boundary layer in a nozzle cascade using a stethoscope and a hot-wire anemometer and concluded that the boundary layer just upstream of the throat was laminar, with transition to turbulence occurring near the throat. He found that the boundary layer within the passage was independent of the state and thickness of the upstream boundary layer but, being unaware of the precise details of secondary flows, thought that this was due to the large acceleration in the passage causing relaminarization of the endwall boundary layer. Much later, Sjolander (1975) noted that, in fact, the old boundary layer was swept off the endwall and that a new boundary layer formed downstream of the horseshoe/ passage vortex lift-off line.

Nevertheless, a 3D boundary layer calculation by Senoo gave reasonable predictions. Surprisingly, a 2D prediction was equally accurate. This appeared to be fortuitous, as the passage convergence tends to make the boundary layer thicker than a 2D boundary layer with the same pressure distribution but cross-flows tend to make it thinner. However, he suggests that 2D predictions in many different nozzles might be reasonably accurate for the same reason.

Johnson (1960) found from his own experimental data and from that of Gruschwitz (1935) and Kuetha et al. (1949) that rather than expressing the crossflow velocity w in a boundary layer as a separate function of height (and other parameters) it was better to express it as a function of the main flow component u. This is Johnson's

triangular model, shown in fig.1.6a. "A" may be determined from the main flow parameters. For instance, if main flow streamlines follow a circular arc with turning α then $A=-2\alpha$. "e" represents the skew of the limiting streamlines relative to the main flow and is treated as an unknown. The velocity is assumed to vary linearly with height in the inner region.

Boundary layer calculations using Johnson's triangular model have shown some success. For example, Dring (1971) claims to calculate losses typically within 30%. Such methods have three drawbacks. The first has already been mentioned, i.e. that they assume that the inlet boundary layer remains attached to the endwall. The second is that they assume that the presence of the sides of the passage (i.e. the blade surfaces) does not unduly influence the boundary layer. This implies that the boundary layer thickness is small compared with the passage width, an assumption which is often not valid for turbines. Horlock (1973b) considered a bounded three-dimensional boundary layer, i.e. one which is thick compared with the passage width, but only obtained good results for lightly loaded blades and low turning (up to around 30°).

The third drawback of the triangular cross-flow model is that the boundary layer in a turbine is not just the product of a simple flow turning. At any one point in the boundary layer there may be fluid from different parts of the passage which may have undergone different amounts of turning and been influenced by lift-off lines and vortices. Langston (1980) measured the endwall boundary layer in a turbine cascade and found "crossover crossflow" profiles like those shown in fig.1.6b&c. Sieverding et al. (1984) presented more such profiles but concluded that they are too complex to be useful, and only a full numerical solution of the Navier-Stokes equations can accurately predict such a flow.

Nevertheless, a two-dimensional boundary layer calculation may provide a reasonable approximation to the endwall loss, as Senoo suggested. Simple axisymmetric models were not found to be accurate (Gregory-Smith, 1970 and Carrick, 1977) but Boyle et al. (1981) found that a 2D boundary layer calculation coupled with a

quasi-3D inviscid flow analysis predicted losses reasonably well. The more recent loss model of Gregory-Smith (1982) incorporating a 2D boundary layer model on the endwall will be discussed below.

(ii) Gregory-Smith's Loss Model

It has already been seen that generation of secondary flow is primarily an inviscid effect resulting from the turning of the vorticity in the upstream boundary layer, and often turbine flows can be adequately predicted by inviscid techniques (e.g. Stow, 1985 and Arts, 1985). Gregory-Smith's model (1982) is therefore based on an inviscid calculation of the exit flowfield using classical secondary flow theory (§1.2). This gives a prediction of the exit flow angles and losses are calculated as the sum of a number of components:

- A loss core, assumed to consist of all of the inlet boundary layer fluid but with no additional loss. This is concentrated in a triangular area against the suction surface and near the endwall;
- A new endwall boundary layer, assumed to be turbulent and collateral and to start at the throat;
- Extra secondary loss, taken to be equal to the secondary kinetic energy (see eq.(1,9)) of the exit flow.

Comparisons with data of Marchal & Sieverding (1977) and Hunter (1979) and later work by Graves (1985) show good qualitative agreement but so far poor quantitative agreement.

(iii) Constant Dissipation Integral

As any boundary layer grows there is not only local entropy generation but also generation of non-uniformities which lead to further entropy generation downstream as mixing makes the flow uniform once again. For a collateral boundary layer the relationship between the boundary layer parameters and the total loss (including

downstream mixing) is straightforward (see for example Horlock, 1973a). The local loss coefficient (based on $\frac{1}{2}\rho U^2$) is $\delta_e/(s-\delta^*)$ whereas if the flow subsequently mixes out at constant area to a uniform flow the ultimate loss coefficient will be $2\theta/s$.

Prediction of θ usually entails solution of the momentum integral equation:

$$\frac{d\theta}{dx} + \frac{1}{U}\frac{dU}{dx}\theta(H+2) = \frac{\tau_w}{\rho U^2} = \frac{C_F}{2} \qquad (1,13)$$

This requires a knowledge of the shape factor H and the skin friction coefficient C_F, which depends upon both H and Re_θ (fig.1.7b). In contrast, the energy integral equation

$$\frac{1}{U^3}\frac{d}{dx}\left(U^3\delta_e\right) = \frac{D}{\rho U^3} = C_D \qquad (1,14)$$

uses the dissipation integral C_D, which is almost independent of H (fig.1.7a). Note that $\frac{1}{2}\rho U^3\delta_e$ is the flux of kinetic energy deficit and D is the shear work done in the boundary layer per unit solid surface area, given by

$$D = \int_0^U \tau \, dv \qquad (1,15)$$

It is assumed that this is all dissipated, i.e. turbulence kinetic energy is neglected (Truckenbrodt, 1955).

Based on work by Rotta, Truckenbrodt derived the relation:

$$C_D = \frac{\beta(H)}{Re_\theta^n} \qquad (1,16)$$

By assuming constant values of n and β (table 1.2) Truckenbrodt solved the energy integral equation for δ_e then obtained θ by assuming a constant ratio δ_e/θ (also given in table 1.2).

	Laminar	Turbulent
n	1	$1/6$
β	0.173	0.0056
δ_e/θ	1.57	1.72

Table 1.2 Constant values assumed by Truckenbrodt

The values of n and β assumed by Truckenbrodt lead to a variation of C_D with Re_θ as given in fig.1.7c.

If all boundary layers are thin, then the local loss coefficient (i.e. neglecting mixing loss) is proportional to the integral $\int U^3 C_D dA$ evaluated over all solid surfaces. For a turbulent boundary layer the dependence of C_D upon Re_θ is so weak that, within a reasonable range of Re_θ, it may be considered to be constant. Moore & Moore (1983) showed that for the boundary layer measured by Samuel & Joubert (1974), for which $5\times10^3 < Re_\theta < 18\times10^3$, C_D took a fairly constant value of 0.0012. Denton & Cumpsty (1987) suggested that an assumption of constant mean C_D might give a useful estimate of loss but that a higher value, say 0.002, might be more appropriate for the levels of Re_θ typically found in turbomachines. If this assumption is made then loss is simply proportional to $\int U^3 dA$, where U may be derived, for example, from inviscid three-dimensional predictions or from axisymmetric streamline curvature calculations via the method described by Walker (1988).

Some of the drawbacks of this method will be discussed in chapter 4 but it is worth noting that the fact that entropy generation rates vary much less than skin friction may partly explain why some simple boundary layer calculations have been moderately successful at calculating loss even in the highly complex flow on turbine endwalls.

1.6 Three-Dimensional Design

There are a number of ways in which blade designs can be changed in an attempt to reduce losses, some of which are reviewed by Tall (1977), Hourmouziadis & Hubner (1985) and Richards (1985). By paying due attention to three-dimensional flows it may be possible to reduce secondary losses by modifying blade angles to change the radial work distribution but three particular design changes intended to reduce secondary loss will be considered here: endwall grooves or fences; endwall profiling and blade lean. Particular attention will be given to lean.

1.6.1 Endwall Fences

It is sometimes assumed (e.g. Yamamoto & Yanagi, 1985) that the accumulation of low-energy fluid into a loss "core" is itself a mechanism of loss generation. This is not necessarily true, but since secondary flows give rise to a mixing loss downstream as the secondary kinetic energy is dissipated it may nevertheless be advantageous to restrict the secondary flows. One way to do this is to put grooves or fences on the endwall aligned with the main flow. The flow over these will induce a loss but it is hoped that the reduction in secondary losses more than compensates for this. Prumper (1972) and Gallus & Kummel (1977) found that fences and grooves did reduce the overall loss. Coghlan & Hodgson (1986), however, reported an increase in loss, despite earlier encouraging results in a constant-area curved channel by Abraham & Bethel (1984).

1.6.2 Endwall Profiling

Whilst endwall grooves or fences inevitably cause some local extra entropy generation and may present cooling problems, this is not necessarily true of changes to the overall passage shape. Changes to the endwall shape are the most straightforward from a practical point of view since the endwalls are virtually unstressed. Waterman & Tall (1976) tested three part-annular cascades of nozzle blades and concluded that endwall contouring (in this case also involving passage contraction) redistributed the losses but did not significantly change the overall level. Boletis (1985) and Kopper et

al. (1981) reported overall improvements due to endwall contouring but in both cases there was an overall gas path contraction due to the revised endwall shape.

An overall contraction (with exit area fixed) may reduce losses simply by virtue of the reduced velocity levels in the early part of the blade passage but this is not always an option which is available to a turbine designer. Atkins (1987) reviewed other investigations into endwall profiling and tested a variety of endwall shapes on a linear cascade. He tested both axisymmetric and non-axisymmetric shapes with and without overall passage contraction and found that most changes increased the loss. Any improvements could generally be attributed to annulus contraction.

1.6.3 Blade Lean

Throughout this dissertation blade lean with an acute angle between the pressure surface and the endwall will be called positive lean, and vice versa.

The stacking of sections to form a rotor blade is usually dictated by stress considerations. There is no such restriction on stator blade design, though, and lean can be used to powerful effect. Lean has been used in turbines in two ways. The first is to control reaction in low hub/tip ratio stages. In such stages the swirl in between the stator and the rotor tends to lead to a large radial static pressure gradients, giving a low stage reaction at the hub and a high value at the casing. Leaning the stator so as to give positive lean at the hub introduces a radial component of blade force which counteracts the undesirable radial pressure gradient and thereby improves the reaction distribution. This was the approach of Deych & Troyanovskiy. More recently, flow calculations by Kirillov et al. (1984), Denton (1987) and Grant & Borthwick (1987) have demonstrated that stator lean is a powerful aid to controlling stage reaction.

Lean can only influence reaction if its effect on pressure extends some way downstream of the stator. Walker (1988) showed that this is only true if the aspect ratio is large, or more precisely if the parameter Z is small, where

$$Z = \frac{4 + \tan^2(\text{exit flow angle})}{4(\text{aspect ratio})}$$

At low aspect ratios and high hub/tip ratios, as found in high pressure turbines, lean only affects the pressures within the bladerow. Rather than controlling stage reaction, then, lean can be used in an attempt to reduce stator losses and to improve the flow onto the rotor. The effect of lean on flow within a bladerow is best described with reference to contours of static pressure on a radial-circumferential plane, e.g. fig.1.8 taken from calculations by Walker (1988). The streamline curvature in the blade-blade plane dominates the flow, so pressure contours remain nearly radial even when the blades are leaned. This has a number of effects at the "positive" end (and of course the opposite effects at the negative end):

- Mean velocities are lower, so rates of entropy generation in boundary layers are smaller;

- The static pressure is increased so the incoming endwall boundary layer is decelerated and therefore thickened as it approaches the bladerow. It therefore tends to be turned more by the blade-to-blade pressure gradient and hence generate more secondary flow;

- The above effect is countered by the fact that the blade loading is lower. It is not immediately obvious whether the net effect will be to increase or decrease crossflow on the endwall;

- There is a gradient of static pressure along the suction surface away from the endwall. This tends to remove low momentum fluid and avoid an accumulation in the suction surface/endwall corner.

On the whole this would suggest that losses would be reduced at the positive endwall. This is confirmed by Fillipov & Van (1964). Since losses would be increased at the negative end (or at midspan with compound lean) there is not necessarily an overall improvement. Indeed, a numerical study by Dawes (1986) predicted a redistribution of loss rather than a net reduction and Huber et al. (1985) concluded that efficiency gains, if any, are due to the indirect effects of improved flow.

In a number of experimental investigations blade lean has been just one of several changes made to blade designs to improve performance. Schlegel et al. (1976) reported a 25% reduction in stator loss, giving a 1.2% point improvement in stage efficiency. They did not deliberately incorporate lean but the fact that stator blade sections were stacked on their trailing edges meant that in practice there was a strong negative compound lean. The improvement in performance was largely due to unchoking the stator at the design point. Liu et al. (1979) deliberately used positive compound lean of a stator. Based largely on 3D viscous numerical predictions they report a net loss reduction at high Mach number but at lower speed only the distribution of loss was improved. Diakunchak (1988) reports a remarkable 6% point stage efficiency improvement from a package of changes including simple stator lean (positive at the hub) but this is compared with a previous design which was acknowledged to have performed badly. In all of these cases, because several parameters were changed at once, it is impossible to deduce the contribution of blade lean.

An early investigation, by Breugelmans et al. (1984), into the effect on a linear cascade of lean alone was not encouraging. Straight lean reduced the losses at the positive endwall but overall losses increased. Compound lean (using a different blade profile and comparing with Salvage, 1974) also increased losses. However, this study used compressor profiles and is therefore not directly applicable to turbines. Furthermore, the study of straight lean used one set of aerofoils mounted at different angles, so blade angles and blockage were not held constant.

Wang et al. (1981) carried out a numerical study on turbines with some limited experimental work and concluded, rather daringly, that compound lean can always give an efficiency improvement. Experiments on an annular cascade (Wang et al., 1987) showed that the greatest effect of simple lean is prevention of loss accumulation in the hub/suction surface corner which otherwise could lead to boundary layer separation. It was also shown that there is an optimum lean angle, above which losses begin to increase again. In the following year parallel experiments with straight lean in a linear cascade (Wang et al., 1988) and an annular cascade (Han et al., 1988) confirmed that the dominant effect of lean is on the radial pressure gradient acting on the latter part of the suction surface boundary layer. The net effect of 20° straight lean on the linear cascade was an increase in loss but on the annular cascade loss was reduced because lean was able to counteract the radial pressure gradient resulting from the annular geometry.

The above experiments (and intuition) indicate that better results could be obtained using compound lean. This was confirmed by Shi et al. (1986) who recorded a 0.8% point improvement in stage efficiency for a transonic turbine stage at its design point and up to 2% point improvement at lower speeds. Nagayama et al. (1987) investigated a turbine stator with very low turning (30°) as part of a full stage. They reported a loss reduction due to compound lean and, surprisingly, even found that midspan loss was reduced. Walker (1988) measured a 2% point drop in stator loss coefficient with compound lean but attributed this to "improved aerodynamics" (e.g. delayed boundary layer transition) rather than secondary flow effects.

1.7 Project Objectives

The foregoing literature review has shown that stator lean may have a strong beneficial effect upon losses in a low aspect ratio, high hub/tip ratio, high pressure turbine. There are, however, a number of deficiencies in work published to date.

1.7.1 Secondary Loss Generation

Turbine secondary flows are reasonably well understood but loss generation is not. There is disagreement over the relative significance of the various mechanisms of loss generation and how to predict them. This seems to be partly due to a confusion on the part of some investigators between loss migration/accumulation and loss generation, but mainly due to insufficient detail in measurements. Several experimental investigations have included measurements within blade passages but it is vital that boundary layers are measured in sufficient detail if sources of entropy are to be quantified. It is also important to know the state of boundary layers (i.e. laminar or turbulent) and to take full account of mixing losses, which can comprise a large fraction of the total loss.

1.7.2 The Influence of Lean

It has been established that the radial pressure gradients in an annular geometry can cause inward migration of low-momentum fluid in the suction surface boundary layer and the wake. This can have two detrimental effects: it causes an accumulation of boundary layer fluid in the hub/suction surface corner which may lead to boundary layer separation and it causes large secondary velocities in the wake which contribute to the downstream mixing loss. Simple lean can counteract this migration and so reduce losses. In any experiment with an annular geometry this performance improvement may mask the other effects of lean so a detailed investigation of loss mechanisms on a linear cascade is required if the other effects are to be understood.

Experiments on a full stage have a further drawback because stator lean will inevitably change the flow onto the rotor. Since the rotor is usually not changed to receive this flow, overall stage measurements must be interpreted with caution.

1.7.3 Loss Prediction

A better understanding of mechanisms of loss generation will aid design and may lead to more reliable prediction by simple techniques. Ultimately, though,

improvements in predictive capability will be by three-dimensional numerical methods. These techniques are still at an early stage of development and therefore need reliable, detailed experimental data against which they can be validated.

The above requirements may be satisfied by detailed flow and loss measurements within and downstream of a large-scale, linear cascade, supplemented by measurement of endwall boundary layer surface shear stresses and determination of the state of all boundary layers. It was the aim of the present project to perform such measurements on unleaned, simple leaned and compound leaned blades, giving particular attention to the mechanisms by which entropy is generated and the ways in which blade lean influences these mechanisms, and then to compare experimental results with current prediction techniques.

CHAPTER 2

EXPERIMENTAL APPARATUS AND PROCEDURES

2.1 Choice of Cascade

The previous chapter has shown that blade lean can have a beneficial effect in an annular geometry by opposing the radial migration of wake fluid, and therefore experiments on a linear cascade are necessary to eliminate this effect and so investigate the other effects of lean. It has also been shown that detailed boundary layer measurements are needed, and a linear cascade is ideal for this because the blades can be much larger than in an annular cascade.

The blades were chosen to be typical of modern high-pressure turbine blades, i.e. high turning, high loading and low aspect ratio. Blade angles of +40° inlet and approximately −65° exit (from axial) were chosen so that the flow would be strongly influenced by secondary flows. The only departure from normal turbine practice was a very thin trailing edge, so that trailing edge losses did not mask the other losses and manufacturing differences between the different sets of blades had minimum effect.

The three different sets of blades tested are shown in fig.2.1, which also defines the sign convention for lean. All blades had the same section, which was constant over the entire span, and the lean was in the pitchwise direction. Blade sections remained parallel to the endwalls, i.e. the blades were sheared rather than tilted, in order to maintain blade angles and blockage.

2.2 Profile Design

A blade profile was designed specifically for this project in order to ensure that it performed well at the low Mach numbers encountered. A profile was first of all sketched by hand on a parabolic camberline and its performance analysed using the finite element

analysis program FINEL. The blade pressures already matched the design intent fairly well but improvements were made using FINEL's design mode. The final design was checked using a Martensen code (Wilkinson, 1967), whose predictions agreed well with FINEL. Predicted and measured blade pressures will be presented below.

Blade boundary layers were predicted using the "NGTE" code (Herbert & Calvert, 1982) with Martenesen pressure predictions. The "NGTE" code uses Thwaites' method for the laminar part of the boundary layer and Green's lag entrainment method for the turbulent part. There was uncertainty over the transition point and hence the turbulent boundary layer parameters, but maximum shape factors in the turbulent part between 1.6 and 1.8 indicated that turbulent separation would not be a problem.

The amount of lean was decided upon using Denton's inviscid, three-dimensional time-marching code (Denton, 1985). It is hard to know what criterion should be used for this choice so amounts of lean were chosen which had a strong effect on static pressures but did not lead to excessive suction surface diffusion.

The profile had to be modified slightly to overcome a manufacturing error on the first set of blades so only predictions for the final (i.e. manufactured) profile will be presented. The profile is outlined in fig.2.2 and full details are given in Appendix 1. Fig.2.3 compares 2D predictions (by the Martensen method) with midspan measurements on the unleaned blades. The midspan Zweifel coefficient on set 1 is 1.10.

2.3 Cascade Design and Operation

2.3.1 Cascade Construction and Equipment

The cascade was mounted on the "Duplex" low-speed wind tunnel. Having decided that four blades were required to ensure periodic flow, the tunnel exit size fixed the scale of the blades (pitch 230mm, true chord 278mm). To achieve a blade aspect ratio close to unity inserts were fitted in the tunnel contraction to reduce the width further, giving a blade span of 300mm.

Blades were CNC machined from solid aluminium alloy. For batches of four this method was no more expensive than epoxy moulding or construction from laminated wood and had the advantage of superior dimensional accuracy and strength, particularly important for the thin trailing edges. It also made surface static tappings easier to fit. Slots were milled in the surface into which steel hypodermic tube was laid. The tubes were covered over with "Plastic Padding" and 0.4mm diameter holes drilled into them 7, 50 and 150mm from each end on set 1 and 8, 25, 60, 100 and 150mm from each end on sets 2 and 3. Tapping positions around the blade profile are shown in fig 2.2 and included in Appendix 1. When measuring static pressures all tappings but one on each tube were covered with tape 0.05mm thick.

The rest of the cascade was largely constructed from plywood on a wooden base supported on steel trestles. The cascade layout is shown in fig.2.4a. The blades were supported by dowels at each end into holes accurately drilled in the walls by CNC machine. Traversing was through a sliding Perspex window so one blade had to be cantilevered from the back wall and supported near the other end by a length of piano wire. (This wire did not interfere in any way with the passage being measured). The end of the cantilevered blade was sealed against the Perspex with a layer of felt. Although the blades were precisely located onto the endwalls, the endwalls, being wood, could distort slightly so care was taken when setting up the cascade to ensure accurate positioning of blades relative to one another.

A row of tappings in the Perspex window allowed endwall static pressures to be measured and probes could be inserted through a slot which was sealed with T-shaped inserts. This arrangement allowed complete freedom of choice of measurement location. The probe was mounted onto a small, manually operated turntable (Unislide A3082TS) which allowed it to be rotated about its own axis. This in turn was mounted onto a motorized dovetail slide (Unislide B2518) driven by stepper motor under computer control. This drove the probe parallel to its own axis, i.e. in the spanwise direction, and could be mounted perpendicular to the endwall (for sets 1 and 3) or at 20° from perpendicular (set 2). The motorized slide was supported on a long, manually

operated dovetail slide (Unislide A4048) which allowed movement in the pitchwise direction, parallel to the slot in the Perspex window. This manual slide formed the hypotenuse of a triangular frame (fig.2.4b) which could be traversed along a horizontal bar fixed to the cascade.

Automated traversing and data logging were controlled by an Apricot Xen microcomputer via a Biodata Microlink interface. All pressures were measured using a Furness FC012 micromanometer, serial number FCB7577.

2.3.2 Periodic Flow

Ensuring periodic flow in a linear cascade with few blades can be difficult, and particularly so on a cascade of leaned blades. The flow was adjusted using two aluminium endplates (fig.2.4a). The initial endplate setting was calculated so that the ratio of throat width to ideal inlet streamtube height was equal for all five flow passages (see fig.2.5 for clarification). The plates were then adjusted and periodicity was checked by a number of techniques:

- Midspan static pressures on the two middle blades were compared using a manometer bank. This method was quick and easy but not particularly sensitive as incidence changes tended to make pressures on the two blades move up and down nearly in unison. Slight errors in static tapping positions meant that pressures could not be matched precisely in regions with high pressure gradients.

- The wake orientation at the endwall, revealed by surface oil flow visualization, was much more sensitive to periodicity. This was the main method used to check periodicity on set 1.

- After cascade setup, exit five-hole probe traverses confirmed that the flow angle at $x/C_x=1.23$ was periodic to within 1° on sets 1 and 3 and 2° on set 2.

The above techniques were used on all three sets of blades. The following were only used on the simple and compound leaned blades:

- Endwall static pressures along a line just upstream of the blade leading edges were used in a similar way to blade static pressures.
- Short, fine lengths of cotton were stuck to the blade leading edges to show the position of the stagnation point.
- Longer pieces of cotton (about 200mm) were stuck to the trailing edges of all four blades to check the exit flow angle along the whole span.

2.3.3 Flow Conditions

Upstream flow conditions were determined using a mercury thermometer, Pitot probe and single wall static pressure tapping at the top of the cascade. Atmospheric pressure was taken as downstream static pressure. The exit free stream Mach number was only 0.14 so incompressible flow has been assumed throughout and the errors arising from this assumption will be discussed in Appendix 3. A hot wire probe measured the upstream turbulence level, which was 0.4%rms.

Tunnel flow conditions tended to vary through a run as ambient temperature changed but exit Reynolds' number, based on true chord, was kept between 8.5×10^5 and 9×10^5. This is safely above the level at which one would expect cascade performance to cease to depend strongly on Reynolds' number and is reasonably typical of Reynolds' numbers encountered in engines. Exit free stream dynamic pressure ($p_{01}-p_a$) was measured after, at most, every three or four other pressure readings and all pressures were normalized by this pressure in order to eliminate errors due to drift in tunnel conditions. There was also higher frequency unsteadiness, notably fluctuations of 1% to 1.5% of dynamic head (peak-peak) at a frequency of 1–2Hz. There was a diffuser (part of another test rig) upstream of the wind tunnel inlet and a piece of paper suspended near the wall of this diffuser flapped at roughly the same frequency, so it was concluded that unsteady separation in the diffuser was largely to blame for this

fluctuation. Trials with each probe used showed that averaging a large number of readings over a period of at least 1.8s minimised errors due to unsteadiness. As an additional check to eliminate the effect of large random fluctuations, the standard deviation over each measuring period was monitored and if it exceeded an arbitrarily specified limit then the averaging period for that reading was doubled.

2.3.4 Upstream Boundary Layer

The cascade inlet geometry was identical for the three cascade configurations so it should be reasonable to assume that the upstream boundary layer was the same in each case. As a check, the endwall boundary layer was traversed at the same point relative to the blades (x=–124mm, y=250mm; see fig.2.2) on all three configurations and results are presented in table 2.1 and fig.2.6a. The three-hole cobra probe was used on set 3 and the positive end of set 2 but there was no way to mount it at the negative end of set 2 so a flattened Pitot probe (1.22mm×0.38mm external dimensions) was used there. The boundary layer upstream of set 1 was measured before the running conditions had been finalised so the set 1 values presented in table 2.1 are the mean of values obtained at Reynolds' numbers (based on true chord and exit flow) of 7.3×10^5 and 10.9×10^5. They were obtained before the three-hole probe was available using a different flattened Pitot probe (2.49mm×0.30mm external dimensions).

Set number	δ^*(mm)	θ(mm)	δ_e(mm)	H	$\frac{p_{01}-p_{local}}{p_{01}-p_a}$	Y_{eff}
1	2.6	1.9	3.3	1.36	0.28	0.0062
2 (+ve end)	4.0	2.6	4.5	1.50	0.23	0.0069
2(–ve end)	2.3	1.8	3.2	1.30	0.30	0.0063
3	2.7	2.0	3.5	1.34	0.26	0.0061

Table 2.1 Upstream Boundary Layer at x=–124mm, y=250mm

It will be seen from table 2.1 that even at x=–124mm there is a slight influence of the blade lean on static pressure. The entropy flux in the boundary layers can only be compared directly by referring each boundary layer to the same dynamic head. Noting that the full span is 300mm, an effective loss coefficient based on the exit dynamic head is:

$$Y_{eff} = \frac{\delta_e}{150-\delta^*} \frac{p_{01}-p_{local}}{p_{01}-p_a}$$

The accuracy of Y_{eff} is estimated to be ±0.0002 so table 2.1 confirms, except on the positive wall of set 2, that the contribution of the upstream endwall boundary layer to overall loss coefficient was the same for each blade set. The discrepancy on set 2 may be because the horseshoe vortex lift-off line is further upstream on the positive wall than on the negative wall or the other two blade sets (see chapter 3), so that the boundary layer at (–124, 250) is influenced by the horseshoe vortex. Traverses were therefore performed further upstream with the flattened Pitot probe to check that the boundary layers upstream of set 2 were the same on each endwall. The traverse positions relative to the blades were not identical ((–366, 13 on the positive wall and (–315, 61) on the negative wall) because the cascade layout would not permit this, but they were both the same distance downstream of the inlet flange. The results, shown in fig.2.6b, confirm that the two inlet boundary layers were indeed similar.

All of the values of Y_{eff} given in table 2.1 are relatively small compared with the cascade exit loss coefficients (chapter 3) and the discrepancies between them are small compared with the accuracy of area traverse measurements (appendix 3). The inlet boundary layers to all three cascades will therefore be assumed to contribute 0.006 to the overall cascade loss coefficients.

2.4 Flow Visualization

Surface flow visualization using a suspension of fluorescent powder in oil was used successfully at the full Reynolds' number. Smoke flow visualization was unsuccessful

except at unrealistically low Reynolds' numbers (at least two orders of magnitude less than the normal test value) so these will not be presented.

Endwall heat transfer measurements were made using a sheet of encapsulated liquid crystal which changes colour according to its temperature. This was stuck to the Perspex endwall and heated using two 1kW lamps. Accurate calibration was out of the question because the input heat flux was non-uniform and unknown. For the purposes of this project it was wall shear stresses, not heat transfer coefficients, which were required. The technique was not quantitative in this respect because Reynolds' analogy does not apply if the boundary layer is skewed or if the momentum and thermal boundary layers do not originate in the same place. The liquid crystal showed endwall flow features clearly but in less detail than oil flow visualization, so no results will be presented.

A flattened Pitot probe and stethoscope proved to be very good for detecting boundary layer transition on the blade suction surface. If the probe was slid along the surface a rapid increase in noise level, from near silence to a loud roar, was heard at transition. The technique was not so successful on the endwall, for reasons which will be discussed in a later chapter.

2.5 Pressure Probe Traverses

Five-hole probes were made by soldering together lengths of 1.07mm O.D. stainless steel tubing and chamfering the outer tubes to give an included angle of about 100° (fig.2.7a). The resulting probe head size was rather large but was necessary partly to give a reasonably fast response but mainly to ensure a sufficiently large probe Reynolds' number (5300 based on probe diameter and inlet free stream flow) to minimize sensitivity of the calibration to Reynolds' number. The stem diameter was also larger than desired: a 10mm O.D. stainless steel tube was necessary to avoid undue deflections under aerodynamic loading (this was determined by simple calculations and rudimentary experiments).

A "shepherd's crook" probe shape was out of the question because of the necessity to traverse near both endwalls so to reduce the influence of stem blockage on probe

measurements the probe head was placed 30mm upstream of the stem. Two probes were constructed, kinked in opposite directions so that when traversing near blade surfaces the stem could be kept well away from the blade (see fig.2.2). Details of five-hole probe calibration are given in Appendix 2 and accuracy is discussed in Appendix 3.

Area traverses were performed at the locations shown in table 2.2. The full span was always covered on set 2 but on sets 1 and 3, once a coarse traverse at x/C_x=1.23 had confirmed that the flow was symmetrical about midspan, only the half span near the Perspex was covered. Where appropriate, data have been reflected about midspan for ease of comparison with set 2 results.

x (mm)	x/C_x	Set 1	Set 2	Set 3
–65	–0.30	•	•	•
7	0.03	•		
50	0.22	•	•	
100	0.45	•		
150	0.67	•	•	
185	0.83	•	•	
230	1.03	•		
274	1.23	•	•	•

Table 2.2 Area Traverse Locations

The coarseness of the traverse grid was varied according to the detail required, from a minimum spacing of 2mm in the passage vortex to 20mm in the free stream. The initial coarse traverse downstream of set 1 located the passage vortex and thereafter a measurement grid based on an educated guess of the regions of interest proved acceptable.

The five-hole probes were traversed almost as close to solid surfaces as was physically possible but measurements closer than 1.5 to 2.0 probe diameters are likely to be inaccurate. For this reason a three-hole "cobra" probe (fig.2.7b) was used to traverse the endwall boundary layer at each location except x/C_x=–0.30. Calibration of this probe is also described in Appendix 2. At all locations except very near the blade suction surface, where there are strong radial components of velocity, and at x/C_x=0.03 near the pressure surface, where the velocity is low and the horseshoe vortex leads to extremely high boundary layer skew (180° or more), the three-hole and five-hole probe data match one another well. The two sets of data have been merged, with the crossover occurring about 5mm from the wall. Within the regions covered by three-hole probe data, components of velocity perpendicular to the wall were assumed to be zero, static pressure was linearly interpolated between the endwall and the nearest five-hole probe measurement and stagnation pressure and flow direction were derived from three-hole probe pressures.

Blade boundary layers were traversed using a flattened Pitot probe (fig.2.7c). A reference probe position was found by electrical contact with the blade and the probe head was moved through the boundary layer by rotating the probe stem. The effective measuring position was taken to be further from the blade than the centre of the probe by a distance 0.19 × the probe thickness (Quarmby & Das, 1969). Calibration tunnel measurements showed that in a free stream, provided pitch angle and yaw angle remained less than 10°, the error due to probe incidence was less than 2% of local dynamic head. There was no convenient way to check the error in a boundary layer, much less a skewed boundary layer. Nevertheless, in skewed parts of the suction surface boundary layer, measurements were repeated with the probe bent in increments of 20° and at each location the highest pressure measured was taken to be the local stagnation pressure. Static pressure was linearly interpolated between the blade surface and the nearest five-hole probe measurements, as were flow direction cosines (the flow direction at the blade surface was known from blade geometry and oil flow visualization).

2.6 Shear Stress Measurements

2.6.1 Hot Film Gauge

A stick-on hot film gauge, Dantec type 55R47, with dimensions 0.1mm × 0.9mm was used to measure surface shear stress on the Perspex window. In fact, one gauge was used for sets 1 and 2 but was damaged while measuring on set 3 so all set 3 measurements were repeated using a nominally similar gauge. The gauge was stuck onto a small piece of acetate sheet which was taped to the Perspex window in such an orientation that shear stresses parallel to the direction of sliding of the window (ϕ=–35°) should be measured correctly. In each run, typically lasting 2-3 hours, the window was moved so that shear stress readings could be taken at about 25 positions through the cascade. The tunnel was then turned off while the gauge was moved to another position on the window for the next run. The anemometer output low-pass filter was set to 10kHz and at each gauge position data were logged at 20kHz for 0.5s, investigations with an oscilloscope having shown that this was sufficient to record any frequencies of interest present in the signal.

A relationship

$$\tau_w = K_1 \left(\frac{E^2 - E_0^2}{\Delta T} \right)^3 \qquad (2,1)$$

is assumed (Hanratty & Campbell, 1983), where ΔT is the difference between the gauge temperature (140°C) and the air temperature. E is the anemometer output voltage and E_0 is the voltage at zero flow, with the anemometer output amplifier gain set to 5. E_0 was determined by holding a plastic cup over the gauge but the voltage took some time to settle and values were not particularly consistent. Since E_0^2/(gauge resistance) represents the heat lost to the substrate it was assumed that

$$E_0^2 = K_2 \Delta T$$

so that

$$\tau_w = K_1 \left(\frac{E^2}{\Delta T} - K_2 \right)^3 \qquad (2,2)$$

For each run K_2 was determined from a number of measurements of E_0. Scatter in values of K_2 for different runs indicated an uncertainty of at least ±10% in τ_w. Comparisons of mean $\left(\frac{E^2}{\Delta T} - K_2 \right)$ measured at given locations on different days indicated a greater overall uncertainty, possibly ±20%. There are two major sources of error in addition to this:

- Measurements with different gauge orientations indicate that variation in shear stress direction can cause the calculated value of τ_w to be too low by up to about 40% on sets 1 and 2 or about 60% on set 3.

- There will be a certain amount of heat transfer into the boundary layer via the substrate, so for mean shear stress measurements the effective gauge size will be larger than the actual size. At high frequencies this sideways conduction will be less significant so the effective size and actual size will be very nearly equal. If the effective gauge length and area are denoted by L_e and A_e, a theoretical analysis (Hanratty & Campbell, 1983) shows that

$$K_1 \propto \frac{L_e}{A_e^3}$$

so the value of K_1 for mean shear stress may not be constant and will be very different from that for the fluctuating component.

It is clear that a hot film gauge can give little better than a qualitative picture of wall shear stress, so no attempt has been made to correct for gauge incidence effects. A single value of K_1=150°CNm^{-2}V^{-2} has been used for both gauges based on a small number of Law-of-the-Wall ("Clauser") plots of the upstream boundary layer (e.g. fig.2.8) and comparisons with the oil dot measurements described below.

Hanratty & Campbell (1983) and Bellhouse & Schultz (1967) quote a number of criteria which should be satisfied for eq.(2,1) to be valid. It has been confirmed that, for most of the measurements taken, these are indeed satisfied, but since absolute shear stress values are so inaccurate in any case no details will be presented here.

2.6.2 Oil Dot Measurements

The following measurements were carried out on blade set 1 by Ian Starling and Enoch Lam as part of an undergraduate project supervised by Dr. J-J. Camus in 1988. The author had virtually no involvement with this work but the method will be discussed briefly here and results presented in the next chapter for comparison with hot film data. This work was completed before the hot film measurements were commenced.

The method is based on that of Tanner & Blows (1969). Drops of oil of known viscosity are placed on the endwall and allowed to smear under the action of the shear stress. Once a clear leading edge is visible the drops are photographed under laser light so that their thickness can be measured by counting interference fringes from the leading edge. The drops are photographed again after a known length of time (typically 1-2 hours in this case) and the wall shear stress may be derived from the rate of smearing. It is possible to compensate for the effects of gravity but provided a suitable viscosity and run time are chosen this correction is negligible. Based on comparisons with other shear stress measurement techniques in collateral boundary layers in a different wind tunnel, Camus, Starling and Lam claim ±10% accuracy.

CHAPTER 3

EXPERIMENTAL RESULTS

3.1 Introduction

This chapter will present the experimental results and outline the differences between the three cascades but will not discuss the mechanisms of loss generation. Detailed discussion of loss generation will appear in chapter 4.

Numerous figures are necessary to describe fully the complex flows in these cascades. These are needed both in order to understand the flow structures and for detailed comparison with theoretical predictions. Ideally, they should be studied *en bloc* and so they have been presented in a sequence designed to facilitate this. The discussion in this chapter, however, will not always follow the same sequence and some of the figures presented with this chapter will actually be discussed in later chapters.

Note that five-hole probe traverses on sets 1 and 3 only cover a half span but that for clarity and easy comparison with set 2 the data have been reflected about midspan. Normalization of data, the definition of secondary velocity and the method for calculation of vorticity are given in Appendix 4. Fig.2.1 shows the definition of "positive" and "negative" walls of set 2.

3.2 Flow Structure

3.2.1 Basic Flow : Set 1 (unleaned)

Fig.3.1 shows set 1 oil flow visualization. Where wall shear stresses are too low to disturb the oil, e.g. on the wall near the pressure surface, brush marks are still visible.

The lift-off line around the blade leading edge, associated with the horseshoe vortex, is very clearly visible in fig.3.1a with endwall flow converging strongly towards it from the downstream side. Ahead of this line there is a diamond-shaped area of low wall shear stress. On one side of this diamond, adjacent to the lift-off line, there is a patch roughly 15mm across where the oil has been disturbed but no flow in any particular direction is visible. (This mottled patch shows up much better in reality than on the photograph). The appearance of this oil suggests a large unsteadiness and this is probably the location of the saddle point. Its position corresponds to a local maximum static pressure (fig.3.20c). The suction side leg of the lift-off line (S_S) as it passes around the blade leading edge may in fact be two lines about 4mm apart but these are by no means clear and even if two lines exist they combine before the line meets the blade suction surface. The pressure side leg S_P is definitely a single line and no additional separation or reattachment lines emanate from the saddle point.

These oil flow patterns match Eckerle and Langston's model of horseshoe vortex formation (fig.1.2d&e) except that no line S_1 emanates from the saddle point, probably because the separation there is highly unsteady. Line S_P (fig.3.1a) corresponds to S_2 (fig.1.2d). Further evidence for this model is provided by a secondary velocity vector plot at x/C_x=0.22 (fig.3.2) which shows both legs of the horseshoe vortex lying directly over their respective lift-off lines rather than to one side as might be expected. A slight kink in the secondary velocity vectors near the endwall under the pressure side leg confirms that the position of the lift-off line is indeed where the oil flow visualization shows it to be, and has not been shifted by probe interference effects.

Downstream of the point where S_S meets the blade suction surface, the fluid near the endwall flows towards the blade surface, so a small corner vortex forms. The lift-off line associated with this vortex is visible in fig.3.1a and shows that the vortex grows until S_P meets the blade. Thereafter the corner vortex lift-off line remains about 8mm from the suction surface with S_P parallel to it and a further 3-4mm from the blade. There is a reattachment line (i.e. with divergent rather than convergent flow) on the suction surface associated with the corner vortex. It lies only a few millimetres from

the endwall and once again it is clearer in reality than in fig.3.1b. This vortex, although small, is strong enough to cause a "kink" in the oil flow pattern immediately downstream of the trailing edge (fig.3.1a). Investigation with a wool tuft confirmed that this kink in the flow is confined to within a few millimetres of the wall.

In common with the findings of other workers (e.g. Sjolander, 1975 and Langston et al., 1977) the saddle point is some distance away from the leading edge, so formation of the horseshoe vortex is not a process which is confined to the leading edge region. A large proportion of the inlet endwall boundary layer fluid is therefore involved in the formation of the horseshoe vortex. Some is entrained into it at an early stage and the rest is swept across the passage between S_P and S_S and forced up the suction surface. Fig.3.2 shows the development of the two legs of the horseshoe vortex and shows that the pressure side leg grows and becomes the passage vortex rather than the two vortices developing separately. The continuation of S_S after it meets the suction surface (line "A" in fig.3.1b) is therefore another lift-off line associated with the passage vortex.

Another line on the suction surface, nearer to midspan than the passage vortex lift-off line, can be seen in fig.3.1b (labelled "B"). The line appears to start where the blade leading edge meets the endwall but there is no convergent or divergent flow relative to it and on some runs it was not apparent at all. The line appears on the blade surface even if only the endwall is initially coated with oil, so it clearly consists of oil swept off the endwall. It is therefore concluded that this line does not represent a flow feature but is caused by an accumulation of oil at the leading edge, either by gravity or due to the action of the horseshoe vortex, which then flows along the blade surface, washing dye with it.

Line "C" in fig.3.1b will be discussed in §3.4. There were no features of interest on the pressure surface: the flow remained parallel to the endwalls.

Hawthorne's "classical" analysis of secondary flow should only be applied with great caution to a real bladerow. Nevertheless, downstream of the cascade there are clear vortices (fig.3.2b, x/C_x=1.23, and fig.3.3) which correspond broadly to the three

classical components of streamwise vorticity (see §1.2): the passage vortex; the trailing filament vortex just above it in the wake, rotating in the opposite direction; and the trailing shed vorticity near the endwall (part in the corner vortex and part in the skewed endwall boundary layer). These are further highlighted by contours of streamwise vorticity (fig.3.4).

The passage vortex is surprisingly strong, with maximum secondary velocities well over half the exit free stream velocity. The vortex causes a large amount of over- and underturning (fig.3.18) and has a marked effect on static pressures (figs.3.5, 3.16a and 3.17a). It causes a trough of low pressure along the endwall, and the pressure minima on the endwall and suction surface are both moved away from the blade-endwall corner.

3.2.2 The Effect of Lean : Set 2 (straight lean)

Fig.3.12 shows that, apart from the local effect of the passage vortices, the influence of lean on static pressures is as discussed in §1.6.3. Isobars remain roughly perpendicular to the endwalls so that at the positive wall the mean static pressure is high and the cross-passage pressure gradient is low, while the converse is true at the negative wall. There is therefore a spanwise static pressure gradient along the blade surfaces which has a particularly strong effect on the suction surface towards the middle of the passage (fig.3.16b).

The high pressure at the positive endwall results in lower velocities there. The first effect of the component of blade force towards the positive wall is therefore to shift streamlines in the opposite direction (fig.3.7), something which might not intuitively have been expected.

Downstream of the trailing edge the streamline shift is in the opposite direction, towards the positive wall, and this shift is not complete by x/C_x=1.23. The shift is not the result of a boundary layer separation on the negative wall: streamwise velocities remain reasonably large and positive. Numerical predictions (to be presented in chapter

5) agree very well with fig.3.7, so the streamline shift is not a result of the termination of the negative wall at x/C_x=1.55. (The positive wall is the sliding Perspex window, which extends much further downstream.) The shift is unlikely to be affected significantly by differences in wake and boundary layer thicknesses between the two ends. The main cause is therefore the spanwise variation in flow angle: higher velocities within the blade passage lead to greater blade loading (fig.3.16b), hence greater flow turning (fig.3.18), hence lower exit axial velocity for a given streamwise velocity.

The streamwise positions and velocity vectors in fig.3.7 are seen to be compatible with one another, confirming that the net radial velocities observed in fig.3.10 are genuine and not a result of measurement errors.

The potential effect of lean extends upstream of the bladerow. The upstream boundary layer on the positive wall faces an adverse pressure gradient just upstream of the blade, which thickens it. Since the inlet flow angle is not axial the boundary layer is also skewed, with the incidence being increased near the wall. This results in a saddle point (fig.3.8a) which is even further from the blade leading edge than on set 1 and a clearly defined horseshoe vortex lift-off line which is further forward, probably indicating a larger vortex. The lift-off line remains further forward as it crosses the passage, indicating that although the pitchwise pressure gradient is lower it sweeps endwall boundary layer fluid away more quickly because that fluid has less momentum.

An additional line is visible on the endwall in fig.3.8a, joining S_S from one blade to S_P from the next. The cause of this line is unclear. It may be that, as the inlet boundary layer is thick and the crossflow is strong, the boundary layer separates well before the suction surface. This would cause much of the boundary layer fluid to leave the wall at an early stage, possibly being entrained into the passage vortex. This theory is supported by the observation that the corner vortex lift-off line only becomes visible much later than on set 1.

On the negative wall the flow pattern is quite different (fig.3.8b). Here the upstream potential effect of the blades tends to thin the endwall boundary layer and reduce the incidence, so the horseshoe vortex is much smaller and the saddle point is directly opposite the blade leading edge. Furthermore, a distinct horseshoe/passage vortex lift-off line is only apparent very near to the leading edge. No single line crosses the blade passage, but there is clearly still crossflow at the endwall. The corner vortex lift-off line (fig.3.8b) and the clear reattachment line on the suction surface ("D" in fig.3.8c) show that the corner vortex is much larger than at the positive end. This indicates that more boundary layer fluid remains against the endwall as it flows towards the suction surface.

Also on the suction surface the passage vortex lift-off lines (A) are visible as on set 1. The additional lines (B) are present too, and once again they do not appear to represent a local flow feature. The spanwise migration of the suction surface boundary layer, particularly near the trailing edge, is clear but of course surface flow visualization alone cannot show how great the spanwise mass flow is. Line C (which marks transition) will be discussed in §3.4.

The reason for the difference between the two endwall flow patterns was partly explained by using a wool tuft to identify vortex positions. This tuft, about 60mm long, rotated vigorously in a vortex and the direction of rotation was determined by holding a wire against it and observing which way the tuft wound around the wire. Because access was from downstream the tuft could not be used upstream of mid-chord.

On set 1 the tuft revealed the passage vortex, corner vortex and, downstream of the trailing edge, the trailing filament vortex. These were quite clear and agreed with positions shown by surface flow visualization and probe traverses (e.g. fig.3.3). On set 2, however, the flow patterns at the two ends were different (fig.3.9). At the positive end the passage (A), trailing filament (B) and corner (C) vortices were seen as for set 1 but at the negative end, instead of a single passage vortex, there were two

distinct but much weaker vortices rotating in the same direction. Vortex "A_1" appears to originate near the leading edge of the adjacent blade, i.e. it appears to be the pressure side leg of the horseshoe vortex. Vortex "A_2" appears to originate near mid-passage, i.e. it appears to be the passage vortex.

Comparison of fig.3.9 with figs.3.10 and 3.11 clarifies the flow pattern. Velocity vector plots can sometimes be misleading because their appearance depends upon the direction of projection chosen. A vortex which is not aligned with the projection direction, for instance a streamwise vortex where the local flow has a spanwise component, may not be shown clearly by vectors projected parallel to the endwalls. Components of vorticity in the local flow direction, on the other hand, are likely to give a truer representation of the vortices present. Fig.3.11 indicates, most clearly at x/C_x=0.83, that whereas at the positive end the passage vorticity is concentrated in a single vortex, at the negative end this is not the case. Although the two vortices may not be quite as distinct as the wool tuft would suggest, it seems that the horseshoe and passage vortices may be separate from one another. It follows that whether the horseshoe and passage vortices develop together (Klein's model) or separately (Langston's model, see §1.3.2), and whether there is a distinct lift-off line on the endwall, depends upon the position of the endwall saddle point relative to the blades.

The development of the main vortices within the blade passage is very different at the two ends (fig.3.10). At the positive end the strong crossflow and clear lift-off line cause the low-momentum fluid to roll up very quickly into a distinct vortex whereas at the negative end it stays on the endwall for longer and is not so clearly identifiable as a vortex until much nearer the trailing edge plane. Whereas high static pressure at the positive wall leads to low streamwise velocities and hence a large vortex, the vortex at the negative wall remains more compact right up to the trailing edge.

The influence of the horseshoe/passage vortex on static pressures at the positive end can be seen in fig.3.17b. The strong endwall lift-off gives rise to a more prominent pressure trough than on set 1. Further downstream, however, the vortex is larger than

on set 1, so has a smaller influence on static pressures (compare fig.3.12 with fig.3.5b). The pressure minimum on the endwall (fig.3.17b) is therefore not so definite or so far from the blade.

Wall pressures were not measured at the negative end but the corner vortex at that end is also seen to have a strong influence on static pressures (fig.3.17b). The pressure 8mm from the negative endwall (fig.3.16b) suddenly rises at $x/C_x=0.6$ (i.e. $(p_{01}-p)/(p_{01}-p_2)$ falls). This rise coincides with the point where the line of pressure tappings crosses the corner vortex lift-off line (fig.3.8c).

It can be seen from figs.3.10 and 3.11 that what has been labeled the "trailing filament" vortex at $x/C_x=1.23$ appears larger and stronger at the positive end than at the negative end. An explanation for this, using the "classical" approach, is to recognize that, even discounting the effects of secondary flow, there is a spanwise variation of blade loading (see fig.3.16b). Trailing shed vorticity will therefore appear distributed along the span rather than just at the blade ends. This has the same sense as the trailing filament vorticity at the positive end, so the trailing filament vortex is reinforced, and vice versa at the negative end. The physical mechanism by which this occurs is that the pressure gradient along the suction surface sets up a secondary flow in the suction surface boundary layer which reinforces and opposes the two trailing filament vortices respectively.

3.2.3 Compound Lean : Set 3

Endwall flow visualization on cascade 3 (fig.3.14a) is as expected: the saddle point and main lift-off line S_p are further from the blade than on cascade 1 but not as far as on the positive wall of cascade 2 and lines "A" and "B" appear on the suction surface (fig.3.14c) as on set 1 (cf. §3.2.1 and fig.3.1b). The other features in fig.3.14c will be discussed in §3.4. Probe traverses (fig.3.15) and investigation with a wool tuft show that, as in cascade 1, the pressure side leg of the horseshoe vortex and the passage vortex are indistinguishable. The flow structure is therefore not fundamentally different from that in the unleaned bladerow.

The effect of compound lean on static pressures (figs.3.16c and 3.17c) is also as expected. Static pressures on the endwall are increased compared with set 1 but the low-pressure trough on the endwall, following the line of the horseshoe/passage vortex, is still present. Blade surface pressures, on the other hand, are decreased, with a clear minimum at midspan on the suction surface.

One might expect the flow at exit from cascade 3 to be similar to that from the positive half of cascade 2. This is not the case, however, since the plane of symmetry at midspan prevents the net spanwise flow seen in the straight leaned bladerow. Nevertheless, the "trailing filament" vortex is reinforced and there is a marked reduction in over- and underturning (fig.3.18) compared with the straight blades.

3.3 Generation and Migration of Loss

Development of loss through cascade 1 is shown in fig.3.6 which is largely self-explanatory. Secondary flow sweeps high-entropy fluid in the wake away from the endwall and into the high-loss core, but the wake at midspan does not appear to have been substantially influenced by the secondary flow.

The mean flow is 65.5°, 64.8° and 66.3° from axial respectively downstream of the three cascades, giving contraction ratios ($\cos\phi_1/\cos\phi_2$) between 1.8 and 1.9. Referring to table 1.1 on p.7 it is therefore no surprise that there are two distinct loss cores in each half span at $x/C_x=1.23$ (figs.3.6b, 3.13 and 3.15d) and that these cores are very nearly coincident with the vortices (figs.3.4b, 3.11 and 3.15b).

Lean has a striking effect on development of loss in the straight leaned cascade (fig.3.13). Within the cascade the static pressure is high at the positive end and low at the negative end, so the two main loss cores are very different sizes. However, they each carry roughly the same loss, or entropy, flux. Downstream, therefore, where the pressure is more uniform, they become similar sizes and the spanwise variation of pitchwise integral loss flux (fig.3.19) is fairly symmetrical.

The loss distribution at exit from set 3 (fig.3.15d) is similar to that at the positive half of set 2 except in one respect. Lean causes a static pressure gradient along the suction surface in the spanwise direction which, rather than always acting in the same direction, always acts towards midspan. It therefore reinforces the secondary flow towards midspan and so the wake at midspan is much thicker than for either of the other cascades. (This is also due to the increased blade loading at midspan, fig.3.16.) This increased convergence towards midspan along the suction surface is also apparent from flow visualization (compare figs.3.1b, 3.8c and 3.14c).

Overall mass-averaged loss and mixing loss will be presented and discussed in chapter 4.

3.4 Suction Surface Boundary Layer

3.4.1 Set 1 (unleaned)

The state of the suction surface boundary layer was determined using a flattened probe and stethoscope. A sudden, large increase in noise level clearly identified transition, which occurred over a surface distance of about 10mm at about 75% surface distance at midspan and progressively earlier nearer the endwalls. Oil flow visualization reveals a line just upstream of this (labelled "C" in fig.3.1b) which probably marks the position of a small laminar separation bubble which triggered transition. The oil film just downstream of this line is relatively thin with definite streaks, indicating a forward flow and showing that the extent of the separation bubble is very small. As the blade surface is nearly vertical in this region it is possible that gravity has slightly affected the position of the line in the oil. If the boundary layer was tripped by holding a piece of wire against the blade just upstream of the line, then the line disappeared. A sudden thinning of the oil film indicates that the surface shear stress increased as the line was crossed but there was no evidence of reverse flow on either side of the line: the mark at midspan in fig.1b is where accumulated oil had to be

wiped away to prevent it from running back down the blade when the flow was turned off.

Unsuccessful attempts were made to observe transition on the suction surface of set 1 using a hot wire held a small distance away from the suction surface. In the laminar boundary layer the hot wire detected a clear but incoherent signal at a frequency of about 2kHz which confused the measurements. This frequency is an order of magnitude lower than the expected Tollmein-Schlichting frequency (Schlichting, 1968) so the signal probably does not originate in the boundary layer. No such signal was observed in the free stream but it is conceivable that a disturbance which is too weak to be detected in the free stream may disturb the boundary layer slightly and so be picked up by a hot wire near the edge of the boundary layer. No firm conclusion has been arrived at concerning the origin of the signal.

The 2kHz signal in the laminar boundary layer was only just detectable by a hot film gauge glued to the surface, so this probably could have been used to pin-point transition. Measurements taken far apart were inconclusive, however, and to take any more measurements closer together would involve removing and remounting the film each time, a process which is time-consuming and risks damage to the film. In view of this, the high thermal conductivity of the aluminium, which would compromise accuracy, and the clear indication of transition already obtained by other methods, the hot film was not used any further on the blade surfaces.

3.4.2 Sets 2 and 3

Suction surface boundary layer transition on the leaned blades (set 2) is quite different from that on the unleaned blades. The spanwise pressure gradient causes marked spanwise flows within the laminar boundary layer (upstream of line "C" in fig.3.8c) which seem to prevent a laminar separation bubble. Transition is indicated by a change of direction in the oil patterns as the surface shear stress rises and forces the flow near the surface more towards the free stream direction, and by a decrease in oil thickness, indicating an increase in shear stress. This occurs at roughly 50% surface

distance at midspan. An increase in noise level at transition was still heard using the flattened probe and stethoscope but this increase was not as sudden as on set 1.

It may seem surprising in view of the striking effect of lean on blade surface pressures (fig.3.16) that there are no major turbulent separations on any of the bladerows, particularly at the negative end of set 2. Line plots of static pressure at a constant spanwise position are misleading in this case. Comparing contours of static pressure over the whole surface (fig.3.17b) with surface oil flow visualization (fig.3.8c) it is seen that no streamlines follow this rapid deceleration. Instead, low momentum fluid is carried away from the corner along a less unfavourable pressure gradient by the secondary flow.

Boundary layer behaviour on the suction surface of bladerow 3 is different again. Line "C" (fig.3.14c) starts near the leading edge where, as on set 1, it is not a transition or separation line but simply marks the interface between the laminar blade boundary layer and the turbulent boundary layer consisting of fluid swept up from the endwall. Beyond 33% surface distance, however, the oil layer upstream of the line (i.e. near midspan) is thick, with prominent streaks. Downstream of the line, around the $^1/_3$ span positions near 40% surface distance, the shear stress is clearly very low, with no streaks visible. Since the blade surface here is nearly vertical with the forward flow direction upwards, the absence of reverse oil flow suggests that there is no reverse air flow, i.e. the boundary layer is still attached. Nevertheless it must be close to separating, if not actually separated, and it is this which causes transition to turbulence. Transition was detected by the stethoscope a little further downstream (around 55% surface distance at midspan) and marked by dotted lines on fig.3.14c.

3.5 Endwall Boundary Layer

Results of measurements by the oil dot technique on the endwall of set 1 are presented in fig.3.20 together with "free stream" dynamic head derived from upstream stagnation pressure and local wall static pressure. The shear stress is very low near the saddle point and there is a ridge of high shear stress corresponding to the ridge of high velocities along

the line of the passage vortex. Behind the passage vortex lift-off line, particularly in the first half of the passage, the shear stress coefficient rises dramatically as the boundary layer is suddenly thinned by the passage vortex.

Hot film measurements in the same cascade are presented in fig.3.21 (N.B. fig.3.21c is a repeat of fig.3.20c). Given the poor accuracy of mean shear stress measurements by a hot film (see §2.6.1) and a number of seemingly spurious readings, the agreement between figs.3.20 and 3.21 is quantitatively reasonable and qualitatively very good. The minimum τ_w near the saddle point, the ridge along the line of the passage vortex and the sudden increase in C_F behind the lift-off line are all shown up by both methods.

Sets 2 and 3 (figs.3.22 and 3.23) show broadly similar behaviour. Shear stresses on the positive endwall of set 2 are lower than on set 1 because free stream velocities are lower, but shear stress coefficients are higher, possibly because the passage vortex is stronger and therefore keeps the boundary layer thinner. Since set 3 endwall shear stresses were measured using a different hot film gauge it would be unwise to compare absolute values of shear stress with the other two cascades.

Near the main loss core the edge of the endwall boundary layer cannot be defined from probe traverses because the loss core and boundary layer merge. Elsewhere, however, a momentum thickness θ based only on velocity magnitudes, i.e. neglecting skew, can be derived from three-hole probe traverse data and contours of Reynolds' number Re_θ based on this are presented in fig.3.24. These contours are approximate because they are based on traverses only at the locations given in table 2.2 (p.41) and because in places the boundary layer was too thin for an accurate evaluation of θ. Indeed, in part of the region labelled $Re_\theta<50$ the three-hole probe was too large to detect any boundary layer at all. The accuracy was sufficient, though, to show up the kinks in two of the contours on set 1 as they cross the lift-off line. These are further confirmation that the position of the lift-off line is not influenced by the presence of the probe.

Fig.3.24 shows clearly the extreme thinning of the boundary layer responsible for the high shear stress coefficients downstream of the lift-off line. Note that since the horseshoe/

passage vortex lies over the lift-off line rather than to one side, the endwall boundary layer is thinned upstream as well as downstream of that line. This implies that the fluid in the outer part of the incoming boundary layer does not reach the lift-off line. It must therefore either turn towards the suction surface more sharply than the lower-velocity fluid nearer the wall, or leave the endwall altogether and (presumably) become part of the passage vortex. The former option is highly unlikely so it seems that most of the incoming endwall boundary layer leaves the wall and enters the passage vortex at an early stage rather than first migrating across the endwall and up the suction surface.

Theoretical and experimental studies have shown that there is a limit of Re_θ below which it is virtually impossible for a boundary layer to be turbulent. Schlichting (1968) suggests that this limit is Re_θ=163 for a collateral boundary layer. This is the figure used in the transition model of Abu-Ghannam and Shaw (1980), although they report that under high levels of free stream turbulence boundary layers with Re_θ as low as 130 have sometimes been found to be turbulent. In practice the endwall boundary layer is far from collateral but one would expect the limiting value of Re_θ to be similar. Fig.3.24 therefore suggests that parts of the endwall boundary layer within the passage must be laminar.

The state of the endwall boundary layer could not be determined using a flattened probe and stethoscope, largely because it is extremely thin and highly skewed. A general increase in noise was heard as the probe was moved downstream or towards the blade suction surface but this may have been due to the growth of the boundary layer enabling the flattened probe to penetrate further into it. Transition therefore has to be inferred from raw hot film output traces.

Fig.3.25 shows a selection of hot film traces on the endwall of cascade 1. (Each trace is drawn to the same time and shear stress scales and has a true origin). The traces confirm that the boundary layer is laminar wherever Re_θ is less than 100. Turbulent bursts indicating transition cover a small area near the trailing edge plane, where the streamwise pressure gradient is still favourable but reducing. Transition begins where Re_θ is around 100-200 and $C_F \approx 0.004$ and ends where $Re_\theta \approx 500$. Only near the suction surface, i.e. close to the

high turbulence in the passage vortex, does the endwall boundary layer remain turbulent throughout.

On set 2 the lower free stream velocities near the positive endwall result in lower values of Re_θ. Transition begins at about the same position as on set 1 (fig.3.26), where Re_θ is still less than 200 ($C_F \approx 0.004$), but covers a much greater area of the endwall. Over most of the pitch the boundary layer is still not fully turbulent by the furthest downstream measurement location and the later transition results in a much slower growth of Re_θ than on set 1. The reason for the slower transition is that as the influence of lean on wall static pressures diminishes downstream of the trailing edge plane the pressure tends to reduce. The wall boundary layer thus experiences a slighly more favourable pressure gradient.

The extremely thin laminar boundary layer on the endwall is made possible because the old endwall boundary layer is completely removed from the wall ahead of the lift-off line. Oil flow visualization on the negative wall of set 2 (fig.3.8b) does not show a lift-off line across the passage. This suggests that the old boundary layer may not be completely removed and hence that the boundary layer on that wall may remain turbulent and (relatively) thick throughout the passage. Unfortunately, the cascade design did not enable this to be confirmed.

No endwall boundary layer traverses were performed on set 3 except at $x/C_x=1.23$, so values of Re_θ are not known within the blade passage. The lower free stream velocities near the endwall compared with set 1 seem to have had little or no influence upon the boundary layer state (fig.3.27). Note, though, how the lower exit flow angle near the wall of cascade 3 causes the transition patch to be inclined at a different angle from that on set 1 (fig.3.25).

CHAPTER 4

DISCUSSION

Incompressible flow will be assumed throughout this chapter.

4.1. Overall Loss Measurements

Mass average loss coefficients for the three cascades at x/C_x=1.23 are 0.048, 0.050 and 0.048 respectively. The experimental accuracy of loss coefficient is estimated to be ±0.003 (Appendix 3.5) so even the difference in overall loss between set 2 and the other two sets is not significant. Trailing edge thicknesses were only consistent to ±0.1mm within each set of blades and mean thicknesses were 1.9mm, 2.4mm and 2.1mm respectively for the three sets but the expected discrepancy in loss as a result of this is also less than experimental accuracy.

The overall loss from set 1 is represented schematically in fig.4.1, where it is shown divided into components in two different ways. The first is the conventional division into inlet loss, "profile" loss (defined as being equal to the midspan loss) and "secondary" loss (the remainder). As is to be expected from a low aspect ratio bladerow, the secondary loss accounts for a large part of the total.

The second method used in fig.4.1 to divide the loss into components entails limited area integration at x/C_x=1.23 (fig.4.2). Although the division between the endwall boundary layer and the passage vortex loss core is clear, that between the passage vortex and trailing filament loss cores is not, so this method is very approximate. Nevertheless, it does demonstrate that the main (i.e. passage vortex) loss core contains much more than just inlet boundary layer fluid but also includes a large part of the wake loss. This explains why this loss core dominates the exit flowfield even though the inlet boundary layer only accounts for just over 10% of the total loss. It also accounts for the observation by other workers (see

§1.5.1) that the "new" loss (i.e. exit minus inlet loss) is generally independent of the inlet boundary layer thickness.

The area of flow which can clearly be recognized as the endwall boundary layer only represents about a third of the "secondary loss" (as defined above) and only about 17% of the total "new" loss. This is despite the fact that the area of endwall downstream of the lift-off line, i.e. the area covered by "new" boundary layer, represents 23% of the total solid surface area within $-0.56<x/C_x<1.23$. The remainder of the secondary loss will arise from a number of sources, notably:

- Loss generated on the endwall but swept away by the passage vortex before $x/C_x=1.23$.
- Increased mixing upstream of $x/C_x=1.23$ caused by the secondary flow.
- Increased suction surface boundary layer loss away from midspan due to earlier transition.

Since the divisions in fig.4.1 are only approximate and since the midspan loss out of sets 2 and 3 is more strongly influenced by secondary flows, similar breakdowns of sets 2 and 3 overall loss would not be informative.

4.2 Comparison with Simple Predictions

Measurements on set 1 have been compared with the empirical loss correlations discussed in §1.5.1. Predicted profile loss coefficients were 0.078 (Ainley and Mathieson) and 0.040 (Baljé and Binsley) compared with 0.020 measured at midspan. The low measured loss is partly a result of the uncharacteristically thin trailing edge, but these figures still highlight the limited usefulness of simplistic correlations which ignore the detailed profile shape.

Dunham's secondary loss correlation, eq.(1,11), predicts 0.050. This includes the inlet boundary layer loss and it is not clear whether it is also meant to include downstream mixing losses. The mixing loss coefficient for set 1 calculated by eq.(1,6) is 0.013 so the prediction

should be compared with an experimental figure of either 0.028 or 0.041. Once again the limitation of a simplistic correlation is shown. In particular, the term in eq.(1,11) containing the inlet boundary layer thickness amounts to 0.029, more than half of the predicted secondary loss, compared with a measured inlet boundary layer loss of only 0.006.

Sharma and Butler's correlation, eq.(1,12), does not depend upon the inlet boundary layer and is much more accurate. Predicted (secondary loss/profile loss) is 2.0, compared with the measured value of 2.2. This method clearly has potential, although bear in mind that it does not predict mixing loss or model, for instance, the effect of blade lean.

A 2D boundary layer prediction can only reliably be applied at midspan on set 1: away from midspan on sets 1 and 3 and over the whole of set 2 there is considerable crossflow in the suction surface boundary layer, and oil flow visualization shows strong convergence towards midspan on the suction surface of set 3. The "NGTE" boundary layer program (discussed in §2.2) has been tested against suction surface boundary layer traverses at midspan on set 1. A good profile loss prediction based on a boundary layer calculation relies on a number of other aspects of the flow being predicted accurately. These are:

- The static pressure distribution;
- The point of transition;
- The trailing edge loss.

These factors have been eliminated by using measured pressures and transition point as input and only comparing the measured and predicted boundary layer upstream of the trailing edge. The comparison (see fig.4.3) is good – the predicted exit momentum thickness is just over 15% too small. This may not necessarily be an error in the prediction since secondary flows will thicken the midspan boundary layer by an amount which can neither be predicted by the 2D analysis nor measured.

4.3 Boundary Layer Loss

In §1.5.3(iii) it has been shown that one way to predict loss is to consider quite separately the entropy generation in boundary layers and by mixing in the free stream. The boundary layer loss can then be roughly predicted via the energy integral equation by assuming a constant value of the dissipation integral C_D (eq.(1,15) and (1,16)). The contribution of boundary layer loss to the cascade loss coefficient is then given by

$$Y_{BL} = \frac{2\rho C_D}{mU_2^2} \int U^3 dA_w \qquad (4,1)$$

where m is the overall mass flow and the integral is evaluated over all solid surfaces. Free stream velocities could be derived from inviscid two-dimensional or (ideally) three-dimensional flow predictions or from measurements. In practice, though, it is often not possible to define a "free-stream" velocity U near a given point on a solid surface, either because a nearby loss core means that there is no local "free stream" or because there are large velocity gradients even in the relatively loss-free parts of the flow. A better, and simpler, way to define a local value of U is to base it upon the upstream (i.e. "free stream") stagnation pressure p_{01} and the local surface static pressure p_w:

$$p_{01} - p_w = \tfrac{1}{2}\rho U^2 \qquad (4,2)$$

This is how the values of $\int U^3 dA_w$ presented below have been derived. Since static pressures were not measured on the negative wall of cascade 2, static pressures from the nearest five-hole probe measurements have been used instead.

4.3.1 Accuracy of the simple formula

Clearly a formula as simple as eq.(4,1) has several limitations:

(i) The most obvious has already been stated: mixing losses are not considered. These will include not only downstream mixing of boundary layers but also trailing

edge losses and mixing of secondary flows both upstream and downstream of the trailing edge;

(ii) The assumption of constant C_D holds for turbulent boundary layers only. For laminar boundary layers the dependence of C_D on both shape factor and Re_θ is stronger (fig.1.7c). In the cascades tested the entire pressure surface, up to 40% of the suction surface and a large area of the endwall are in fact covered by laminar boundary layers. In places, particularly near the leading edge, these boundary layers will be thin (i.e. $Re_\theta<100$) and so will have a dissipation integral higher than the assumed value. The converse will be true further downstream, since the pressure surface boundary layer is still laminar at the trailing edge (with Re_θ between 200 and 250) and transition at midspan on the suction surface does not occur until $Re_\theta \approx 1000$, 500 and 700 respectively the three sets. On the endwall the majority of the laminar part of the boundary layer has $Re_\theta>100$, with values of 200 or 300 being reached before transition occurs (see previous chapter). It is therefore not clear whether the overall average value of C_D will be higher or lower than typical values for turbulent boundary layers.

(iii) The line for turbulent boundary layers in fig.1.7c is based on Truckenbrodt's (1955) experiments over a range of shape factors $1.2<H<2.0$ (fig.1.7a). Even where the boundary layer is turbulent, the formula will not apply if the shape factor is well outside this range and C_D will not be constant if Re_θ varies widely. In particular, a separated boundary layer will not obey the relationship. In practice the dependence of C_D on Re_θ is only weak and no major separations were detected in any of the cascades tested. Even so, Re_θ of turbulent boundary layers varies from about 300 ($C_D \approx 0.0022$) just after transition on the endwall to about 4000 ($C_D \approx 0.0014$) at midspan just upstream of the trailing edge on the suction surface of set 3.

(iv) Eq.(1,16) was derived from measurements of collateral boundary layers, so there will be an error when the boundary layer is skewed. Gallus and Kummel (1977)

split C_D in the skewed boundary layer on the endwall into two orthogonal components but since shear stresses were not measured as part of this project this is not possible. A rough estimate of this error may be obtained using three-hole probe endwall boundary layer traverses from cascade 1. For a skewed boundary layer eq.(1,15), giving the dissipation rate, becomes

$$D = \rho U^3 C_D = \int_0^U \underline{\tau}.\underline{dv} \qquad (4,3)$$

(see appendix 5). For a laminar boundary layer this becomes:

$$D = \int_0^\delta \tau \frac{\partial v}{\partial y} dy = \mu \int_0^\delta \left(\frac{\partial v}{\partial y}\right)^2 dy \qquad (4,4)$$

If the right hand side of eq.(4,4) is evaluated for a skewed laminar boundary layer by expressing the velocity v as a vector then this gives the true dissipation integral C_D. If, on the other hand, it is evaluated by considering only velocity magnitudes then a smaller value of C_D is obtained which represents the dissipation integral of a boundary layer with the same velocity profile but which is collateral. The ratio of these two quantities will give an idea of the error due to the neglect of skew. (Although this argument is strictly only applicable to laminar boundary layers one would expect a similar relationship for turbulent boundary layers). Evaluating this ratio from endwall boundary layer traverses suggests an error less than 3% in most cases and below 10% in nearly all cases, despite boundary layer skews in excess of 50°. This error is relatively small because large values of $\partial v/\partial y$ only occur in the inner part of the boundary layer, where the rate of skew is quite small (Johnston, 1960).

In practice, then, (i) and (ii) are likely to lead to the largest errors in the predicted loss but (iii) and (iv) may also be significant.

4.3.2 Midspan Prediction

To give an indication of actual values of C_D encountered, predictions and measurements at midspan on set 1 are presented in fig.4.4. Note that it is only possible to make this comparison on set 1 since the flow through set 2 is not symmetrical about midspan and there is a strong convergence towards midspan on the suction surface of set 3, causing the boundary layer to be much thicker than a 2D boundary layer would be. The assumed value of C_D=0.0014, corresponding to a laminar boundary layer with $Re_\theta \approx 120$ or a turbulent boundary layer with $Re_\theta \approx 4000$, was chosen arbitrarily. Entropy generation is clearly dominated by the suction surface boundary layer and so the variation of C_D along the blade is dominated by the variation of Re_θ on the suction surface (figs.4.3 and 1.7c). Initially the true value of C_D is higher than the assumed value of 0.0014 due to the very thin boundary layer near the leading edge. (Interpolating between x/C_x=0.00 and the first measurement location at x/C_x=0.22 yields a mean C_D=0.0017). The boundary layer then remains laminar but thickens so C_D quickly drops (mean C_D=0.0008 between measurements at x/C_x=0.22 and 0.67). After transition ($x/C_x \approx 0.80$) C_D rises again to a mean of 0.0016 between x/C_x=0.83 and 0.99.

The constant C_D model only considers boundary layer loss. It takes no account of mixing outside boundary layers and therefore does not attempt to model the sudden increase in loss immediately downstream of the trailing edge. Downstream mixing loss at midspan may be estimated by the formula

$$\Delta Y = \frac{2\theta}{s} + \left(\frac{\delta^*+t}{s}\right)^2 - \frac{t}{s}C_{PB} - \frac{\delta_e}{s-t-\delta^*} \qquad (4,5)$$

where t is the trailing edge thickness, the pitch s is measured perpendicular to the mean flow direction and the base pressure coefficient is given by

$$C_{PB} = \frac{p_B - p_2}{p_{02} - p_2}$$

where p_B is the effective mean trailing edge pressure. A value C_{PB}=–0.1 is assumed. Work by Sieverding and Heinemann (1989) suggests that this probably gives a low estimate of the trailing edge loss. ΔY is marked on fig.4.4 and is seen to compare reasonably with the jump in loss just downstream of the trailing edge. The value of C_D=0.0014 which was assumed is seen to be reasonably accurate overall.

4.3.3 Endwall Boundary Layer Prediction

The only other area of the flow which can be clearly identified at x/C_x=1.23 (fig.4.2) is the endwall boundary layer, which is quite distinct from the wake. The pressure side leg of the endwall lift-off line (fig.3.1a) is prevented from reaching the blade suction surface by the corner vortex. It therefore seems reasonable to assume that most of the "new" endwall boundary layer fluid remains on the endwall rather than being swept up the suction surface with the "old" boundary layer fluid. It is therefore assumed that the loss flux found within 18mm of the wall at x/C_x=1.23 is approximately equal to the loss generation in the "new" boundary layer. On set 1 this contributes 0.0031 per wall to the overall loss coefficient. The corresponding calculated figure, assuming an average C_D=0.0014 over the endwall behind the lift-off line, is also 0.0031. (N.B. a precise evaluation of $\int U^3 dA_w$ over this part of the endwall would involve rather complex computation so for simplicity half the integral between x/C_x=0.0 and 0.5 plus the full integral between x/C_x=0.5 and 1.23 has been taken. The maximum error in $\int U^3 dA_w$ from this approximation is 5%).

4.3.4 Overall Prediction

Fig.4.5 shows the growth of overall loss coefficient through the unleaned cascade. Once again, predictions based on measured pressures with a constant C_D assumption model the growth of loss well. In particular they show that an increase in the rate of growth of loss just upstream of the trailing edge can be expected simply as a result of the high free stream velocities there and is not necessarily evidence for the existence of a

corner separation, as has sometimes been suggested (see §1.4.1). (The sudden jump in loss immediately downstream of the trailing edge is due to wake mixing, as in fig.4.4).

The C_D value assumed in fig.4.5 (0.0020) is very much higher than that which was used for the comparisons at midspan (fig.4.4) and on the endwall. This will be partly a result of earlier suction surface boundary layer transition away from midspan, discussed above, but it also suggests that loss generated by mixing outside the boundary layers is significant even upstream of the trailing edge.

It is apparent that mean values of the dissipation integral over a large surface such as the endwall or the entire blade surface at midspan may lie within a relatively narrow band. This might explain, for instance, why attempts to predict the development of the endwall boundary layer by two-dimensional prediction methods (e.g. Senoo, 1958, Gregory-Smith, 1982) have been moderately successful, since the predicted boundary layer, although it may be very different from the real boundary layer, is likely to have a similar mean C_D. It is also apparent, though, that large local variations of C_D, principally in the laminar boundary layers, and mixing losses outside the boundary layers, render Denton and Cumpsty's assumption unsuitable for accurate loss prediction. Nevertheless, it may still be useful for comparing different blade designs and, in the context of the present project, for analysing some of the effects of blade lean.

4.4 The Effect of Lean on Boundary Layer Loss

4.4.1 Free Stream Velocity

It is not possible to deduce the effect of lean on boundary layer loss directly from loss measurements because loss generation and loss migration cannot be fully separated. At x/C_x=1.23 on set 2, for instance, the "positive" half span carries 54.6% of the total mass flux but only 49.8% of the total loss flux. However, no conclusions can be drawn from this regarding the creation of entropy in the two halves because

spanwise secondary flow in the suction surface boundary layer carries low energy fluid between the two halves.

The first comparison will therefore be based on the $\int U^3 dA_w$ model, since the primary mechanism by which lean influences losses is via the free stream velocity. The static pressure contours in fig.3.17 represent, in effect, U^2. They show how both simple and compound lean reduce the general levels of U near the high pressure endwall but increase them at the opposite end (set 2) or midspan (set 3). Fig.4.6 shows this more clearly. $\int U^3 dA_w$ over the high velocity endwall is nearly twice that over the low velocity wall and compound lean reduces the endwall $\int U^3 dA_w$ by more than 10% compared with zero lean. By comparison the proportional effect on blade surface $\int U^3 dA_w$ is small – less than 5% – but the suction surface accounts for nearly $^2/_3$ of the overall value and so the net effect of lean is seen to be negligible.

This result would not necessarily apply to any bladerow, but for lean to give a significant reduction in $\int U^3 dA_w$ the endwall would have to have a greater overall significance. This implies that a net benefit would only be seen if the bladerow had an even higher pitch/chord ratio or lower aspect ratio than the one considered here.

4.4.2 Blade Boundary Layer Transition

For these cascades, then, lean does not affect overall loss by changing free stream velocity levels. If there is an effect on boundary layer loss it must be through a change of boundary layer state.

Pressure surface boundary layers were laminar throughout. It has been seen in chapter 3 that lean can move the point of transition on the suction surface by up to 20% surface distance at midspan. It is hard to quantify experimentally the effect on loss of this movement of the transition line because transition could not be brought forward substantially without using such a large trip that it would itself influence the loss. The "NGTE" 2D boundary layer calculation (see §2.2) predicted that if transition is brought forward by 20% surface distance then the midspan loss coefficient would rise by about

0.004. The increase away from midspan would be less than this, since transition occurs earlier in any case, so the effect on overall loss would be very small. In an engine environment, high free stream turbulence would force earlier transition irrespective of lean, so the influence of lean would be less still.

4.4.3 Endwall Boundary Layer Transition

Positive lean (i.e. tending to increase the static pressure at the endwall) will influence the loss generated in the "new" endwall boundary layer in three ways:

(i) Free stream velocity levels are reduced (figs.3.17 and 4.6). This will reduce the loss.

(ii) Transition is delayed (figs.3.25-27). This will also tend to reduce the loss.

(iii) The area of endwall covered by a very thin laminar boundary layer ($Re_\theta<100$) is increased (fig.3.24). This is likely to increase the loss (see fig.1.7c).

Once again the assumption is made that the loss generated on the endwall behind the main lift-off line is all found within 18mm of the wall at $x/C_x=1.23$. In table 4.1 this is compared with predictions based on measured static pressures and assuming $C_D=0.0014$, as in §4.3.3. The figures in table 4.1 represent the contribution from one endwall to the overall exit loss coefficient.

	Set 1	Set 2 (positive end)	Set 3
Measured loss within 18mm of endwall at $x/C_x=1.23$	0.0031	0.0025	0.0029
Predicted "new" endwall loss assuming $C_D=0.0014$	0.0031	0.0022	0.0027

Table 4.1 Loss originating in new endwall boundary layer

The reduction in free stream velocities due to lean does indeed reduce the new endwall loss, but by less than the constant C_D model predicts. These figures are only approximate but they show that, at best, the reduction in endwall loss is no more than might be expected from considerations of velocity changes alone. Even though positive lean delays endwall boundary layer transition, any benefit which might arise from this is cancelled by the overall reduction of the endwall boundary layer Re_θ within the passage.

4.5 Mixing Loss

Loss, mixing loss and secondary kinetic energy coefficients are defined in appendix 4.1 and §1.4.2. Table 4.2 shows measured values of these quantities.

Set	$\bar{Y}$	Y_{MIX}	Y_{SKE}	Y_{SKE}/Y_{MIX}
1	0.048	0.0132	0.0120	0.91
2	0.050	0.0207	0.0169	0.82
3	0.048	0.0116	0.0099	0.85

Table 4.2 Mixing loss etc. derived from measurements.

The calculation of mixing loss in §1.4.2 is based on the assumption that mixing takes place at constant area to a completely uniform flow downstream. Before drawing conclusions from values calculated in this way it is necessary to consider how realistic this assumption is.

4.5.1 Spanwise variation of Mean Flow Angle

At exit from set 2 (fig.3.18b) there is an underlying linear variation of mean exit flow angle of about $\pm 4^1/_2°$, arising from the spanwise variation of blade loading. This would probably be recovered by a following bladerow with very little loss (provided

that bladerow had been properly designed to accept the incidence variation). It is therefore more appropriate to calculate set 2 mixing loss assuming that the mixed-out flow still has a linear spanwise variation of flow angle of $\pm 4^1/_2°$. Appendix 6 shows that if this is done then Y_{MIX} should be reduced by 0.002.

Even after applying this correction, Y_{MIX} from set 2 is still much higher than from sets 1 and 3. This is because there is a net radial flow at $x/C_x=1.23$ (fig.3.10) and eq.(1,6) assumes that all radial velocities contribute directly to mixing loss. In practice, however, these radial velocities would diminish further downstream as the mean streamlines reached their equilibrium position (see fig.3.7). At this equilibrium position the spanwise variation in axial velocity would be greater than at $x/C_x=1.23$ so the variation in flow angle would be greater than $\pm 4^1/_2°$. The correction to mixing loss should therefore be greater than the value of 0.002 derived in appendix 6. It is hard to see what the correction should be, however, so we will simply say that truly representative values of Y_{MIX} and Y_{SKE} for set 2 should be much lower than those given in table 4.2.

At exit from all sets the passage vortex has a prominent effect on mean flow angle (fig.3.18). If these mean variations remain as the vortices decay then they too could be accommodated by a following bladerow without contributing to mixing loss. Most measurements of the mixing process downstream of cascades (e.g. Binder and Romey, 1983, Hodson and Dominy, 1987b and Moore and Adhye, 1985) are inconclusive in this respect. Kawai et al. (1985) show the decay process more clearly. They show the passage vortex becoming more circular and axisymmetric (about its own axis) as it decays, indicating that mean yaw angle variations are not preserved. Even if the vortices do not decay fully before entering the next bladerow the vigorous manner in which they are chopped makes it unlikely that the spanwise variation of mean yaw angle would be recovered. It therefore seems reasonable to assume that none of the energy of the passage vortices is recoverable and to calculate set 1 and 3 mixing losses based on a completely uniform flow downstream.

4.5.2 Effect of a following bladerow

§1.4.3 has shown that in a real turbine the stator exit flow will not be fully mixed out before it enters the rotor, so the simplified mixing analysis of §1.4.2, even with the correction for set 2 described above, does not represent the real mixing process. The real flow, with acceleration, turning, wake and vortex chopping and unsteady effects is extremely difficult to model but this section will attempt to show the effect of acceleration by analyzing two idealized flows.

(i) Collateral Boundary Layer or Wake

Consider a flow with free stream velocity U_1, free stream stagnation pressure p_{01} and mass average stagnation pressure $\bar{p}_{01}$, containing a collateral boundary layer or wake with momentum thickness θ_1 in each pitch s_1 (measured perpendicular to the flow). Since the flow is collateral the secondary kinetic energy is clearly zero.

Now consider isentropic acceleration or deceleration to a new condition denoted by U, θ and s, followed by mixing at constant area to a uniform flow with stagnation pressure p_{0M}. Provided the wake or boundary layer is thin or shallow before mixing occurs, the total loss coefficient is given by

$$\frac{p_{01}-p_{0M}}{\frac{1}{2}\rho U^2} = \frac{2\theta}{s}$$

$$\therefore \quad \frac{dp_{0M}}{dU} = -\frac{d}{dU}\left(\frac{\rho U^2\theta}{s}\right)$$

By continuity, if the flow is incompressible and the wake is thin,

$$U\,s = U_1\,s_1$$

$$\therefore \quad \frac{dp_{0M}}{dU} = -\frac{\rho}{U_1 s_1}\frac{d}{dU}(U^3\theta)$$

$$= -\frac{\rho}{U_1 s_1}\left(3U^2\theta + U^3\frac{d\theta}{dU}\right)$$

But since the velocity change is isentropic there are no external shear stresses so the boundary layer momentum integral equation becomes

$$U\frac{d\theta}{dU} = -\theta(H+2)$$

so

$$\frac{dp_{0M}}{dU} = \frac{\rho U^2\theta}{U_1 s_1}(H-1)$$

The effect of the acceleration/deceleration on the mixing loss based on the original free stream conditions is therefore given by

$$\frac{d}{dU}(Y_{MIX}) = \frac{d}{dU}\left(\frac{\bar{p}_{01}-p_{0M}}{\frac{1}{2}\rho U_1^2}\right)$$

$$= -\frac{2U^2\theta}{U_1^3 s_1}(H-1)$$

and since the shape factor H must always be greater than unity $d(Y_{MIX})/dU$ must always be negative. It follows that acceleration of a collateral flow before mixing always decreases the mixing loss, and vice versa.

Denton and Cumpsty (1987) considered an initial flow with free stream velocity U_1 and a "wake" of uniform velocity $(U_1-\Delta U)$ which filled 10% of the total flow area. This flow is then accelerated to a new free stream velocity U_2 before mixing to a uniform flow and the mixing loss coefficient (based on $\frac{1}{2}\rho U_1^2$) is calculated. The results of their calculations are presented in fig.4.7.

(ii) Streamwise Vortex

Consider an incompressible flow through a circular pipe of radius r_3 comprising:

$0 \leq r \leq r_1$ A forced vortex with uniform axial velocity;

$r_1 \leq r \leq r_2$ A free vortex with uniform axial velocity and hence uniform stagnation pressure. Pressure and axial and tangential velocity are continuous at radius r_1. Maximum tangential velocity (at r_1) = $v_{\theta max}$.

$r_2 < r \leq r_3$ Uniform axial velocity U_1 with zero swirl and uniform stagnation pressure p_{01}. Static and stagnation pressures are continuous at radius r_2 but axial and tangential velocities are not.

Now consider acceleration or deceleration (without mixing) to a new condition where the velocity in the outer region is U_2, followed by mixing at constant area with no net external forces to a uniform flow with zero swirl. (Note that although zero net external forces are assumed there must have been a net external torque to remove the swirl. This is not necessarily unrepresentative of a real flow since at exit from a symmetrical linear cascade there are two vortices, of opposite sign, which could be assumed to cancel one another out without any externally applied torque.)

This flow has been calculated numerically (see appendix 7) and $\bar{Y}$, Y_{MIX} and Y_{SKE}, all normalised by $\frac{1}{2}\rho U_1^2$, have been evaluated for the accelerated/decelerated flow just before mixing begins. Values assumed are $(r_1/r_2)=0.3$, $(r_2/r_3)=0.7$ and $(v_{\theta max}/U_1)=0.25$, estimated from set 1 measurements ($x/C_x=1.23$, fig.3.2). The effect of acceleration or deceleration on mixing loss is the opposite to its effect on a collateral flow. If the free stream velocity increases then the vortex radius reduces. As a result tangential velocities, and hence Y_{SKE} and Y_{MIX}, increase. The mixing loss is roughly proportional to the free stream velocity at the start of mixing (see fig.4.8) except at very low velocities when the forced vortex core is close to reversing.

Incidentally, this may be one explanation for the effectiveness of endwall grooves or fences: they cause the secondary vortices to mix out earlier, i.e. at a higher pressure, thus incurring less mixing loss.

4.5.3 Experimental Mixing Data

A number of points should be noted from table 4.2:

- It has already been pointed out in §4.5.1 that Y_{MIX} and Y_{SKE} for set 2 are unrealistically large.

- In common with other investigators' findings, the mixing losses are large compared to the measured losses (about $^1/_4$). Mixing losses should never be ignored when analysing blade performance and great care needs to be taken to ensure that a realistic figure is arrived at.

- Y_{SKE}/Y_{MIX} must be zero for a collateral boundary layer or wake and it has been shown to be very close to unity for a streamwise vortex (appendix 7). Values of Y_{SKE} should be interpreted with caution since it has no physical meaning and since Moore et al. (1987) have shown how kinetic energy can be transferred, via pressure terms and turbulence, between the three co-ordinate directions (see §1.4.2). Nevertheless, actual values of Y_{SKE}/Y_{MIX} are large, indicating that the majority of mixing loss arises from destruction of the secondary vortices rather than as a result of primary velocity deficits in the endwall boundary layer and wake.

We would therefore expect from the arguments in §4.5.2 that acceleration in a following bladerow would increase rather than decrease the mixing loss, so the values given in table 4.2 are probably an underestimate. Furthermore, since Y_{SKE} for set 3 is 17% less than set 1, the increase would be less severe downstream of set 3.

- Set 3 has a 12% lower Y_{MIX} than set 1. The reason for this can be explained by comparing the ratio $Y_{MIX}/\bar{Y}$ for a streamwise vortex and a collateral boundary layer. For a collateral boundary layer

$$\bar{Y} = \delta_e/s$$

$$\text{and} \quad (\bar{Y} + Y_{MIX}) = 2\theta/s$$

$$\therefore \; Y_{MIX}/\bar{Y} = 2\theta/\delta_e - 1$$

Truckenbrodt assumed $\delta_e/\theta=1.72$ for a turbulent boundary layer (table 1.2, p.25) so $Y_{MIX}/\bar{Y}$ is only 0.16. In contrast, appendix 7 has shown that $Y_{MIX}/\bar{Y}$ is 2.6 for a typical streamwise vortex. Thus a given amount of entropy occurring at midspan acts only to thicken the wake and so is likely to contribute relatively little to the mixing loss, whereas the same amount of entropy near the endwall is likely to reinforce the passage vortex and therefore lead to much more mixing loss. The overall loss from set 3 is the same as set 1 but Y_{SKE} and Y_{MIX} are lower because more of the loss is concentrated at midspan (fig.3.19). This is partly because a greater proportion of the overall loss is generated near midspan, for reasons which have already been discussed (see for example fig.4.6). It is also because the spanwise static pressure gradient tends to make suction surface boundary layer fluid migrate towards midspan early in the bladerow.

4.6 Real Turbine Flow

It is recognized that the flow in a linear cascade is not representative in every respect of the flow in a turbine. This section speculates on the effects of some of the features of turbine flow on the findings of this investigation.

4.6.1 Stage Performance

It is assumed that the cascade tested for this project represents a stator row which would, in practice, form part of a full turbine stage. Compound lean has been shown to

decrease the mixed-out loss coefficient of the bladerow but the resultant improvement in stage efficiency would depend upon a number of factors:

- The stage reaction.
- The effect of the presence of the rotor on mixing losses arising from the stator secondary flows. This has already been discussed in §4.5.2.
- The effect of the stator exit flow on the rotor losses.

The rotor loss may be affected in several ways. The overall mean stator exit flow angles are –65.5°, –64.8° and –66.3° from axial respectively from the three sets. If stator lean is to be introduced as a design change, due attention must be given to re-matching the rotor, particularly with straight lean when the change of stator exit angle at a given radius may be especially large. This would almost certainly result in a different rotor loss coefficient. Alternatively, the stator could be redesigned to bring the exit flow angle back to its original value, but this would probably change the stator loss coefficient.

The passage vortices give rise to a significant spanwise variation of stator exit flow angle (fig.3.18). Compound lean reduces the strength of the stator secondary flows and hence reduces this variation from 12.7° to 7.9°. This is more significant than fig.3.18 would suggest because it is magnified by the relative motion of the bladerows. For instance, fig.4.9 shows the stator exit flow viewed in a frame of reference relative to the rotor of a 50% reaction stage. In such a stage, compound lean of the stator would reduce spanwise variations of rotor incidence from 22.8° to 14.3°. This improvement is likely to reduce rotor losses, particularly away from the design operating point.

By reducing the strength of the stator secondary flows, compound lean also reduces the unsteadiness in the relative inlet flow to the rotor. This, too, would probably reduce rotor losses.

4.6.2 Blade Reynolds' Number and Free Stream Turbulence

The cascade tests were performed at a Reynolds' number (based on exit flow and true chord) between 8.5×10^5 and 9.0×10^5. This is reasonably representative of turbine flow conditions. Higher Reynolds' numbers would bring transition forward whereas lower speeds would delay transition and might therefore allow a laminar separation to occur on the suction surface. No measurements were taken at any other flow speed but it was confirmed using a wool tuft that there were no major boundary layer separations on set 3 even when the Reynolds' number was reduced to 1.0×10^5.

The inlet turbulence (r.m.s./mean velocity) for the cascade tests was only 0.4%, which is much less than would be encountered in practice. Suction surface transition in the cascade occurred quite late at midspan (see §4.4) whereas realistic turbulence levels would be likely to bring this forward. Boundary layer predictions on the suction surface at midspan on set 1 (see §4.2) indicate that if transition occurred as soon as Re_θ reached 160 (i.e. at 13% surface distance) it would result in a 0.43mm larger momentum thickness at the trailing edge. This would give rise to an increase of nearly 0.010 in midspan loss coefficient. The change in overall $\bar{Y}$ would obviously be less than this, perhaps around 0.003, because transition occurred earlier away from midspan even in the wind tunnel.

In contrast the endwall boundary layer only remained laminar while it was very thin ($Re_\theta<200$). The boundary layer state would therefore probably be the same in a turbine as in the cascade, irrespective of the free stream turbulence level, provided the lift-off of the inlet boundary layer was not fundamentally changed.

4.6.3 Endwall Boundary Layer Lift-off

On set 2 at the low pressure end the acceleration of the incoming boundary layer causes it to skew in such a way that the blade incidence within the boundary layer is reduced. This has the effect of moving the saddle point right up to the blade leading edge (fig.3.8) so that the lift-off line is only a local phenomenon which does not cross

the passage. It can be surmised that most of the endwall boundary layer remains on the endwall and therefore remains relatively thick and turbulent, although this could not be confirmed experimentally. At inlet to all bladerows in a turbine except the first nozzle the relative motion of the blades results in the inlet boundary layer being skewed in roughly the same way (without acceleration). It is conceivable that it might influence the endwall flow in the same way, too. Note, however, that Walsh and Gregory-Smith (1987) did not find this to be the case. Inlet boundary layer skew changed the position of their lift-off lines but did not remove them altogether.

4.6.4 Other Influences

The effect of the radial pressure gradient in an annular geometry and the use of simple lean to counteract this have been discussed in chapter 1.

A high subsonic Mach number would change the static pressure field for a given blade shape, but the influence of lean would not be expected to be fundamentally different. Lean might have a more radical effect on a transonic flow, however, by changing the position of, or even causing or preventing, shock waves. A particularly powerful example of this is the use of stator simple lean in low hub/tip ratio turbines to reduce the hub Mach number.

If the bladerow inlet flow is heavily distorted in some way (non-uniform stagnation temperature, stagnation pressure or flow direction) then this will clearly affect the flow. Lean might be used to counteract detrimental effects but this is outside the scope of the present project. Each individual case would have to be considered on its merits.

The very large unsteadiness associated with passing of upstream blade wakes may change the endwall flow but this connot be determined from the current experiments. Work by Hebert and Tiederman (1989) on a cascade with moving bars upstream indicate that the effect of a passing wake is only temporary, with the secondary flow reverting to a quasi-steady state in between wakes.

CHAPTER 5

NUMERICAL PREDICTIONS

Two-dimensional flow predictions are useful in the early stages of turbine design but they cannot, in general, deal with blade lean and they can never predict secondary flows. For the kind of turbine blade tested in this project, whose performance is dominated by secondary flows, a truly three-dimensional prediction technique is necessary. In this chapter one such technique, Denton's time-marching program, is compared with cascade test data.

5.1 Practical Details

Two versions of Denton's program were used:

(i) The basic (inviscid) Euler solver, BAS3D28;

(ii) A viscous version, LOSS3D30, which has a simple boundary layer loss model incorporated. In LOSS3D30 the skin friction is calculated by assuming a law-of-the-wall profile between the wall and the next calculation node and an eddy viscosity is derived from simple mixing-length theory. The version used (subroutine LOSS5) assumes that all boundary layers are turbulent.

The grid used was 32×65×32, extending from x/C_x=–0.97 to x/C_x=1.61, and is shown in fig.5.1. For the symmetrical bladerows (sets 1 and 3) only half a span was used so the density of nodes in the spanwise direction, on average, was twice that on set 2. The same grids were used for the inviscid and viscous versions, although in principle the inviscid program does not need such a fine grid near the blade surfaces since there should be no blade boundary layers.

The endwall boundary layer used as the upstream boundary condition at x/C_x=–0.97 was based on measurements at x/C_x=–0.56 but the discrepancy was not thought to be significant as the predicted increase in loss coefficient between these two locations was less

than 0.005. Details are given in table 5.1. The downstream static pressure was set to 90000 Nm^{-2} and the inlet boundary layers on the two endwalls of set 2 were identical. Fig.5.2 shows that the outer part of the boundary layer was resolved well but that even this fine mesh could not resolve the inner part.

Sets 1 and 3		Set 2	
z (mm)	p_0 (Nm^{-2})	z (mm)	p_0 (Nm^{-2})
0.00	97281	0.00	97281
0.30	98000	0.53	98099
0.65	98150	1.26	98325
1.09	98280	2.32	98564
1.66	98430	3.79	98801
2.40	98580	5.90	99067
3.34	98740	8.85	99401
4.53	98900	13.06	99809
6.01	99080	19.38	99989
7.84	99291	28.86	99998
10.21	99550	42.03	100000
13.17	99819	57.83	100000
16.86	99980		
21.30	99995		
26.48	99998		
32.40	99999		
39.05	100000		
46.45	100000		

Table 5.1 Inlet endwall boundary layer input to time-marching

To convert boundary layer measurements to stagnation pressures for use as an upstream boundary condition, a value of upstream static pressure has to be assumed. The assumed value turned out to be wrong, so that the predicted upstream static pressure (97500 Nm^{-2}) was higher than the stagnation pressure at the wall. The program corrects for this by locally altering the static pressure so that the velocity remains finite. Additional inviscid predictions with a modified stagnation pressure at the wall were obtained. They are not presented here

but they confirmed that the change in wall stagnation pressure had no effect on the overall predictions, particularly the results reported in §5.2 below.

The program becomes slow to converge at very low Mach numbers so an exit free stream Mach number 0.39 was specified, compared with 0.14 for the experiments. Program convergence is monitored by calculating the change in meridional velocity per time step at each node and expressing the maximum and average magnitudes of this as percentages of the mean velocity for the entire flowfield. In all cases the calculation was allowed to proceed until this quantity ceased to diminish. Final average values were between 0.001% and 0.003%. The program consumed approximately 3 hours CPU per 1000 time steps on an Alliant FX/80 single vector processor and full convergence generally took between 2000 and 3000 steps. LOSS3D30 did not take appreciably longer to run than BAS3D28.

5.2 Inviscid Predictions (set 1)

The blade profile in question has a particularly large radius of curvature at its minimum axial position. This leads to a highly distorted calculation grid which tends to give rise to generation of numerical entropy (i.e. entropy arising out of numerical errors rather than the flow physics). A close grid spacing was used near this point and several grids tried until a suitable one was found. With no inlet boundary layer, and hence no secondary flow, the numerical entropy generation by the inviscid program was negligible. With an inlet boundary layer it was still small at the leading edge but there was considerable entropy generation near and at the trailing edge (fig.5.3). This is probably a result of the skewed grid in the latter part of the passage (fig.5.1) and the fact that secondary flow causes the axial component of velocity to fall very near to zero near the endwall (fig.5.4).

When performing a number of similar time-marching calculations CPU time can be saved by using one solution as an initial guess, or "restart", for another calculation. Two inviscid solutions are shown in figs.5.3 & 5.4. These used identical input datasets and were both fully converged, but they started from different restart files. The principal difference was that run A started from a viscous solution whereas run B used an inviscid solution. The only other differences between the restarts were in the second level of multigrid and the

amount of negative feedback used to supress instabilities. Runs A and B will be compared with set 1 experimental results before proposing reasons for the discrepancy between the two predictions.

5.2.1 Comparison Between Predictions and Measurements

The predicted endwall flow is shown in fig.5.4, which should be compared with flow visualization (fig.3.1a). Figs.5.5-5.8 show secondary velocities and stagnation pressures. These are directly comparable with figs.3.2 & 3.6 except that the pitchwise positions relative to the blades of the measurement and calculation "windows" downstream of the trailing edge are different and to save space the predicted data are not reflected about midspan.

Neither prediction shows the suction side leg of the horseshoe vortex. This is not surprising since the centre of the horseshoe vortex, where it forms, is only six grid nodes away from the endwall and the suction side leg would have to pass in the pitchwise direction around the leading edge through a region where the grid is highly distorted. There is some evidence for a suction side leg, however, in the fact that at x/C_x=0.03 and x/C_x=0.22 the endwall boundary layer is markedly thinner adjacent to the suction surface.

The pressure side leg is not so clear as in the measurements but it is discernible at x/C_x=0.22. Both predictions show very clearly the pressure side leg growing into the passage vortex and moving towards and along the suction surface, but at very different rates, so that the vortices are in very different positions at the exit plane. The physical size of the vortex is predicted correctly but in both cases it is too weak. Secondary velocities are much lower than were measured and hence the predicted secondary kinetic energy coefficient Y_{SKE} at x/C_x=1.23 is too small (0.0056 and 0.0036 from runs A and B and 0.0041 from the viscous prediction compared with 0.0120 from experiment). This finding is not unique to this program or this bladerow. Gregory-Smith (1989) found that three similar time-marching programs, including Denton's, all predicted

secondary flows which were too weak on a turbine bladerow tested at Durham university.

Fig.5.9 shows three predictions of pitchwise average exit flow angle. Only the position of the passage vortex varies: the overall mean angle (–66.2°) and the amount of over- and under-turning are the same in each case.

Two other features of the real flow at x/C_x=1.23 are predicted: the trailing filament vortex in the wake, rotating in the opposite direction to the passage vortex; and the accumulation of endwall boundary layer loss near the suction side. This latter feature is surprising since there should be no "new" endwall boundary layer loss from an inviscid prediction. Either the inner part of the inlet endwall boundary layer remains on the wall and is not swept across the passage until a late stage or, more likely, some numerical entropy does indeed arise at the endwall because of the boundary layer skew.

5.2.2 Discrepancies Between Inviscid Predictions

The discrepancies between the two inviscid predictions appear to stem from the formation of the horseshoe vortex (fig.5.4). The saddle point (i.e. the point where the incoming boundary layer first separates) is further upstream in run A and there is more reverse flow immediately behind it. This is thought to be because of a "switch" in the program when the axial velocity becomes negative. The viscous solution from which run A started may have had more reverse flow which did not switch back after the restart. The pressure side leg of the endwall lift-off line can be identified by following the velocity vectors from the saddle point to the point on the suction surface where the flow direction suddenly ceases to be parallel to the blade outline. In both cases the lift-off line is too far upstream compared with fig.3.1a: run A puts it furthest upstream and more distinct, with the flow behind it skewed further from axial.

If the details of the separation of the upstream boundary layer and formation of the horseshoe vortex can have such a marked effect on inviscid predictions this implies that such details must be predicted correctly if the overall predicted flow is to be correct.

One important distinction between the predictions and measurement has yet to be mentioned. The measurements show loss and vortex cores to be roughly coincident at bladerow exit whereas both predictions show them to be completely separate. Also, in the first half of the passage, measurements reveal two loss peaks corresponding to the two legs of the horseshoe vortex whereas there are no peaks shown by the predictions, only a general migration towards the suction surface. An explanation for this is that in practice most of the incoming endwall boundary layer fluid leaves the endwall ahead of the lift-off line and forms a strong passage vortex/loss core, whereas in the prediction most of it remains on the endwall. The little which does lift off forms a discrete but weak passage vortex. The rest is swept along the endwall and suction surface by this vortex and by the blade-to-blade pressure gradient, so at bladerow exit it is found in the wake rather than in the passage vortex.

In an inviscid flow through a bladerow the total exit secondary circulation is fixed by the inlet endwall boundary layer and the bladerow turning. One might therefore expect that, provided the effects of viscosity are small, any three-dimensional flow calculation should predict the overall secondary flow reasonably well even though the details may not be accurately modelled. However, although the turning angle fixes the total secondary circulation it does not fix the strength of the secondary flows, which depend also on the precise blade shape. Prediction of the strength of the secondary flow is therefore dependant to some extent on detailed flow predictions rather than merely the gross flow. The differences between runs A and B have shown that the overall secondary flow prediction may be extremely sensitive to certain detailed predictions, notably the endwall boundary layer separation and horseshoe vortex formation.

5.3 Viscous Predictions (all three sets)

In view of the uncertainty which has been demonstrated in inviscid predictions it would not be constructive to compare the two programs to determine the influence of viscosity on secondary flows. However, given the choice between the two programs, since the viscous

one has the potential to model the growth of blade and endwall boundary layers without any appreciable penalty in CPU time (for the same grid), there is no reason not to use it in preference to the inviscid program. Viscous predictions for the three sets of blades tested will now be presented and discussed.

5.3.1 Overall Predictions

Overall measured and predicted quantities for the three blade sets are shown in table 5.2. The flow angle predictions are quite good, and broadly reflect the measured differences between the three bladerows. The predicted loss is consistently too high: this will be partly a result of numerical entropy but will also be due to the assumption of turbulent boundary layers throughout. The accuracy and consistency of time-marching loss predictions are unfortunately not good enough to draw a conclusion from the similarity between the three predicted values. The predicted mixing loss is only slightly low, although it should be remembered that the low predicted secondary kinetic energy and the high predicted loss will tend to have opposite effects on mixing loss.

		Mean exit flow angle	$\bar{Y}$	Y_{MIX}	Y_{SKE}	Y_{BL} (eq.4,6) C_D=0.0020
Set 1:	Measurement	–65.5°	0.048	0.0132	0.0120	0.034
	Prediction	–66.2°	0.064	0.0089	0.0041	0.031
Set 2:	Measurement	–64.8°	0.050	0.0207	0.0169	0.034
	Prediction	–64.9°	0.064	0.0189	0.0130	0.031
Set 3:	Measurement	–66.3°	0.048	0.0116	0.0099	0.034
	Prediction	–66.2°	0.066	0.0111	0.0056	0.032

Table 5.2 Measured and Predicted Overall Flow at x/C_x=1.23

The spanwise variations of loss flux (fig.5.10) confirm that the predicted loss is too high and that the positions of the loss cores are not predicted consistently. On set 3 the loss cores even merge at midspan, a feature which is not seen in the measurements. Pitchwise average exit flow angles (fig.5.11), however, show that not only is the overall mean flow direction predicted fairly accurately but also the gross spanwise variation from set 2 is modelled well. The characteristic over- and under-turning due to the passage vortex is apparent but is generally much too weak.

Boundary layer losses predicted from surface static pressures using eq.(4,6) have been presented in table 5.2. The value C_D=0.0020 was chosen to be consistent with the previous chapter. Measured and predicted values are in broad agreement except that predicted values are all slightly lower than measured ones. This is partly because the predictions have been carried out at a higher Mach number, so since all pressures and losses are normalized using exit dynamic head the predicted inlet dynamic head is lower than the measured one.

5.3.2 Detailed flow predictions

Predicted flow at exit from sets 1 and 3 is shown in fig.5.12. As with the inviscid predictions on set 1 the passage vortices are too weak and do not coincide with the loss cores. Because there is a suction surface boundary layer as well as an endwall boundary layer, high-loss fluid is carried further around the vortex than in the inviscid predictions.

Comparing fig.5.13 with fig.3.12 it is seen that the effect of lean on static pressures is modelled well, with contours generally remaining roughly normal to the endwalls. Since pressures and gross variations in exit flow angle are well modelled, so is the deflection of the mean streamlines (figs.5.14 and 3.7). This affects the two inlet endwall boundary layers in the way which has been discussed in chapter 3, so that the difference between the two endwall flows (figs.5.15 and 3.8) is seen clearly. At the positive wall the saddle point is well upstream and away from the leading edges with a prominent lift-off line crossing the passage near the leading edge plane. There is no

evidence of a corner vortex to prevent the line from reaching the suction surface and the point where it does so is marked by a sudden change in flow direction. At the negative wall the thinner boundary layer and slightly lower incidence within the boundary layer cause the saddle point to be very near to the leading edge. Although a lift-off line can be traced from this point there is only a weakly convergent flow towards it and it meets the suction surface almost at a tangent.

The contrast between the flow at the two ends of the leaned bladerow results largely from the difference in static pressure and so figs.5.16 and 5.17 show this contrast reasonably well (compare figs.3.10 and 3.13). The thicker inlet boundary layer at the positive end gives rise to a more prominent loss core, although there is still no evidence of a suction side leg of the horseshoe vortex as seen at x/C_x=0.22 in fig.3.13. The passage vortex at the positive end is not as strong as in the measurements but it is stronger than at the negative end.The contrast between the flows in the two halves at x/C_x=0.67 and 0.83 is partially obscured in fig.5.17 by the fact that the suction surface boundary layer is too thick and there is no tight horseshoe vortex/loss core near the suction surface at the negative end. Despite this, and the error in spanwise location of the passage vortex, the exit over- and under-turning (fig.5.11) is predicted more accurately at the negative end of set 2 than anywhere else. Since this is the only endwall where oil flow visualization did not show a prominent lift-off line, this may be further confirmation that it is the failure to predict the lift-off accurately which leads to an underestimation of the strength of secondary flows.

Fig.5.18 shows predicted surface static pressures and should be compared with fig.3.17. Absolute levels as well as qualitative patterns are generally predicted well. The effects of the passage vortex (low pressure along the endwall lift-off line and minima on the suction surface and endwall towards the trailing edge) are visible but weak. The minimum suction surface pressure is not low enough on any of the blades. This may be an effect of the suction surface boundary layer being too thick, and on the curved blades it is aggravated by the loss cores being too close to midspan.

CHAPTER 6

CONCLUSIONS AND SUGGESTIONS FOR FURTHER WORK

A single, high-turning turbine blade profile has been tested in a low-speed linear cascade in three stacking configurations: zero lean; simple (straight) lean at 20° and compound (curved) lean (30° at each end). The following conclusions and suggestions for further study have been drawn from the experimental results and associated theoretical and numerical work.

6.1 Secondary Flow and Loss Generation

In general the pressure side leg of the horseshoe vortex and the passage vortex form and grow as one. The high velocities associated with this vortex lead to locally low static pressures and high surface shear stresses on the endwall. Because the vortex lies directly over the endwall lift-off line rather than to one side of it, these low pressures and high shear stresses thin the endwall boundary layer upstream as well as downstream of the line.

Most of the inlet endwall boundary layer fluid leaves the endwall and enters the horseshoe/passage vortex before it reaches the blade suction surface. The rest is swept over to the blade suction surface ahead of the lift-off line. A new endwall boundary layer therefore forms which is extremely thin and laminar over a large portion of the endwall area within the bladerow. The fact that this boundary layer is so thin suggests that similar behaviour would be observed even with the high levels of free stream turbulence encountered in a real turbine.

Boundary layer loss predictions based on a simplification of Truckenbrodt's method by Denton and Cumpsty, assuming a constant dissipation integral C_D, are not sufficiently accurate to be used for quantitative predictions. There are two principal reasons for this:

(i) Substantial areas of laminar flow, in which C_D is far from constant, are likely to exist on the pressure surface, the early part of the suction surface and part of the endwall;

(ii) There are indications that free stream mixing, which is ignored by the simple method, makes a significant contribution to loss even upstream of the trailing edge.

The method is sufficiently accurate, though, to form a basis for obtaining a physical insight into the effect of lean on loss.

Downstream mixing losses are a significant proportion of overall bladerow loss so care should always be taken to include them when measuring or predicting bladerow performance. If mixing is not complete before the flow enters the subsequent bladerow, the acceleration in that bladerow will tend to increase mixing losses.

6.2 The Influence of Blade Lean

Simple lean reduces velocities and hence loss generation substantially at one endwall and increases them at the other. Compound lean reduces endwall losses but at the expense of midspan loss.

The constant C_D model has been used to estimate the overall effect of velocity changes (i.e. ignoring changes to boundary layer state and mixing losses outside the boundary layers). The net effect of lean is predicted to be negligible for the cascades tested. A net improvement from compound lean would only be expected on a bladerow with even higher pitch/chord ratio or lower aspect ratio than that tested.

Simple lean causes boundary layer transition on the lightly loaded endwall to occur later but also increases the area covered by a very thin (i.e. high rate of entropy generation) laminar boundary layer. On the endwalls of both the simple and compound leaned bladerows the measured reduction in loss generation is no more than would be expected simply by taking account of the decrease in free stream velocities.

The overall performance of the three bladerows is summarized in table 6.1.

	Exit flow angle (from axial)	Loss coefficient ($\bar{Y}$)	Mixing loss coefficient (Y_{MIX})
Unleaned	–65.5°	0.048	0.0132
Simple lean	–64.8°	0.050	0.0207
Compound lean	–66.3°	0.048	0.0116

Table 6.1 Overall cascade performance

All three cascades had the same exit loss coefficient, to within experimental certainty. However, compound lean increased flow turning, reduced downstream mixing losses and substantially reduced spanwise variations in mean flow angle, so with a suitably matched rotor, stage efficiency would probably be enhanced.

6.3 Numerical Predictions

Denton's programs BAS3D28 (inviscid) and LOSS3D30 (viscous with all boundary layers turbulent) predict static pressures and overall mean exit flow angles very well. The gross effects of straight lean, i.e. mean streamline shift, spanwise variation of exit flow angle and the difference between the two endwall flows, are also well predicted.

The predicted secondary flows are too weak. There is some evidence that this is because in the prediction too much of the incoming boundary layer fluid remains on the endwall rather than being drawn into the horseshoe/passage vortex ahead of the lift-off line.

Careful choice of calculation grid can virtually eliminate numerical entropy generation at the leading edge. Numerical entropy generation upstream of the trailing edge due to strong secondary flows, and at the trailing edge itself, could not be eliminated. This amounted to a loss coefficient between 0.02 and 0.03 and therefore casts doubt on loss predictions by the viscous program.

Converged inviscid solutions with identical input data but different "restart" files can differ greatly from one another in the position of the passage vortex and the main loss core. The root cause of the difference seems to be in the separation of the incoming endwall

boundary layer. This implies that the formation of the horseshoe vortex is critical to the later secondary flow development and must be predicted accurately if the overall prediction is to be correct. This is likely to be difficult because at its origin the vortex is very small and so would require a very fine grid to resolve it.

6.4 Further Research

6.4.1 Experimental

Oil flow visualization at the "negative" (low pressure) end of the straight leaned blades suggests that the endwall flow may be fundamentally different from that at the positive end. It is possible that the inlet boundary layer is not completely removed from the wall so that the very thin, laminar, "new" endwall boundary layer, with associated high shear stresses and entropy generation rates, cannot form. Further experiments on a modified rig would be needed to confirm whether this is the case.

Previous work has shown the effectiveness of simple lean when used to counteract the radial pressure gradient in an annular geometry. The present project has investigated the other effects of lean and has shown that, on the whole, on the blades tested, these effects are small. Tests on very different bladerows are required to show whether this conclusion is always true.

Other work is required to show how applicable these cascade results are to turbine flows. There are two questions in particular to be answered:

(i) Does the high turbulence or high unsteadiness (due to wake passing) radically change the structure of the endwall flow, in particular the horseshoe vortex formation and state of the endwall boundary layer? This could be answered by tests on either a full stage or a cascade with turbulence grid and moving bars upstream;

(ii) How does the downstream flow change the mixing losses? The flow in a full stage would probably be too complex to allow this question to be addressed. A cascade

with vortex generators upstream (to simulate passage vortices) would be of some use provided the vortex generators were moving so that vortex chopping was properly simulated. However, the mixing loss arising from the flow out of the upstream bladerow (or vortex generators) would be inseparable from the new loss generated in the downstream row. For this reason a theoretical study, probably using an unsteady, inviscid prediction, holds out most promise.

6.4.2 Numerical

The high levels of numerical entropy generated by Denton's code are cause for concern and show that with any such code the numerical entropy should be carefully monitored, especially where there are strong secondary flows, and minimized.

Attention should be given to the prediction of the endwall boundary layer lift-off and formation of the horseshoe vortex, as this has been shown to have a surprisingly strong influence on the overall secondary flow. Correct prediction of the lift-off should improve the accuracy of secondary kinetic energy predictions and reduce the sensitivity of the final solution to the initial guess.

This project has shown that substantial parts of the blade and endwall boundary layers are laminar and so it is important that numerical predictions reflect this. A simple transition model has already been incorporated into Denton's code.

REFERENCES

Abraham, S. and Bethel, J. M., 1984, "Endwall Loss Control in a Turbine Cascade.", Undergraduate part II project, Whittle Laboratory, Cambridge University Engineering Department.

Abu-Ghannam, B. J. and Shaw, R., 1980, "Natural Transition of Boundary Layers – The Effects of Turbulence, Pressure Gradient and Flow History.", IMechE *Journal of Mechanical Engineering Science,* Vol. 22, pp. 213-228.

Armstrong, N. D., 1955, "The Secondary Flow in a Cascade of Turbine Blades.", ARC R&M 2979.

Arts, T., 1985, "Effects of Tip Endwall Contouring on the Three-Dimensional Flow Field in an Annular Turbine Nozzle Guide Vane. Part 2 – Numerical Investigation.", ASME paper 85-GT-108.

Atkins, M. J., 1987, "Secondary Losses and End-Wall Profiling in a Turbine Cascade.", Paper No. C255/87 from "*Turbomachinery - Efficiency Prediction and Improvement.*", Institution of Mechanical Engineers International Conference No. 1987-6..

Baljé, O. E. and Binsley, R. L., 1968, "Axial Turbine Performance Evaluation. Part A – Loss-Geometry Relationships.", ASME *Journal of Engineering for Power,* pp.341-348.

Belik, L., 1968, "An Approximate Solution for Kinetic Energy of Secondary Flow in Blade Cascades.", *International Journal of Mechanical Science,* Vol. 10, pp. 765-782.

Belik, L., 1972, "Secondary Flow in Blade Cascades of Axial Turbomachines and the Possibility of Reducing its Unfavourable Effects.", *2nd International JSME Symposium of Fluid Machinery and Fluidics,* Tokio.

Bellhouse, B. J. and Schultz, D. L., 1967, "The Measurement of Fluctuating Skin Friction in Air with Heated Thin Film Gauges.", *Journal of Fluid Mechanics*, Vol. 32, part 4, pp. 675-680.

Binder, A. and Romey, R., 1983, "Secondary Flow Effects and Mixing of the Wake Behind a Turbine Stator.", ASME *Journal of Engineering for Power,* Vol. 105, p. 40.

Binder, A., 1985, "Turbulence Production due to Secondary Vortex Cutting in a Turbine Rotor.", ASME *Journal of Engineering for Gas Turbines and Power,* Vol. 107, pp. 1039-1046.

Binder, A., Forster, W., Mach, K. and Rogge, H., 1986, "Unsteady Flow Interaction Caused by Stator Secondary Vortices in a Turbine Rotor.", ASME paper 86-GT-302.

Boletis, E., 1985, "Effects of Tip Endwall Contouring on the Three-Dimensional Flow Field in an Annular Turbine Nozzle Guide Vane. Part 1 - Experimental Investigation.", ASME *Journal of Engineering for Gas Turbines and Power,* Vol. 107, pp. 983-990.

Boyle, R. J., Rholik, H. E. and Goldman, L. J., 1981, "Analytic Investigation of Effect of End-Wall Contouring on Stator Performance.", NASA TP-1943.

Breugelmans, F. A. H., Carels, Y. and Demuth, M., 1984, "Influence of Dihedral on the Secondary Flow in a Two-Dimensional Compressor Cascade.", ASME *Journal of Engineering for Gas Turbines and Power,* Vol. 106, pp. 578-584.

Bryer, D. W. and Pankhurst, R. C., 1971, "Pressure-Probe Methods for Determining Wind Speed and Flow Direction.", National Physical Laboratory / HMSO 1971.

Came, P. M., and Marsh, H., 1974, "Secondary Flows in Cascades: Two Simple Derivations for the Components of Vorticity.", *Journal of Mechanical Engineering Science*, Vol. 16, pp. 391-401.

Carrick, H. B., 1977, "Secondary Flow and Losses in Turbine Cascades with Inlet Skew.", paper 9 of *Secondary Flows in Turbomachines,* AGARD CP-214.

Chen, L. D. and Dixon, S. L., 1986, "Growth of Secondary Flow Losses Downstream of a Turbine Blade Cascade.", ASME *Journal of Engineering for Gas Turbines and Power,* Vol. 108, pp. 270-276.

Coghlan, R. P. G. and Hodgson, T. C., 1986, "The Application of Endwall Groove Patterns to Reduce Secondary Flow Losses in an Axial Turbine Cascade.", Undergraduate part II project, Whittle Laboratory, Cambridge University Engineering Department.

Dawes, W. N., 1986, "A Numerical Method for the Analysis of 3D Viscous Compressible Flow in Turbine Cascades: Application to Secondary Flow Development in a Cascade With and Without Dihedral.", ASME

Denton, J. D., 1973, "A Survey and Comparison of Methods for Predicting the Profile Loss of Turbine Blades.", Institution of Mechanical Engineers C76/73, pp. 204-212.

Denton, J. D., 1985, "The Calculation of Fully Three-Dimensional Flow Through Any Type of Turbomachine Blade Row", Paper 9 of AGARD lecture series 140 *"3D Computation Techniques Applied to Internal Flows in Propulsion Systems".*

Denton, J. D., 1987 "3D Flow Calculations in a Hypothetical Steam Turbine Last Stage.", Chapter 3.1 of "Aerothermodynamics of Low Pressure Steam Turbines and Condensers.", ed. M. J. Moore and C. H. Sieverding, publ. Hemisphere Publishing Corporation.

Denton, J. D., and Cumpsty, N. A., 1987, "Loss Mechanisms in Turbomachines.", IMechE Paper No. C260/87 from *"Turbomachinery - Efficiency Prediction and Improvement.*", Institution of Mechanical Engineers International Conference No. 1987-6.

Deych, M. Ye. and Troyanovskiy, B. M., "Investigation and Calculation of Axial-Turbine Stages.", CIRC Translation MT6500409.

Diakunchak, I. S., 1988, "Cold Flow Turbine Rig Tests of the Original and Redesigned Compressor Turbines of an Industrial Gas Turbine Engine.", ASME paper 88-GT-74.

Dring, R. P., 1971, "A Momentum-Integral Analysis of the Three-Dimensional Turbine End-Wall Boundary Layer.", ASME *Journal of Engineering for Power,* p. 386.

Duncan, W. J., Thom, A. S. and Young, A. D., 1970, "Mechanics of Fluids.", Second Edition, publ. Edward Arnold.

Dunham, J., 1970, "A Review of Cascade Data on Secondary Losses in Turbines.", *Journal of Mechanical Engineering Science*, Vol. 12, pp. 48-59.

Eckerle, W. A. and Langston, L. S., 1987, "Horseshoe Vortex Formation around a Cylinder.", ASME *Journal of Turbomachinery,* Vol.109, p. 278.

Fillipov, G. A. and Van Chzhun-Tsi, 1964, "The Effect of Flow Twisting on the Characteristics of Guide Rows.", Teploenergetika, Vol. 11, No. 5, pp. 54-57.

Gallus, H. E. and Kummel, W., 1977, "Secondary Flows and Annulus-Wall Boundary Layers in Axial-Flow Compressor and Turbine Stages.", paper 4 of *Secondary Flows in Turbomachines,* AGARD CP-214.

Gaugler, R. E. and Russell, L. M., 1982, "Flow Visualisation Study of the Horseshoe Vortex in a Turbine Stator Cascade.", NASA Technical Paper 1884.

Glynn, D. R. and Marsh, H., 1980, "Secondary Flow in Annular Cascades.", *Internaitional Journal of Heat and Fluid Flow*, Vol. 2, No., 1, pp.29-33.

Govardhan, M., Venkatrayulu, N. and Prithvi Raj, D., 1986, "Secondary Losses in a Large Deflection Annular Turbine Cascade: Effect of the Entry Boundary Layer Thickness.", ASME paper 86-GT-171.

Grant, J. and Borthwick, D., 1987, "Fully 3D Inviscid Flow Calculations for the Final Stage of a Large, Low-Pressure Steam Turbine.", Paper No. C281/87 from "*Turbomachinery - Efficiency Prediction and Improvement.*", Institution of Mechanical Engineers International Conference No. 1987-6..

Graves, C. P., 1985, "Secondary Flows and Losses in Gas Turbines.", Durham University Engineering Department PhD Dissertation.

Gregory-Smith, D. G., 1970, "An Investigation of Annulus Wall Boundary Layers in Axial Flow Turbomachines.", ASME *Journal of Engineering for Power,* pp.369-376.

Gregory-Smith, D. G., 1982, "Secondary Flows and Losses in Axial Flow Turbines.", ASME *Journal of Engineering for Power*, Vol. 104, pp. 819-822.

Gregory-Smith, D. G. and Graves, C. P., 1983, "Secondary Flows and Losses in a Turbine Cascade.", paper 17 of *Viscous Effects in Turbomachines,* AGARD CP-351.

Gregory-Smith, D. G., 1989, "A Comparison of Three Calculation Codes for the Flow in a Turbine Cascade.", Durham University Engineering Department report to Rolls-Royce plc, Brochure PVD1-89D.

Gruschwitz, E., 1935, "Turbulent Reibungsschichten mit Seckundarstromung.", *Ingenieur-Archiv.*, vol. 4, pp. 355-365.

Han Wan-Jin, Wang Zhong-Qi and Xu Wen-Yuan, 1988, "An Experimental Investigation into the Influence of Blade Leaning on the Losses Downstream of Annular Cascades with a Small Diameter-Height Ratio.", ASME paper 88-GT-19.

Hanratty, T. J. and Campbell, J. A., 1983, "Measurement of Wall Shear Stress.", Chapter 11 of "*Fluid Mechanics Measurements*", ed. Goldstein, R. J., publ. Hemisphere / Springer-Verlag.

Hawthorne, W. R., 1955, "Rotational Flow through Cascades.", *Quarterly Journal of Mechanics and Applied Mathematics*, Vol. VIII, pp. 266-292.

Hebert, G. J. and Tiederman, W. G., 1989, "Comparison of Steady and Unsteady Secondary Flows in a Turbine Stator Cascade.", ASME paper 89-GT-79.

Herbert, M. V., and Calvert, W. J., 1982, "Description of an Integral Method for Boundary Layer Calculation in use at NGTE, with Special Reference to Compressor Blades.", NGTE Memorandum M82019.

Herzig, H. Z. and Hansen, A. G., 1955, "Visualisation Studies of Secondary Flows with Applications to Turbomachines.", ASME *Transactions,* pp. 249-266.

Hodson, H. P. and Dominy, R. G., 1987a, "Three-Dimensional Flow in a Low Pressure Turbine Cascade at its Design Condition.", ASME *Journal of Turbomachinery,* Vol. 109, pp. 177-185.

Hodson, H. P. and Dominy, R. G., 1987b, "The Off-Design Performance of a Low Pressure Turbine Cascade.", ASME *Journal of Turbomachinery,* Vol. 109, pp. 201-209.

Horlock, J. H., 1973a, "Axial Flow Turbines – Fluid Mechanics and Thermodynamics.", publ. Robert E. Krieger.

Horlock, J. H., 1973b, "Cross Flows in Bounded Three-Dimensional Turbulent Boundary Layers.", *Journal of Mechanical Engineering Science,* Vol. 15, No. 4, pp 274-284.

Horlock, J. H., 1977, "Recent Developments in Secondary Flow.", paper 1 of *Secondary Flows in Turbomachines,* AGARD CP-214.

Houghton, E. L. and Brock, A. E., 1975, "Tables for the Compressible Flow of Dry Air.", 3rd edition, publ. Edward Arnold.

Hourmouziadis, J. and Hubner, N., 1985, "3-D Design of Turbine Aerofoils.", ASME paper 85-GT-188.

Huber, F.W., Rowey, R. J. and Ni, R. R., 1985, "Application of 3D Flow Computations to Gas Turbine Aerodynamic Design.", AIAA-85-1216.

Hunter, I. H., 1979, "Endwall Boundary Layer Flows and Losses in Axial Turbomachines.", PhD thesis, University of Cambridge.

Hunter, I. H., 1982, "Endwall Boundary Layer Flows and Losses in an Axial Turbine Stage.", ASME *Journal of Engineering for Power,* Vol. 104, p.184.

Ishii, J. and Honami, S., 1986, "A Three-Dimensional Turbulent Detached Flow with a Horseshoe Vortex.", ASME *Journal of Engineering for Gas Turbines and Power,* Vol. 108, No. 1, pp.125-130.

Jilek, J., 1986, "An Experimental Investigation of the Three-Dimensional Flow within Large Scale Turbine Cascades.", ASME paper 86-GT-170.

Johnston, J. P., 1960, "On the Three-Dimensional Turbulent Boundary Layer Generated by Secondary Flow.", ASME *Journal of Basic Engineering*, March 1960, p.233.

Kawai, T., Adachi, T. and Akashita, K., 1985, "Structure and Decay of Secondary Flow in the Downstream of a Cascade.", *Bulletin of JSME*, Vol. 28, No. 242, pp. 1642-1650.

Kirillov, A. I., Sirotkin, Ya. A. and Lapshin, K. L., 1984, "Aspects of Calculating Turbine Stages with Tangentially Inclined Stator Blades.", *Energomashinostroenie,* No. 7, pp. 2-5.

Klein, A., 1966, "Untersuchungen uber den Einfluss der Zustrom-grenzschicht auf die Sekundarstromung in den Beschaufelungen von Axialturbinen.", *Forsch. Ing.* Bd 32, Nr. 6. (English translation: Investigation of the Influence of the Entry Boundary Layer on the Secondary Flows in the Blading of Axial Turbines, BHRA T 1004, 1966)

Kopper, F. C., Milano, R. and Vanco, M., 1981, "An Experimental Investigation of Endwall Profiling in a Turbine Vane Cascade.", *AIAA Journal,* Vol. 19, pp. 1033-1040.

Kuethe, A. M., McKee, P. G. and Curry, W. H., 1949, "Measurements in the Boundary Layer of a Yawed Wing.", NACA TN 1946.

Langston, L. S., Nice, M. L. and Hooper, R. M., 1977, "Three-Dimensional Flow Within a Turbine Cascade Passage.", ASME *Journal of Engineering for Power,* p. 21.

Langston, L. S., 1980, "Crossflows in a Turbine Cascade Passage.", ASME *Journal of Engineering for Power,* Vol.102, p.866.

Liu, H. C., Booth, T. C. and Tall, W. A., 1979, "An Application of 3D Viscous Flow Analysis to the Design of a Low Aspect Ratio Turbine.", ASME paper 79-GT-53.

Marchal, P. and Sieverding, C. H., 1977, "Secondary Flows in Turbomachinery Bladings.", paper 11 of *Secondary Flows in Turbomachines,* AGARD CP-214.

Moore, J., 1983, "Flow Trajectories, Mixing and Entropy Fluxes in a Turbine Cascade.", paper 5 of *Viscous Effects in Turbomachines,* AGARD CP-351.

Moore, J. and Moore, J. G., 1983, "Entropy Production Rates from Viscous Flow Calculations: Part 1 – A Turbulent Boundary Layer Flow.", ASME paper 83-GT-70.

Moore, J. and Ransmayr, A., 1984, "Flow in a Turbine Cascade: Part 1 – Losses and Leading Edge Effects.", ASME *Journal of Engineering for Gas Turbines and Power,* Vol. 106, p. 400.

Moore, J. and Adhye, R. Y., 1985, "Secondary Flows and Losses Downstream of a Turbine Cascade.", ASME *Journal of Engineering for Gas Turbines and Power,* Vol. 107, pp. 961-968.

Moore, J. and Moore, J. G., 1985, "Performance Evaluation of Linear Turbine Cascades Using Three-Dimensional Viscous Flow Calculations.", ASME *Journal of Engineering for Gas Turbines and Power,* Vol. 107, p. 969.

Moore, J., Shaffer, D. M. and Moore, J. G., 1987, "Reynolds' Stresses and Dissipation Mechanisms Downstream of a Turbine Cascade.", ASME *Journal of Turbomachinery,* Vol. 109, pp. 258-267.

Moustapha, S. H., Paron, G. J. and Wade, J. H. T., 1985, "Secondary Flow in Cascades of Highly Loaded Turbine Blades.", ASME *Journal of Engineering for Gas Turbines and Power,* Vol. 107, pp. 1031-1038.

Nagayama, T., Masuzawa, C., Sakata, H. and Kimura, Y., 1988, "Computation and Experiment of 3D Stacking Effect on Turbine Stators.", Trans. JSME, series B, vol. 54, no. 501, pp. 1081-1087 (in Japanese).

Perdichizzi, A., 1989, "Mach Number Effects on Secondary Flow Development Downstream of a Turbine Cascade.", ASME paper 89-GT-67.

Prumper, H., 1972, "Application of Boundary Layer Fences in Turbomachinery.", AGARDograph 164, Paper II-3, p.311.

Quarmby, A. and Das, H. K., 1969, "Displacement Effects on Pitot Tubes with Rectangular Mouths.", *Aero. Quarterly,* May 1969, p. 129.

Richards, P. H., 1985, "Review of Geometrical Blade Changes to Improve Secondary Losses in High Hub-Tip Ratio, Low Aspect Ratio Turbines.", Central Electricity Generating Board TPRD/M/1477/N85.

Richards, P. H. and Johnson, C. G., 1986, "Development of Secondary Flows in a Model Turbine.", Central Electricity Generating Board TPRD/M/1549/R86.

Salvage, J. W., 1974, "Investigation of Secondary Flow Behaviour and the End Wall Boundary Layer Development through Compressor Cascades.", VKI TN 107.

Samuel, A. E. and Joubert, P. N., 1974, "A Boundary Layer Developing in an Increasingly Adverse Pressure Gradient.", *Journal of Fluid Mechanics,* vol. 66, pp. 481-505.

Schlegel, J. C., Liu, H. C. and Waterman, W. F., 1976, "Reduction of End-Wall Effects in a Small, Low-Aspect-Ratio Turbine by Radial Work Redistribution.", ASME *Journal of Engineering for Power,* Vol. 98.

Schlichting, H., 1968, "Boundary Layer Theory.", 6th edition, McGraw-Hill.

Senoo, Y., 1958, "The Boundary Layer on the End Wall of a Turbine Nozzle Cascade.", ASME *Transactions* 1958 pp.1711-1720.

Sharma, O. P., and Butler, T. L., 1987, "Predictions of Endwall Losses and Secondary Flows in Axial Flow Turbine Cascades.", ASME *Journal of Turbomachinery*, Vol. 109, pp.229-236.

Sharma, O. P., Renaud, E., Butler, T. L., Milsaps, K., Dring, R. P. and Joslyn, H. D., 1988, "Rotor-Stator Interaction in Multi-Stage Axial Flow Turbines.", AIAA-88-3013.

Sharma, O. P., Huber, F. W. and Langston, L. S., 1989, "Visualization of Secondary Flows in a Turbine Cascade.", NASA MSFC CFD Workshop, 27 April 1989.

Shi Jing, Han Jian-Juan, Zhou Shi-Ying, Zhu Ming-Fu, Zhang Yao-Ko and She Meng-Yu, 1986, "An Investigation of a Highly Loaded Transonic Turbine Stage with Compound Leaned Blades.", ASME *Journal of Engineering for Gas Turbines and Power,* Vol. 108, pp. 265-269.

Sieverding, C. H. and van den Bosche, P., 1983, "The Use of Coloured Smoke to Visualise Secondary Flows in a Turbine-Blade Cascade.", *Journal of Fluid Mechanics,* Vol. 134, pp.85-89.

Sieverding, C. H., van Hove, W. and Boletis, E., 1984, "Experimental Study of the Three-Dimensional Flow Field in an Annular Turbine Nozzle Guidevane.", ASME *Journal of Engineering for Gas Turbines and Power*, Vol. 106, pp. 437-448.

Sieverding, C. H., 1985, "Recent Progress in the Understanding of Basic Aspects of Secondary Flows in Turbine Blade Passages.", ASME *Journal of Engineering for Gas Turbines and Power*, Vol. 107, pp. 248-257.

Sieverding, C. H. and Heinemann, H., 1989, "The Influence of Boundary Layer State on Vortex Shedding from Flat Plates and Turbine Cascades.", ASME 89-GT-296

Sjolander, S. J., 1975 "The Endwall Boundary Layer in an Annular Cascade of Turbine Nozzle Guide Vanes.", Carleton University, Ottawa, Canada, Technical Report ME/A 75-4.

Smeaton, J., 1759, "A experimental Enquiry concerning the natural Powers of Water and Wind to turn Mills, and other Machines, depending on a circular Motion.", *Philosophical Transactions of the Royal Society of London,* vol. 51, pp. 100-174.

Sonoda, T., 1985, "Experimental Investigation on Spatial Development of Streamwise Vortices in a Turbine Inlet Guide Vane Cascade.", ASME paper 85-GT-20.

Squire, H. B. and Winter, K. G., 1951, "The Secondary Flow in a Cascade of Airfoils in a Non-Uniform Stream.", *Journal of Aeronautical Science,* April 1951, p. 271.

Stewart, W. L., Whitney, W. J. and Wong, R. Y., 1960, "A Study of Boundary-Layer Characteristics of Turbomachine Blade Rows and their Relation to Over-All Blade Loss.", ASME *Journal of Basic Engineering,* pp. 588-592.

Stow, P., 1985, "Turbomachinery Blade Design using Advanced Calculation Methods.", from *Thermodynamics and Fluid Mechanics of Turbomachinery,* ed. A. S. Uçer, P. Stow & Ch. Hirsch, publ. Martinus Nijhoff.

Tall, W. A., 1977, "Understanding Turbine Secondary Flow.", paper 14 of *Secondary Flows in Turbomachines,* AGARD CP-214.

Tanner, L.H., and Blows, L.G., 1969, "A Study of the Motion of Oil Films on Surfaces in Air Flow, with Application to the Measurement of Skin Friction.", J. Phys. E., vol. 2, pp. 194-202.

Truckenbrodt, E., 1955, "A Method of Quadrature for Calculation of the Laminar and Turbulent Boundary Layer in Case of Plane and Rotationally Symmetrical Flow.", NACA TM 1379, Translated from *Ingenieur-Archiv,* vol. 20, 1952, pp. 211-228.

Walker, P. J., 1988, "Blade Lean in Axial Turbines. Model Turbine Measurements and Simulation by a Novel Numerical Method.", PhD dissertation, Cambridge University Engineering Department.

Walsh, J. A. and Gregory-Smith, D. G., 1987, "The Effect of Inlet Skew on the Secondary Flows and Losses in a Turbine Cascade.", Paper No. C275/87 from "*Turbomachinery - Efficiency Prediction and Improvement.*", Institution of Mechanical Engineers International Conference No. 1987-6..

Wang Zhong-Chi, Lai Sheng-Kai and Shu Wen-Yuan, 1981, "Aerodynamic Calculation of Turbine Stator Cascades with Curvilinear Leaned Blades and some Experimental Results.", *5th International Symposium on Airbreathing Engines.*

Wang Zhong-Qi, Han Wan-Jin and Xu Wen-Juan, 1987, "An Experimental Investigation into the Influence of Diameter-Blade Height Ratios on Secondary Flow Losses in Annular Cascades with Leaned Blades.", ASME paper 87-GT-131.

Wang Zhong-Qi, Xu Wen-Yuan, Han Wan-Jin and Bai Jie, 1988, "An Experimental Investigation into the Reasons of Reducing Secondary Flow Losses by Using Leaned Blades in Rectangular Turbine Cascades with Incidence Angle.", ASME paper 88-GT-4.

Waterman, W. F. and Tall, W. A., 1976, "Measurement and Prediction of 3D Viscous Flows in Low-Aspect-Ratio Turbine Nozzles.", ASME paper 76-GT-73.

Wilkinson, D. H., 1967, "A Numerical Solution of the Analysis and Design Problems for the Flow Past One or More Aerofoils or Cascades.", ARC R&M No. 3545.

Williams, M. R., 1984, "Large Turbofans to the Year 2000.", *Aeronautical Journal,* p. 419 (paper 1120/2).

Woollatt, G., Soothill, C. D. and Hyde, J. A. C., 1989, "Design and Testing of a 18600 HP Industrial Power Turbine.", from "*Gas Turbines - Technology and Development*", Institution of Mechanical Engineers seminar S777, November 1989.

Yamamoto, A. and Yanagi, R., 1985, "Production and Development of Secondary Flows and Losses Within a Three Dimensional Turbine Stator Cascade.", ASME paper 85-GT-217.

Yamamoto, A., 1987, "Production and Development of Secondary Flows and Losses Within Two Types of Straight Turbine Cascades: Part 1 – Stator Case.", ASME *Journal of Turbomachinery,* Vol.109, pp. 186-193.

Yamamoto, A., 1987, "Production and Development of Secondary Flows and Losses Within Two Types of Straight Turbine Cascades: Part 2 – A Rotor Case.", ASME *Journal of Turbomachinery,* Vol.109, pp. 194-200.

Zunino, P., Ubaldi, M. and Satta, A., 1987, "Measurement of Secondary Flows and Turbulence in a Turbine Cascade Passage.", ASME paper 87-GT-132.

APPENDIX 1

BLADE AND CASCADE DIMENSIONS

The blade profile, static tapping positions and definition of x and y directions are shown in fig.2.2. Manufacturing co-ordinates are as follows (dimensions in mm):

x	y	x	y
221.38	5.71	8.14	208.60
216.11	16.46	10.48	212.24
210.82	27.06	11.11	213.13
204.06	39.99	11.77	214.02
195.71	54.87	12.44	214.90
187.04	69.07	14.60	217.47
178.01	82.42	17.66	220.58
165.37	98.85	23.01	224.92
153.97	111.95	29.32	228.80
142.43	123.80	37.66	232.43
132.59	132.81	51.22	235.70
121.28	141.83	66.45	236.23
111.83	148.30	80.95	233.72
101.26	154.42	92.77	229.47
89.86	159.91	104.48	223.18
72.00	166.65	115.88	215.01
62.70	169.30	125.29	206.66
55.00	171.00	134.31	197.20
49.44	171.94	142.91	186.74
45.72	172.41	151.07	175.37
40.15	172.91	157.54	165.28
33.52	173.17	166.10	150.30
26.15	173.03	171.90	139.06
20.54	172.84	177.43	127.39
16.42	172.85	182.74	115.36
12.19	173.23	187.89	103.01
9.43	173.81	191.90	92.92
7.52	174.47	196.86	80.13
5.65	175.42	201.71	67.01
3.99	176.71	206.54	53.65
2.70	178.32	211.41	40.08
1.54	181.15	214.36	31.83
1.09	184.15	217.34	23.51
1.28	189.21	220.33	15.11
1.94	193.21	221.34	12.29
3.30	198.14	222.35	9.47
5.20	202.97	223.36	6.63

There were large errors in the positions of the slots for static tappings on blade set 1. Slots in sets 2 and 3 were milled correctly:

Set 1				Design (Sets 2 & 3)		
x	y	surface distance		x	y	surface distance
204.7	38.9	37.1		204.9	38.3	36.5
182.9	75.4	79.6		184.7	72.9	76.6
162.3	102.6	113.8		162.5	102.2	113.4
137.0	128.9	150.3		137.3	128.6	149.9
109.5	149.8	184.9		110.1	149.4	184.2
83.6	162.5	213.8		83.8	162.4	213.6
62.0	169.5	236.5		61.3	169.6	237.3
39.2	173.0	259.6		38.4	173.2	260.4
29.6	173.1	269.2	↑	28.4	173.4	270.4
20.2	172.8	278.7	P/S	19.0	172.9	279.8
11.1	173.4	287.8		10.0	173.6	288.8
3.8	176.9	296.0	Leading Edge	3.5	177.2	296.4
1.1	187.2	306.9		1.2	185.4	305.2
2.2	194.2	314.0	S/S	2.1	194.0	313.8
5.1	202.8	323.1	↓	5.0	202.4	322.6
9.5	210.8	332.3		9.2	210.4	331.8
21.4	223.8	350.0		21.4	223.9	349.9
37.8	232.5	368.6		38.4	232.8	369.2
56.0	236.2	387.2		56.8	236.5	388.0
74.5	235.2	405.8		76.4	235.2	407.7
94.0	228.9	426.3		94.0	229.2	426.4
110.4	219.2	445.5		109.5	219.5	444.3
125.6	206.4	465.3		124.7	207.2	464.1
138.3	192.6	484.1		137.7	193.8	482.6
150.0	176.9	503.6		149.5	178.0	502.3
161.0	159.5	524.3		160.5	160.6	522.9
169.8	143.3	542.7		169.6	144.0	541.8
178.3	125.5	562.4		178.1	126.5	561.3
185.7	108.4	581.1		185.1	110.4	578.9
192.0	92.7	597.9		191.7	93.7	596.9
199.1	74.1	617.9		198.0	76.5	615.3
205.3	57.1	635.9		204.2	58.8	634.1
211.7	39.2	655.0		210.7	40.9	653.2

Basic geometric data are as follows:

True chord	278.0 mm
Pitch	230.0 mm
Span	300.0 mm
Trailing edge thickness	2.2 mm
Trailing edge included angle	5.8°
Design inlet flow angle (from axial)	40.0°
Exit blade angle (from axial)	–66.8°

The lean applied to sets 2 and 3 is shown in fig.2.1.

APPENDIX 2

PRESSURE PROBE CALIBRATION

A2.1 Five-Hole Probes

Refer to fig.2.7a for numbering convention and note that p_0 and p_S are true local stagnation and static pressure respectively. A simple way to access calibration data would be to represent required quantities by dimensionless coefficients as follows :

$$\text{Yaw angle } \alpha \;;\; \text{Pitch angle } \beta \;;\; C_{P0} = \frac{p_0 - p_5}{p_5 - p_M} \;;\; C_{PS} = \frac{p_5 - p_M}{p_0 - p_S}$$

$$\text{where} \quad p_M = \frac{p_1 + p_2 + p_3 + p_4}{4}$$

and relate these empirically to two calibration coefficients:

$$C_\alpha = \frac{p_1 - p_3}{p_5 - p_M} \;;\; C_\beta = \frac{p_2 - p_4}{p_5 - p_M}$$

This method is straightforward but has the disadvantage that at incidence angles greater than around 25° the denominator ($p_5 - p_M$) becomes very small and may even change sign. A more sophisticated two-region method was therefore used, as described by Bryer & Pankhurst (1971), which is valid up to at least 40° incidence.

Coefficients

Yaw angle α ; Pitch angle β ; $C_{P0} = \frac{p_0 - p_5}{p_5 - p_i}$; $C_{PS} = \frac{p_5 - p_i}{p_0 - p_s}$

are calibrated against

$$C_\alpha = \frac{p_1 - p_3}{p_5 - p_i} \quad ; \quad C_\beta = \frac{p_2 - p_4}{p_5 - p_i}$$

where i=2 if $p_2<p_4$, otherwise i=4. This effectively leads to two separate calibrations, one for each half of the pitch angle range, and ensures that the denominator remains reasonably large and positive over a wide incidence range.

The calibration was done using a nozzle with exit diameter 100mm mounted on the "Duplex" wind tunnel. The jet from the nozzle was traversed at the measurement plane and found to be very uniform within the centre 50mm. While calibrating, the probe tip was kept within the centre 30mm. To avoid probe interference effects the reference Pitot-static probe was not mounted during the calibration, but was used beforehand to relate reference total pressure to static pressure upstream of the nozzle and reference static pressure to atmospheric pressure. (In both cases the pressures were almost identical). Each probe was calibrated at intervals of not greater than 5° over a range of ±40° in yaw and pitch at two speeds, corresponding to probe Reynolds' numbers approximately 11000 and 6000 (blade chord Re approximately 9.3×10^5 and 5.2×10^5). Only data obtained at the higher speed were used to interpret measurements but the low speed data were used to estimate errors due to Reynolds' number variations. Errors are discussed in Appendix 3.

When using probe calibration data to interpret measurements values were linearly interpolated directly from the calibration data rather than via a polynomial surface fit.

A2.2 Three-Hole Probe

The cobra probe was calibrated in the low-speed laboratory calibration tunnel.

Yaw angle α , $C_{P0} = \frac{p_0 - p_5}{p_5 - p_M}$ and $C_{PS} = \frac{p_5 - p_M}{p_0 - p_S}$

where $p_M = \frac{p_1 + p_3}{2}$

were calibrated against $C_\alpha = \frac{p_1 - p_3}{p_5 - p_M}$

Calibrations were performed at intervals of 2° at a variety of Reynolds' numbers (values given are based on blade chord). Data at $Re=1.0\times10^5$ were discarded because they were subject to large errors due to tunnel unsteadiness. C_α and C_{P0} were found to have only a weak dependence upon Reynolds' number so their calibration was based on the mean of a number of runs (one at $Re=1.8\times10^5$, smoothed to reduce the effect of tunnel unsteadiness, two at $Re=4.1\times10^5$ and one at $Re=7.1\times10^5$). C_{PS} was calibrated against Re as well as C_α but in the event this was not used because static pressures were interpolated between the endwall and five-hole probe measurements. When interpreting measurements values were linearly interpolated from calibration data.

APPENDIX 3

ACCURACY OF PRESSURE PROBE MEASUREMENTS

A3.1 Probe Positioning

Probes were positioned to within the following limits:

Boundary layer measurements (three-hole and flattened Pitot probes)			±0.05mm
Five-hole probe	–	z co-ordinate	±0.05mm
	–	x & y co-ordinates	±0.5mm

When traversing a five-hole probe near a blade surface the position was checked by electrical contact with the blade, so the the accuracy would be much better than ±0.5mm.

A3.2 Five-Hole Probe

Five-hole probe data were interpreted using a probe calibration at a Reynolds' number equivalent to $Re=9.4\times10^5$ based on blade chord. Further calibrations were then performed at the same speed and also at $Re=5.2\times10^5$ and these data were compared with the original calibration. Except for a few spurious points at the limits of the calibration range (40° incidence) the maximum errors were as shown in table A3.1.

	Incidence < 25°		Incidence < 40°	
Probe Re	11000	6000	11000	6000
Maximum error in:				
Flow direction	±0.2°	±0.5°	±0.5°	±2°
Stagnation pressure	±0.1%	±0.3%	±1%	±3%
Dynamic pressure	±1%	±3%	±2%	±10%

Table A3.1 Estimated errors in five-hole probe data.

(Pressure errors expressed as % of local dynamic pressure.)

There was no evidence of a systematic error in any quantity at low Reynolds' number. Wherever possible, the probe was rotated (keeping the probe head position fixed) so as to keep the yaw angle less than ±20°. It was very rare for either yaw or pitch to exceed ±25°. Free stream turbulence was low both downstream of the calibration nozzle and in the cascade. Its effect on accuracy has not been measured, neither has the effect of proximity to solid surfaces. The effect of probe stem blockage and incidence was investigated by repeating one spanwise traverse on set 1 at two probe settings, 10° apart.This traverse was near the throat and near the suction surface, i.e. in a position where the effect of stem blockage is likely to be largest and the flow is complicated by the passage vortex. Maximum discrepancies were approximately:

Flow direction : 0.3°

Speed : 2% of exit free stream value

Total pressure : 1% of exit free stream value except near the endwall, where probe incidence was nearly 50° for one of the traverses.

A3.3 Three-Hole Probe

Maximum errors due to non-zero pitch angle were found to be:

Total pressure : ±1% of local dynamic head for pitch angle less than ±8°

±10% of local dynamic head for pitch angle less than ±16°

Yaw angle : ±1° for pitch angle less than ±10°

Pitch angles are estimated to be less than ±5° for all three-hole probe measurements in the cascade except very near to the suction surface. When traversing, yaw angles have always been kept within ±9°. Other sources of error have not been considered.

A3.4 Stagnation Pressure

The gauzes in the settling chamber of the Duplex tunnel were cleaned before each set of blades was tested but there were still non-uniformities in the cascade inlet flow. Five-hole probe traverses upstream of the middle blade passage showed stagnation pressure variations of up to about $\pm 0.001(p_{01}-p_a)$. Variations over the entire inlet flow area are likely to be even greater than this but the cascade design did not permit the entire upstream flow to be traversed. There were regions in all measurement planes where measured stagnation pressure was higher than at the reference probe upstream. It was concluded that the reference probe, which was located near the top of the cascade (fig.2.4a), read too low a stagnation pressure so all measured stagnation pressures, on all three sets of blades, were decreased by $0.0025(p_{01}-p_a)$ before calculating velocities etc. This figure was chosen to give roughly zero measured stagnation pressure loss in the free stream at all measurement planes.

A3.5 Accuracy of Average Quantities

Provided probe errors are random, the accuracy of average quantities will be better than that of individual values. Overall accuracy of pressure probe traverses has been estimated by comparing the integrated mass flow at each traverse plane. An axial velocity is derived from the measured dynamic head assuming incompressible flow and normalised by inlet free stream velocity. A non-dimensional mass flow is then calculated based on this velocity:

$$v_x' = \sqrt{\frac{p_{01}-p}{p_{01}-p_1}} \quad ; \quad m' = \frac{\iint v_x' \, dydz}{A \cos 40°}$$

where A is the area covered, either $230\times150mm^2$ for a half span or $230\times300mm^2$ for a full span. Ignoring the inlet endwall boundary layer and assuming the the inlet flow angle is 40° from the x direction, as designed, then m' should be 1.0 at every traverse plane. In fact, the mean inlet flow angles were not exactly 40° and there was an inlet endwall boundary layer with displacement thickness δ^*=2.6mm, so the expected value of m' is in fact

$$m' = \left(\frac{150-\delta^*}{150}\right)\left(\frac{\cos\phi_1}{\cos 40°}\right)$$ where ϕ_1 is the actual mean inlet flow angle.

Expected and measured values of m' are presented in table A3.2.

Set number	ϕ_1 (x/C_x=–0.3)	Expected m'	x/C_x	Actual m'
1	40.5°	0.9754	0.03	0.9794
			0.22	0.9575
			0.45	0.9583
			0.67	0.9493
			0.83	0.9551
			1.03	0.9626
			1.23	0.9662
2	37.8°	1.0136	0.22	0.9054
			0.67	0.8941
			0.83	0.8861
			1.23	0.8932
3	37.9°	1.0122	1.23	0.9376

Table A3.2 Measured mass flow.

Other sources of error in m' are:

- Compressibility effects. Incompressible flow has been assumed, i.e.

$$\frac{\rho v}{\rho_1 v_1} = \sqrt{\frac{p_0 - p}{p_{01} - p_1}}$$

Houghton & Brock (1975) give the relation

$$\rho v = \left(\frac{p}{p_0}\right)^{1/\gamma} \sqrt{\frac{2\gamma}{\gamma - 1} p_0 \rho_0 \left(1 - \left(\frac{p}{p_0}\right)^{(\gamma-1)/\gamma}\right)}$$

The maximum Mach number encountered was about 0.17, so substituting

$$p_{01} = p_0 = 100000 \text{ Pa};$$

$$p_1 = 99625 \text{ Pa};$$

$$p = 98000 \text{ Pa}$$

into the above equations gives

$$\frac{\rho v}{\rho_1 v_1} = 2.309 \text{ (incompressible)}; \quad 2.289 \text{ (compressible)}$$

Thus the maximum error in ρv due to the assumption of incompressible flow will be about 1%, and the error in area integrated values will be less than this.

- An error in the numerical integration. Two different algorithms were used which were checked against manual calculations on simple datasets and against numerical predictions (applying a correction for compressibility). A programming error is therefore considered highly unlikely.

- Incorrect upstream static pressure. It has already been seen that there was an error in the upstream reference stagnation pressure. Upstream static pressure was measured by a single wall tapping at the same location and that pressure and that pressure was different from the endwall pressure just upstream of the middle blade passage.

The static pressure error explains why the values of m' for the three sets in table A3.2 differ from one another and from their expected values. Note that elsewhere in this dissertation all measurements have been normalized by exit dynamic head ($p_{01}-p_a$) so are unaffected by errors in p_1. A true measure of overall accuracy is therefore the discrepancy between mass flows at different planes within the same bladerow.

Measurement errors were high at $x/C_x=0.03$ because the horseshoe vortex near the pressure surface led to endwall boundary layer skew in excess of 180°. Elsewhere, however, mass flow discrepancies are within 2.5%. This compares favourably with Graves (1985) and Langston et al. (1977) who each found discrepancies up to 10%.

The effect of these errors on mass-average quantities, e.g.

$$\bar{Y} = \frac{\iint (p_{01}-p_0)\, v_x \, dydz}{(p_{01}-p_a) \iint v_x \, dydz}$$

is hard to estimate but is likely to be very small because v_x appears on both the top and bottom of the fraction.

The overall accuracy of mass-average loss coefficient based on $(p_{01}-p_a)$, taking account of all of the above factors, is estimated to be ±0.003.

APPENDIX 4

DATA PROCESSING

A4.1 Normalizing and Averaging Data

All pressures have been measured relative to inlet stagnation pressure and normalised by exit free stream dynamic head ($p_{01}-p_a$) to eliminate the effects of wind tunnel flow fluctuations. Incompressible flow is assumed throughout so that mass average quantities are defined as follows:

$$\text{Loss coefficient} \quad \bar{Y} = \frac{\iint (p_{01}-p_0)\, v_x \, dydz}{(p_{01}-p_a) \iint v_x \, dydz} \quad ;$$

$$\text{Velocities} \quad \bar{v}_y = \frac{\iint v_y \, v_x \, dydz}{\iint v_x \, dydz} \quad ; \quad \bar{v}_z = \frac{\iint v_z \, v_x \, dydz}{\iint v_x \, dydz}$$

Axial velocity is defined as an area average:

$$\bar{v}_x = \frac{\iint v_x \, dydz}{\iint dydz}$$

The mean flow direction is therefore that which would eventually be reached if the flow mixed out at constant area with no externally applied forces, even in the z direction:

$$\bar{\phi} = \tan^{-1}\left(\frac{\bar{v}_y}{\bar{v}_x}\right) \quad ; \quad \bar{\psi} = \tan^{-1}\left(\frac{\bar{v}_z}{(\bar{v}_x^2+\bar{v}_y^2)^{1/2}}\right)$$

The pitchwise integral stagnation pressure loss flux (fig.3.19) is defined as:

$$\frac{\int_0^s (p_{01}-p_0)\, v_x \, dy}{s\,(p_{01}-p_a)\sqrt{\frac{2}{\rho}(p_{01}-p_a)}}$$

where s represents the pitch. Note that it is not necessary to assume a value of ρ since v_x is derived from the measured dynamic head using the formula

$$v = \sqrt{\frac{2}{\rho}(p_0-p)}$$

A4.2 Definition of Secondary Velocity

All secondary velocity vectors presented in the figures associated with chapters 3 and 5 are projected along the direction $(\bar{v}_x,\bar{v}_y,0)$. This automatically defines the "primary" direction as the mean flow direction and "secondary" velocities as components of velocity perpendicular to the primary direction, and true views of secondary velocity vectors are drawn. This is the most realistic way to present secondary velocities as it does not distort the shape of streamwise vortices.

A4.3 Calculation of Vorticity

The components Ω_x, Ω_y and Ω_z of the vorticity $\underline{\Omega}$ are derived from experimental data as follows. Ω_x is obtained directly from velocity gradients:

$$\Omega_x = \frac{\partial v_z}{\partial y} - \frac{\partial v_y}{\partial z}$$

Following the method of Gregory-Smith et al. (1988), Ω_y and Ω_z are obtained by making use of Crocco's equation:

$$\underline{v}\wedge\underline{\Omega} = \frac{1}{\rho}\nabla p_0$$

Taking the y and z components we obtain

$$\Omega_y = \frac{1}{v_x}\left(v_y\Omega_x + \frac{1}{\rho}\frac{\partial p_0}{\partial y}\right) \quad ; \quad \Omega_z = \frac{1}{v_x}\left(v_z\Omega_x - \frac{1}{\rho}\frac{\partial p_0}{\partial z}\right)$$

Streamwise vorticity is defined as the component of vorticity in the local flow direction. In practice there is hardly any difference between this and the component in the mean flow direction.

APPENDIX 5

DISSIPATION IN A SKEWED BOUNDARY LAYER

Consider the steady flow through a stream tube within a skewed boundary layer (see sketch below). Define a right-handed set of orthogonal co-ordinates (x,y,z) with x always parallel to the local flow direction (i.e. nearly, but not precisely, parallel to the wall) so that $v_y=v_z=0$. y is perpendicular to the flow direction and parallel to the wall.

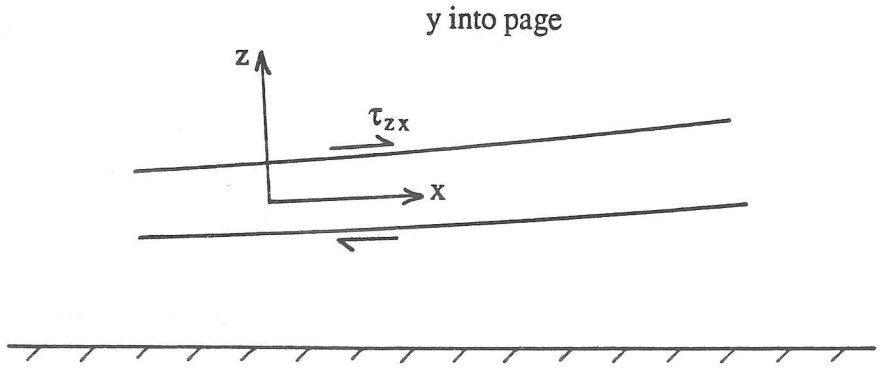

Symbols are defined as follows:

D Shear work in the boundary layer per unit wall surface area. If production and dissipation of turbulence are neglected, then the rate of entropy generation is D/T. If the boundary layer is adiabatic then

$$\int_0^\delta dq = 0 \qquad \text{and} \qquad D = T\int_0^\delta \left(\rho\, v_x \frac{\partial s}{\partial x} \right) dz$$

e Specific internal energy.

h Specific enthalpy.

q Heat flux in the z direction. Heat fluxes in the x and y directions are neglected.

s Specific entropy.

T Temperature (assume constant).

δ Boundary layer overall thickness.

τ_{zx} Shear stress on the z plane in the x direction.

τ_{zy} Shear stress on the z plane in the y direction.

Normal viscous stresses and all shear stresses except τ_{zx} and τ_{zy} are neglected.

Flow equations may be written as follows:

Second law:

$$T\frac{\partial s}{\partial x} = \frac{\partial h}{\partial x} - \frac{1}{\rho}\frac{\partial p}{\partial x}$$

$$= \frac{\partial h_0}{\partial x} - v_x\frac{\partial v_x}{\partial x} - \frac{1}{\rho}\frac{\partial p}{\partial x} \qquad \text{(A5,1)}$$

x momentum:

$$\frac{1}{\rho}\frac{\partial \tau_{zx}}{\partial z} - \frac{1}{\rho}\frac{\partial p}{\partial x} = v_x\frac{\partial v_x}{\partial x} \qquad \text{(A5,2)}$$

Combining equations (A5,1) and (A5,2) gives

$$T\frac{\partial s}{\partial x} = \frac{\partial h_0}{\partial x} - \frac{1}{\rho}\frac{\partial \tau_{zx}}{\partial z} \qquad \text{(A5,3)}$$

Now, neglecting heat flow in the x and y directions, the energy equation may be written:

$$\frac{D}{Dt}\left(e + \tfrac{1}{2}v_x^2\right) = -p\frac{D}{Dt}\left(\frac{1}{\rho}\right) + \left(\frac{1}{\rho}\frac{\partial \tau_{zx}}{\partial z} - \frac{1}{\rho}\frac{\partial p}{\partial x}\right)v_x$$

$$+ \frac{1}{\rho}\left(\tau_{zx}\frac{\partial v_x}{\partial z} + \tau_{zy}\frac{\partial v_y}{\partial z}\right) - \frac{1}{\rho}\frac{\partial q}{\partial z}$$

But in steady flow

$$\frac{D}{Dt} = v_x \frac{\partial}{\partial x}$$

so that

$$v_x \frac{\partial}{\partial x}\left(e + \tfrac{1}{2} v_x^2 + \frac{p}{\rho} \right) = v_x \frac{\partial h_0}{\partial x}$$

$$= \frac{v_x}{\rho}\frac{\partial \tau_{zx}}{\partial z} + \frac{1}{\rho}\left(\tau_{zx}\frac{\partial v_x}{\partial z} + \tau_{zy}\frac{\partial v_y}{\partial z} \right) - \frac{1}{\rho}\frac{\partial q}{\partial z} \qquad \text{(A5,4)}$$

Combining equations (A5,3) and (A5,4) gives

$$v_x T \frac{\partial s}{\partial x} = \frac{1}{\rho}\left(\tau_{zx}\frac{\partial v_x}{\partial z} + \tau_{zy}\frac{\partial v_y}{\partial z} \right) - \frac{1}{\rho}\frac{\partial q}{\partial z}$$

This gives the rate of entropy production along the stream tube. Integrate through the boundary layer, assuming T remains constant, to find the total rate of entropy generation.

$$T\int_0^{\delta}\left(\rho\, v_x \frac{\partial s}{\partial x} \right) dz = \int_0^{\delta} \left(\tau_{zx}\frac{\partial v_x}{\partial z} + \tau_{zy}\frac{\partial v_y}{\partial z} \right) dz - \int_0^{\delta} dq \qquad \text{(A5,5)}$$

Now recall the definition of D for adiabatic flow and so:

$$D = \int_0^{U} \underline{\tau}.d\underline{v}$$

APPENDIX 6

CORRECTION TO MIXING LOSS TO ALLOW FOR SPANWISE FLOW ANGLE VARIATION

Consider an incompressible flow with uniform static and stagnation pressures p' and p_0' (and hence uniform velocity v') but with a spanwise variation of yaw angle. Let x coincide with the mean flow direction and z coincide with the spanwise direction and consider a unit width of flow perpendicular to x and z. Let h be the blade span. Assume that there is no spanwise flow and that the yaw angle ϕ varies linearly according to the relation

$$\phi = \tan^{-1}\left(\frac{v_y'}{v_x'}\right) = \phi_0\left(\frac{2z}{h} - 1\right) \qquad \text{(A6,1)}$$

where ϕ_0 is constant. Now assume that this flow mixes at constant area to a completely uniform downstream flow with stagnation pressure p_{0M}. If externally applied forces are zero then eq.(1,6) becomes

$$p_{0M} = \frac{1}{h}\int_0^h (p'+\rho v_x'^2)dz - \frac{\rho}{2}\left(\frac{\int v_x' dz}{h}\right)^2 \qquad \text{(A6,2)}$$

Now note that

$$\int_0^h v_x' dz = v' \int_0^h \cos\phi \, dz \qquad \text{(A6,3)}$$

$$\int_0^h (p' + \rho v_x'^2)dz = p'h + \rho v'^2 \int_0^h \cos^2\phi \, dz \qquad \text{(A6,4)}$$

$$p_0' = p' + \tfrac{1}{2}\rho v'^2 \qquad \text{(A6,5)}$$

Substitute (A6,3-5) into (A6,2)

$$\frac{p_0' - p_{0M}}{\frac{1}{2}\rho v'^2} = 1 - \frac{2}{h}\int_0^h \cos^2\phi \, dz + \left(\frac{1}{h}\int_0^h \cos\phi \, dz\right)^2$$

Now substitute

$$\zeta = \frac{2\zeta}{h} - 1 \quad ; \quad dz = \frac{h\, d\zeta}{2} \quad ; \quad \phi = \phi_0\zeta$$

$$\therefore \quad \frac{2}{h}\int_0^h \cos^2\phi \, dz = \int_{-1}^{1}\cos^2(\phi_0\zeta)\, d\zeta = \frac{\sin 2\phi_0}{2\phi_0} + 1$$

$$\frac{1}{h}\int_0^h \cos\phi \, dz = \frac{1}{2}\int_{-1}^{1}\cos(\phi_0\zeta)\, d\zeta = \frac{\sin\phi_0}{\phi_0}$$

$$\therefore \quad \frac{p_0' - p_{0M}}{\frac{1}{2}\rho v'^2} = \frac{\sin^2\phi_0}{\phi_0^2} - \frac{\sin 2\phi_0}{2\phi_0} \qquad \text{(A6,6)}$$

$$= 0.002 \quad \text{if } \phi_0 = 4.5°$$

The secondary kinetic energy coefficient is given by

$$Y'_{SKE} = \frac{\int_0^h \frac{1}{2}\rho(v'\sin\phi)^2(v'\cos\phi)dz}{\frac{1}{2}\rho v'^2 \int_0^h (v'\cos\phi)dz}$$

$$= \frac{\int_{-1}^{1} \sin^2(\phi_0\zeta)\cos(\phi_0\zeta)\, d\zeta}{\int_{-1}^{1}\cos(\phi_0\zeta)\, d\zeta}$$

$$= \frac{\sin^2\phi_0}{3} \qquad \text{(A6,7)}$$

$$= 0.002 \quad \text{if } \phi_0 = 4.5°$$

Thus, since ϕ_o=4.5° is seen from fig.3.18 to be a reasonable value for set 2, equations (A6,6) and (A6,7) show that the mixing loss coefficient and secondary kinetic energy coefficient for set 2 should both be reduced by 0.002 to allow for spanwise yaw angle variations.

APPENDIX 7

MIXING OF A STREAMWISE VORTEX

Consider an incompressible flow through a circular pipe of radius r_3 comprising:

$0 \leq r \leq r_1$ A forced vortex with uniform axial velocity;

$r_1 \leq r \leq r_2$ A free vortex with uniform axial velocity and hence uniform stagnation pressure. Pressure and axial and tangential velocity are continuous at radius r_1.

$r_2 < r \leq r_3$ Uniform axial velocity U_1 with zero swirl and uniform stagnation pressure p_{01}. Static and stagnation pressures are continuous at radius r_2 but velocities are not.

Use the following notation:

v_x = axial velocity

v_θ = tangential velocity

γU_1 = $v_{\theta max}$ = maximum v_θ (at $r = r_1$)

Now consider acceleration or deceleration (without mixing) to a new condition, denoted by r', v_θ', γ' etc., where the velocity in the outer region is U_2. This is shown in the sketch below.

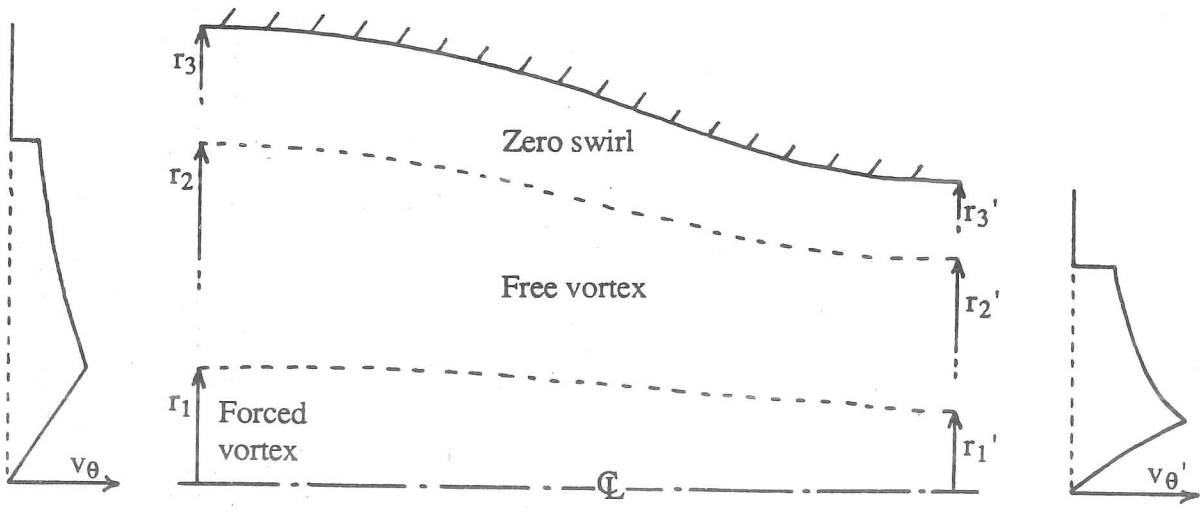

Consider a ring of flow between radii r and (r+δr). After the acceleration/deceleration it has a new radius r' and thickness δr' but the same stagnation pressure. We may write the following equations which apply at all radii:

Continuity:

$$\rho\, v_x\, 2\pi r\, \delta r = \rho\, v_x'\, 2\pi r'\, \delta r'$$

$$\therefore \frac{\delta r'}{\delta r} = \frac{r\, v_x}{r' v_x'} \qquad \text{(A7,1)}$$

Bernoulli's equation:

$$p_0 = p_0' \qquad \text{throughout}$$

$$\therefore \frac{\partial p_0}{\partial r}\delta r = \frac{\partial p_0'}{\partial r'}\delta r'$$

$$\left(\frac{1}{\rho}\frac{\partial p}{\partial r} + v_x\frac{\partial v_x}{\partial r} + v_\theta\frac{\partial v_\theta}{\partial r}\right)\delta r = \left(\frac{1}{\rho}\frac{\partial p'}{\partial r'} + v_x'\frac{\partial v_x'}{\partial r'} + v_\theta'\frac{\partial v_\theta'}{\partial r'}\right)\delta r' \qquad \text{(A7,2)}$$

Radial equilibrium:

$$\frac{\partial p}{\partial r} = \frac{\rho v_\theta^2}{r} \quad ; \quad \frac{\partial p'}{\partial r'} = \frac{\rho v_\theta'^2}{r'} \qquad \text{(A7,3)}$$

Kelvin's circulation theorem:

$$r v_\theta = r' v_\theta' \qquad \text{throughout} \qquad \text{(A7,4)}$$

$$\therefore \left(\frac{\partial}{\partial r}(r v_\theta)\right)\delta r = \left(\frac{\partial}{\partial r'}(r' v_\theta')\right)\delta r'$$

$$\therefore \left(\frac{1}{v_\theta}\frac{\partial v_\theta}{\partial r} + \frac{1}{r}\right) = \frac{\delta r'}{\delta r}\left(\frac{1}{v_\theta'}\frac{\partial v_\theta'}{\partial r'} + \frac{1}{r'}\right) \qquad \text{(A7,5)}$$

Within the forced vortex upstream:

$$\frac{v_\theta}{r} = \frac{\gamma U_1}{r_1} \qquad \text{(A7,6)}$$

Combining equations (A7,2-6) and remembering that constant axial velocity was specified within the vortex before the acceleration/deceleration, i.e. $\partial v_x/\partial r=0$, we obtain

$$\frac{\delta v_x'}{\delta r} = 2\left(\frac{\gamma U_1}{r_1}\right)^2 \frac{r}{v_x'}\left(1 - \frac{r^2}{r'^2}\right) \qquad \text{(A7,7)}$$

After the change of velocity the central part of the flow will no longer be a pure forced vortex so the new flow must be determined numerically, beginning at r=0. The boundary conditions are determined as follows.

Initially the tangential velocity at radius r_2 is given by $v_\theta=\gamma U_1 r_1/r_2$ so the axial velocity, which by definition is uniform for $0 \le r \le r_2$, is given by

$$v_x = U_1 \sqrt{1 - \gamma^2 \left(\frac{r_1}{r_2}\right)^2}$$

Thus v_x at r=0 is known and v_x' at r'=0 may be specified. By continuity

$$\frac{\delta r'}{\delta r} = \sqrt{\frac{v_x}{v_x'}} \qquad \text{at r=0}$$

By symmetry

$$\frac{\partial v_x'}{\partial r'} = \frac{\delta v_x'}{\delta r'} = 0 \qquad \text{at r=0}$$

so we can say that

$$\frac{\delta v_x'}{\delta r} = 0 \qquad \text{at } r=0$$

The flow $r_1' \leq r' \leq r_2'$ is a free vortex with constant axial velocity v_x' and the flow $r_2' < r' \leq r_3'$ is a uniform axial flow, velocity U_2, so having found r_1' and v_x', v_θ' and p' at that radius it is a simple matter to find r_2', r_3', U_2 etc.

It is now possible to evaluate $\bar{Y}$, Y_{MIX} and Y_{SKE} for the flow after the acceleration or deceleration, using equations (0,0), and to normalize them using $\frac{1}{2}\rho U_1^2$. This has been done over a range of values of r_1/r_2, r_2/r_3 and γ and it is found that with zero acceleration before mixing (i.e. $U_2=U_1$) Y_{SKE} is always less than Y_{MIX}. Provided $(r_1/r_2)<0.5$ and $\gamma<0.7$, the ratio Y_{SKE}/Y_{MIX} is always between 0.95 and 1.0, i.e. nearly all of the mixing loss arising from a streamwise vortex is due to dissipation of secondary kinetic energy.

Actual values estimated from set 1 measurements (fig.3.0, $x/C_x=1.23$) are $r_1/r_2=0.3$, $r_2/r_3=0.7$ and $\gamma=0.25$. Using these values with $U_2=U_1$ we obtain $Y_{SKE}/Y_{MIX}=0.997$ and $Y_{MIX}/\bar{Y}=2.6$, so for this flow the additional entropy which can potentially be generated by downstream mixing is even greater than the entropy already present in the flow.

The effect of acceleration or deceleration on mixing loss has been calculated and is shown in fig.4.8. Both mixing loss and secondary kinetic energy are roughly proportional to U_2/U_1 except at very low velocities, when the forced vortex core is close to reversing.

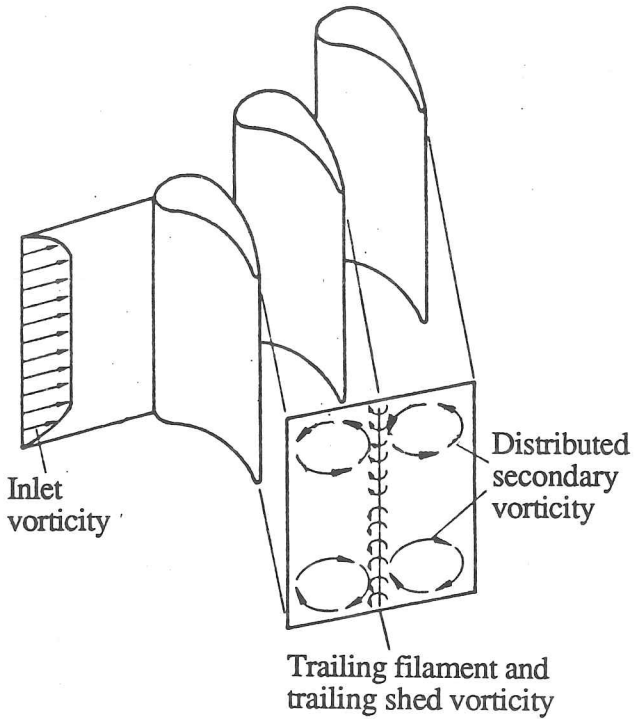

a) The three components of secondary vorticity

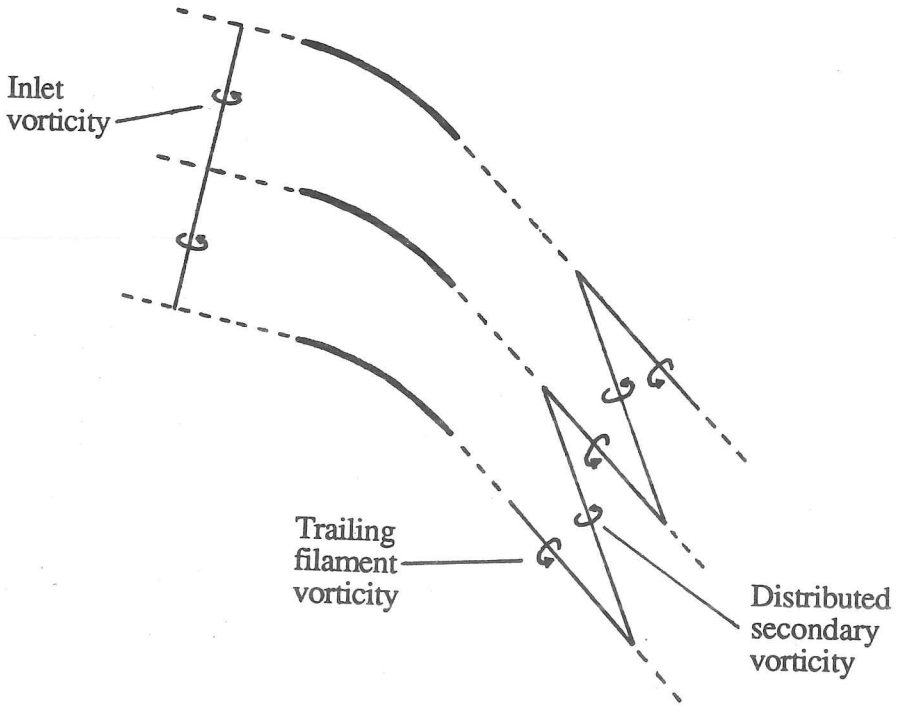

b) Formation if trailing filament and distributed secondary vorticity by stretching of inlet vortex lines (the basis of the simple derivation by Came and Marsh, 1974)

Fig.1.1 Inviscid theory of secondary vorticity

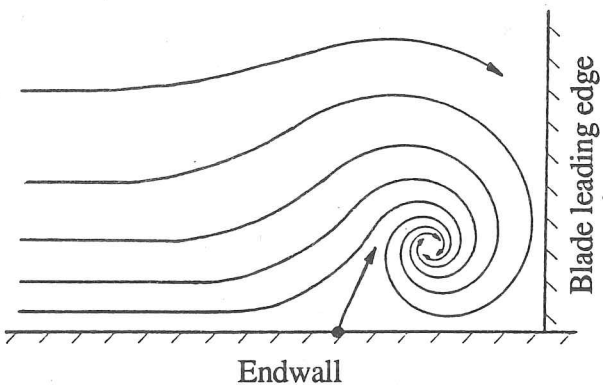

a)

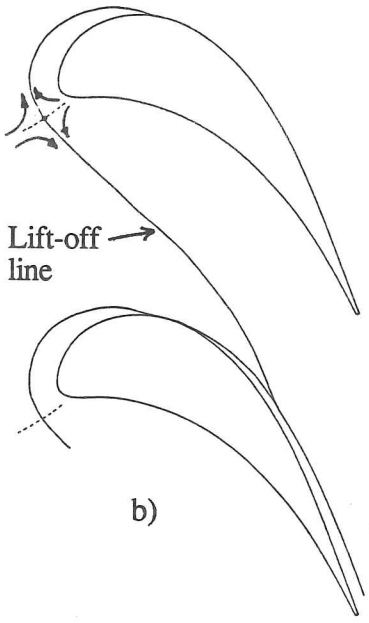

b)

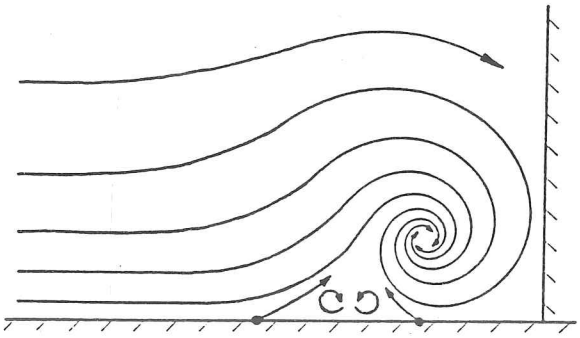

c)

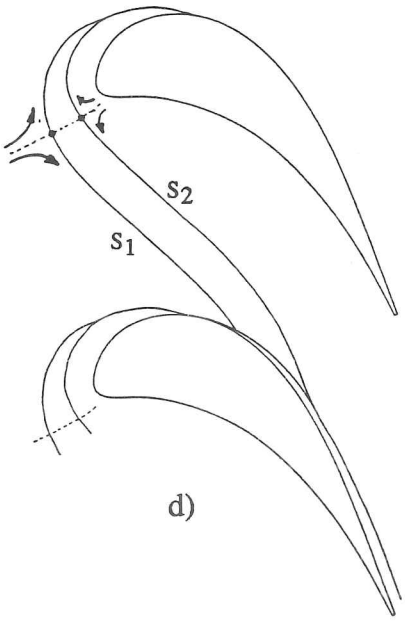

d)

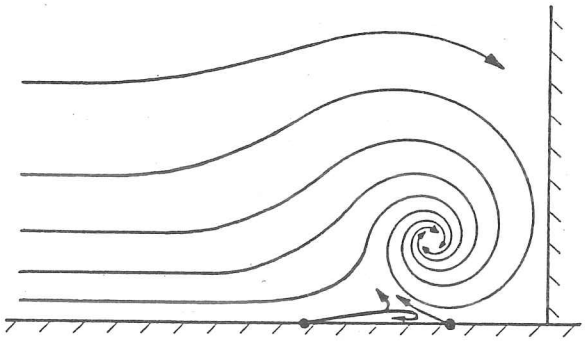

e)

• Saddle point

a) & b) Simple model (e.g. Langston et al., 1977)
c) & d) Revised model (e.g. Marchal and Sieverding, 1977)
d) & e) Eckerle and Langston's model (1987)

Fig.1.2 Models of leading edge vortex formation

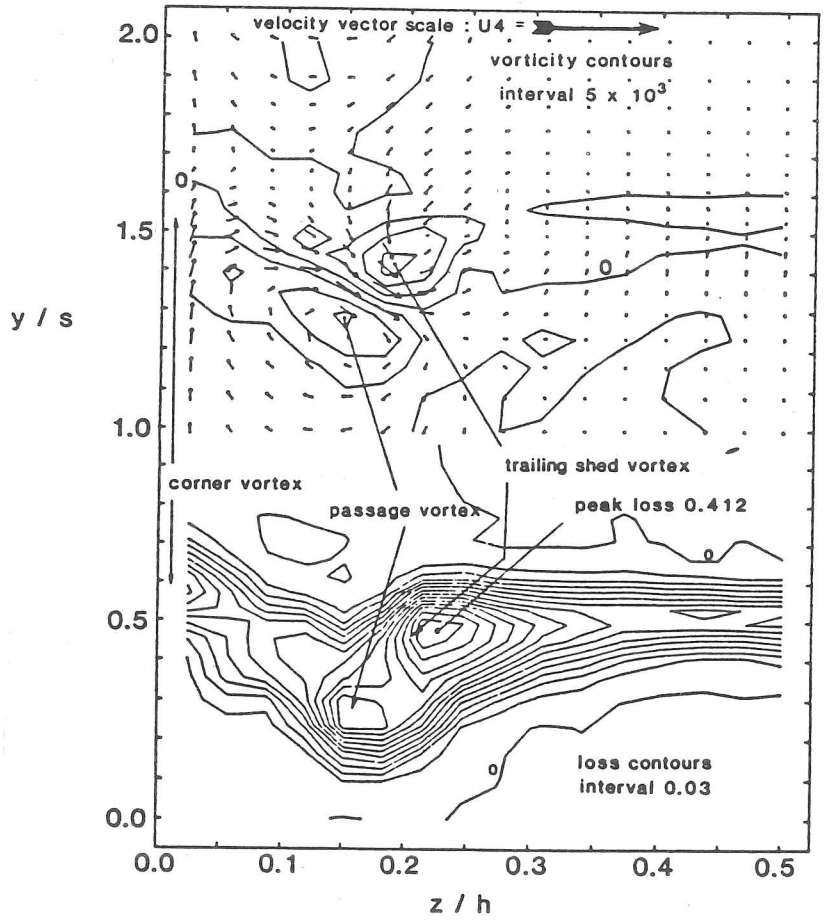

Fig.1.3 **Typical turbine exit flow**
(from Hodson and Dominy, 1987b)

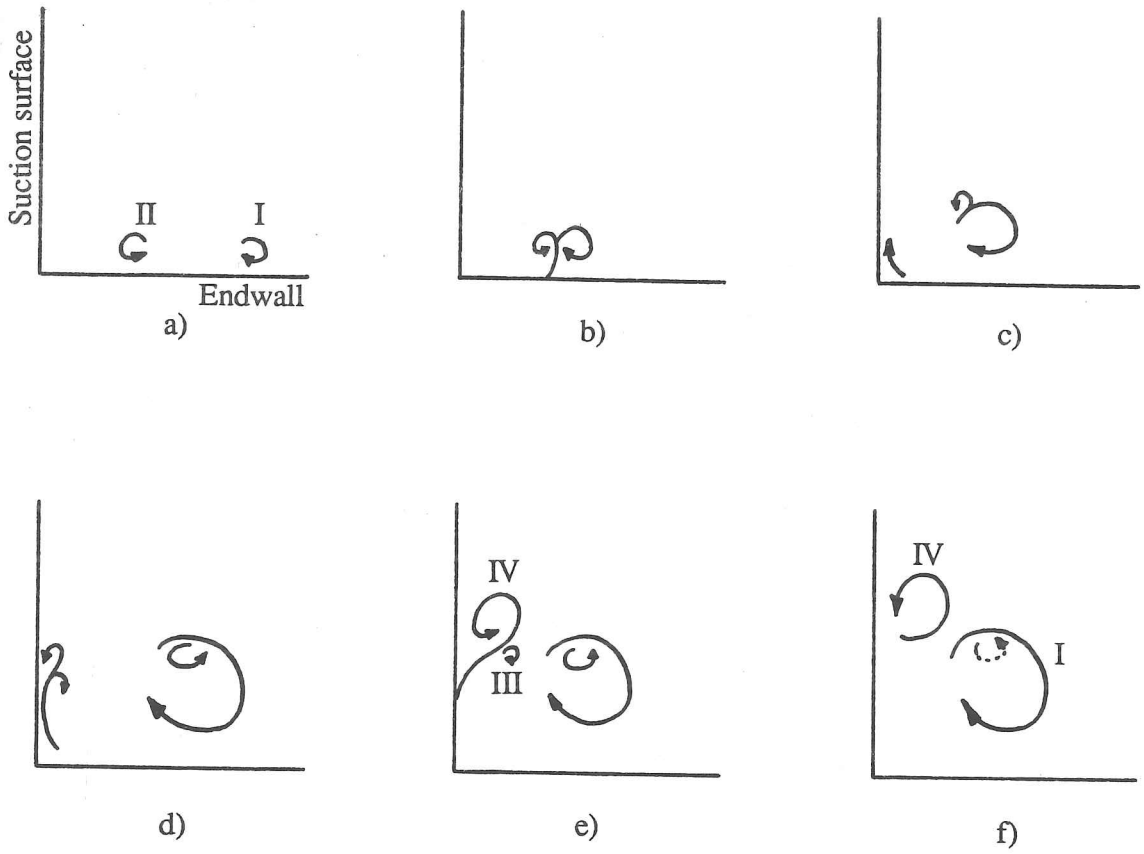

a) & b) The pressure side (I) and suction side (II) legs of the horseshoe vortex form separately but combine and begin to rotate together as the passage vortex

c) & d) The passage vortex causes secondary flow along the suction surface. Boundary layer accumulation and skew on the suction surface give rise to two new vortices.

e) & f) Vortex III is small and quickly merges into the passage vortex. Vortex IV grows and is clearly visible at the cascade exit.

Fig.1.4 **Formation of trailing filament vortex**
(Based on flow visualization by Sonoda, 1985)

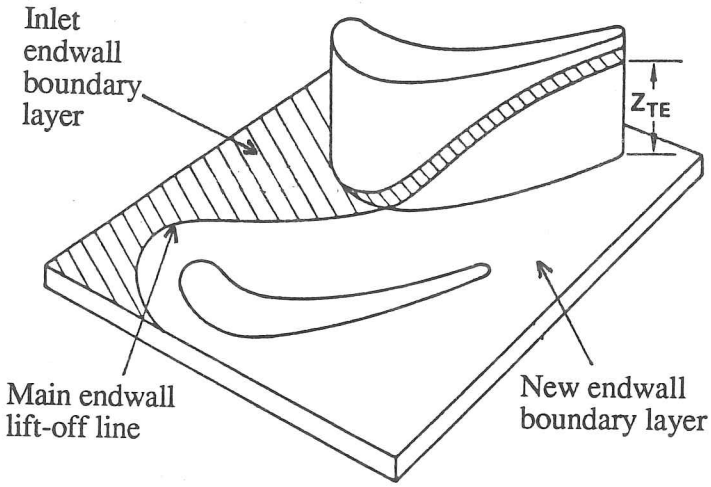

Fig.1.5 **Schematic of turbine endwall flow**
showing distance Z_{TE} used in Sharma and Butler's (1987) secondary loss correlation

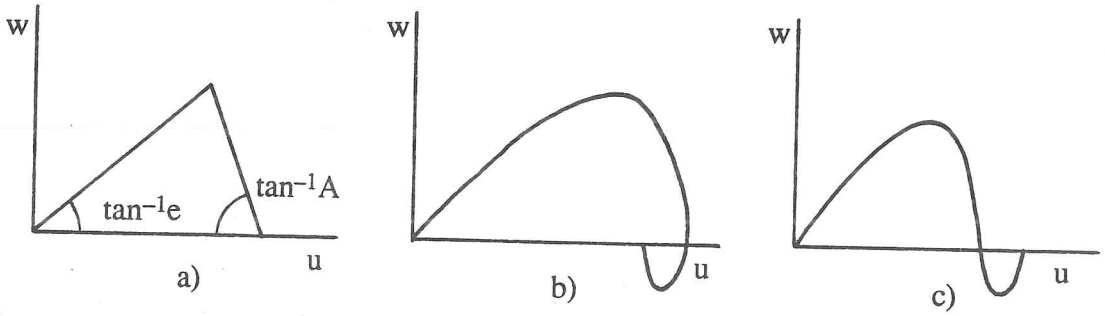

u – primary velocity
w – secondary velocity

a) Johnson's triangular model
b) & c) Crossover crossflow profiles (e.g. Langston, 1980)

Fig.1.6 **Skewed boundary layer profiles**

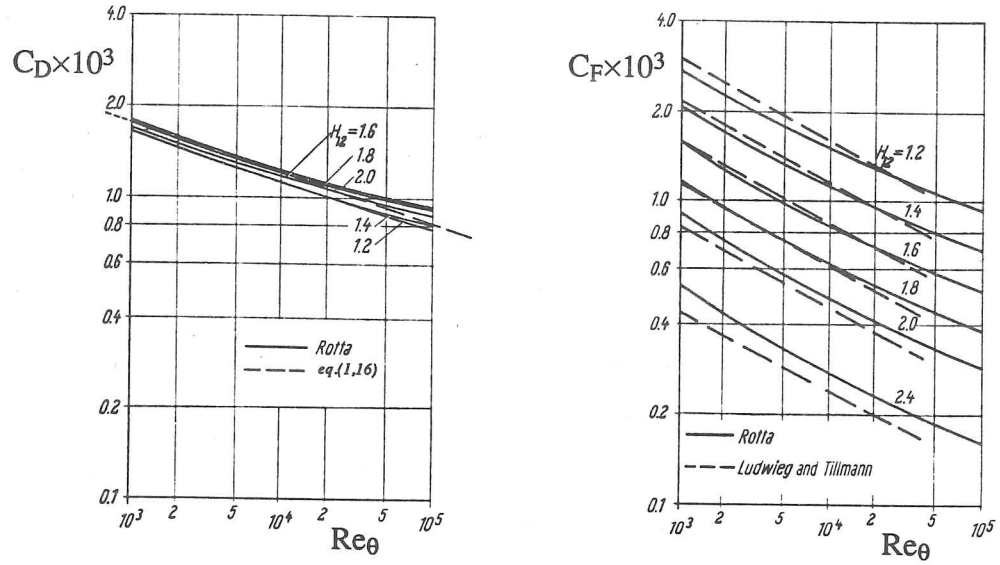

a) b)

a) & b) Turbulent boundary layers.
(Reproduced from Schlichting (1968), with permission.)

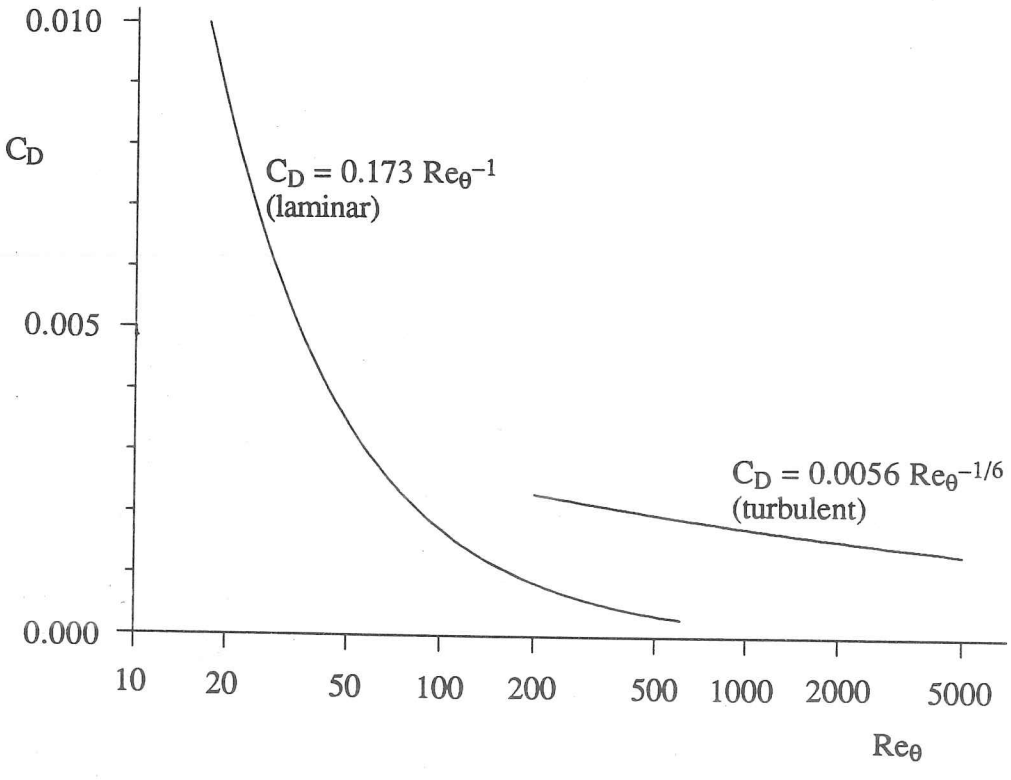

c) Truckenbrodt's relations (eq.1,16) for laminar and turbulent boundary layers.

Fig.1.7 Variation of collateral boundary layer parameters with Re_θ

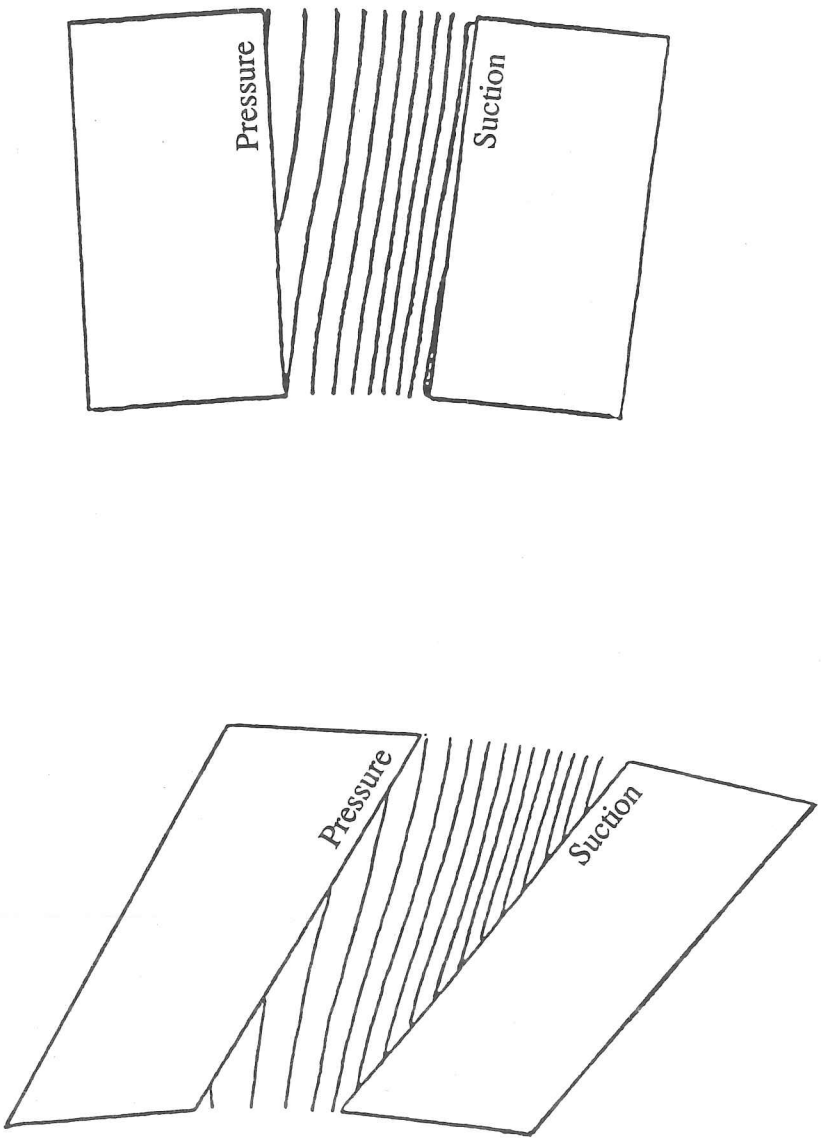

Fig.1.8 **Effect of blade lean on static pressure contours**
(from calculations by Walker, 1987)

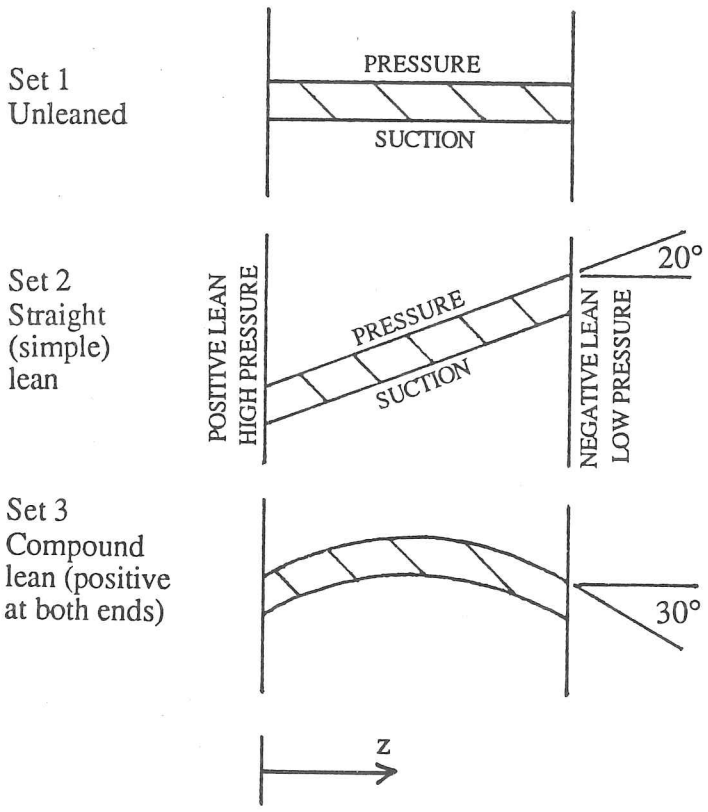

Fig.2.1 Blade Lean

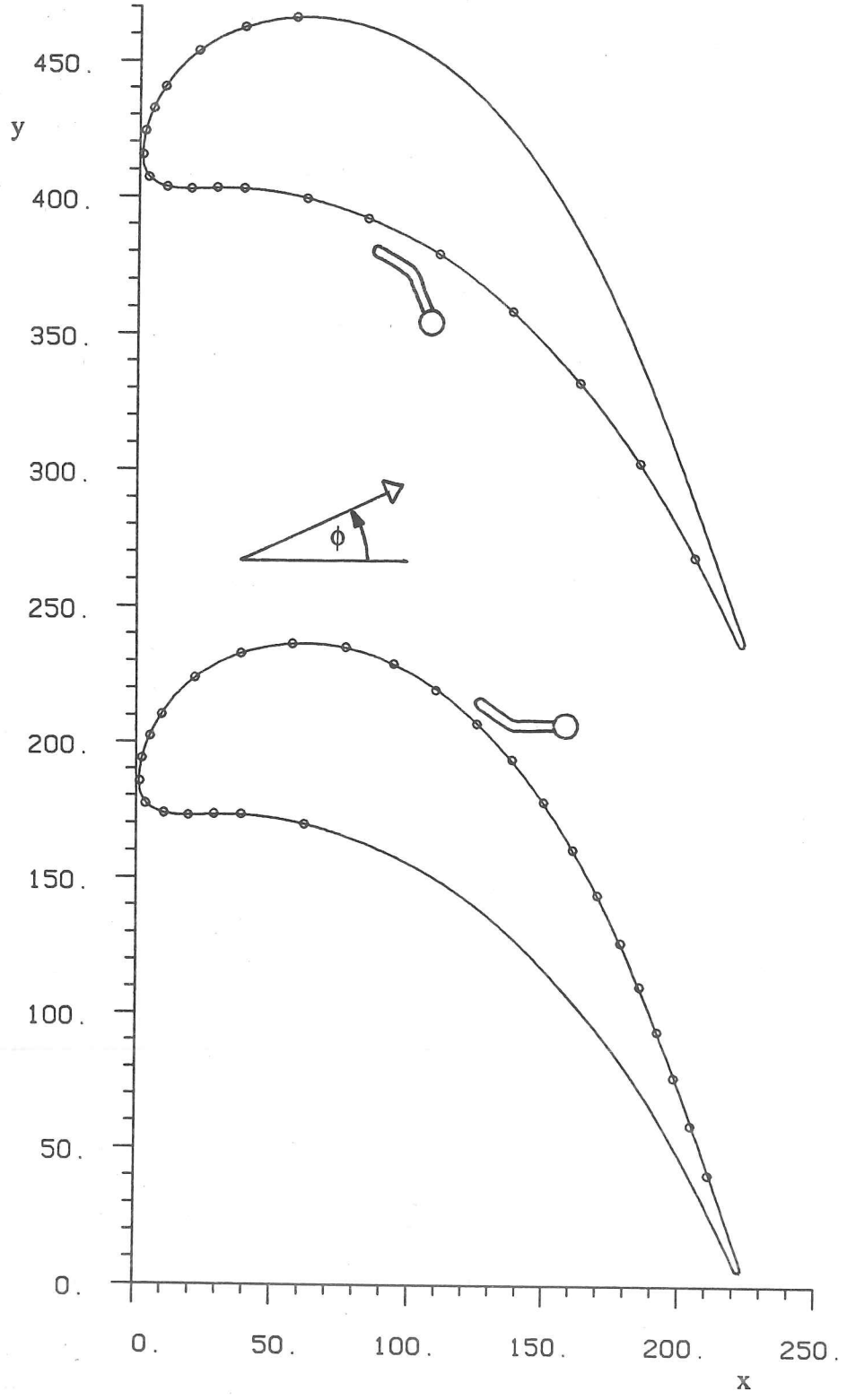

(–124, 250)

Fig.2.2 **Blade profile**
Showing x and y axes, static pressure tapping positions, "kinked" five-hole probes (to scale), upstream boundary layer measurement location and definition of yaw angle ϕ.

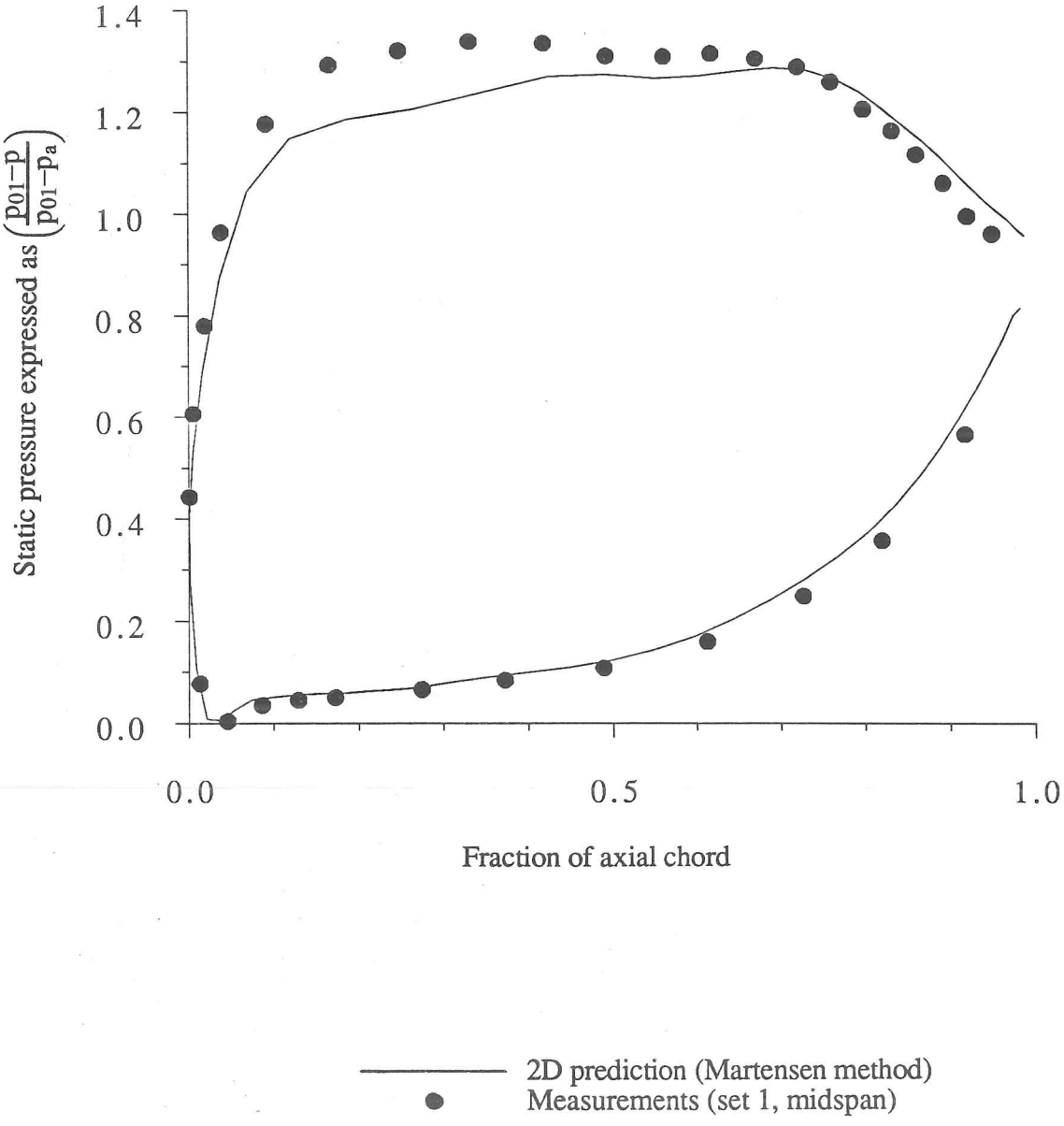

Fig.2.3 Blade surface static pressures

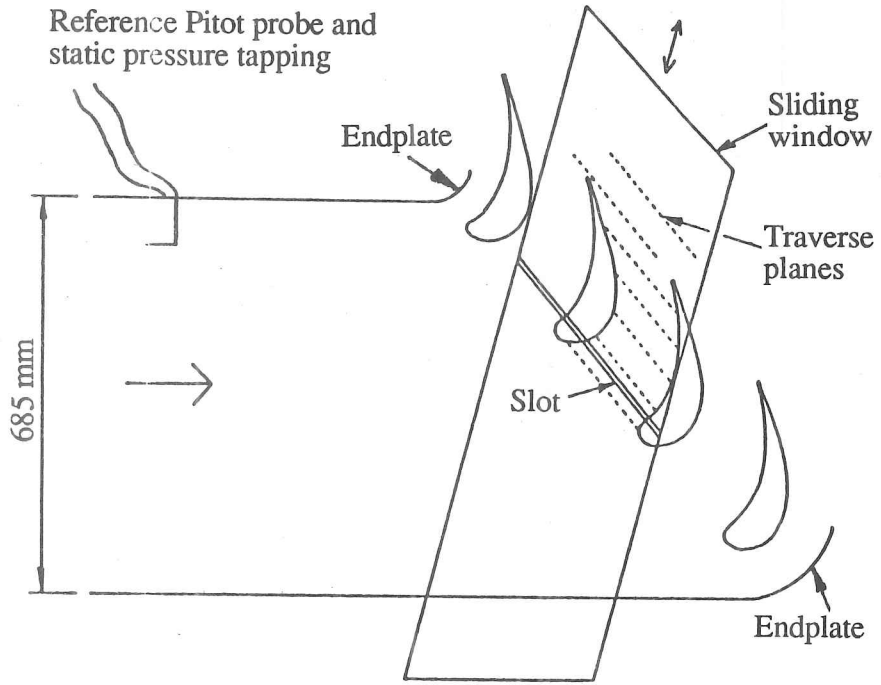

Fig.2.4a Cascade layout

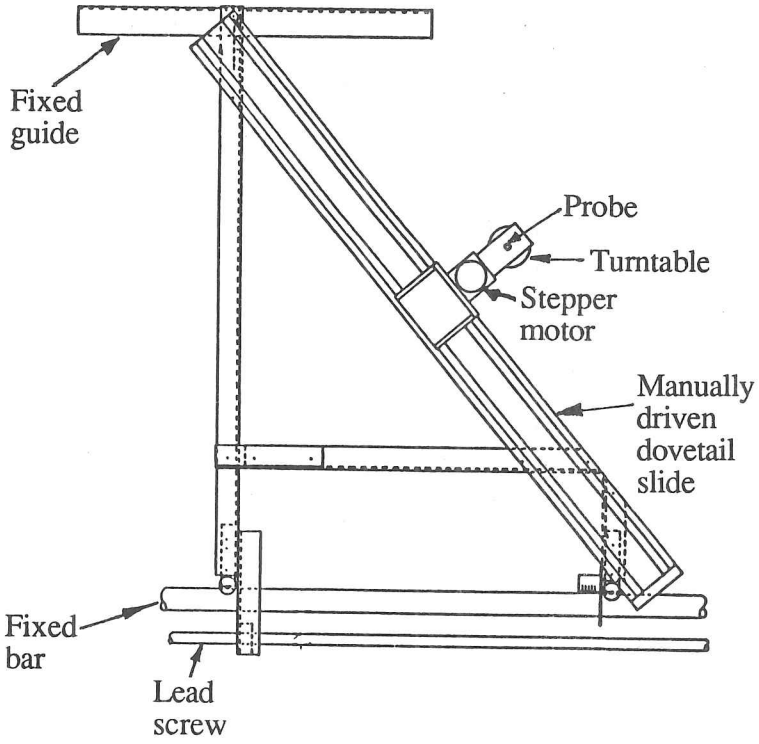

Fig.2.4b Traversing frame

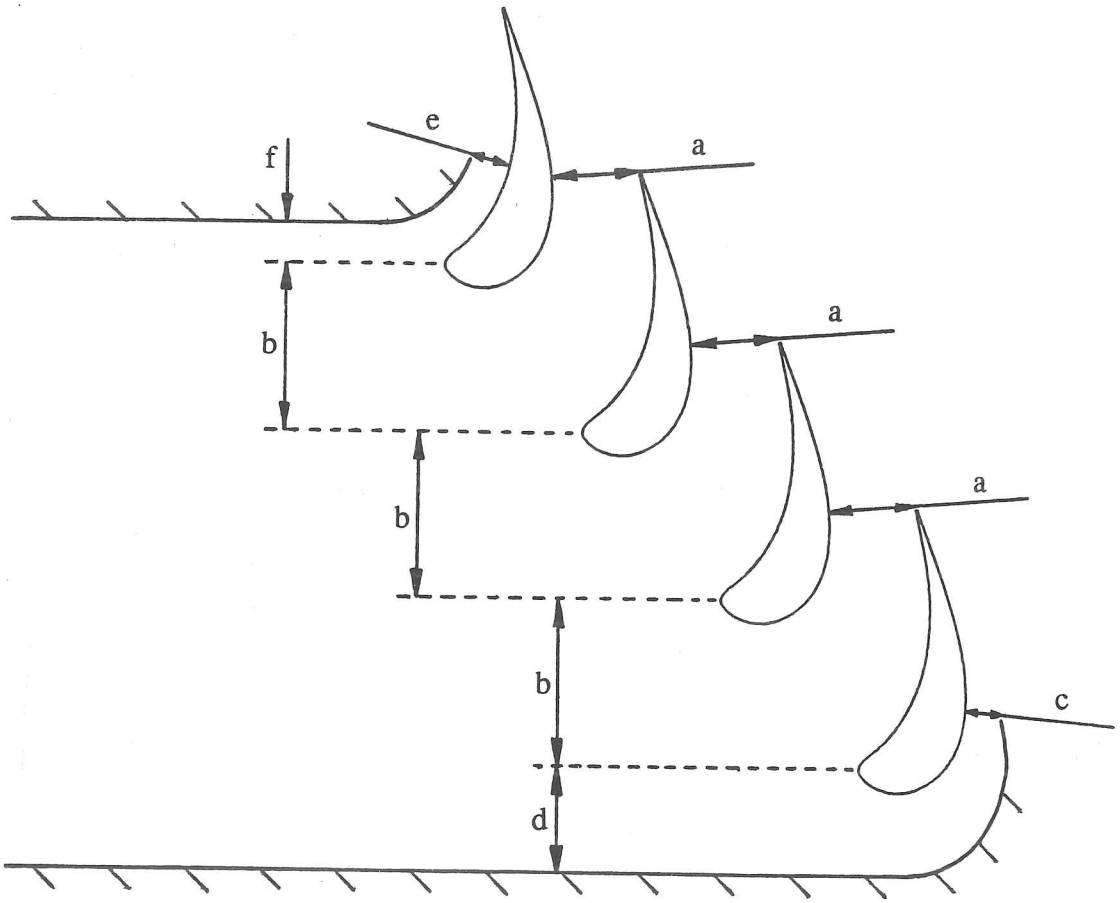

$$\frac{a}{b} = \frac{c}{d} = \frac{e}{f}$$

Fig.2.5 Initial setting of endplates

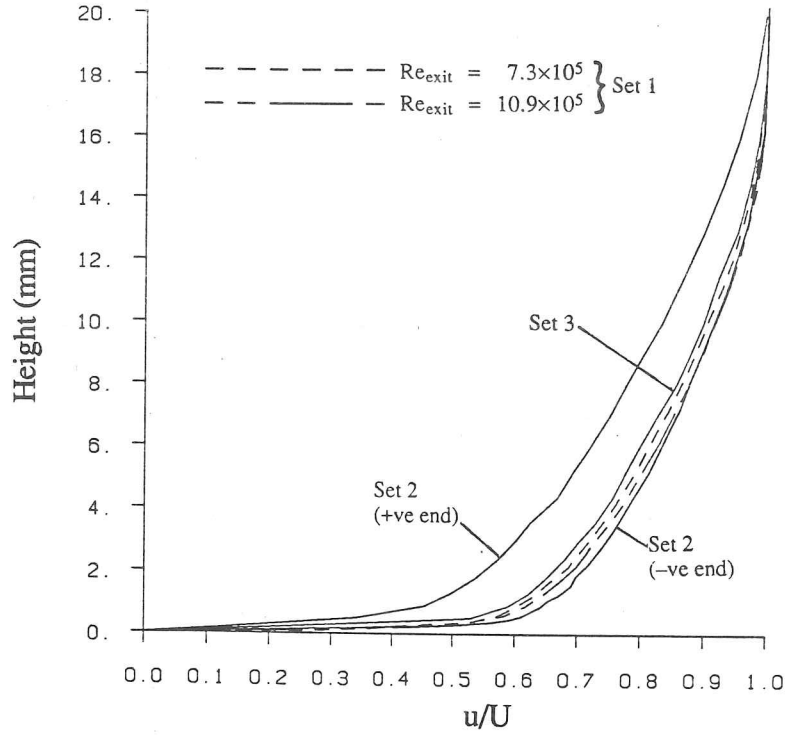

Fig.2.6a Upstream endwall boundary layer at x=–124, y= 250

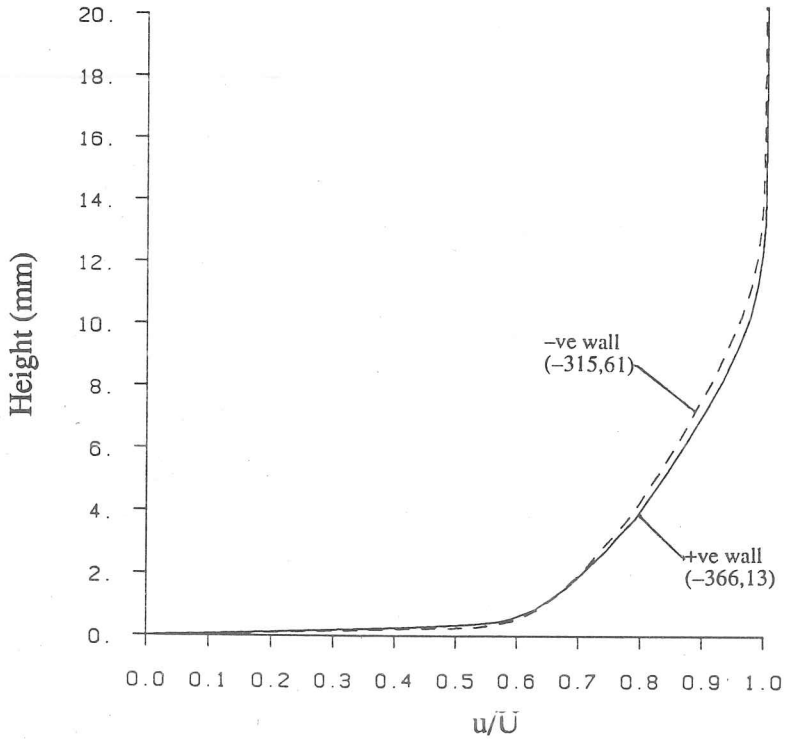

Fig.2.6b Endwall boundary layer upstream of set 2

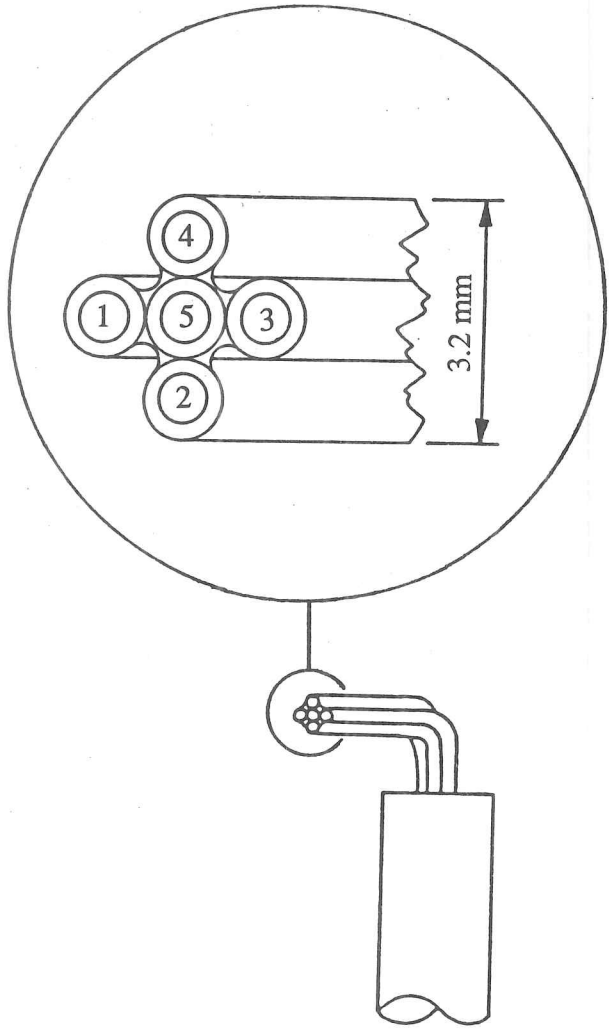

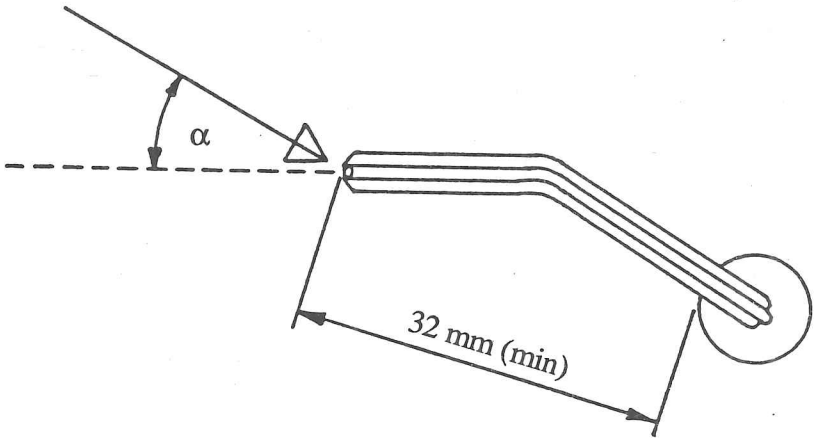

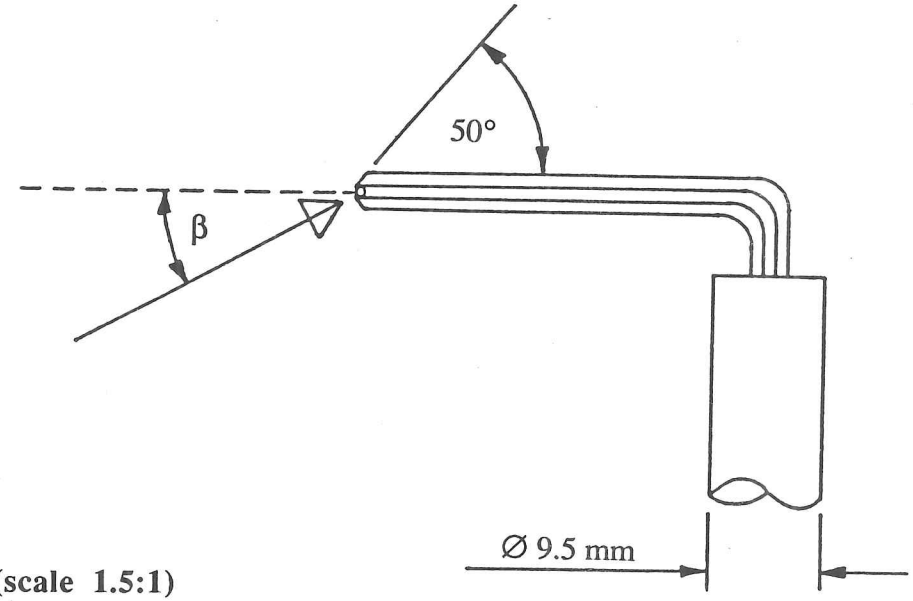

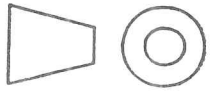

Fig.2.7a Five-hole probe (scale 1.5:1)

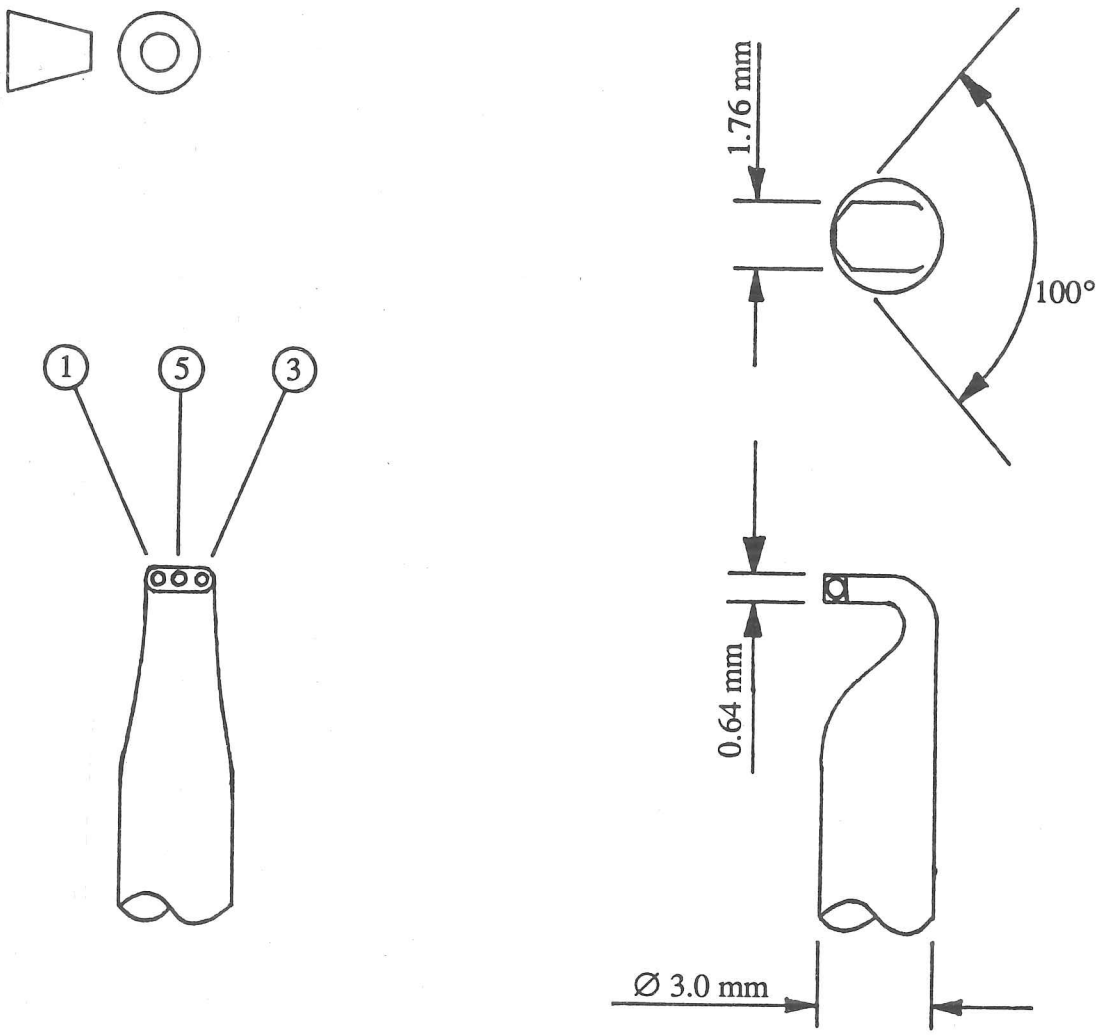

Fig.2.7b Three-hole probe (scale 5:1)

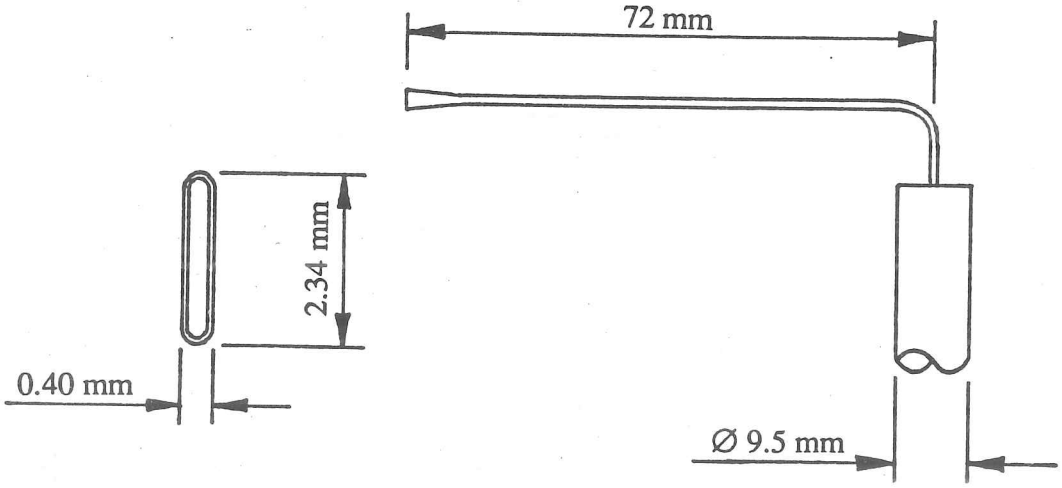

Fig.2.7c Blade boundary layer probe (scale 10:1 & 1:1)

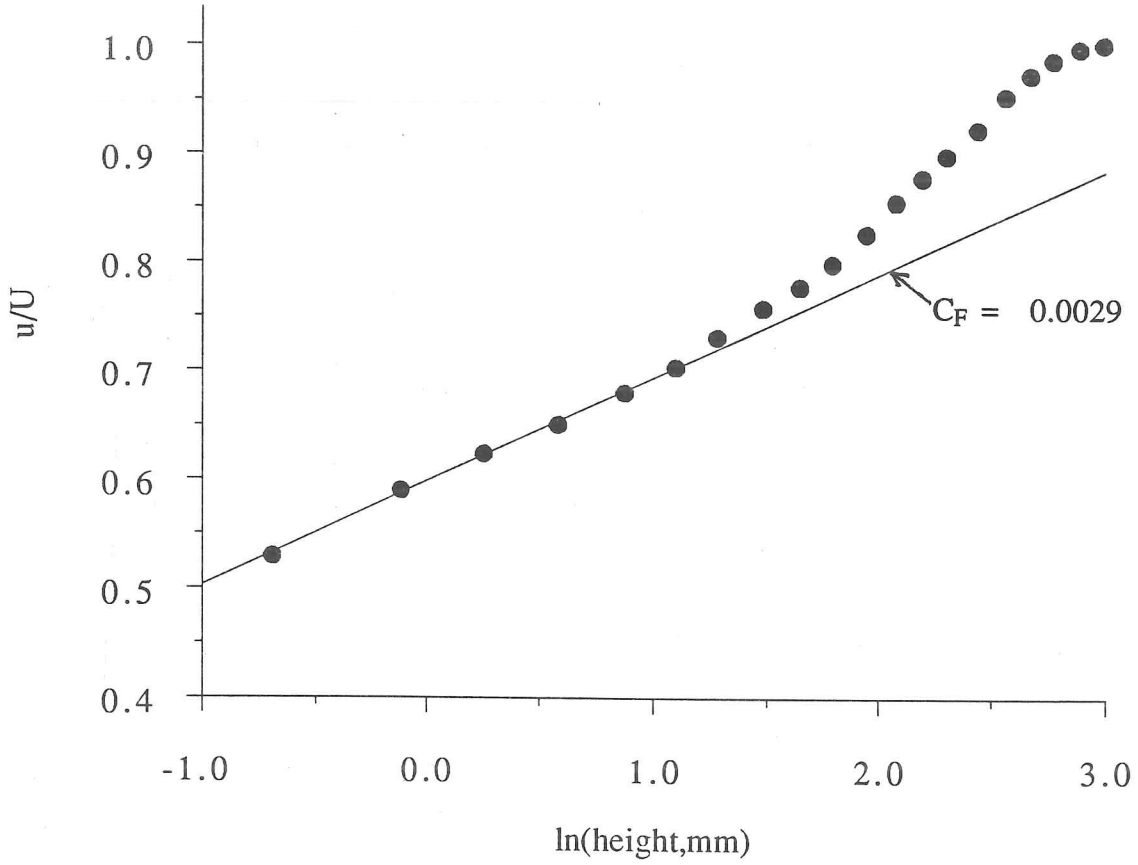

The straight line represents the equation

$$\frac{u}{u_\tau} = A \ln\left(\frac{z u_\tau}{\nu}\right) + B$$

where A=2.5 and B=5.5 (Duncan, Thom and Young, 1970)

and $$\left(\frac{u_\tau}{U}\right)^2 = \frac{\tau_w}{\rho U^2} = \frac{C_F}{2}$$

Fig.2.8 "Clauser" plot of endwall boundary layer on set 3 at x=–124, y=250

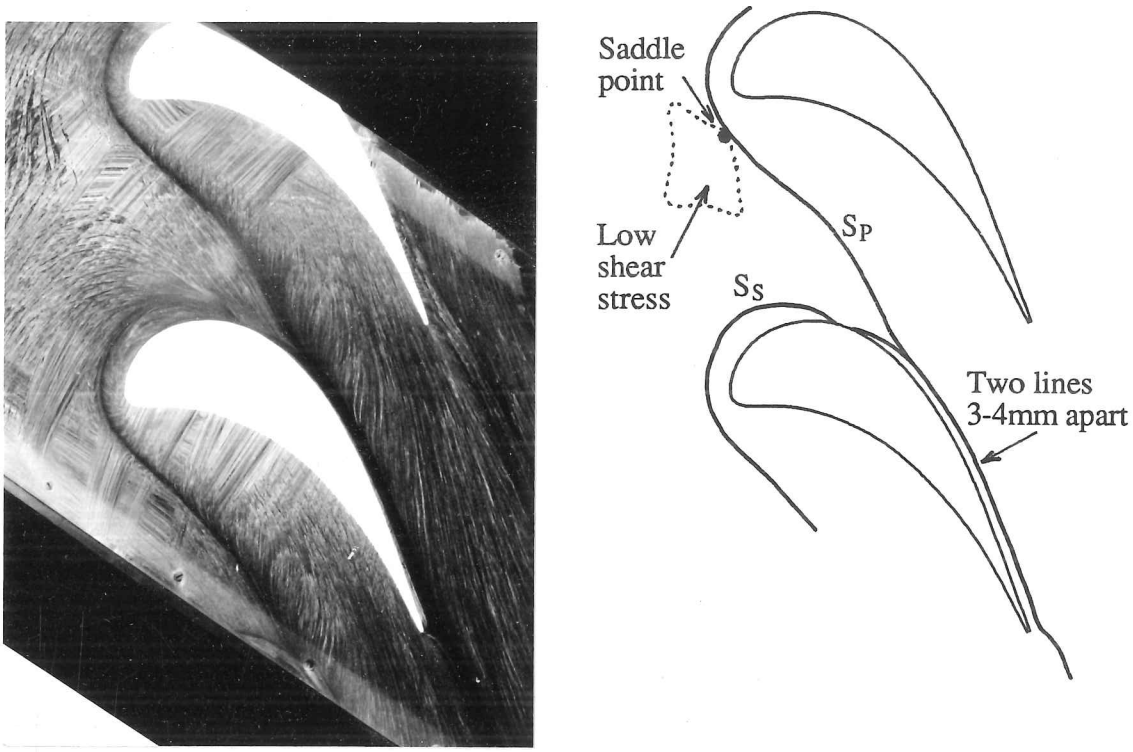

Fig.3.1a Set 1 oil flow visualization (endwall)

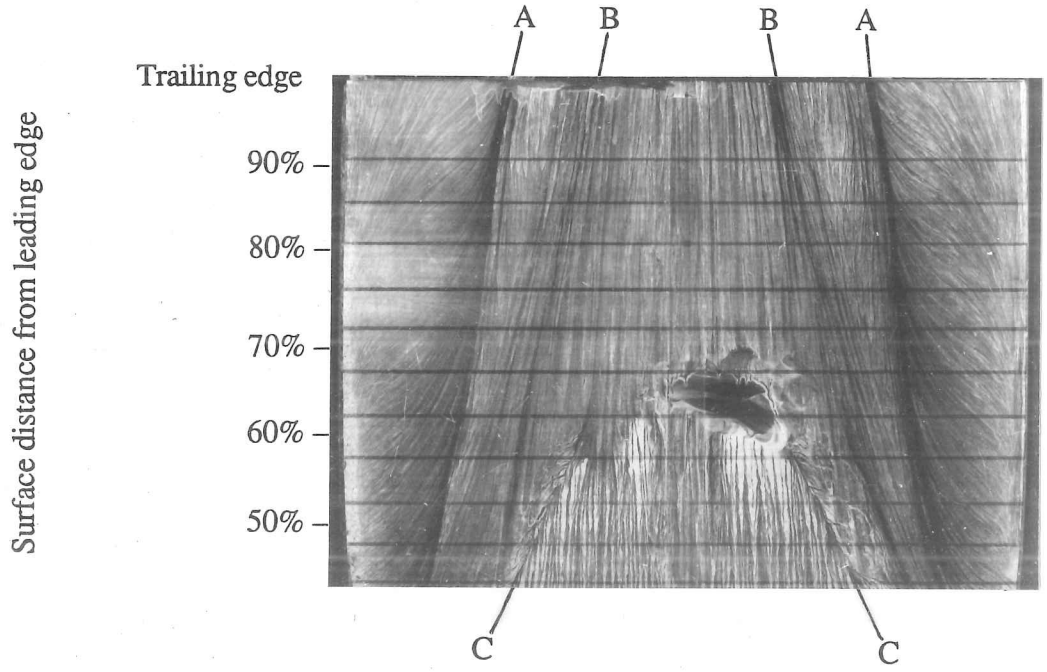

Fig.3.1b Set 1 oil flow visualization (suction surface)

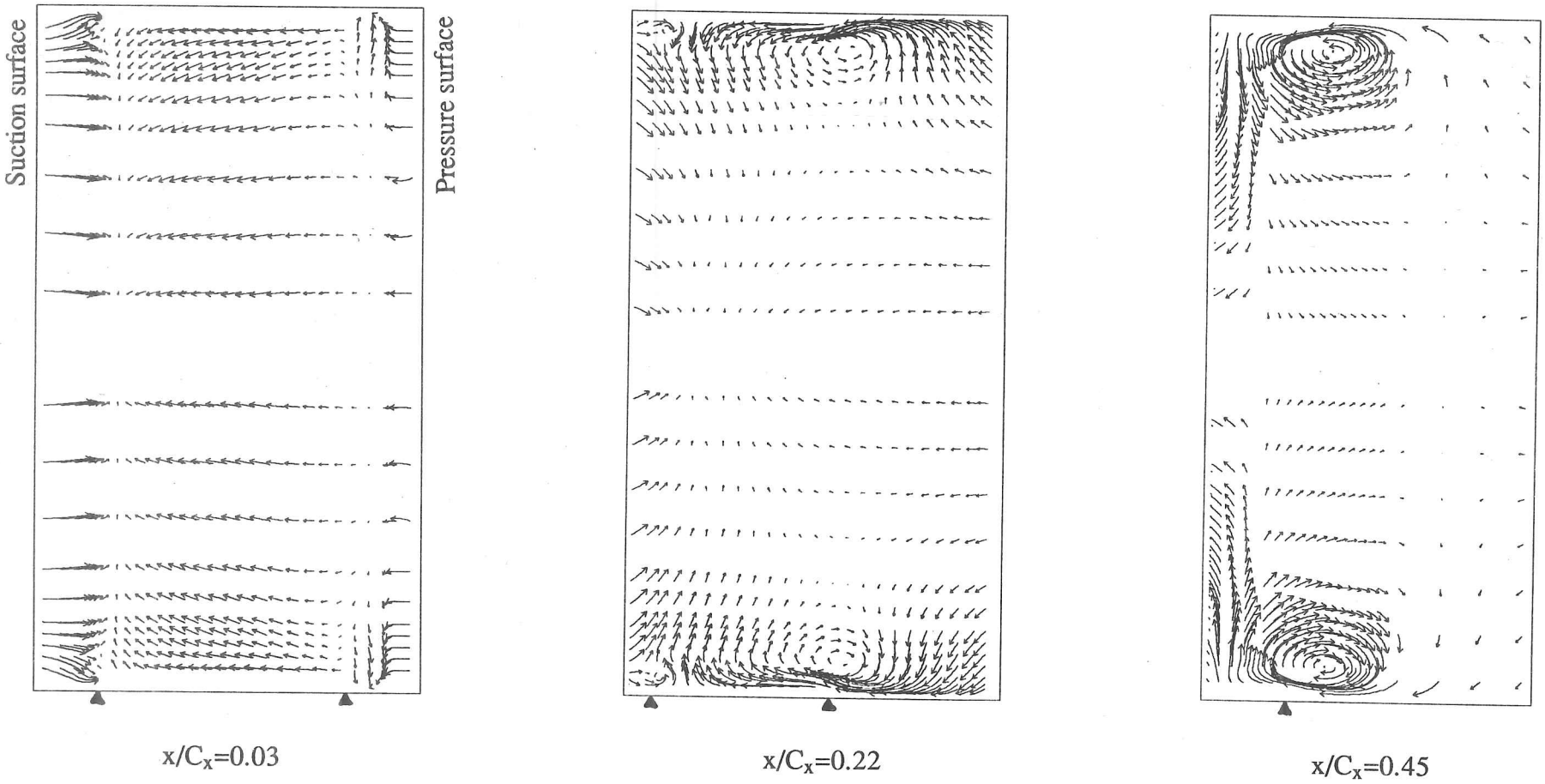

Fig.3.2a Set 1 secondary velocity vectors

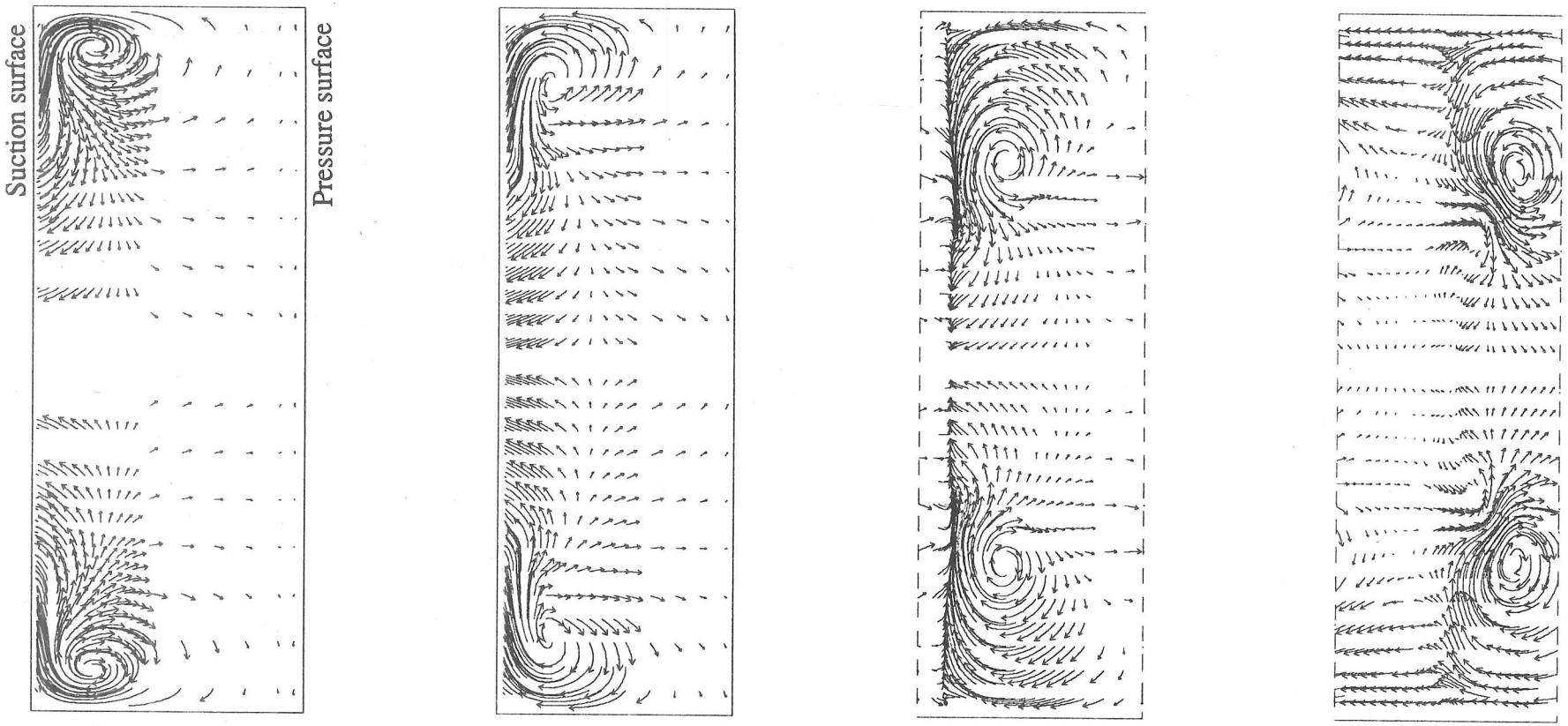

Fig.3.2b Set 1 secondary velocity vectors

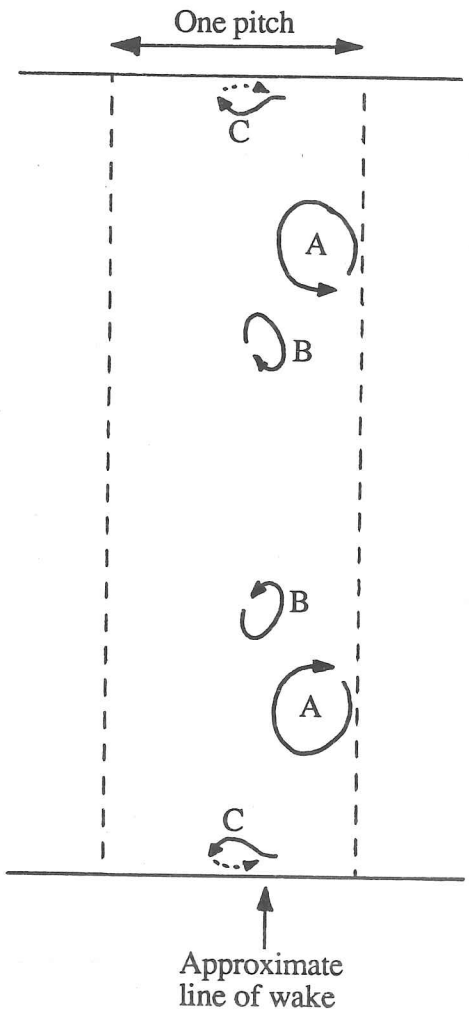

A : Distributed secondary vorticity (passage vortex)

B : Trailing filament vorticity

C : Trailing shed vorticity (The corner vortex contains part of this component. The rest appears as skew in the downstream endwall boundary layer.)

Fig.3.3 Classical components of vorticity seen in secondary velocity vectors downstream of set 1 (x/C_x=1.23, fig.3.2b)

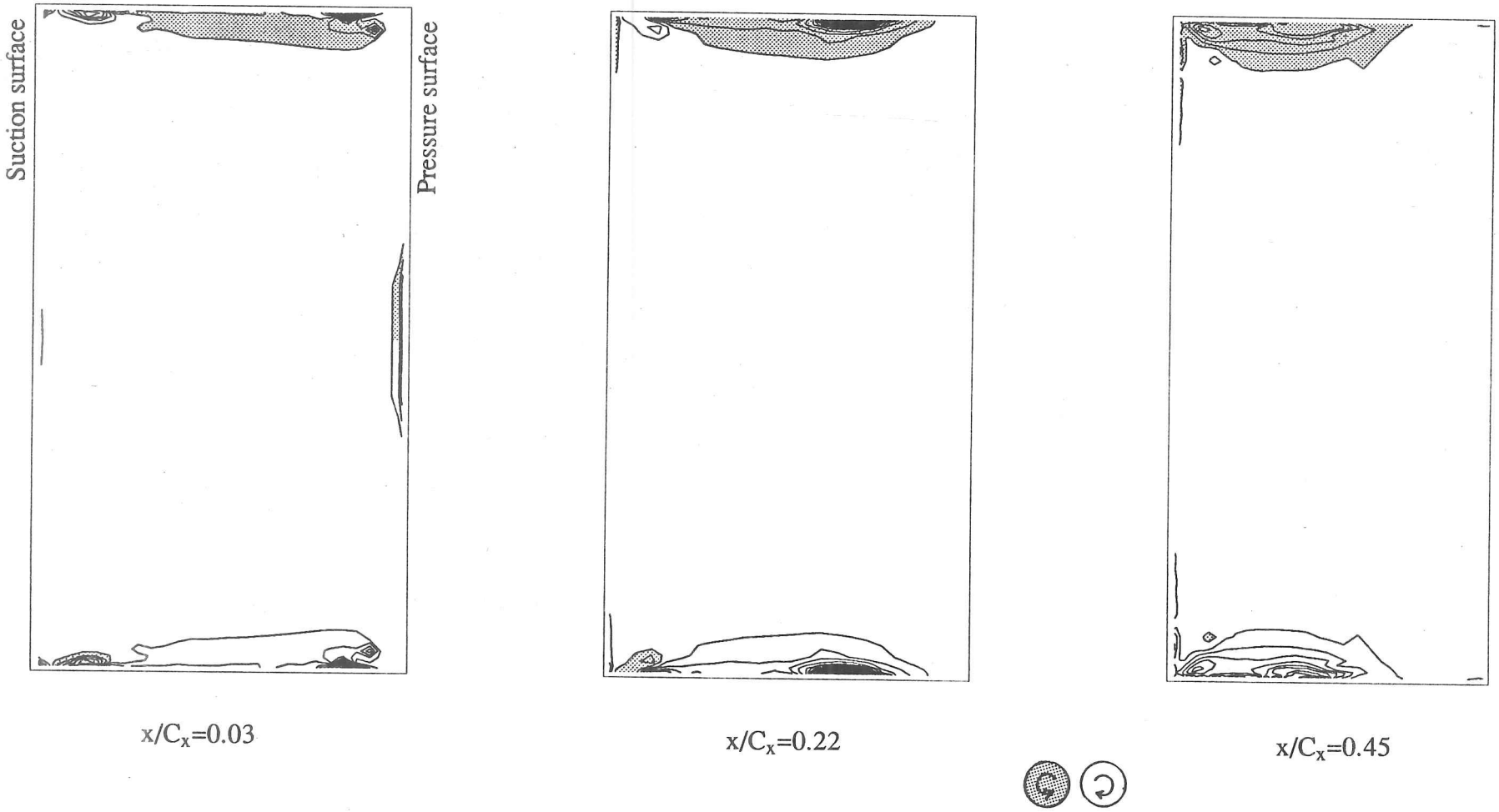

Fig.3.4a Set 1 streamwise vorticity

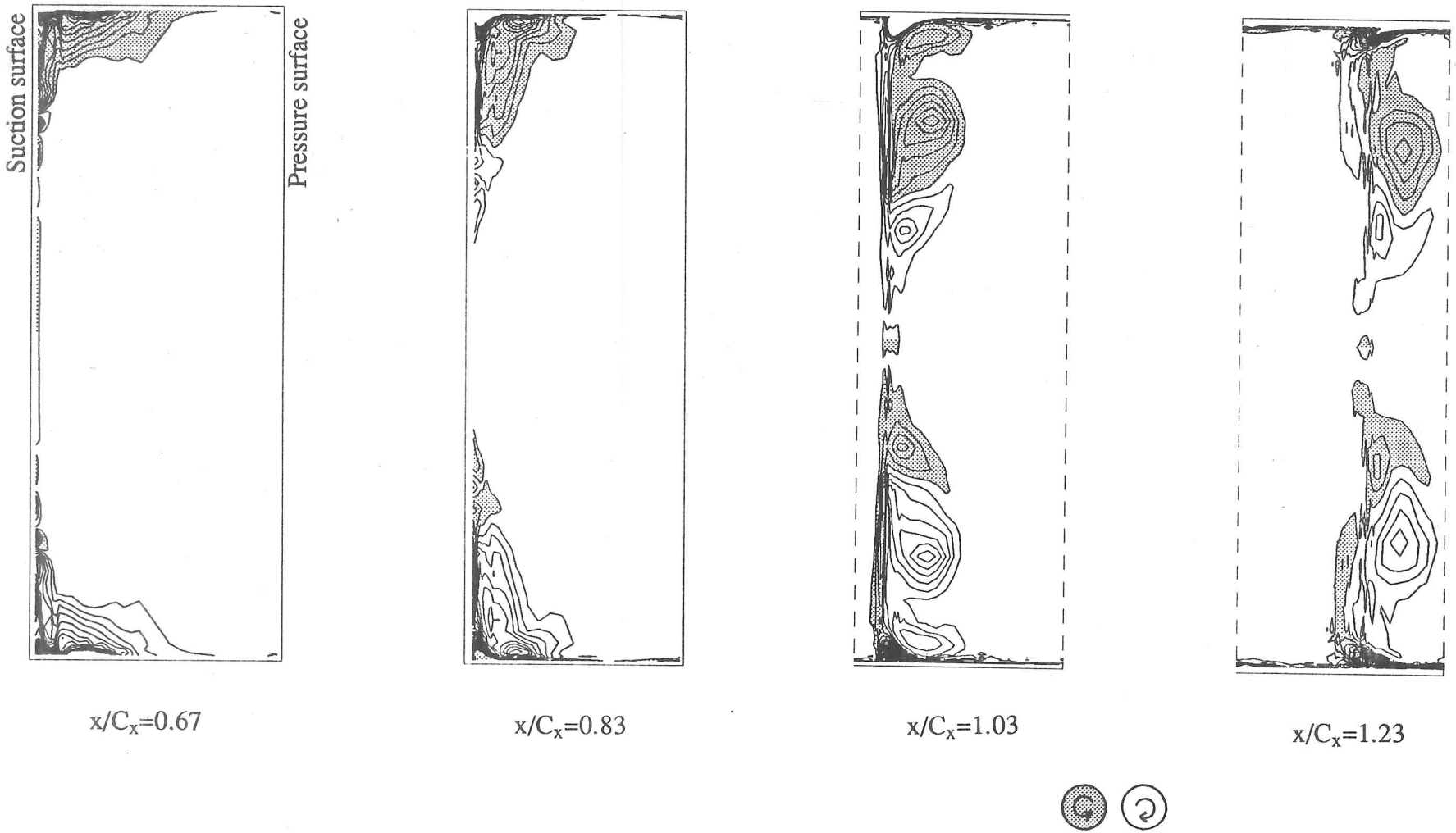

Fig.3.4b Set 1 streamwise vorticity

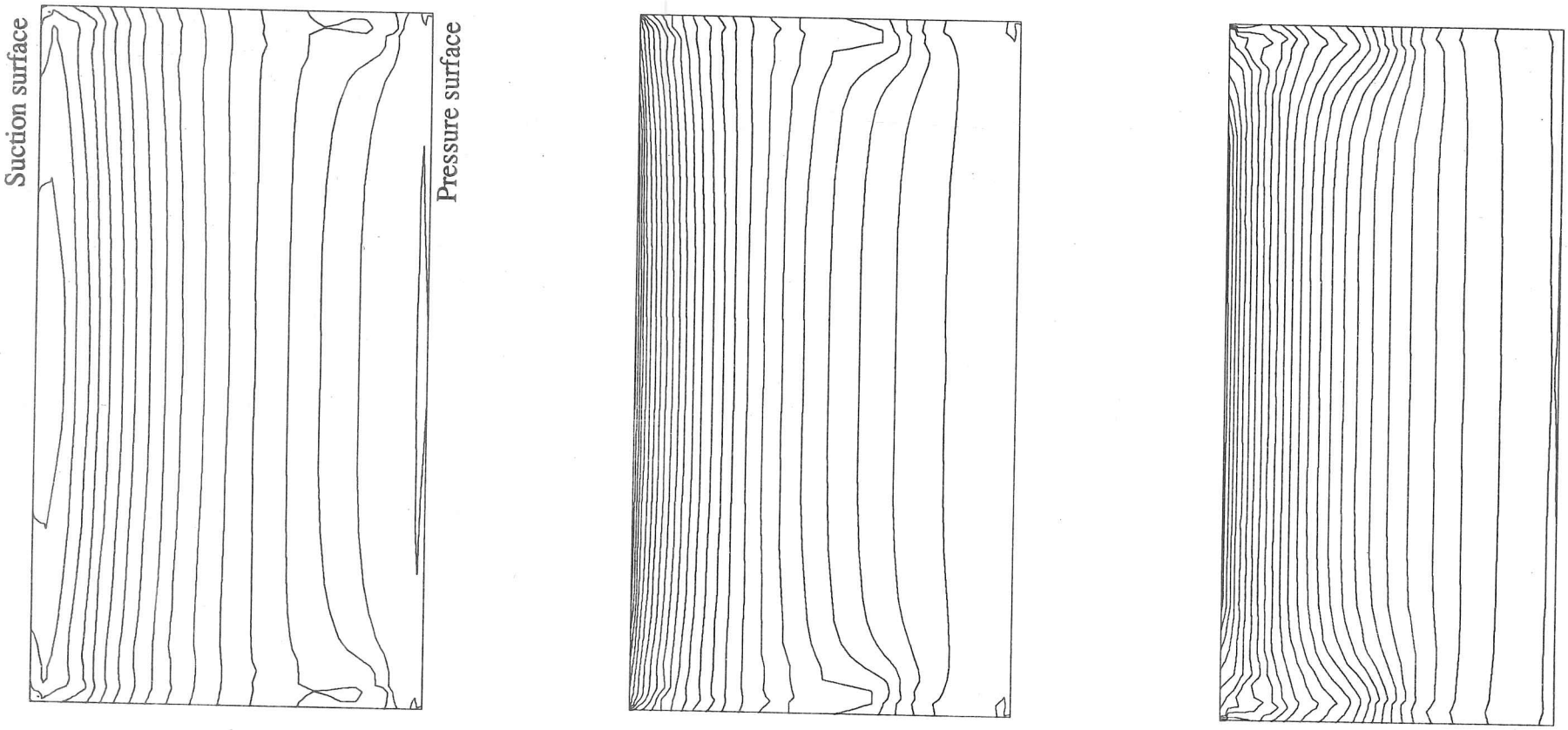

Contour interval $0.05(p_{01}-p_2)$

Fig.3.5a Set 1 static pressure

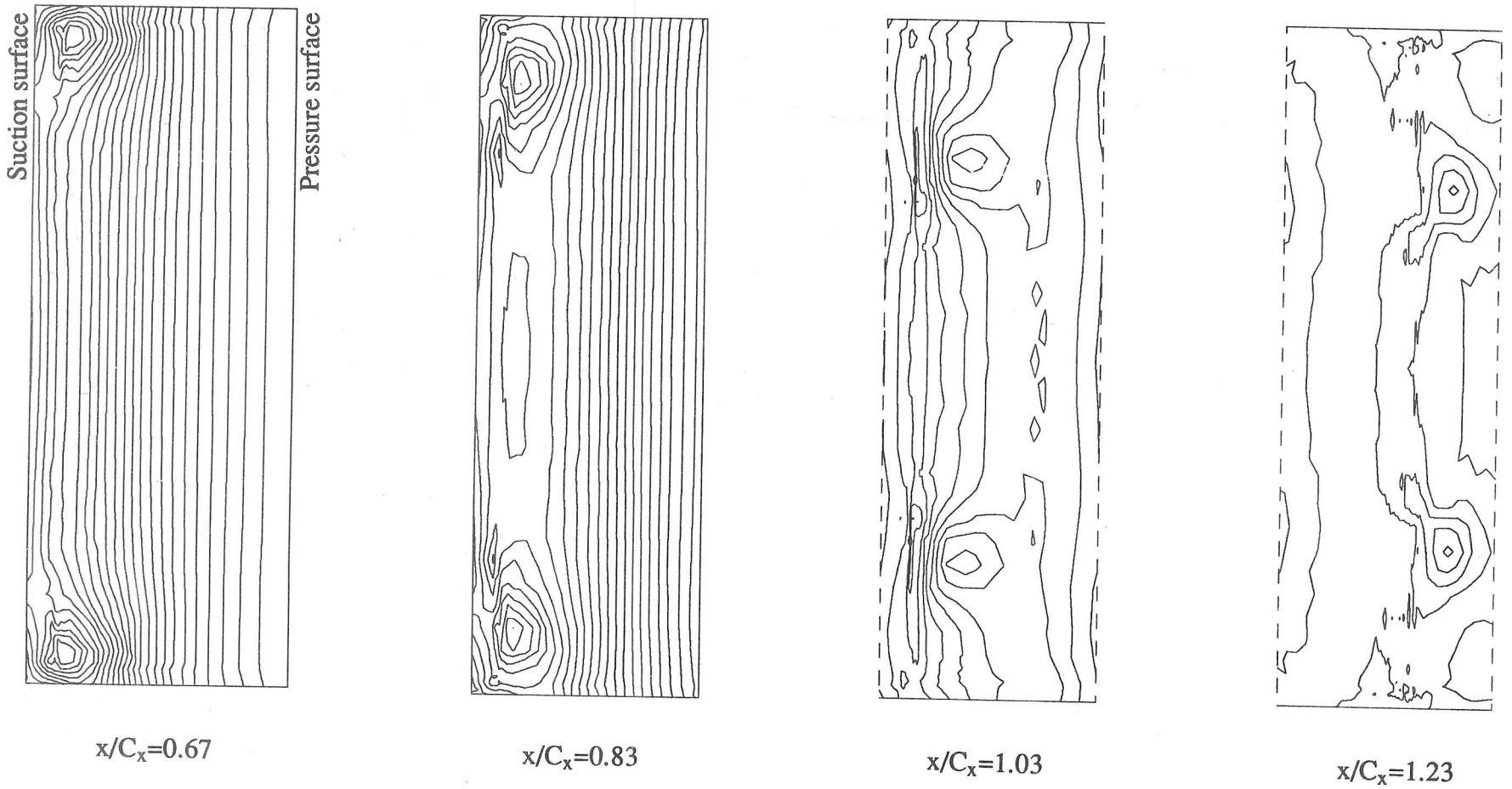

Contour interval $0.05(p_{01}-p_2)$

Fig.3.5b Set 1 static pressure

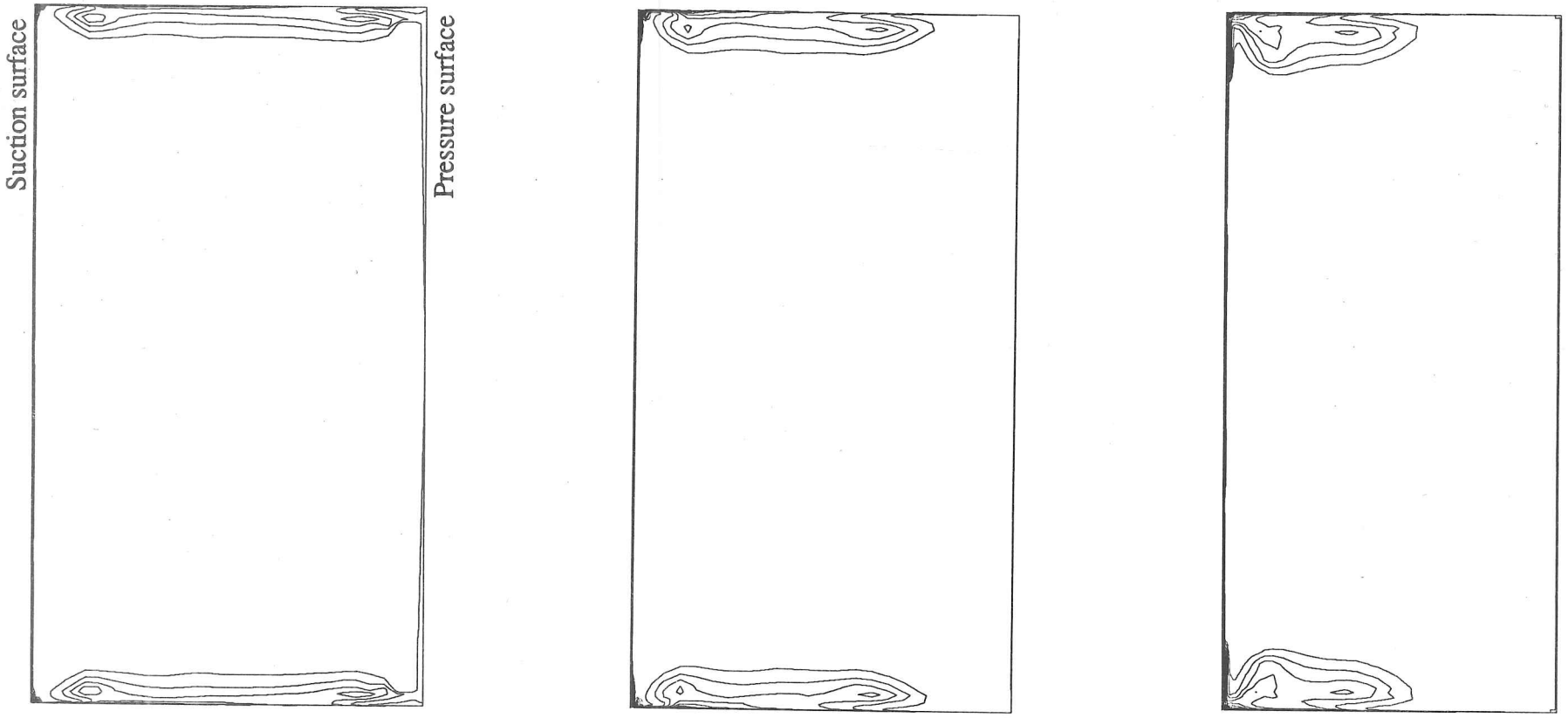

Contour interval $0.05(p_{01}-p_2)$ Zero contour not drawn

Fig.3.6a Set 1 stagnation pressure loss

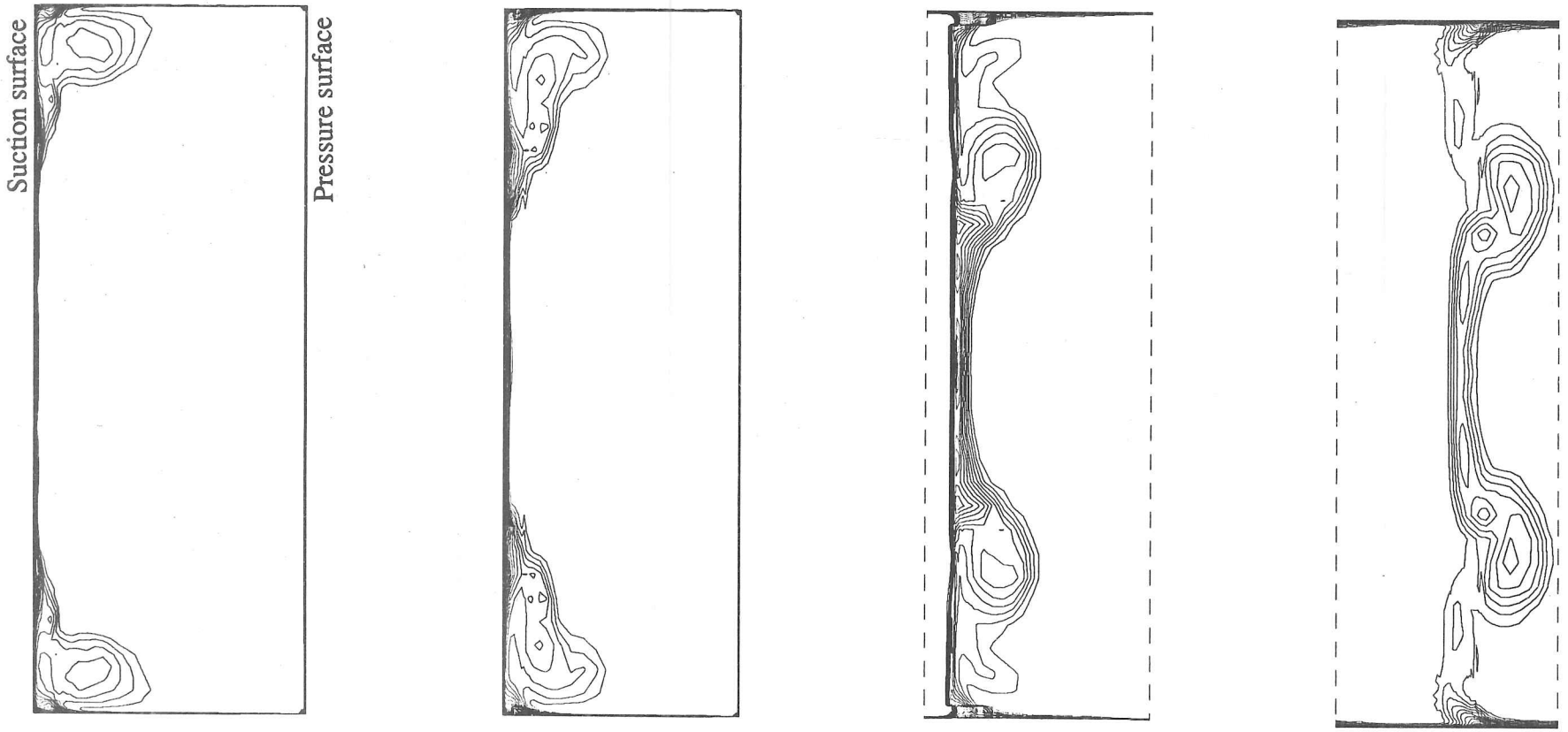

Contour interval $0.05(p_{01}-p_2)$ Zero contour not drawn

Fig.3.6b Set 1 stagnation pressure loss

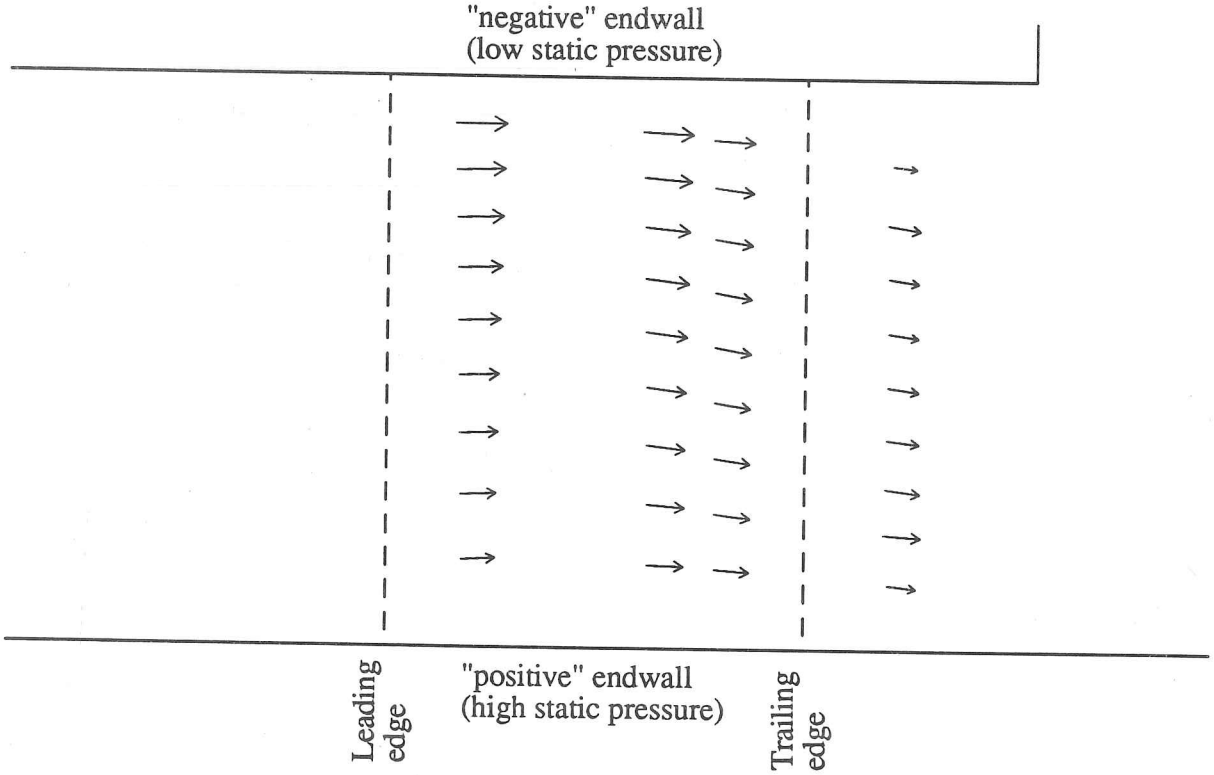

Vectors represent the magnitude and direction of the pitchwise mass average velocity. 10% of the overall mass flow passes between each pair of vectors.

Fig.3.7 **Set 2 mean streamlines**

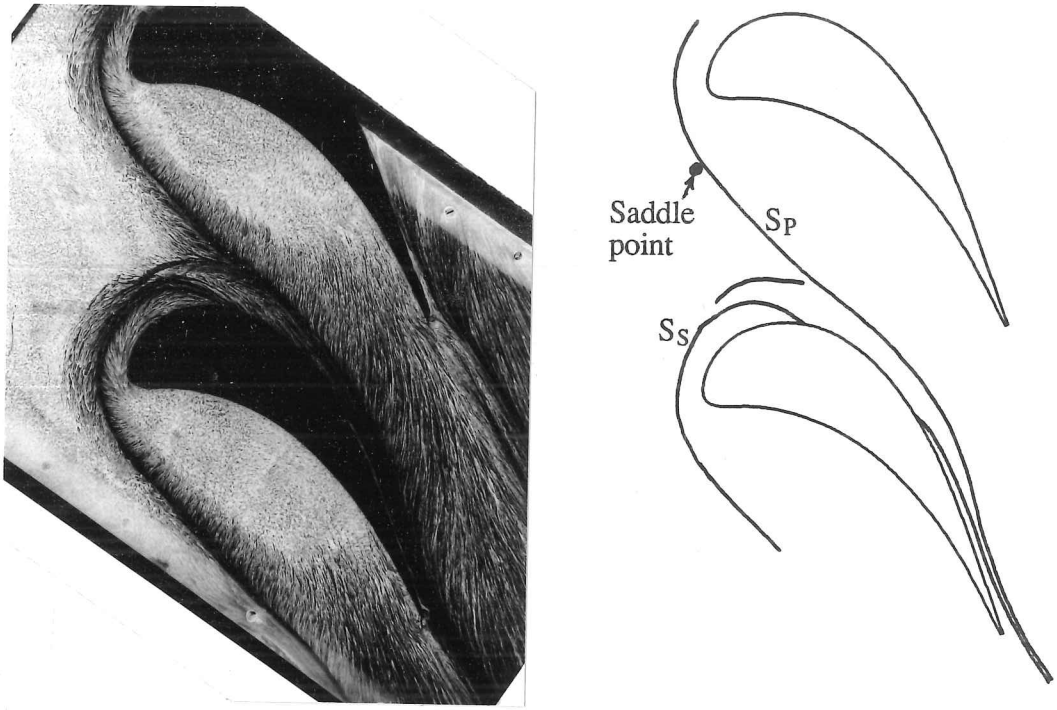

Fig.3.8a **Set 2 oil flow visualization (positive wall)**

Fig.3.8b **Set 2 oil flow visualization (negative wall)**
(also showing blades in position)

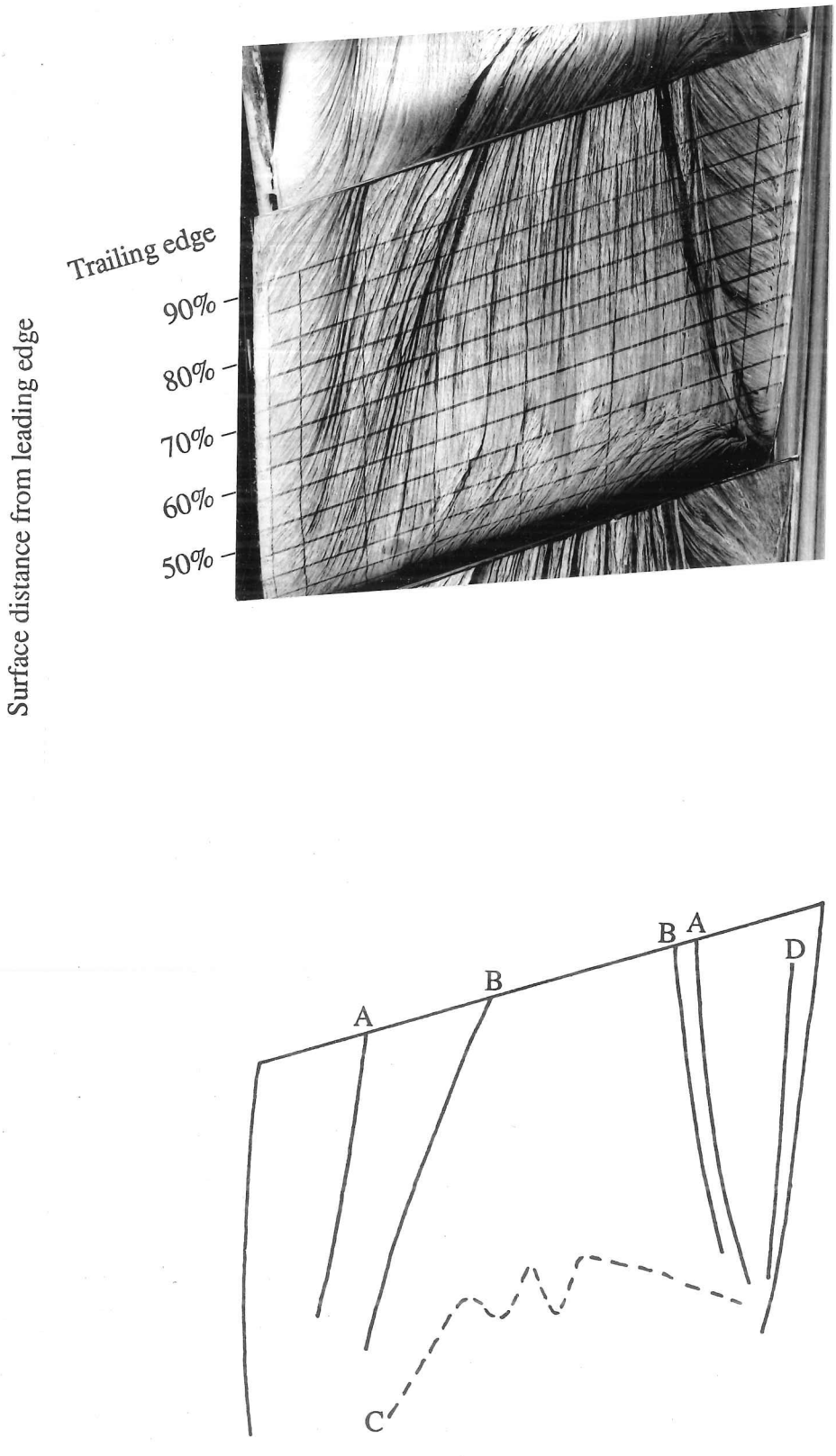

Fig.3.8c Set 2 oil flow visualization (suction surface)

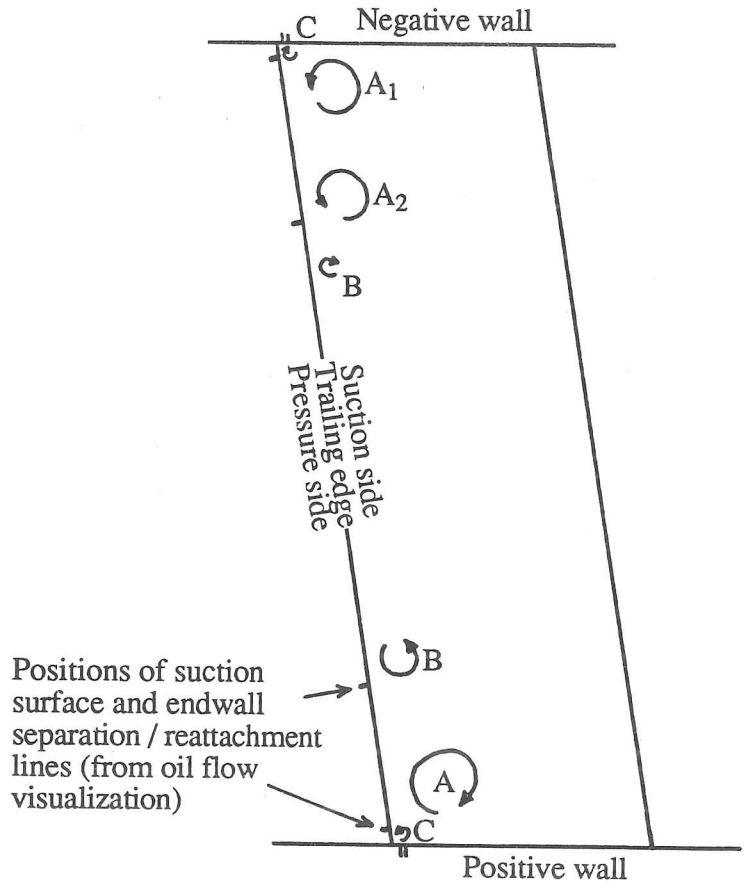

A : Passage or horseshoe vortex

B : Trailing filament vortex

C : Corner vortex

Fig.3.9 **Schematic showing vortices revealed by wool tuft just downstream of set 2 trailing edge**

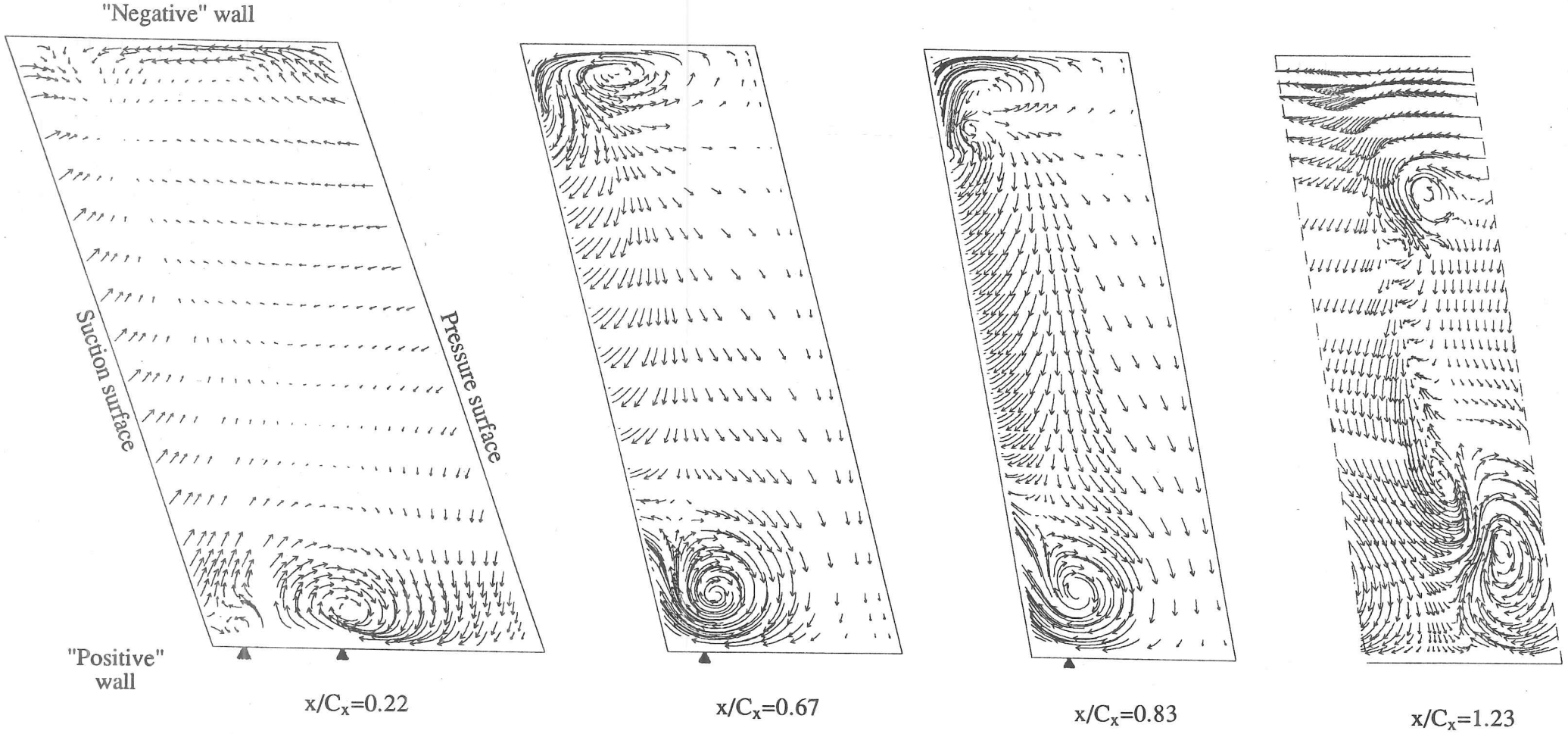

Fig.3.10 Set 2 secondary velocity vectors

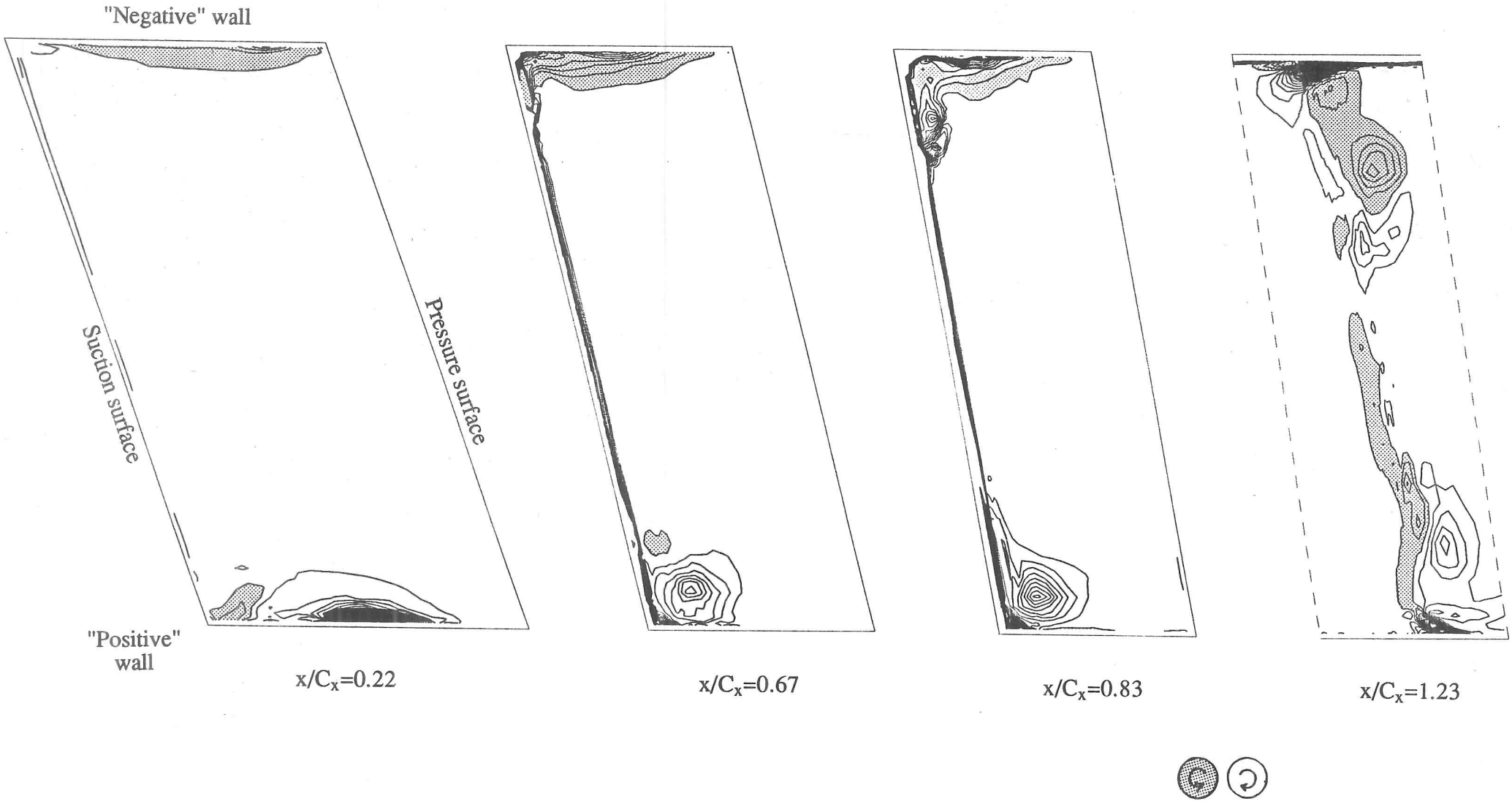

Fig.3.11 Set 2 streamwise vorticity

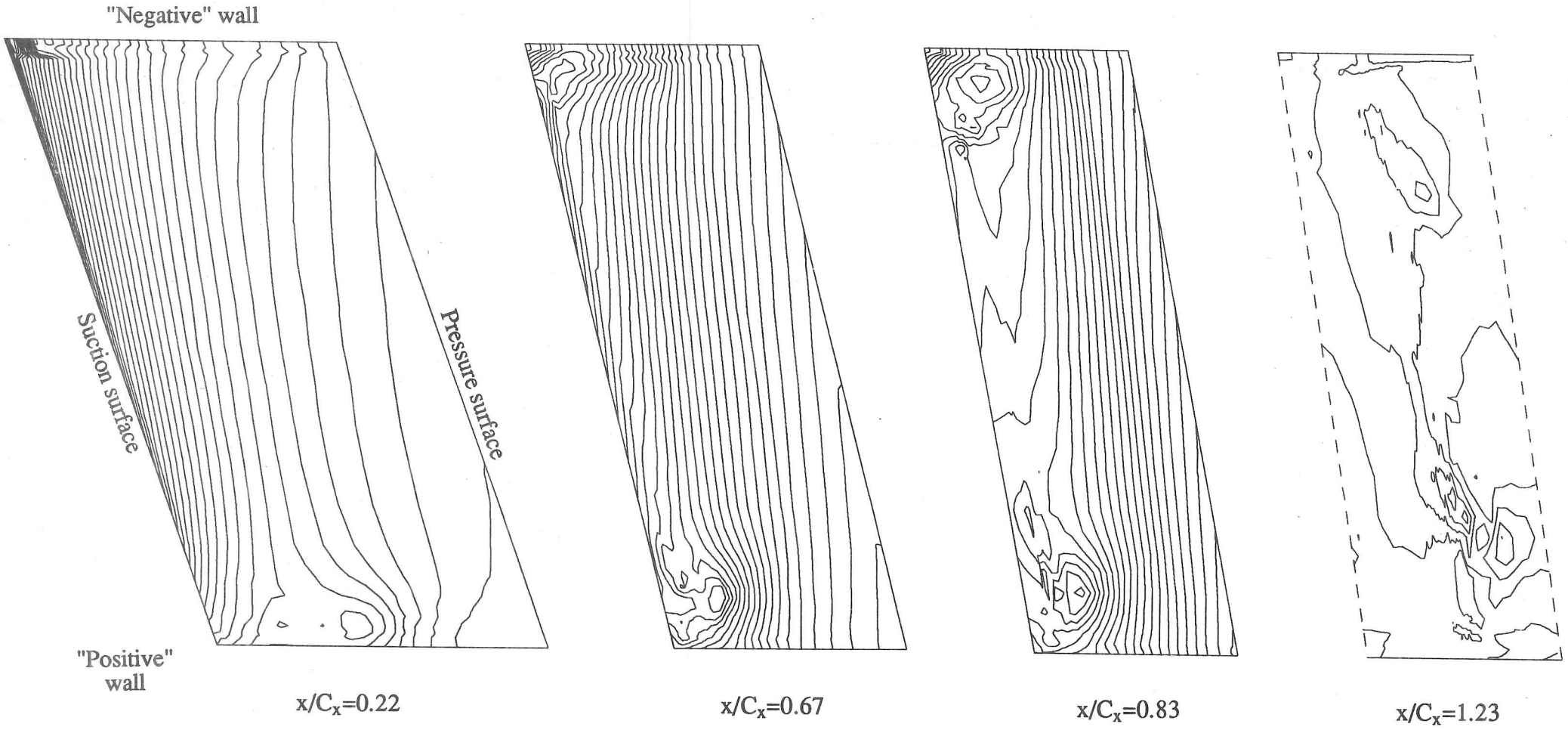

Contour interval $0.05(p_{01}-p_2)$

Fig.3.12 Set 2 static pressure

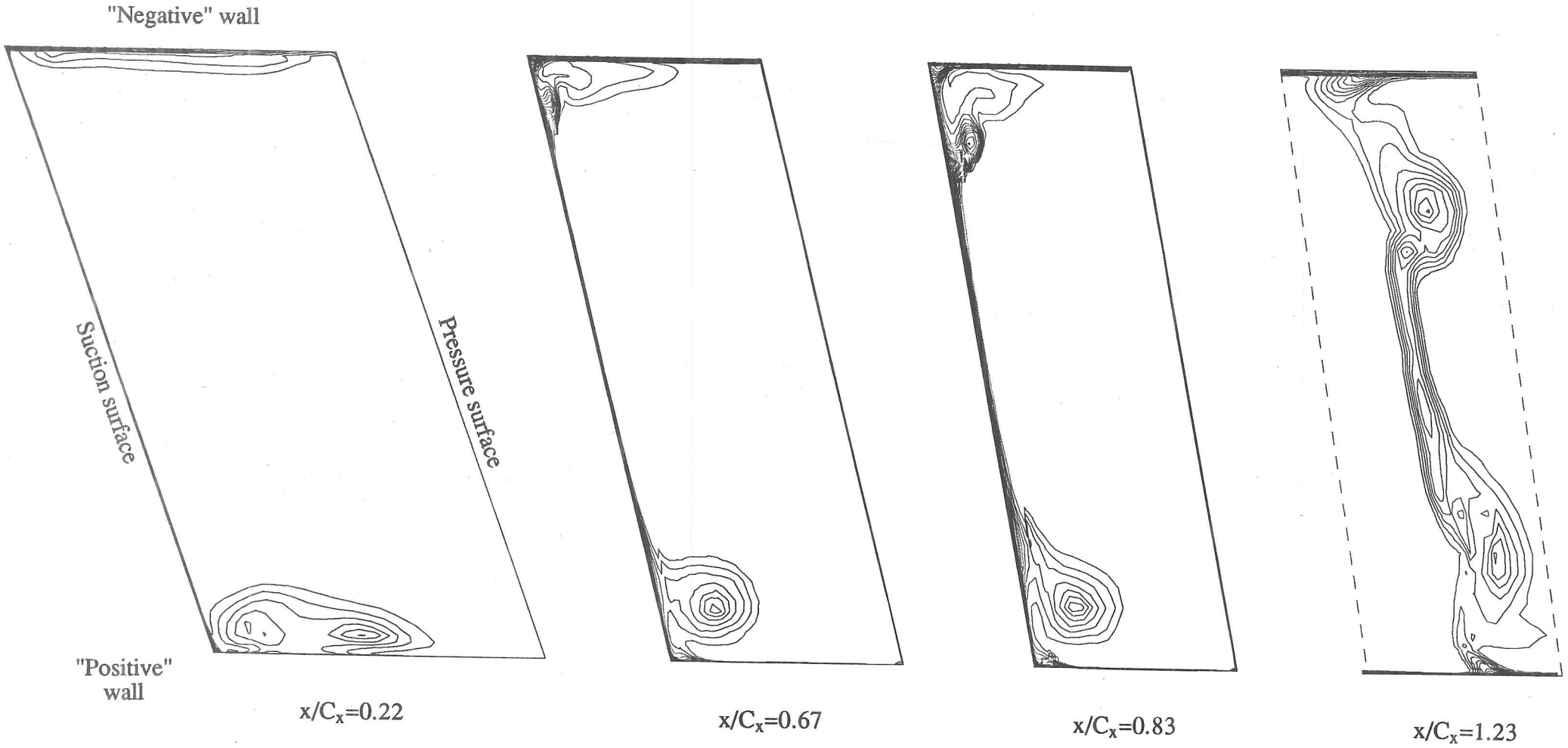

Contour interval $0.05(p_{01}-p_2)$ Zero contour not drawn

Fig.3.13 Set 2 stagnation pressure loss

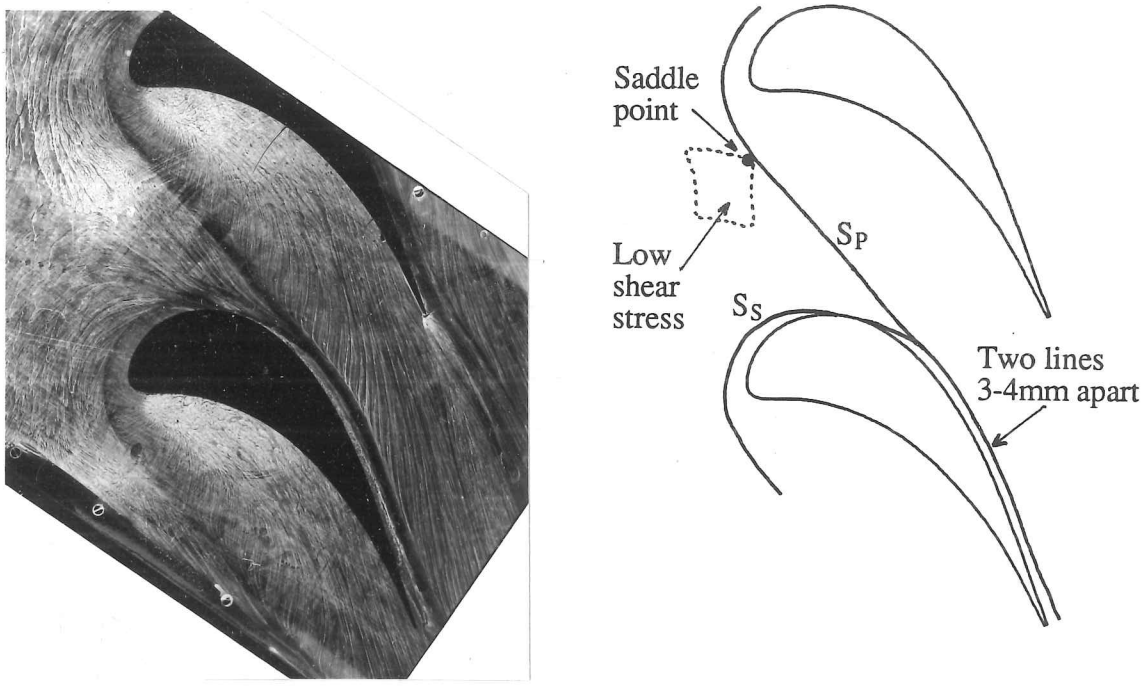

Fig.3.14a Set 3 oil flow visualization (endwall)

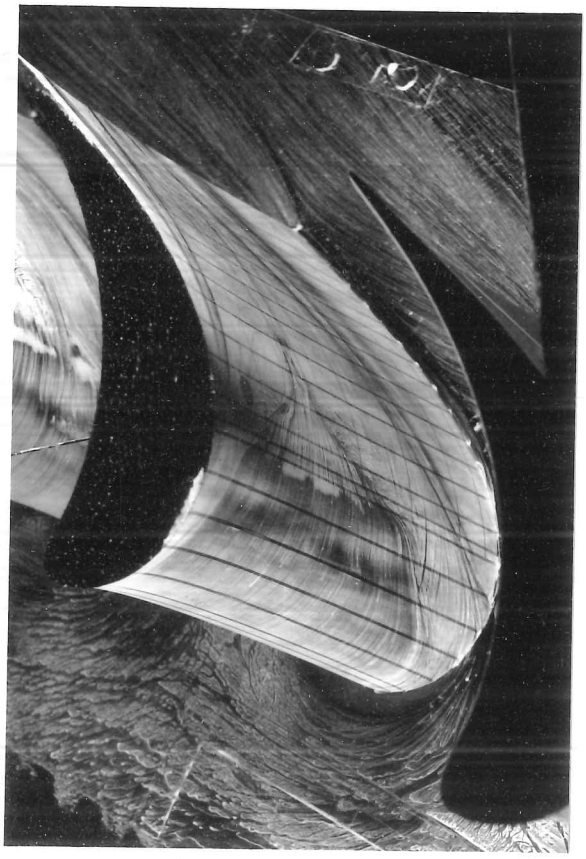

Fig.3.14b Set 3 oil flow visualization (suction surface)

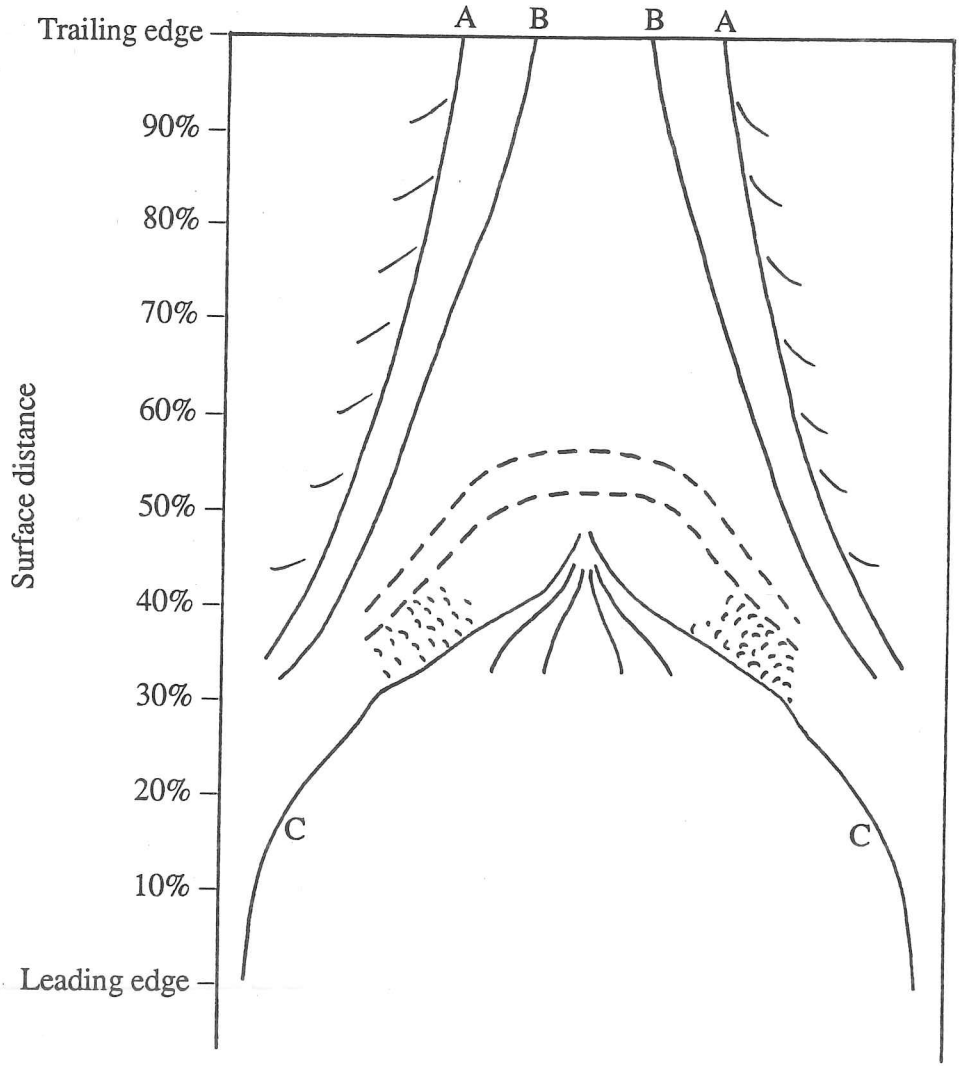

– – – – Start and end of transition, determined using flattened
– – – – probe and stethoscope. No corresponding line in oil.

A, B, C See text.

Fig.3.14c Schematic of set 3 oil flow visualization (suction surface)

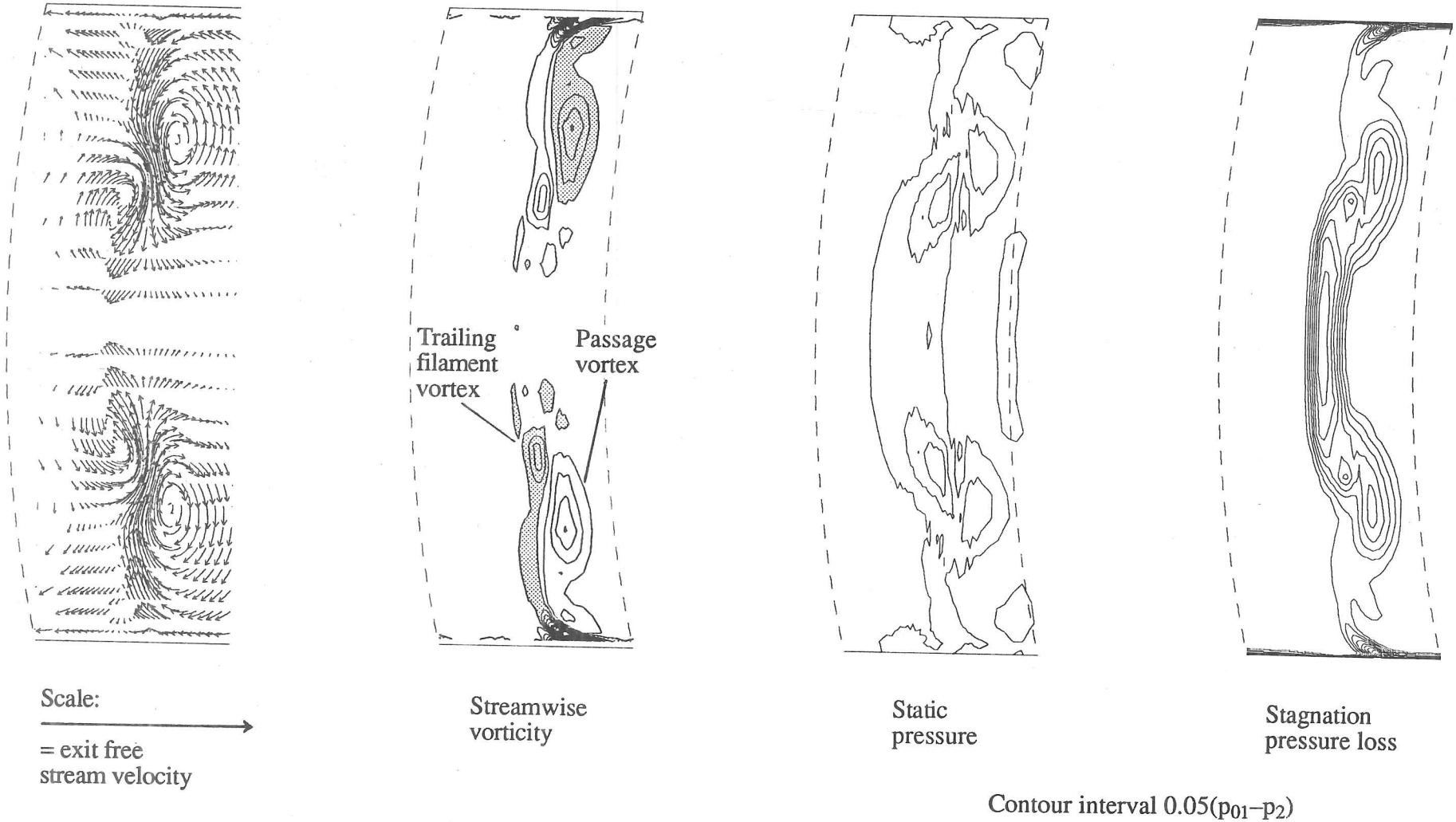

Fig.3.15 Set 3 pressure probe traverse results at $x/C_x=1.23$

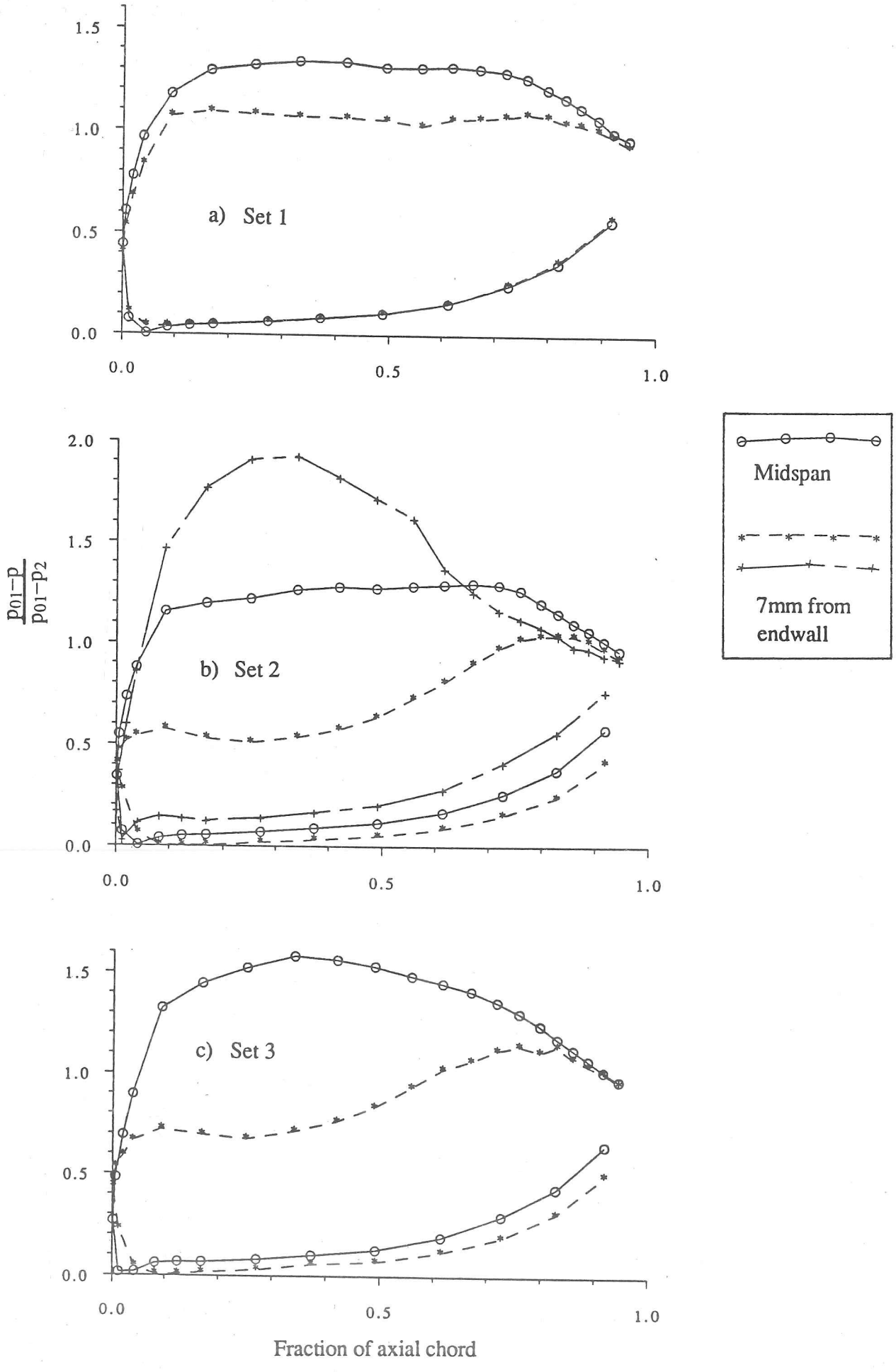

Fig.3.16 Measured blade surface static pressures

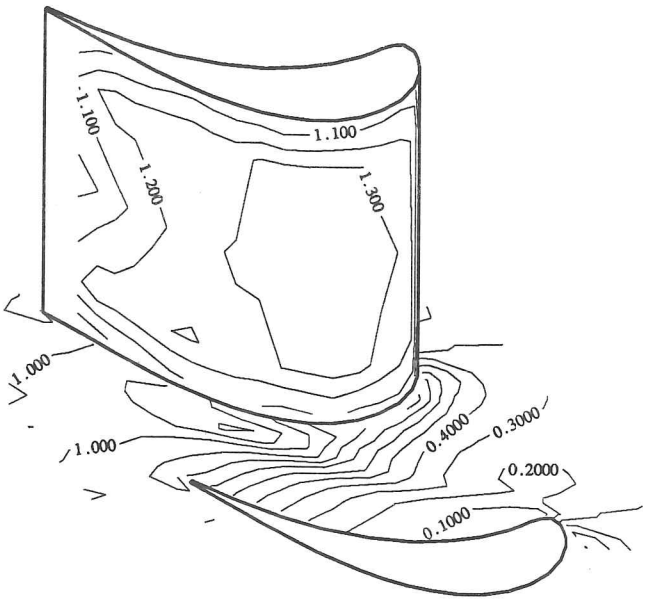

a) Set 1

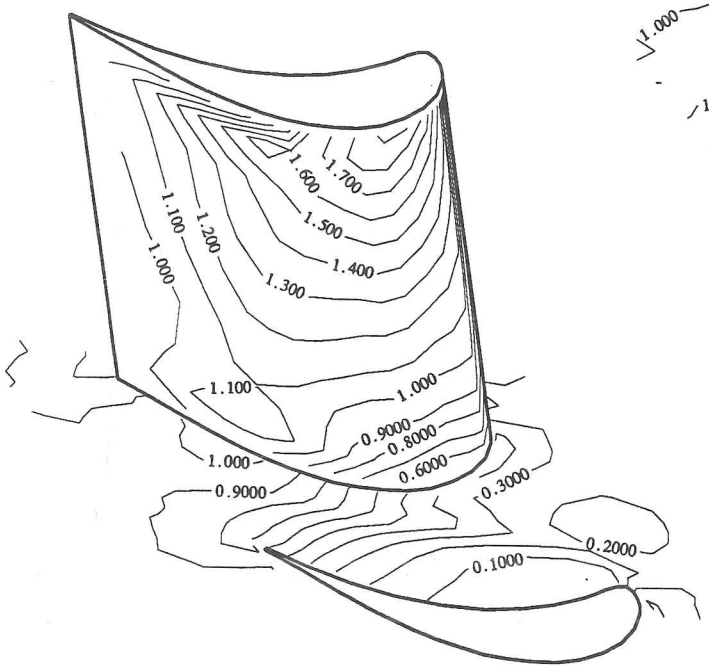

b) Set 2

c) Set 3

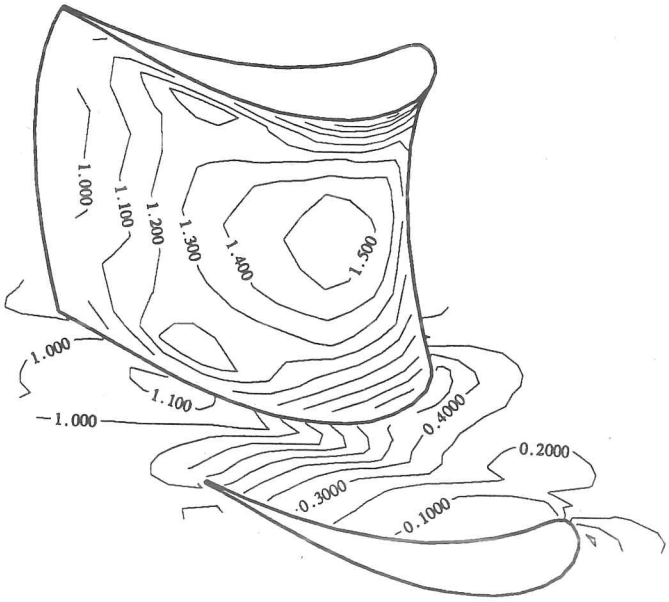

Notes:

Pressures are expressed as $\left(\frac{p_{01}-p}{p_{01}-p_2}\right)$

Full span measurements are presented,
i.e. data have not been reflected about midspan.

Lack of detail on set 1 is a result of the sparse arrangement of pressure tappings (see §2.3.1)

Fig.3.17 Measured surface static pressures

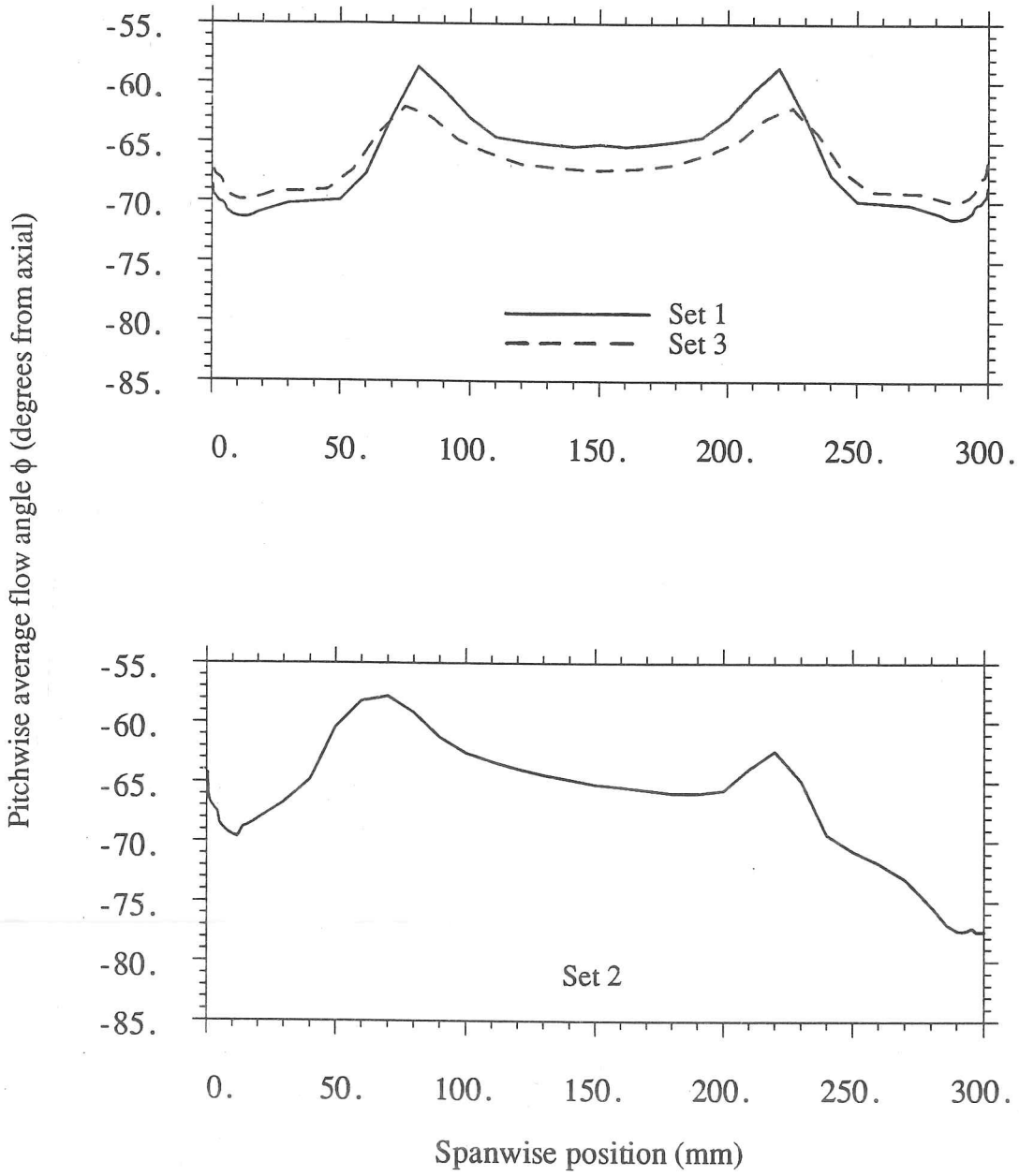

Fig.3.18 Spanwise variation of exit flow direction

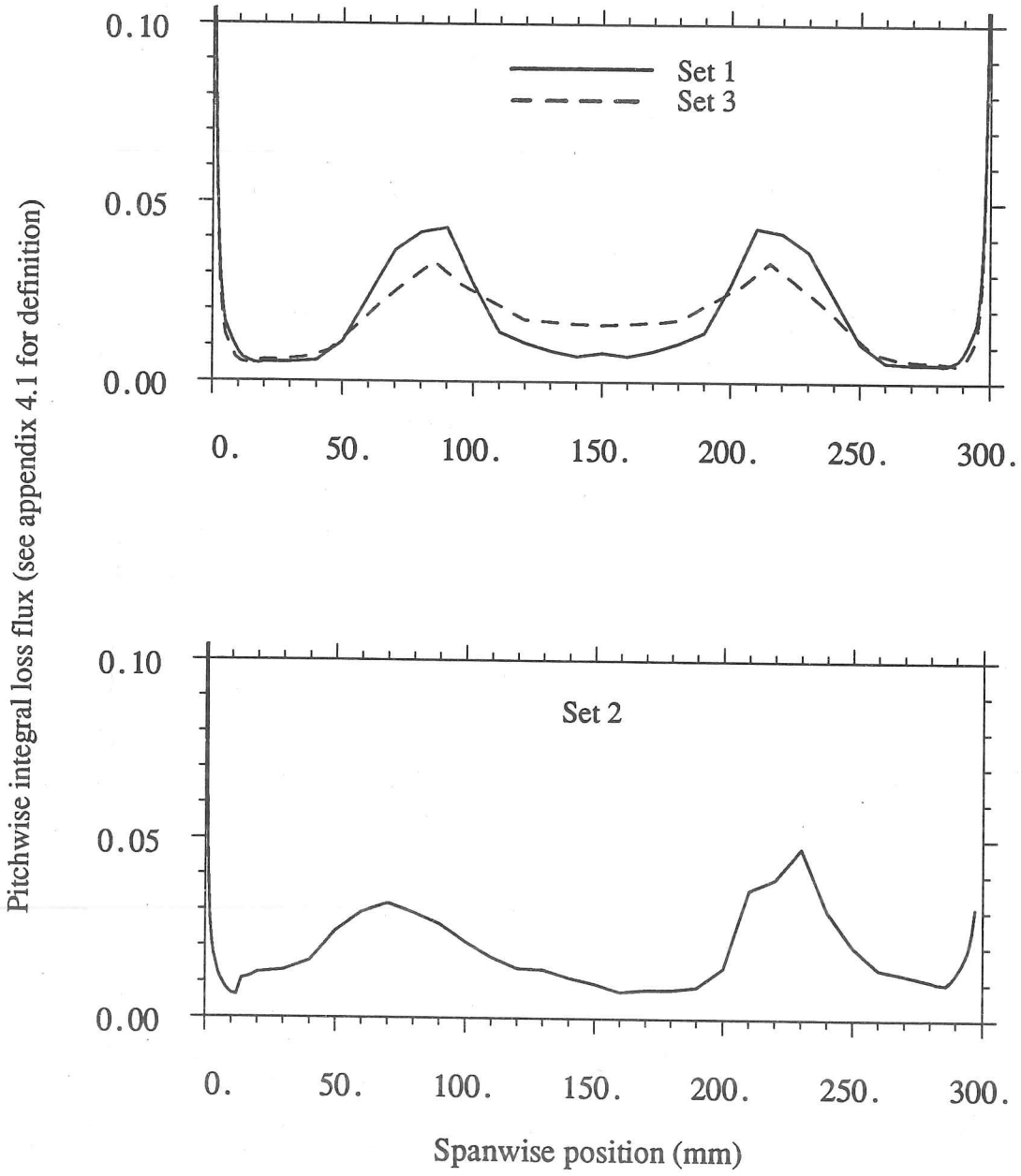

Fig.3.19 Spanwise variation of stagnation pressure loss flux

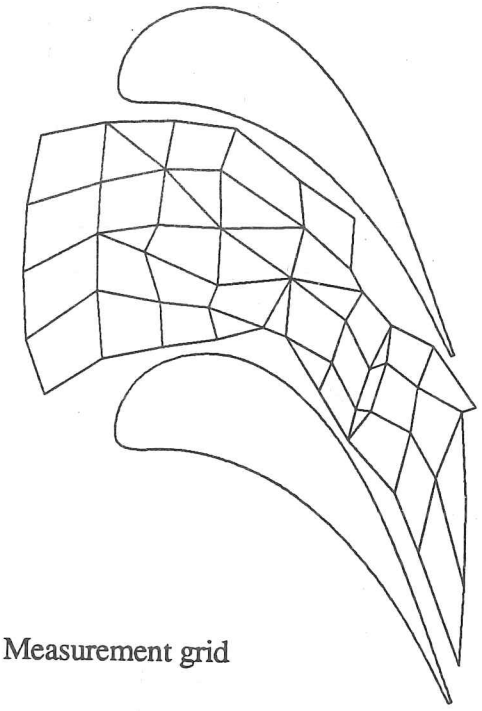

a) Measurement grid

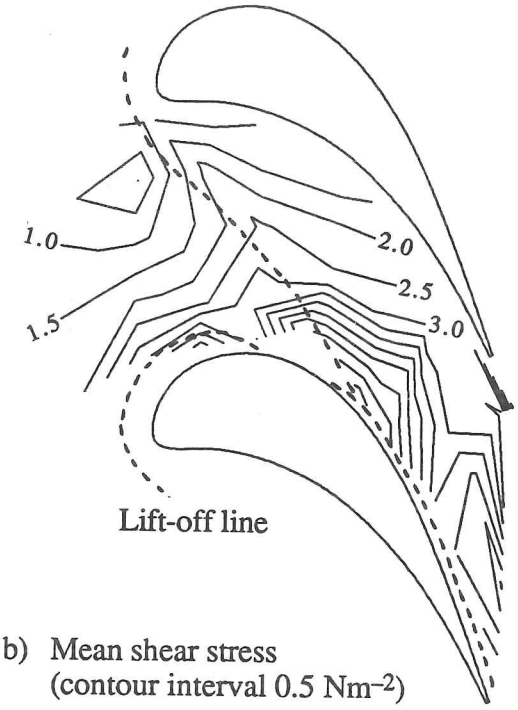

b) Mean shear stress
(contour interval 0.5 Nm^{-2})

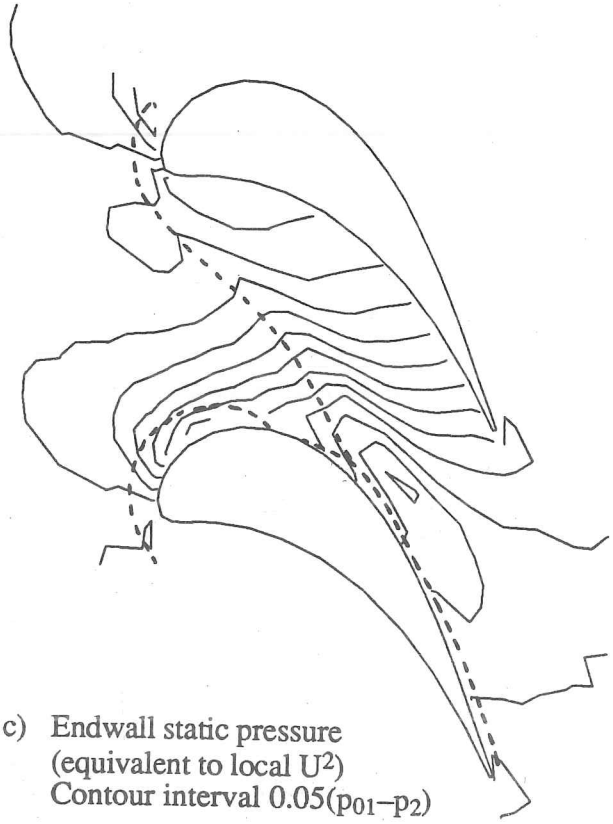

c) Endwall static pressure
(equivalent to local U^2)
Contour interval $0.05(p_{01}-p_2)$

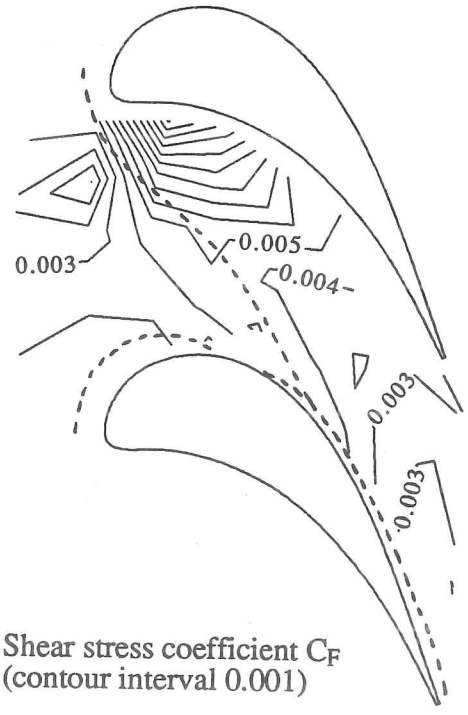

d) Shear stress coefficient C_F
(contour interval 0.001)

Fig.3.20 Set 1 endwall shear stress measurements by the oil dot technique

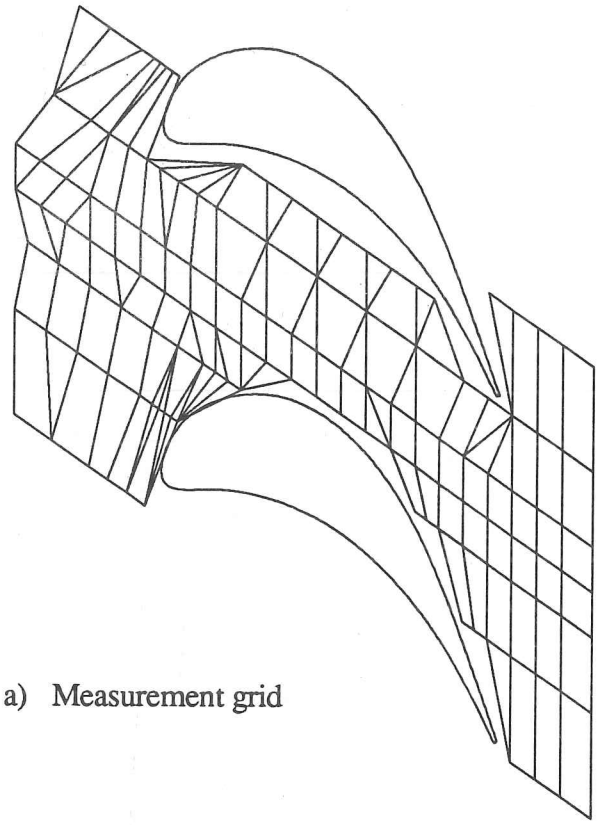

a) Measurement grid

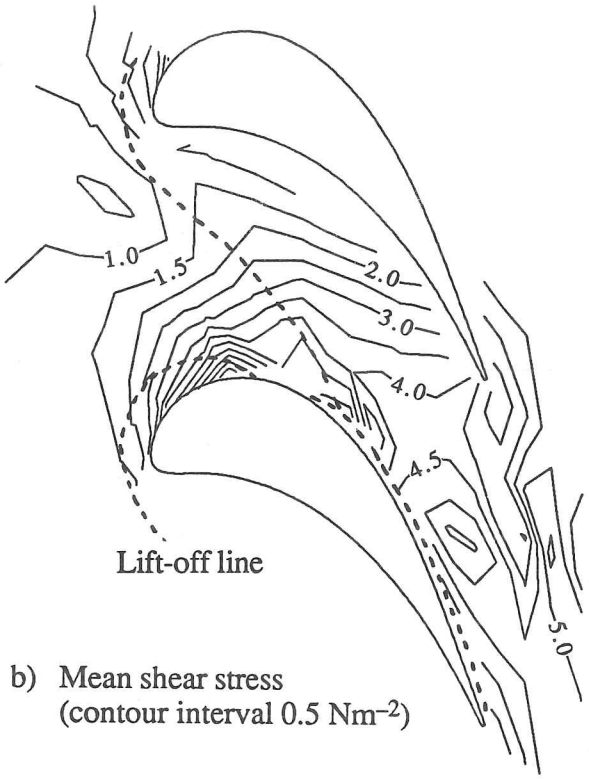

b) Mean shear stress
(contour interval 0.5 Nm^{-2})

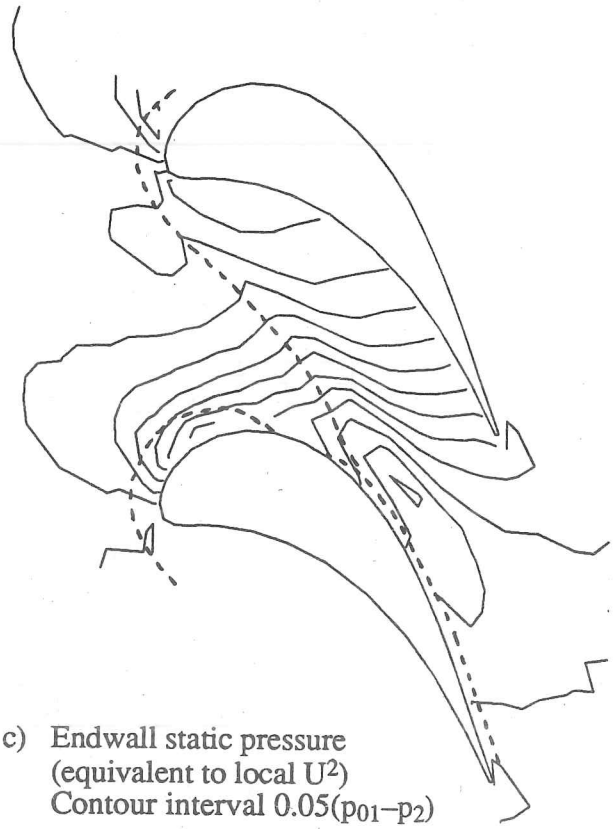

c) Endwall static pressure
(equivalent to local U^2)
Contour interval $0.05(p_{01}-p_2)$

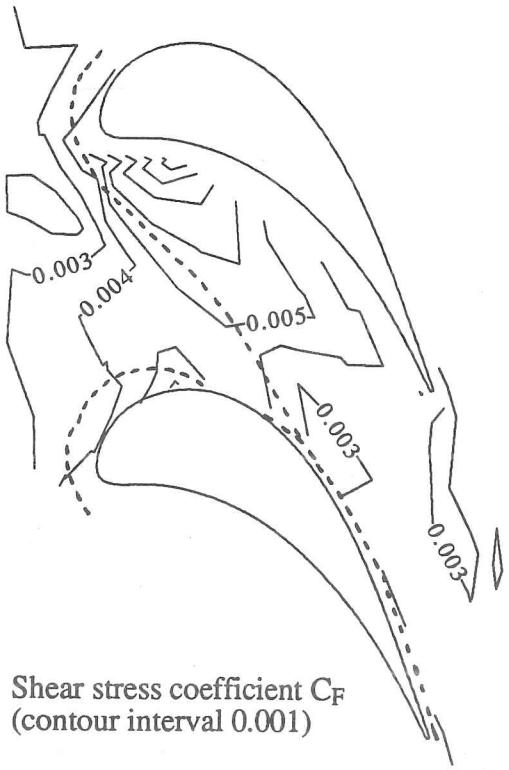

d) Shear stress coefficient C_F
(contour interval 0.001)

Fig.3.21 Set 1 endwall shear stress measurements by hot film gauge

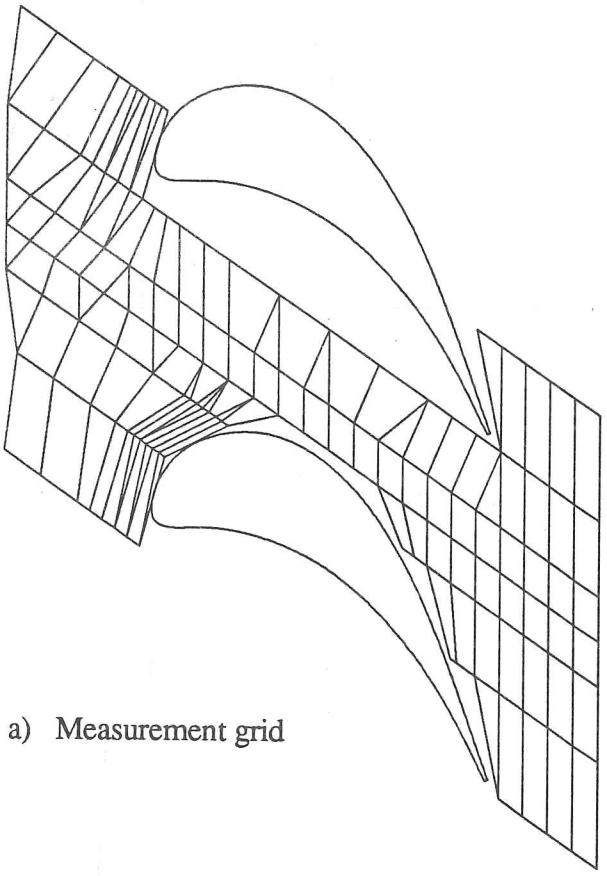

a) Measurement grid

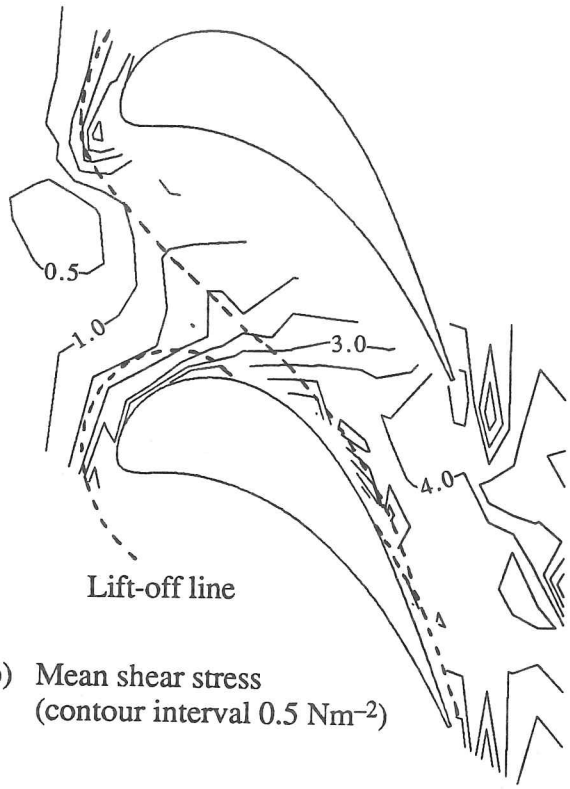

b) Mean shear stress
(contour interval 0.5 Nm^{-2})

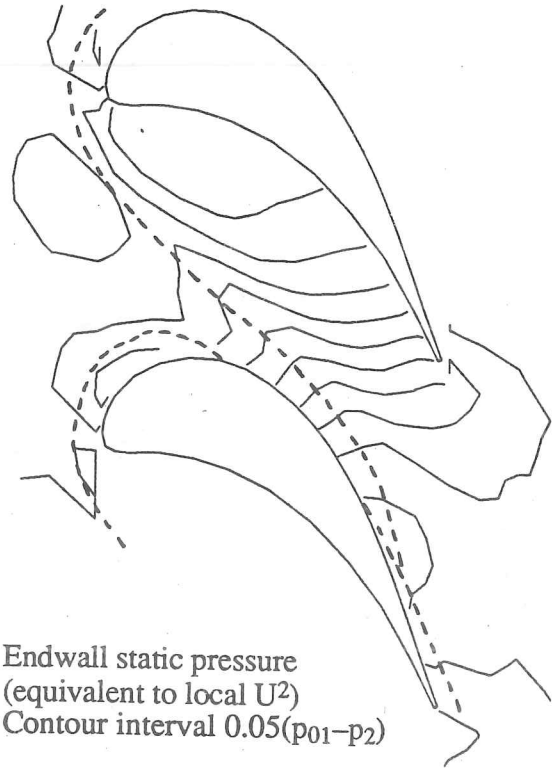

c) Endwall static pressure
(equivalent to local U^2)
Contour interval $0.05(p_{01}-p_2)$

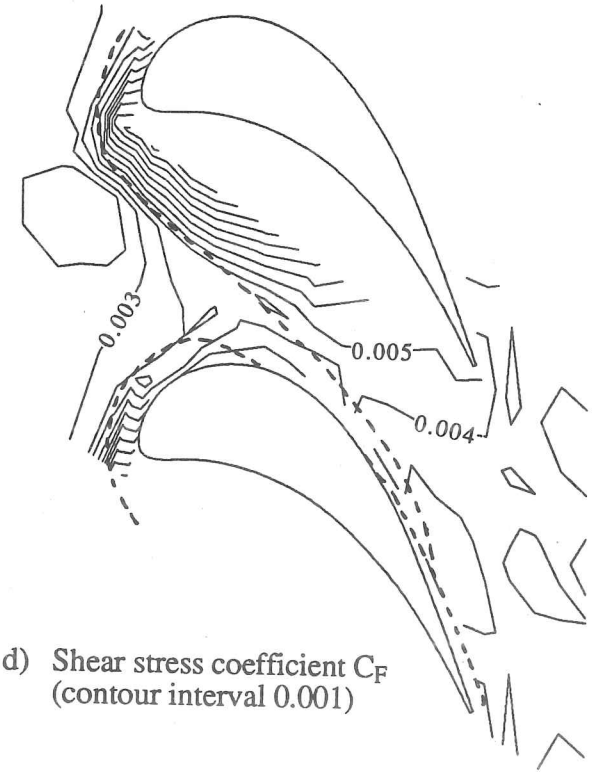

d) Shear stress coefficient C_F
(contour interval 0.001)

Fig.3.22 Set 2 endwall shear stress measurements by hot film gauge (high pressure end)

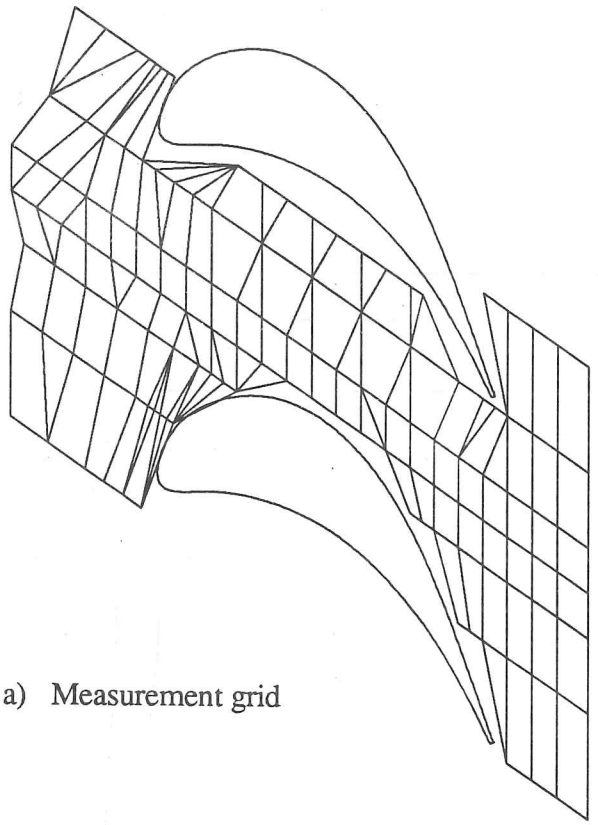

a) Measurement grid

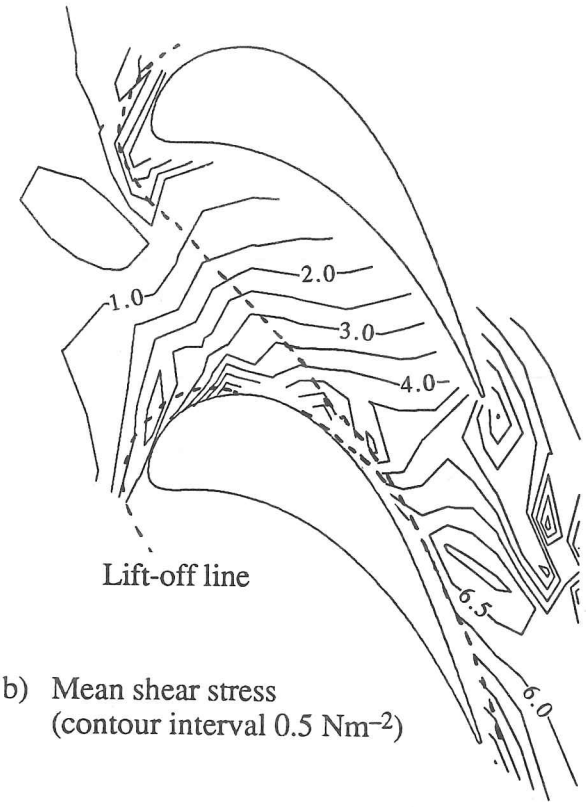

b) Mean shear stress
(contour interval 0.5 Nm^{-2})

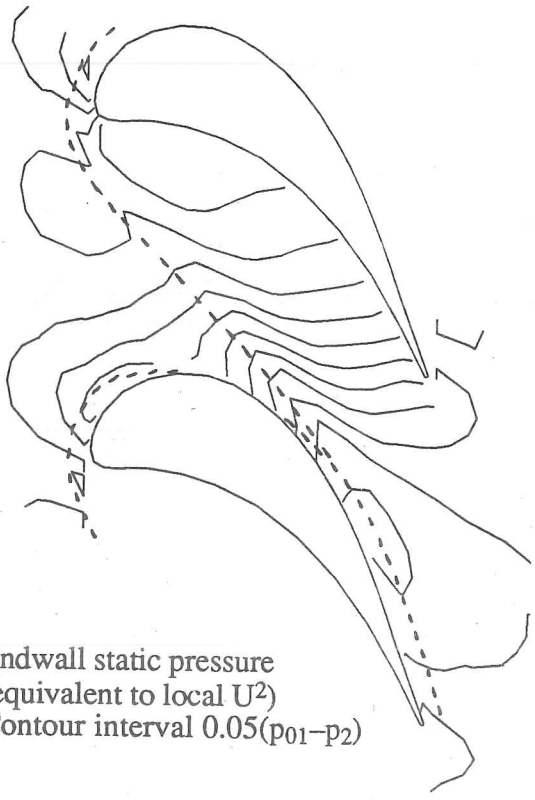

c) Endwall static pressure
(equivalent to local U^2)
Contour interval $0.05(p_{01}-p_2)$

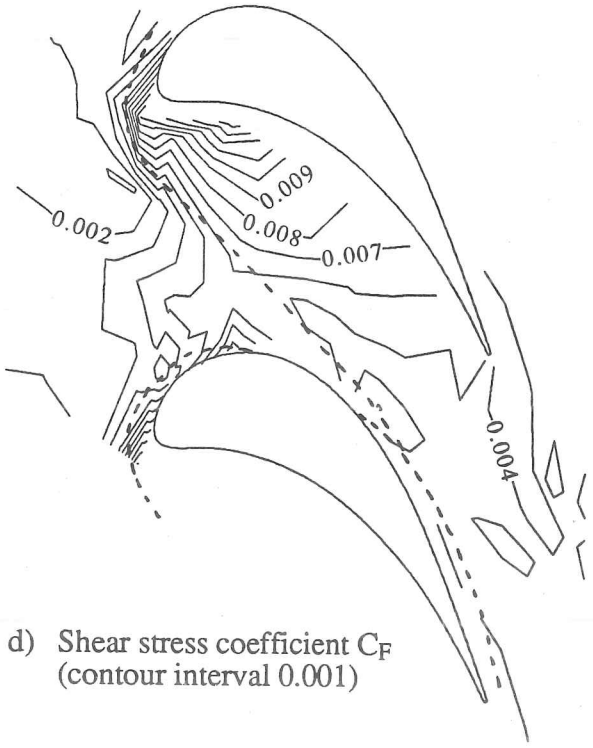

d) Shear stress coefficient C_F
(contour interval 0.001)

Fig.3.23 Set 3 endwall shear stress measurements by hot film gauge

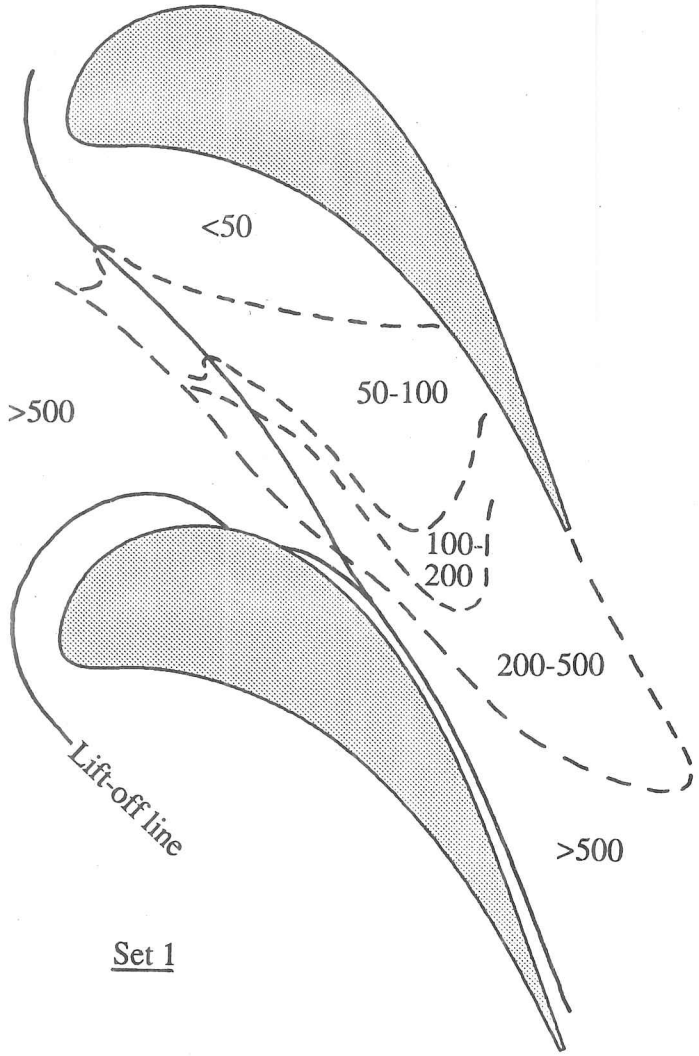

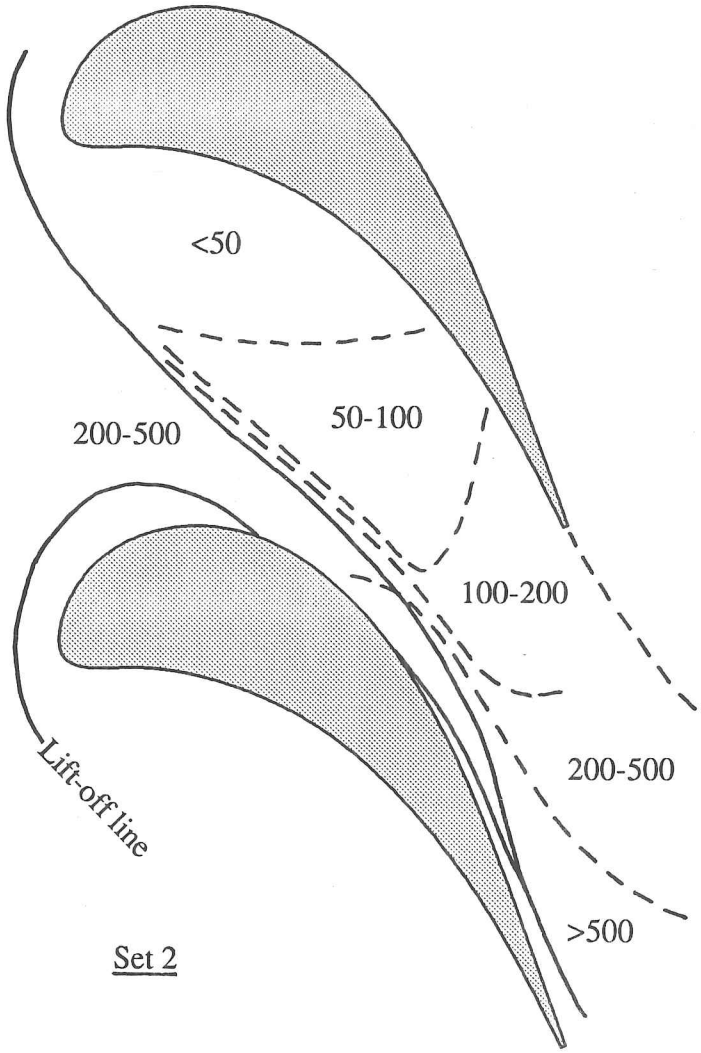

Fig.3.24 **Approximate endwall boundary layer Re_θ** Upstream value 3000

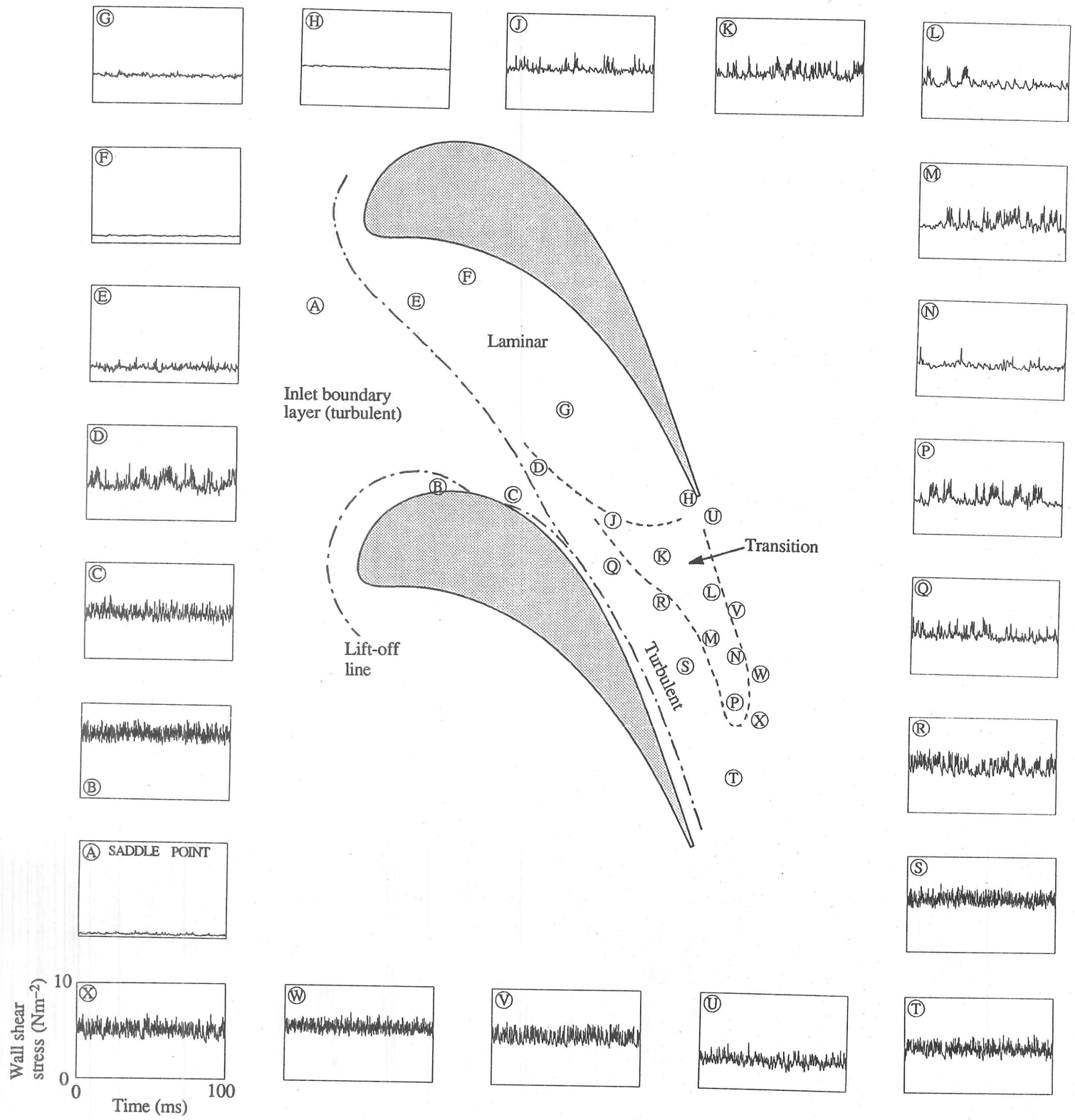

Fig.3.25 Hot film traces on set 1 endwall

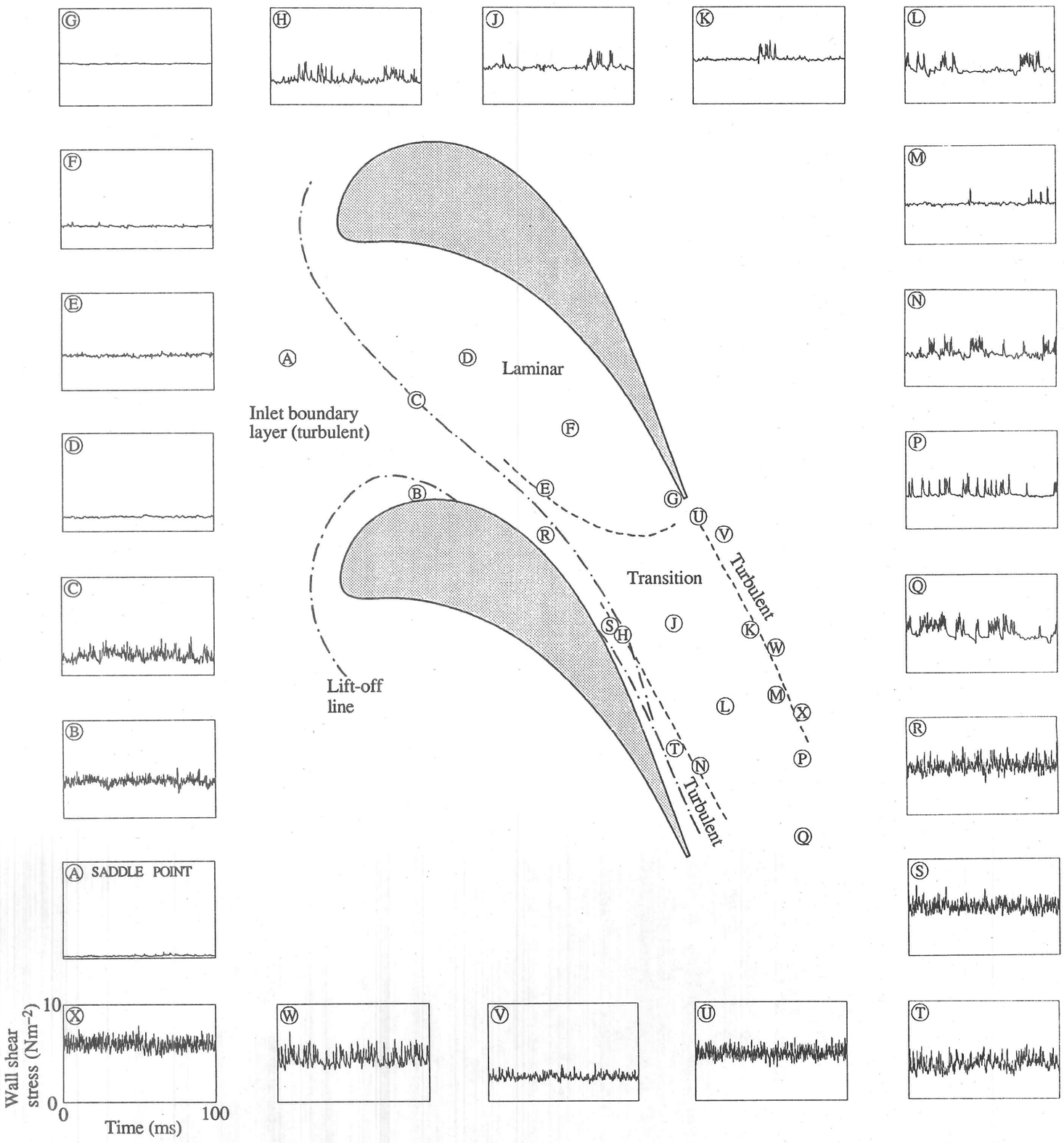

Fig.3.26 Hot film traces on set 2 endwall (high pressure end)

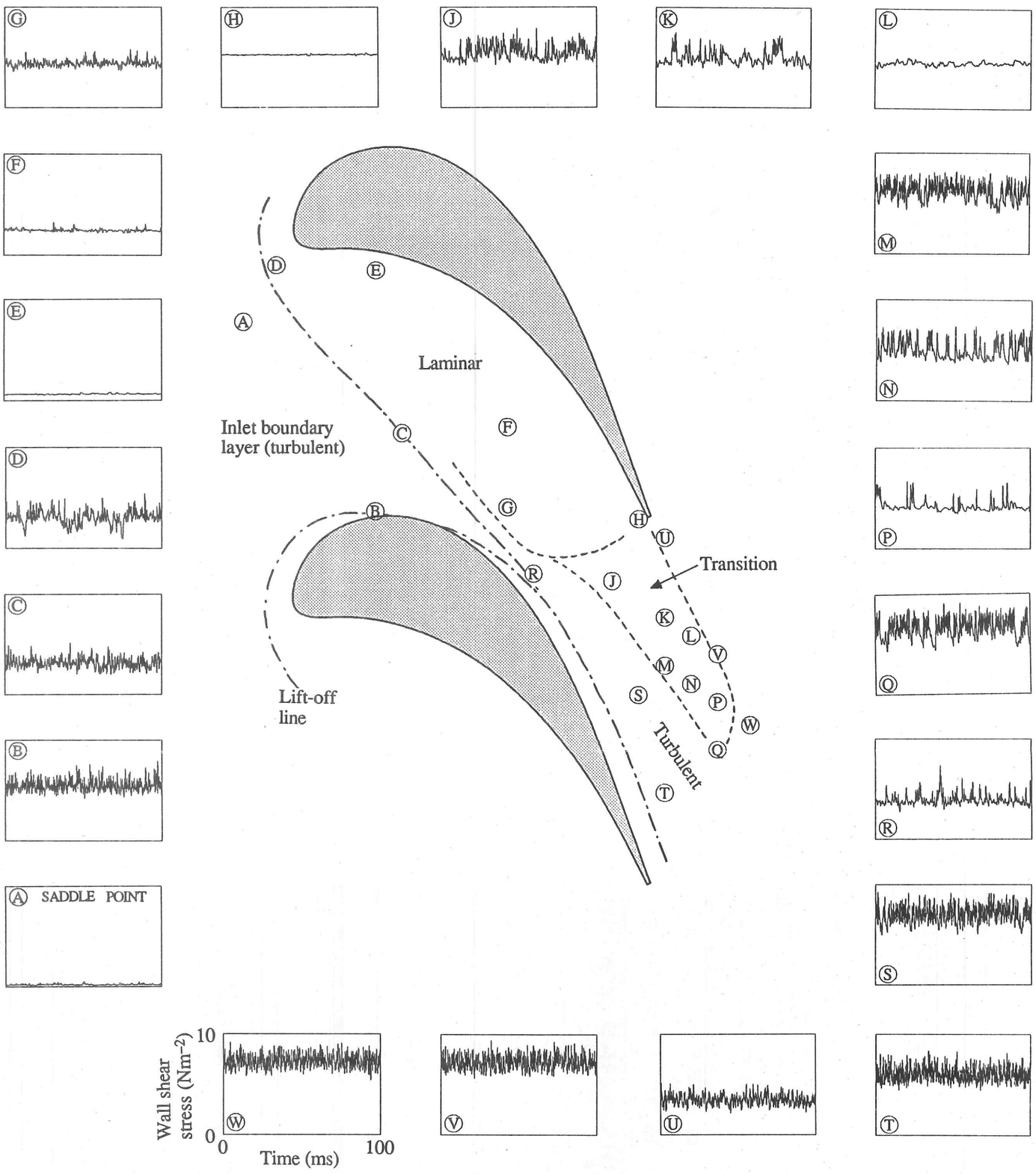

Fig.3.27 Hot film traces on set 3 endwall

<table>
<tr><td colspan="4">Overall
0.048</td></tr>
<tr><td>Inlet
0.006</td><td colspan="2">Midspan
0.020</td><td>Secondary loss
0.022</td></tr>
<tr><td colspan="2">Passage vortex
0.020</td><td>Remaining area
(i.e. wake) 0.022</td><td>Endwall
0.006</td></tr>
</table>

Fig.4.1 Breakdown of set 1 exit loss coefficient into components

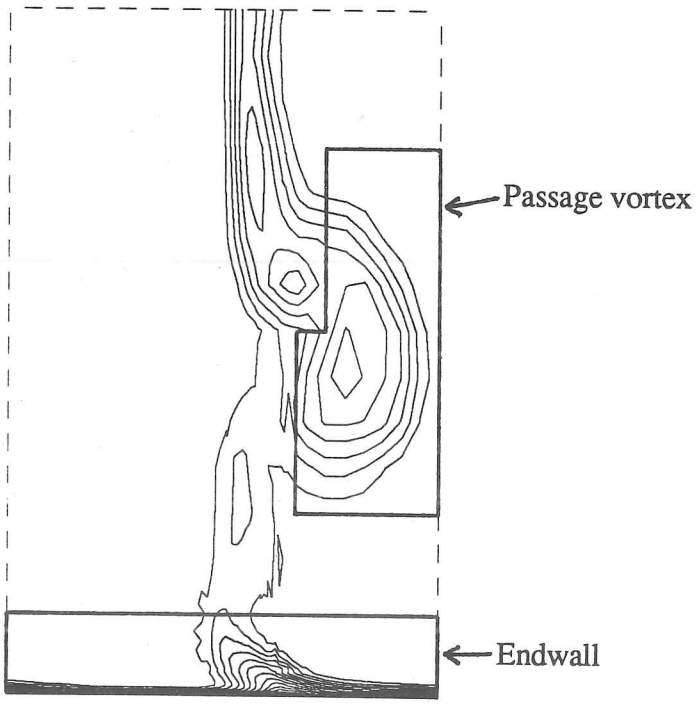

(Contours are of stagnation pressure loss at intervals of $0.05(p_{01}-p_2)$)

Fig.4.2 Division of flow area at $x/C_x=1.23$ used in fig.4.1

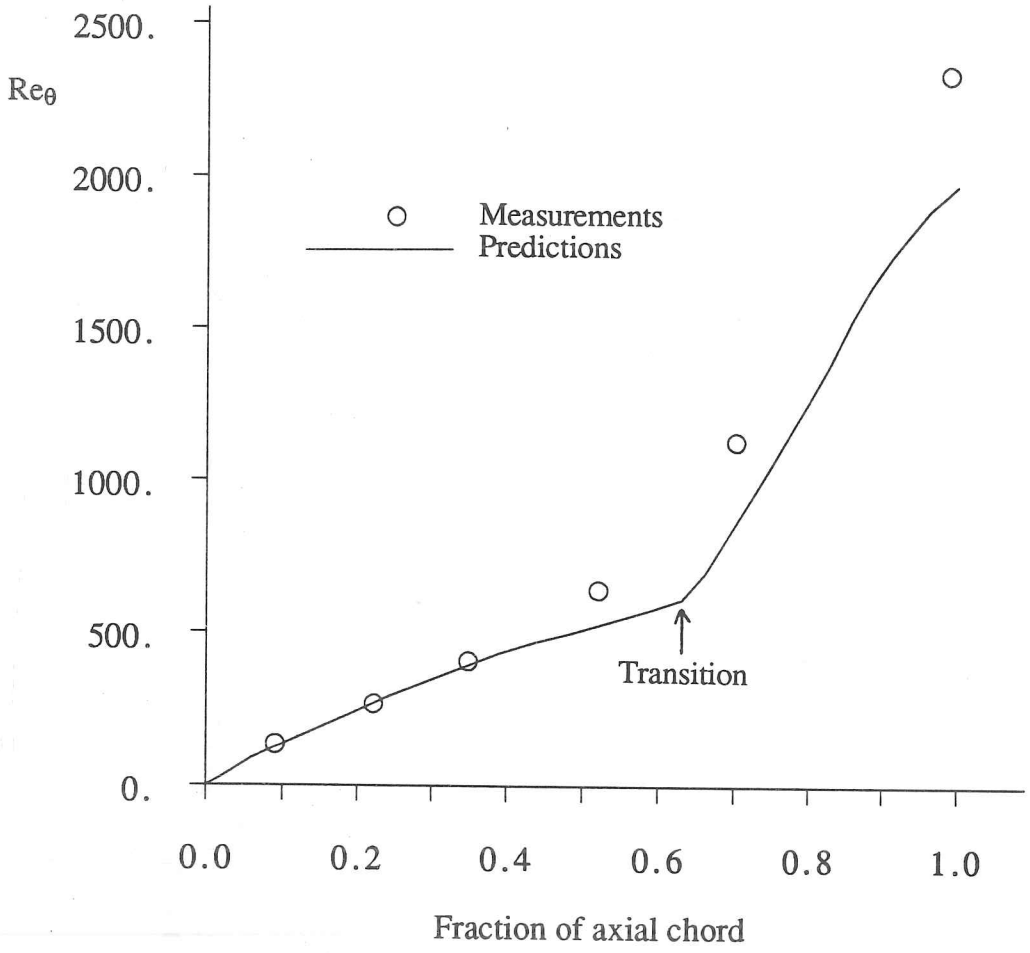

Fig.4.3 Set 1 suction surface boundary layer Re_θ at midspan

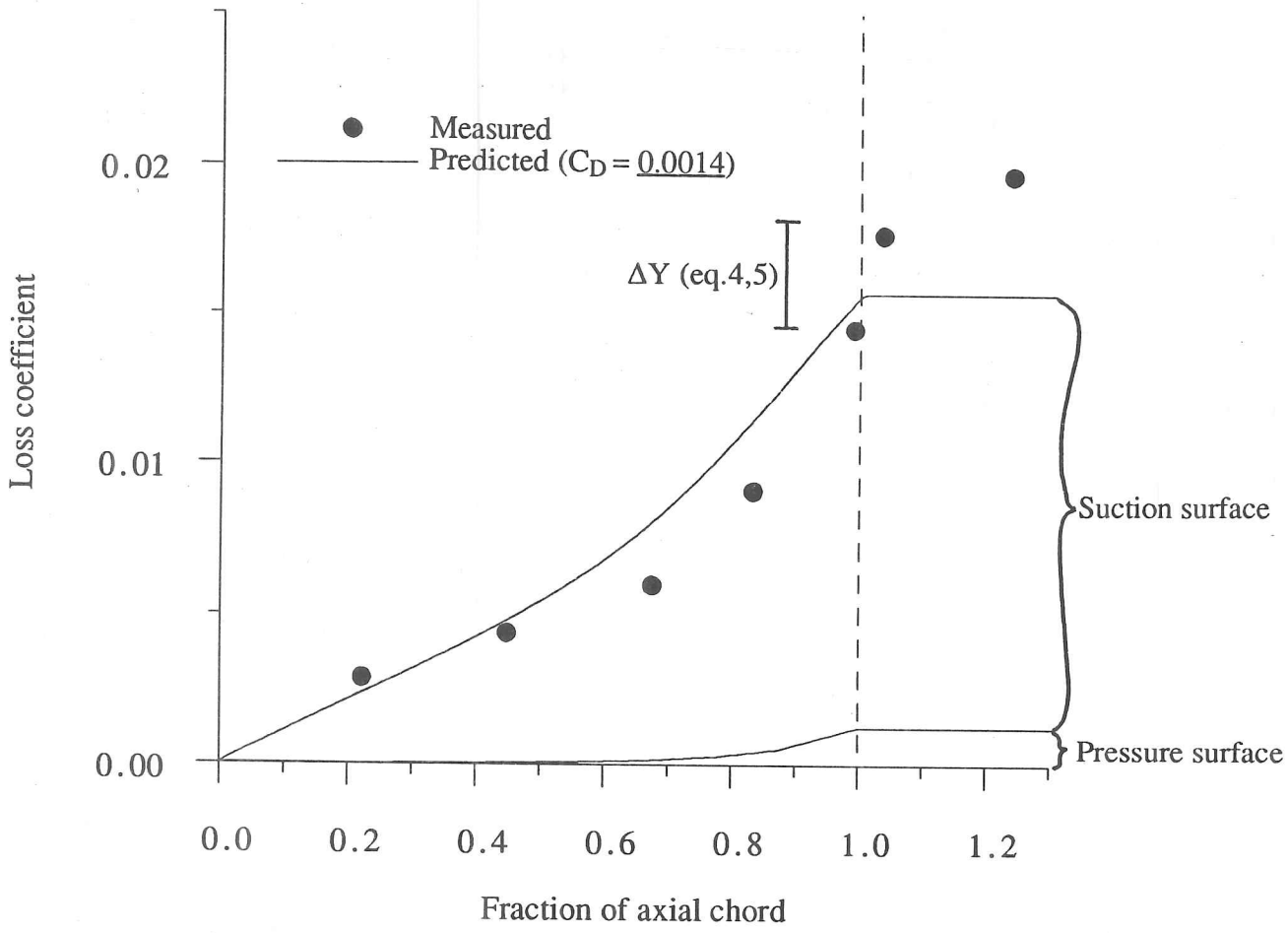

Fig.4.4 Set 1 midspan loss coefficient

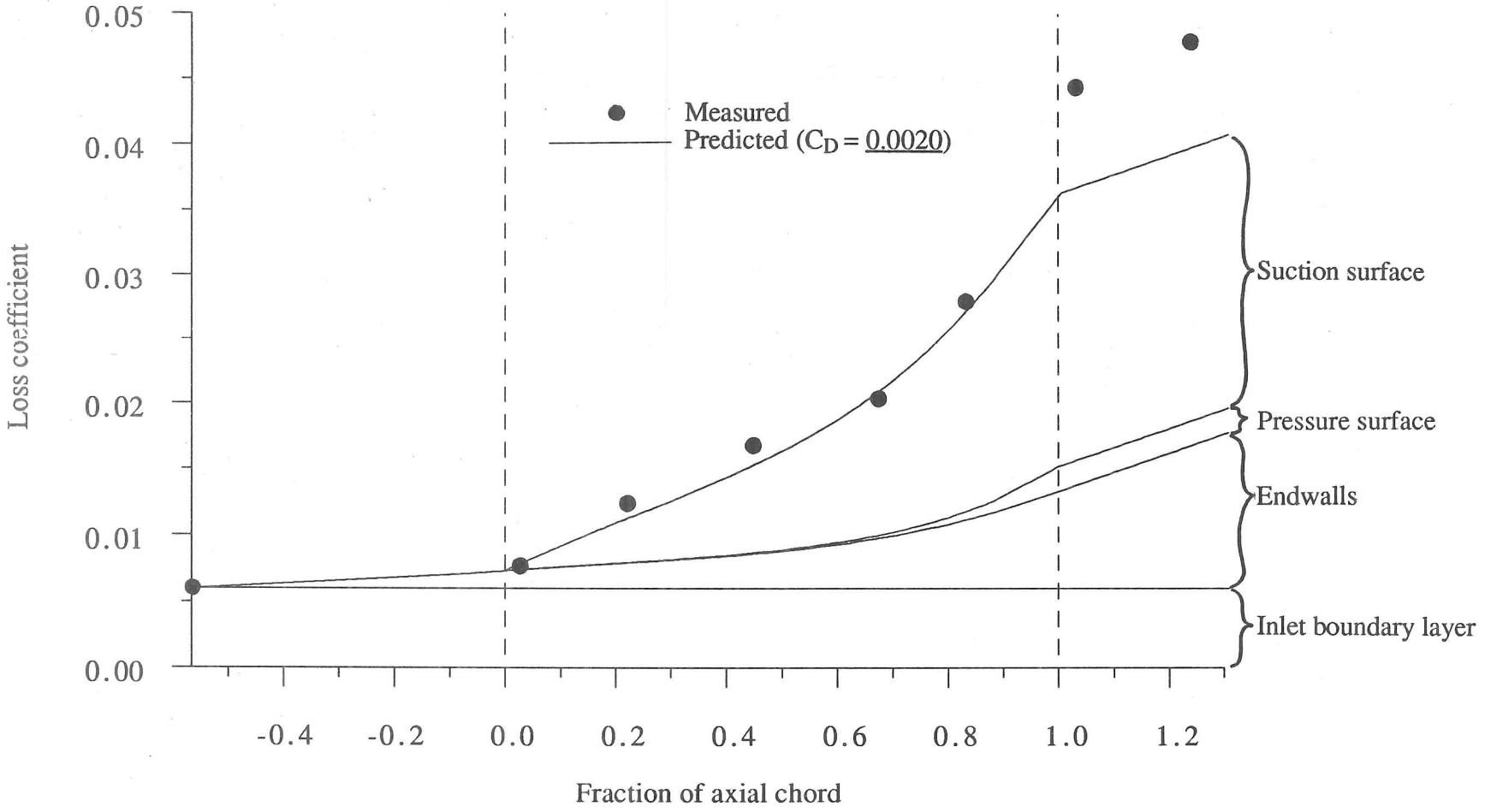

Fig.4.5 Set 1 overall loss coefficient

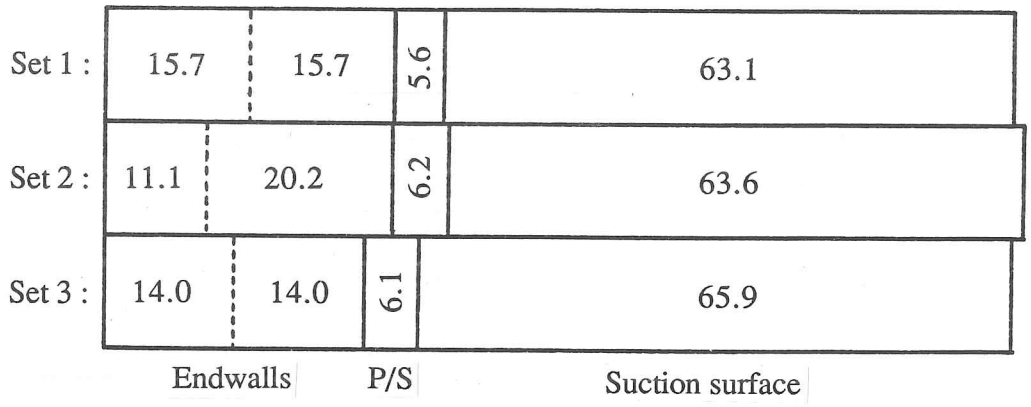

Fig.4.6 $\int U^3 dA_w$ **derived from measured surface pressures**

(Scaled to give set 1 total = 100)

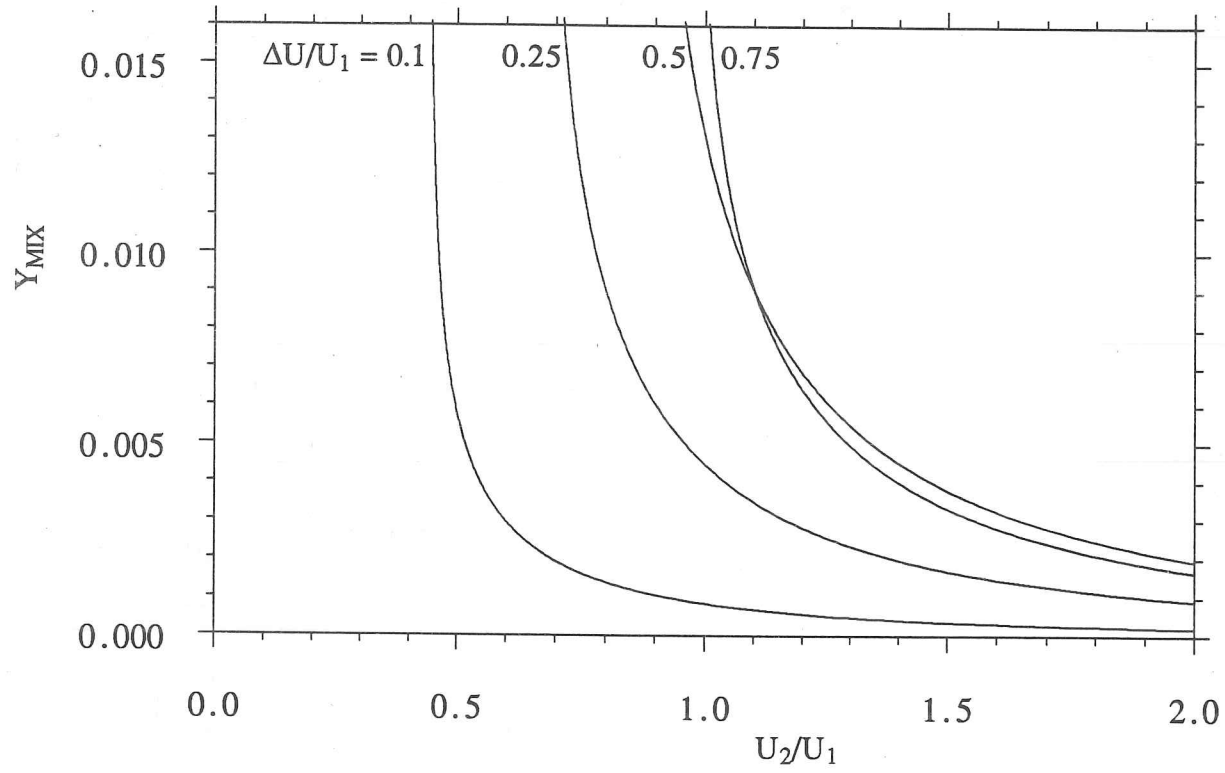

Fig.4.7 **Effect of acceleration on mixing of square wake** (from Denton and Cumpsty, 1987)

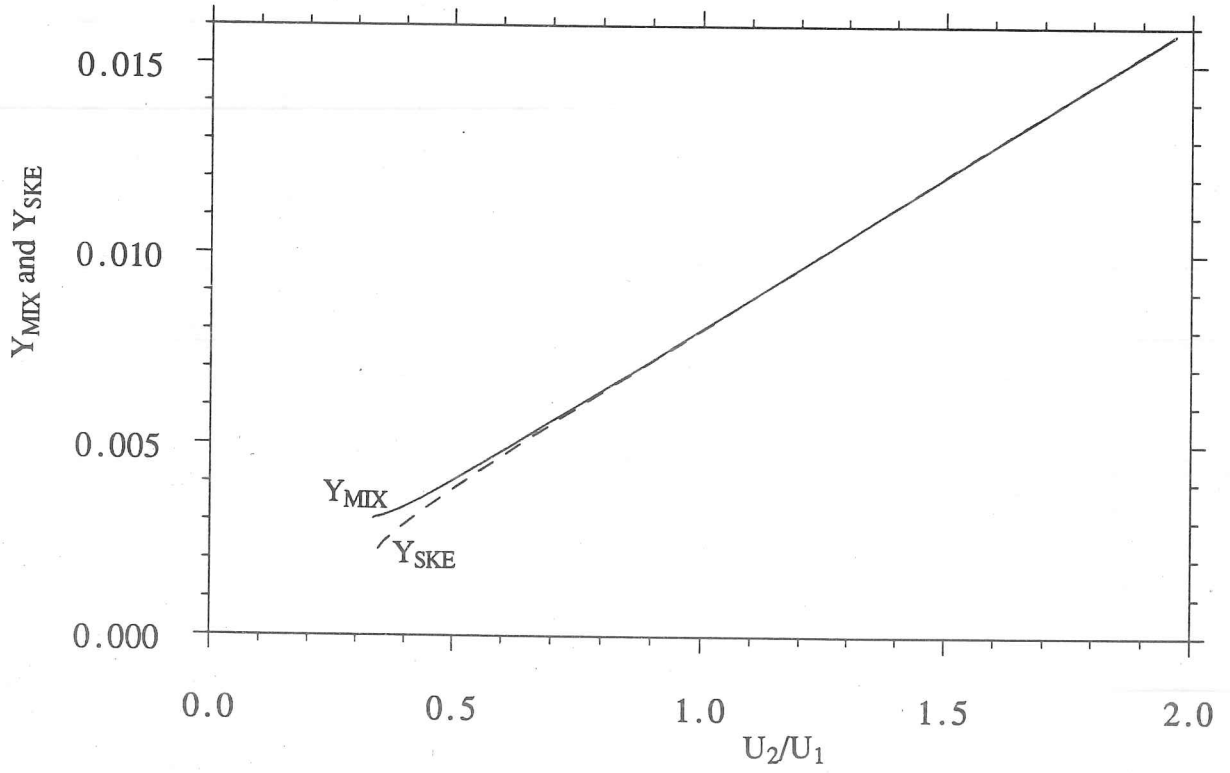

Fig.4.8 **Effect of acceleration on mixing of streamwise vortex**

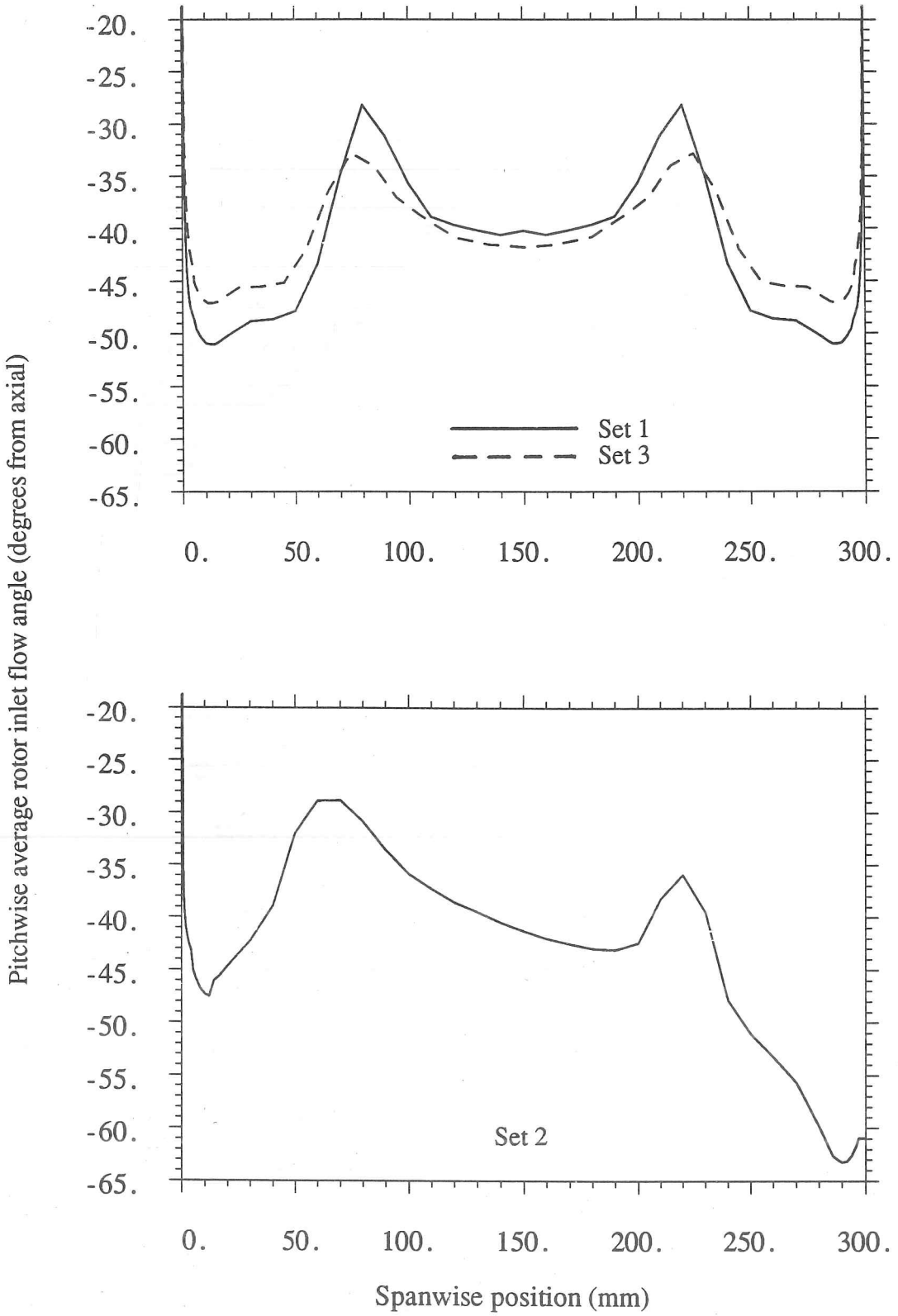

Data derived from measurements by assuming a rotor velocity such that the overall mass-average rotor inlet flow is 40° from axial.

Fig.4.9 Spanwise variation of rotor incidence (50% stage reaction)

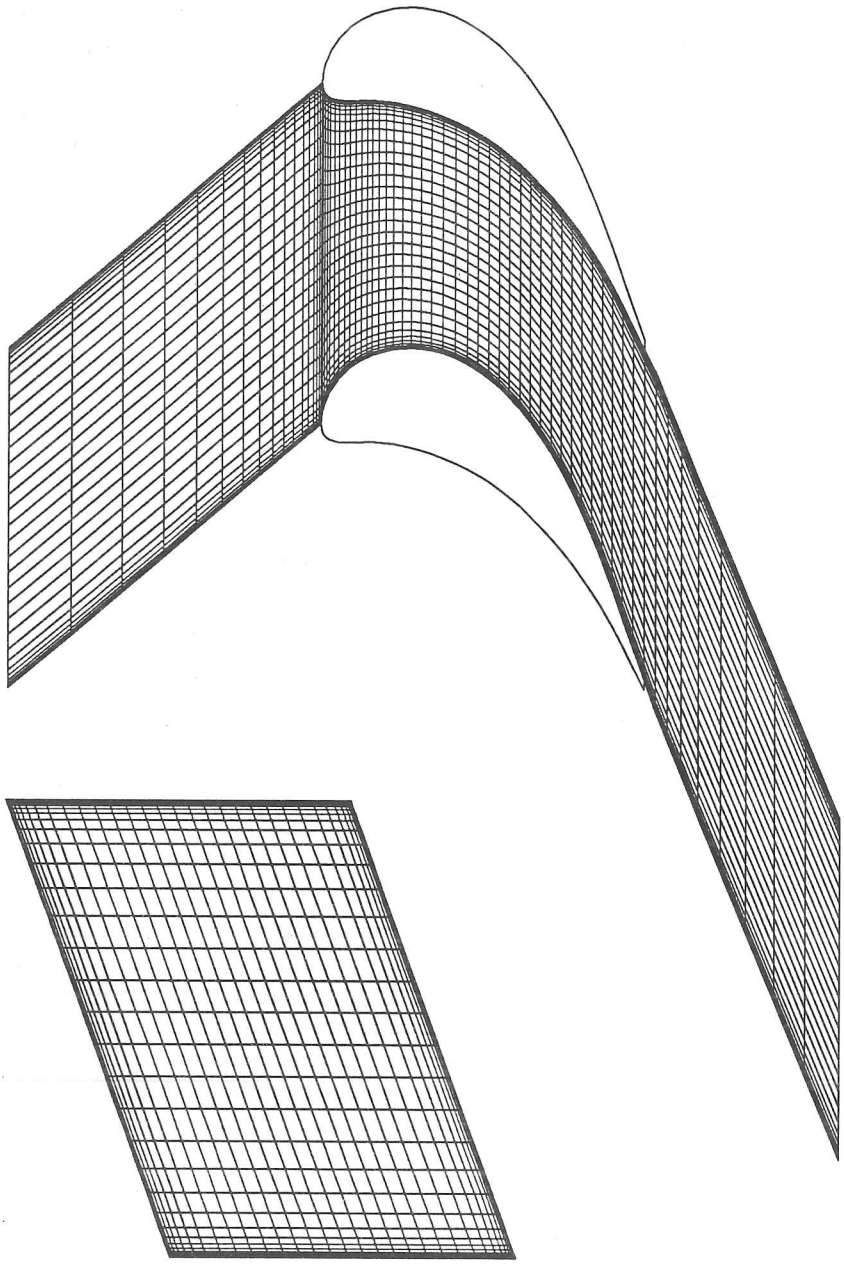

Set 2

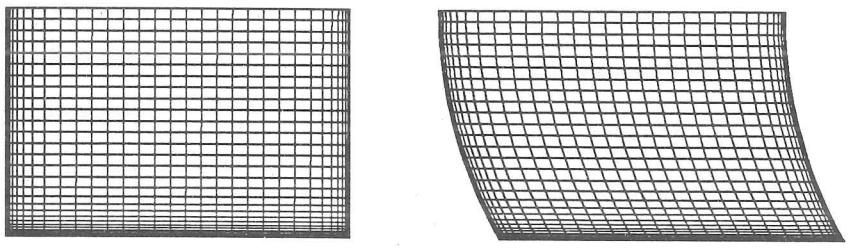

Set 1 Set 3

Fig.5.1 Calculation grids

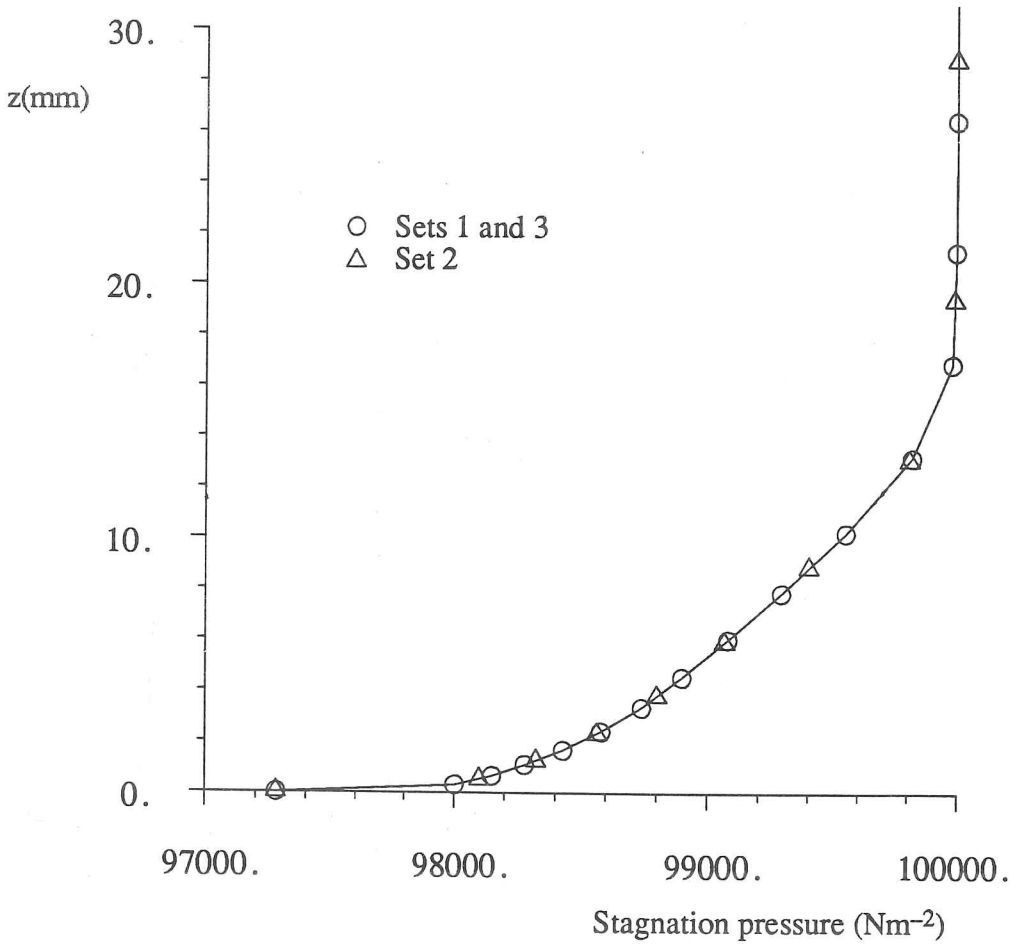

Fig.5.2 **Inlet endwall boundary layer input to time-marching calculations**

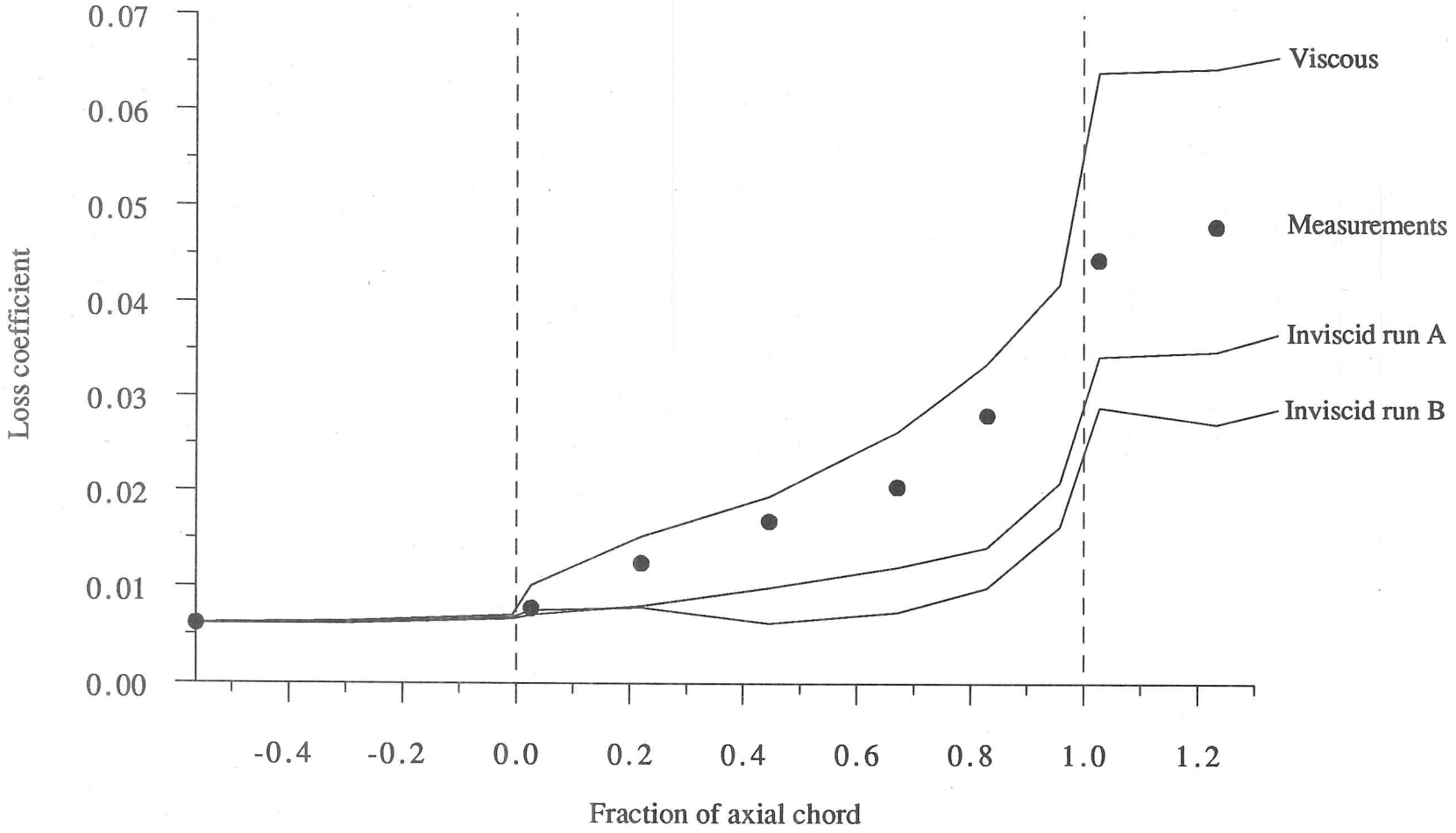

Fig.5.3 Set 1 measured and predicted mass-average loss coefficient

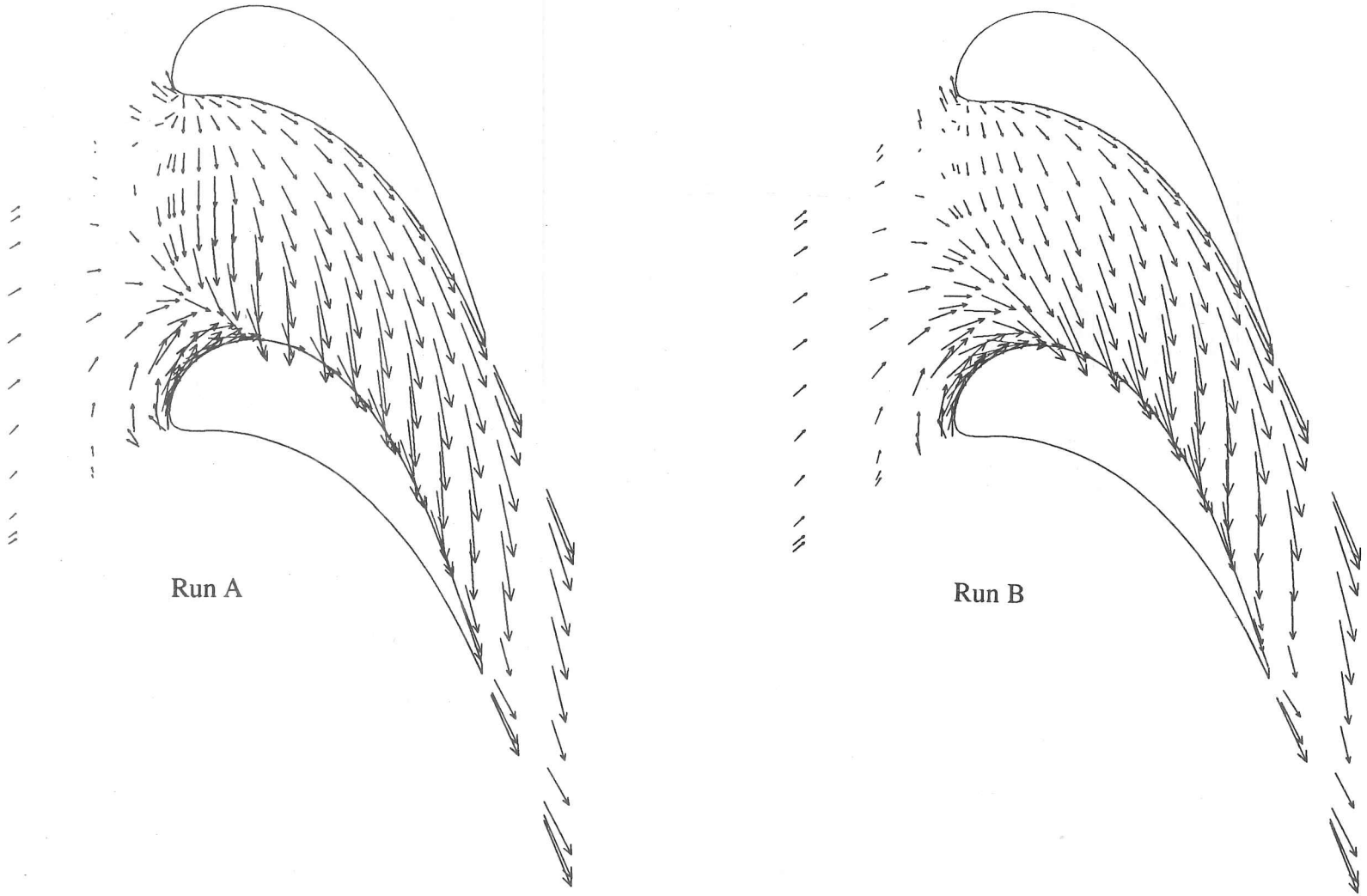

Fig.5.4 Predicted velocities 0.3mm from set 1 endwall (cf. fig.3.1a)

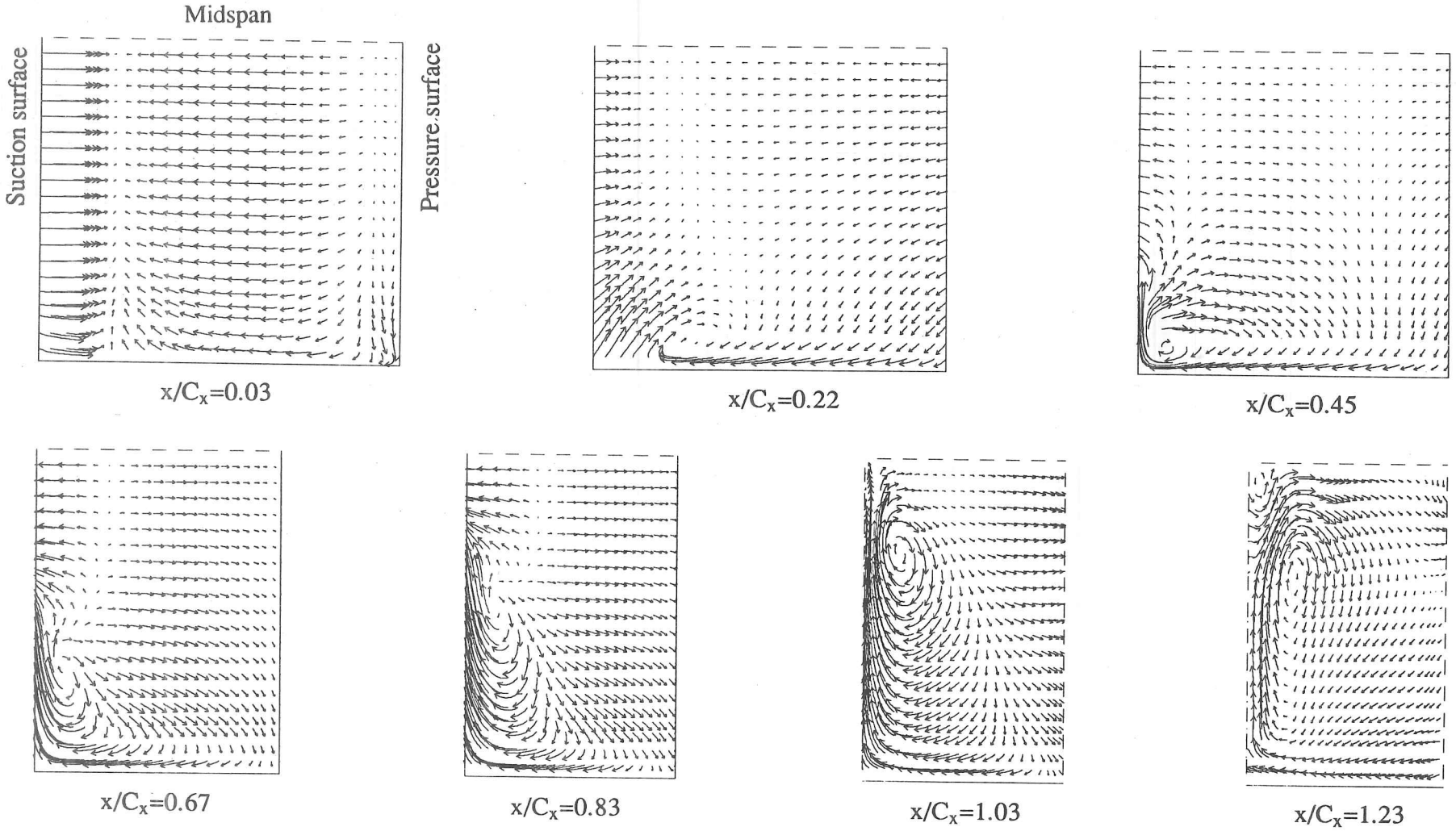

Fig.5.5 **Set 1 secondary velocities (inviscid prediction, run A)** (cf. fig.3.2)

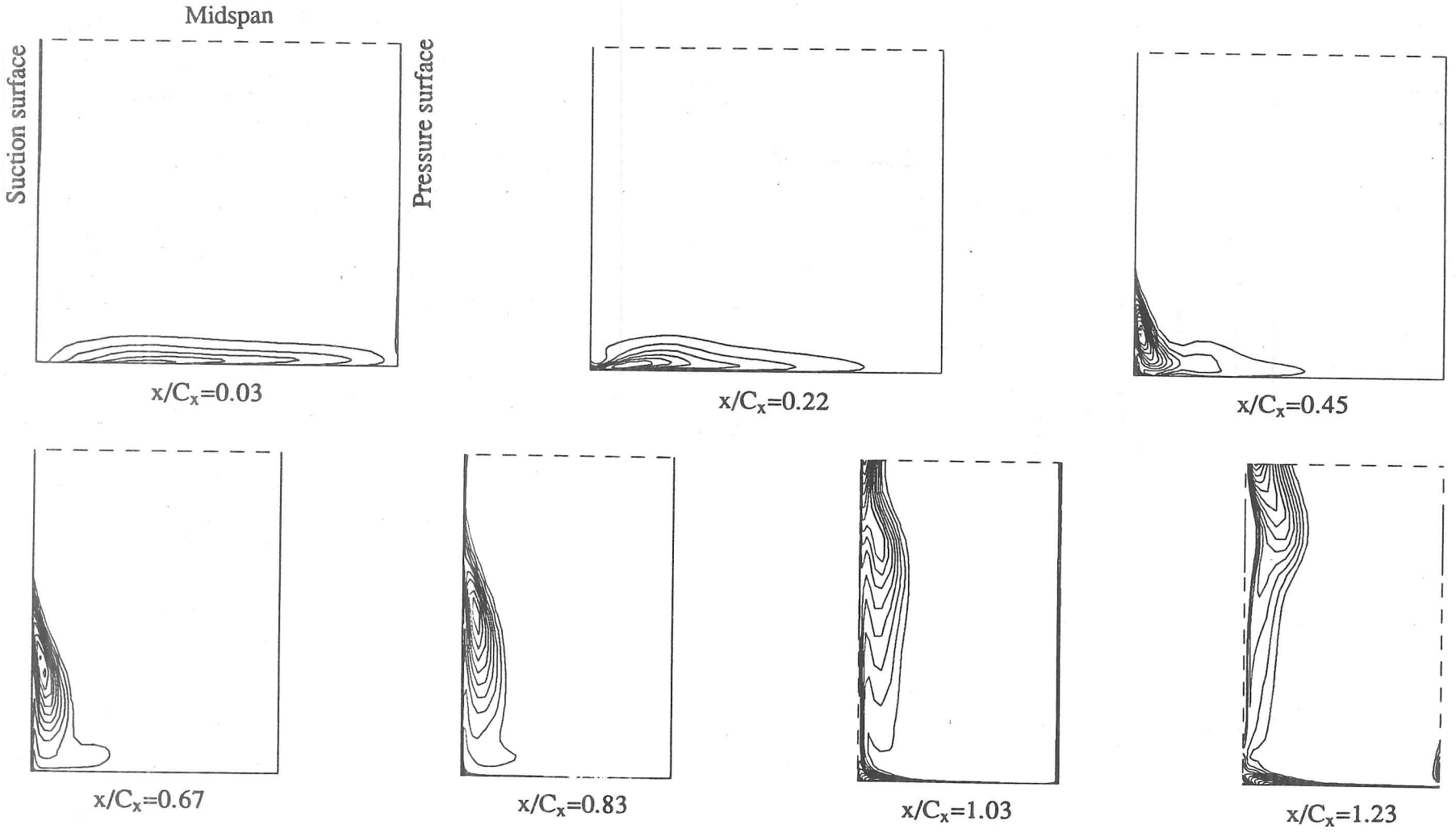

Contour interval $0.05(p_{01}-p_2)$ Zero and negative contours not plotted

Fig.5.6 Set 1 stagnation pressure loss (inviscid prediction, run A) (cf. fig.3.6)

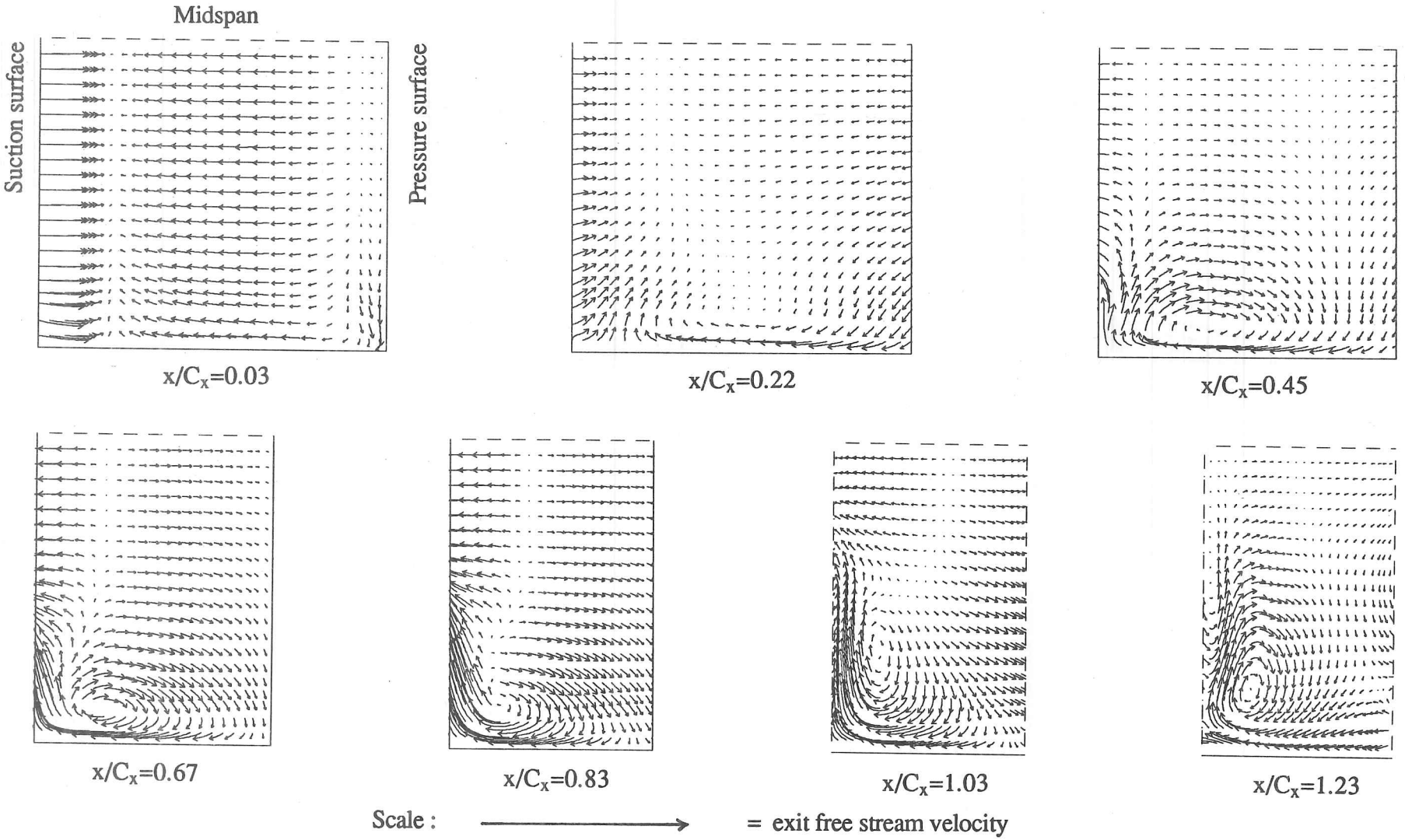

Fig.5.7 **Set 1 secondary velocities (inviscid prediction, run B)** (cf. fig.3.2)

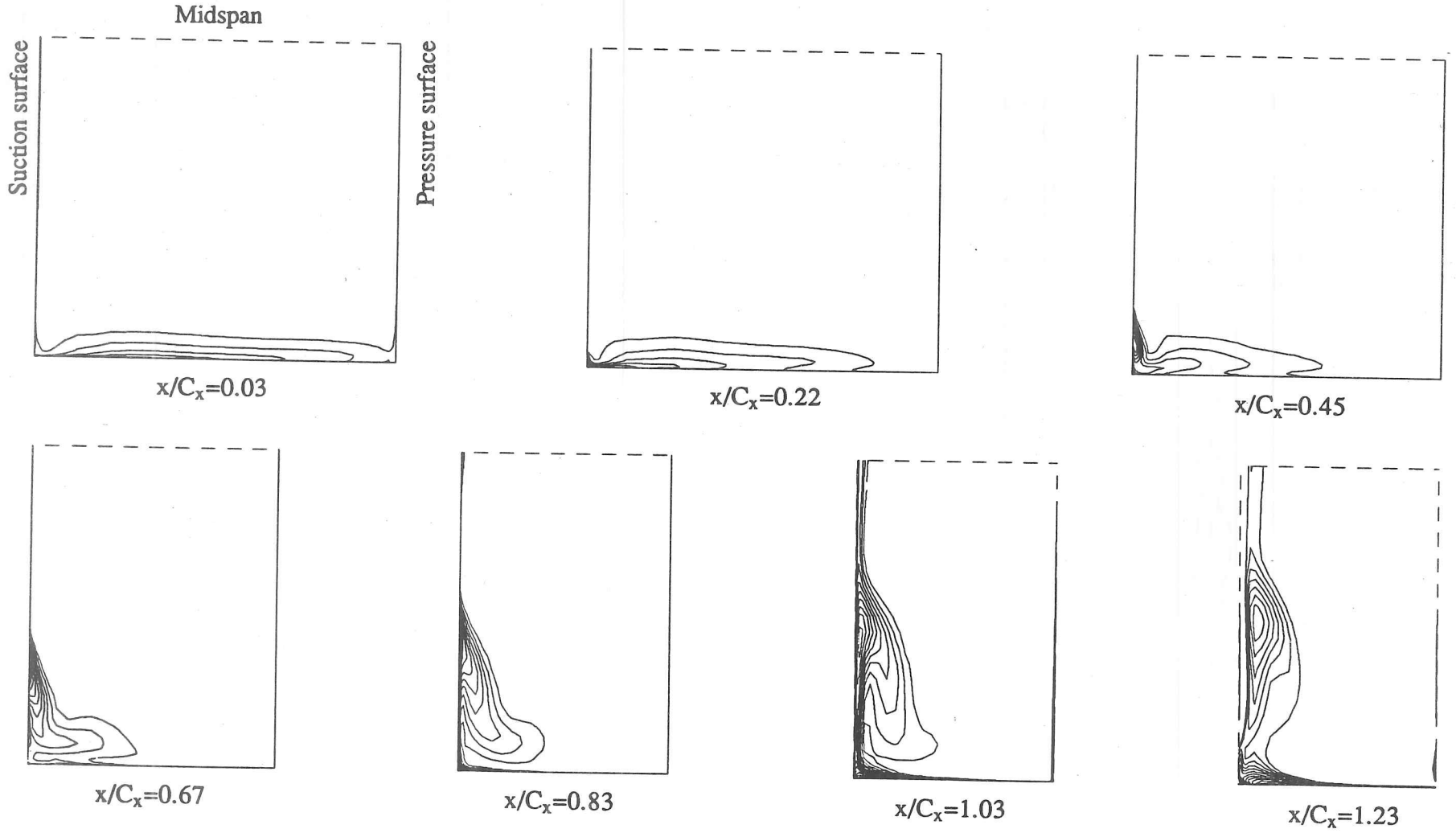

Contour interval $0.05(p_{01}-p_2)$ Zero and negative contours not plotted

Fig.5.8 Set 1 stagnation pressure loss (inviscid prediction, run B) (cf. fig.3.6)

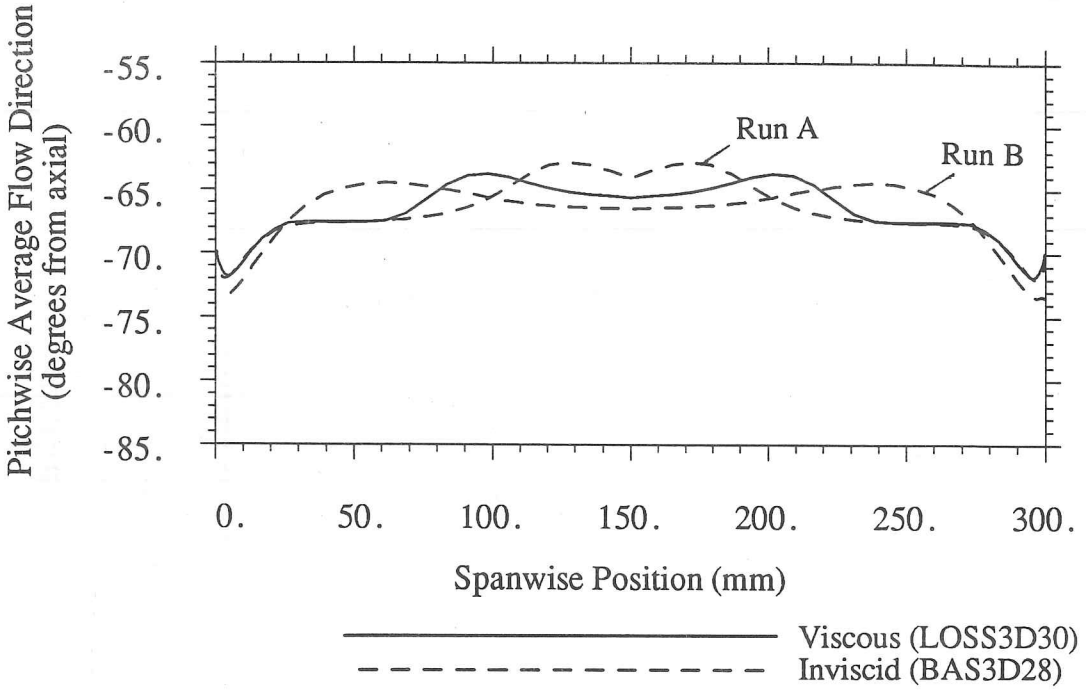

Fig.5.9 Set 1 predicted exit flow direction

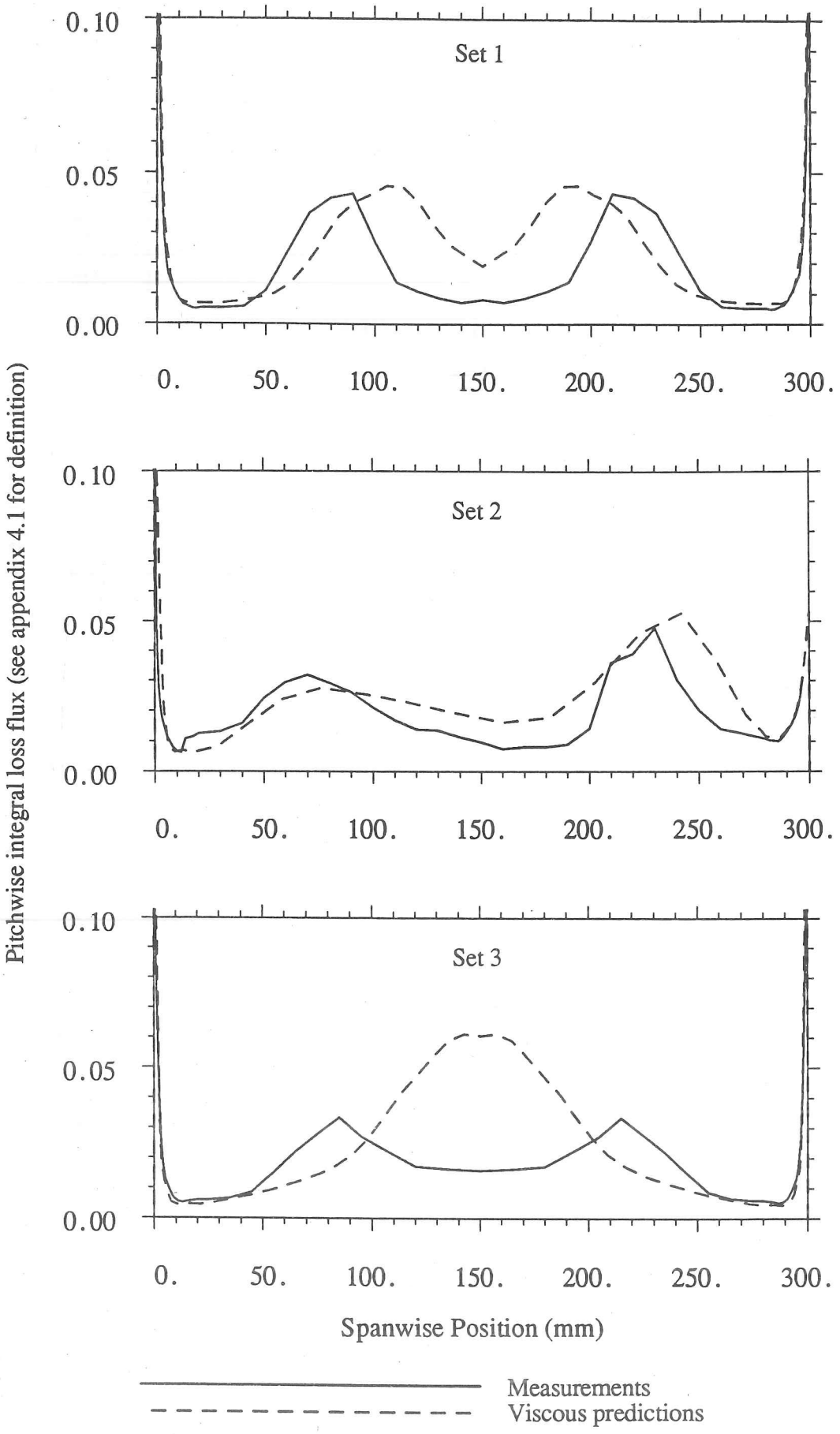

Fig.5.10 Measured and predicted exit loss flux

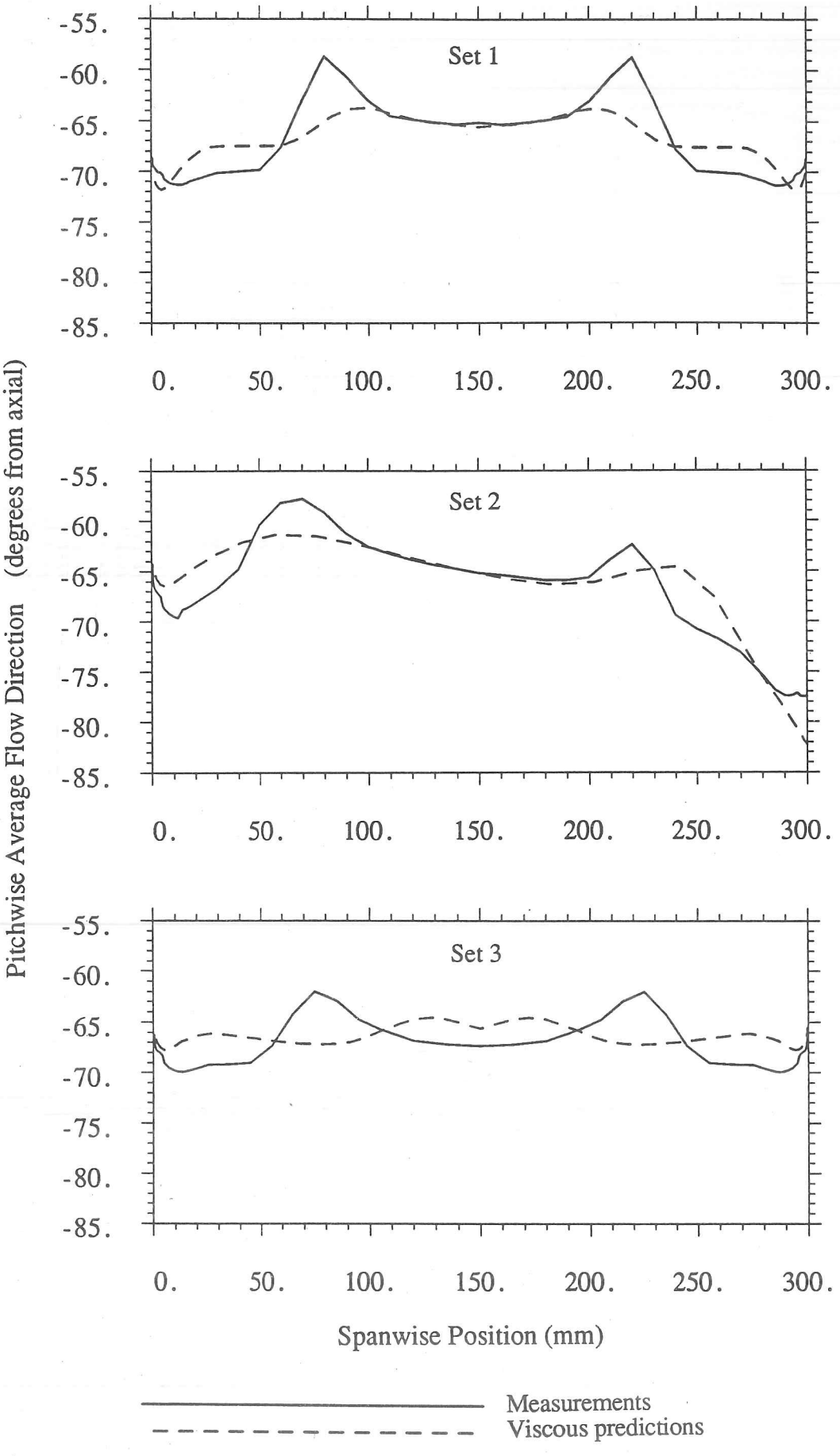

Fig.5.11 Measured and predicted exit flow direction

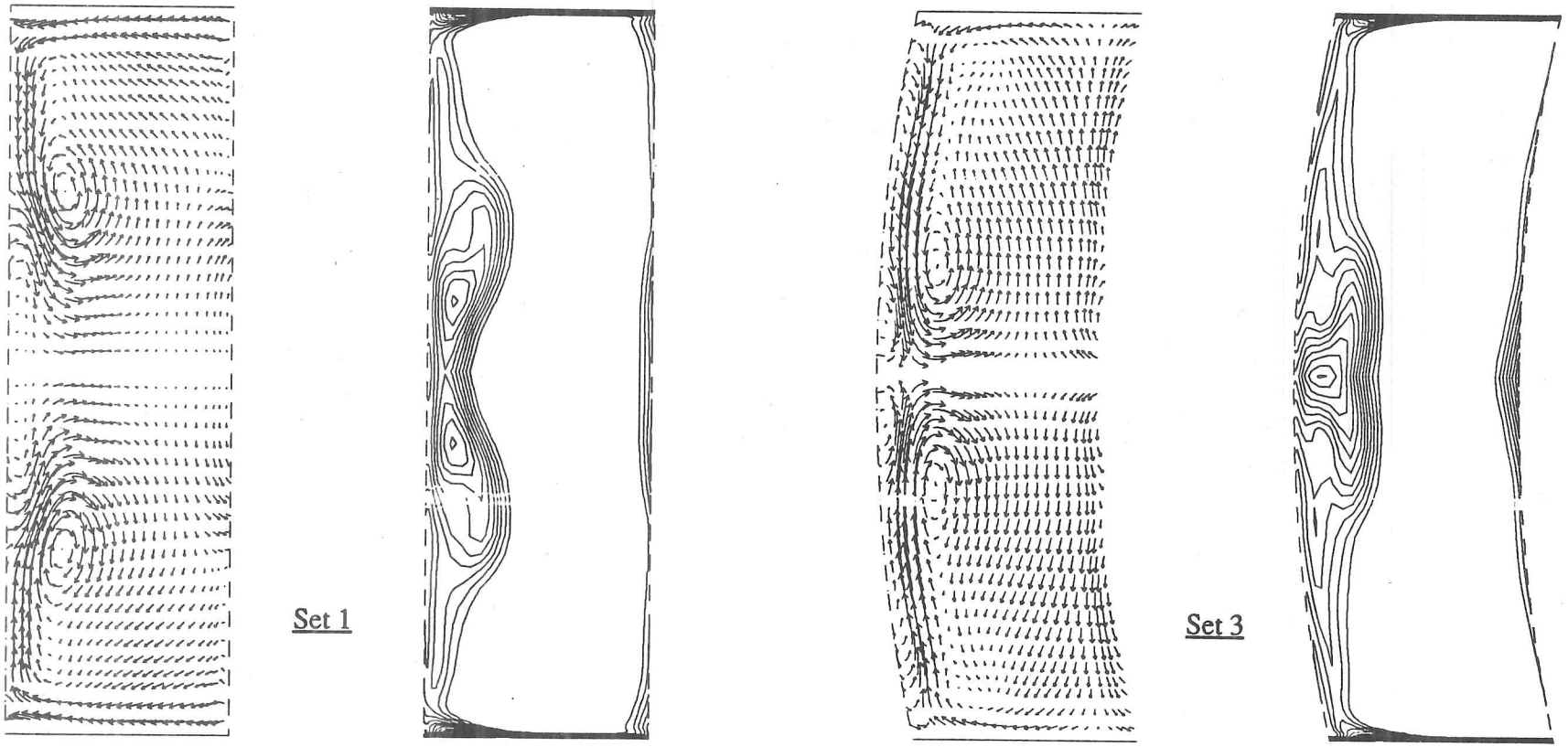

Vector scale : ⟶ = exit free stream velocity

Contour interval $0.05(p_{01}-p_2)$ Zero and negative contours not plotted

Fig.5.12 Secondary velocities and stagnation pressure loss at $x/C_x=1.23$ on sets 1 and 3 (viscous predictions) (cf. figs.3.2, 3.6 & 3.15)

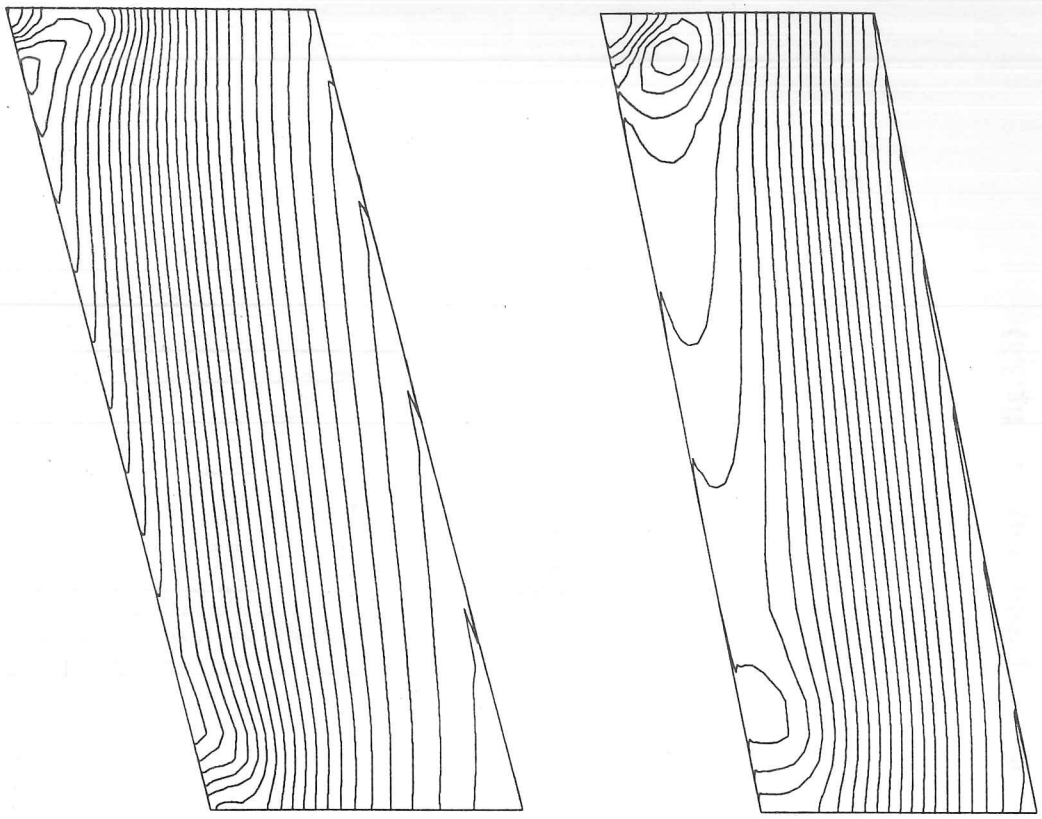

$x/C_x=0.67$ $x/C_x=0.83$

Contour interval $0.05(p_{01}-p_2)$

Fig.5.13 Set 2 static pressure (viscous prediction) (cf. fig.3.12)

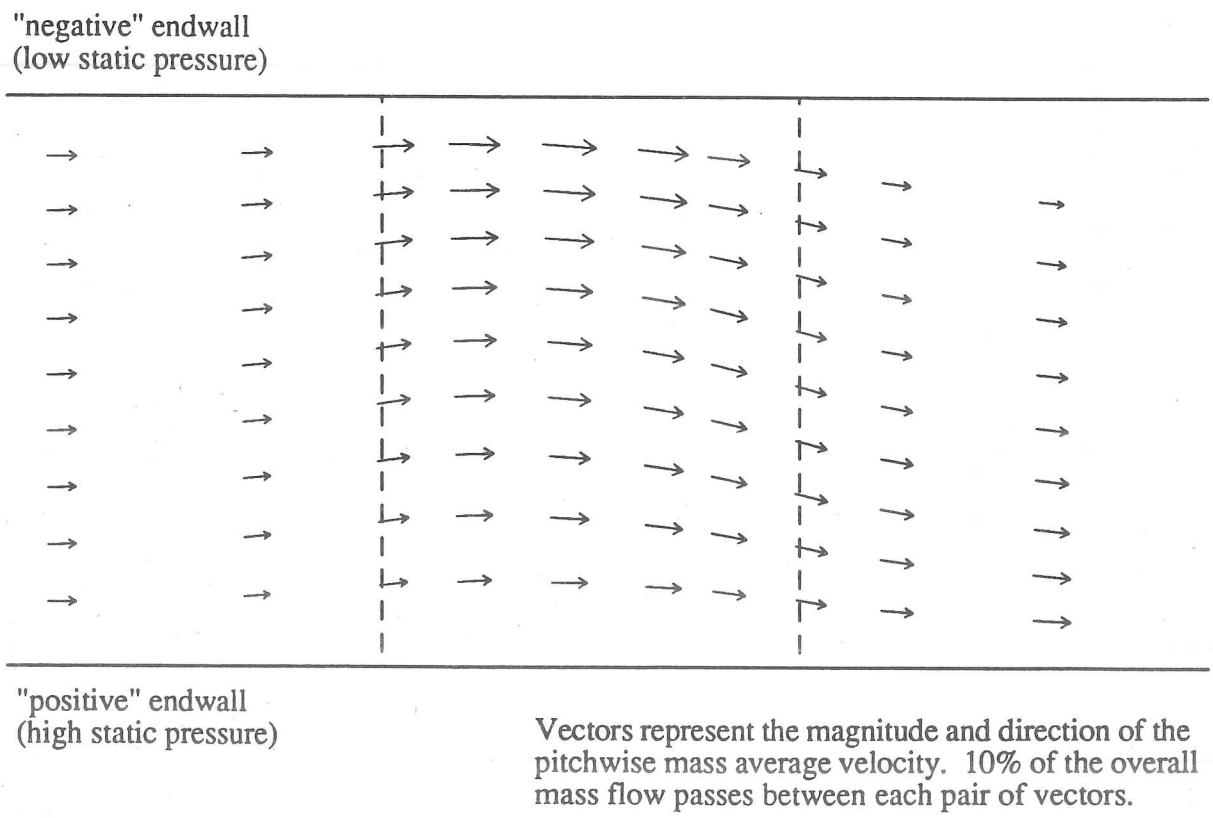

Fig.5.14 Set 2 mean streamlines (viscous prediction) (cf. fig.3.7)

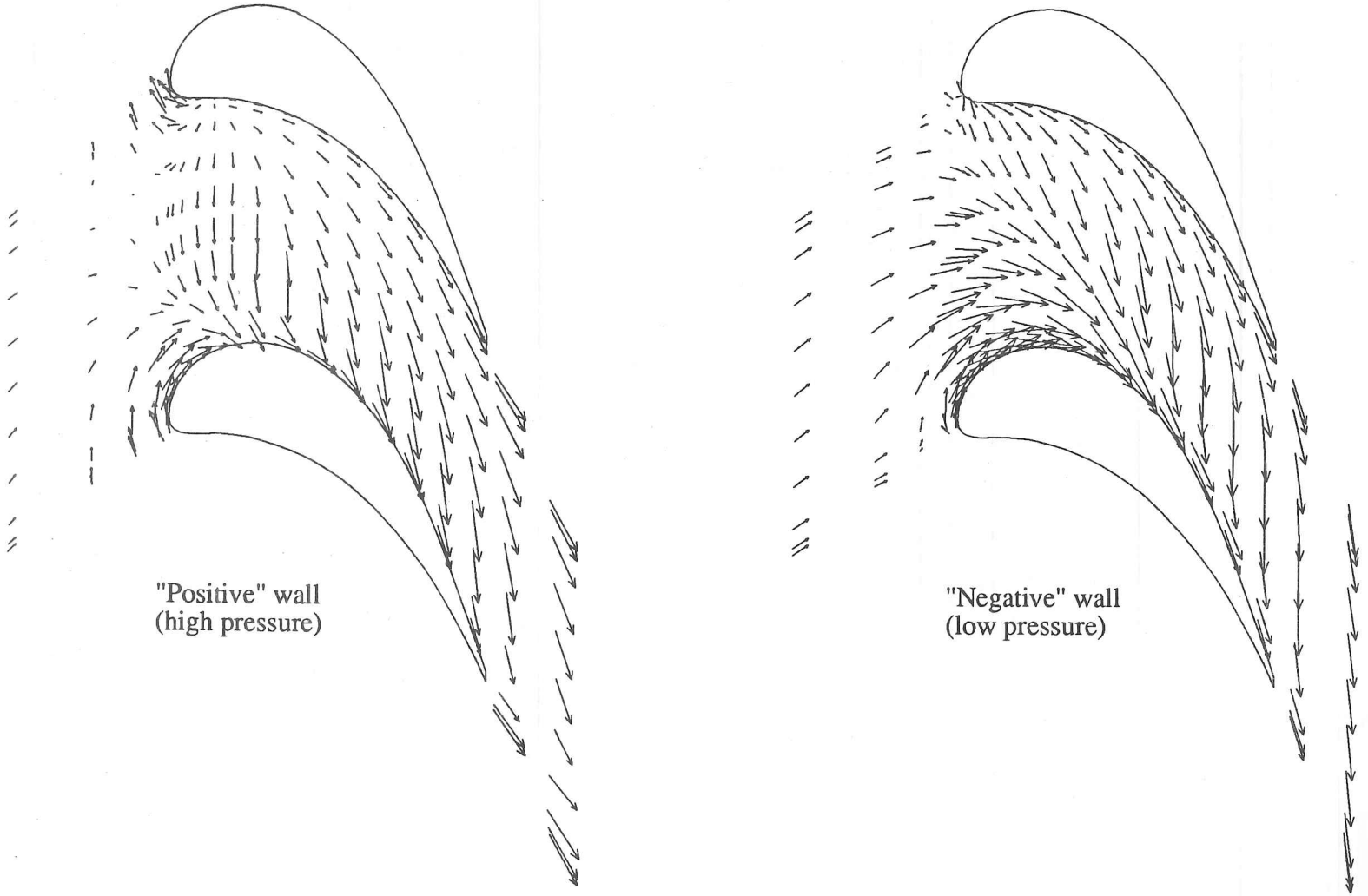

Fig.5.15 Velocities 0.5mm from set 2 endwalls (viscous prediction) (cf. fig.3.8)

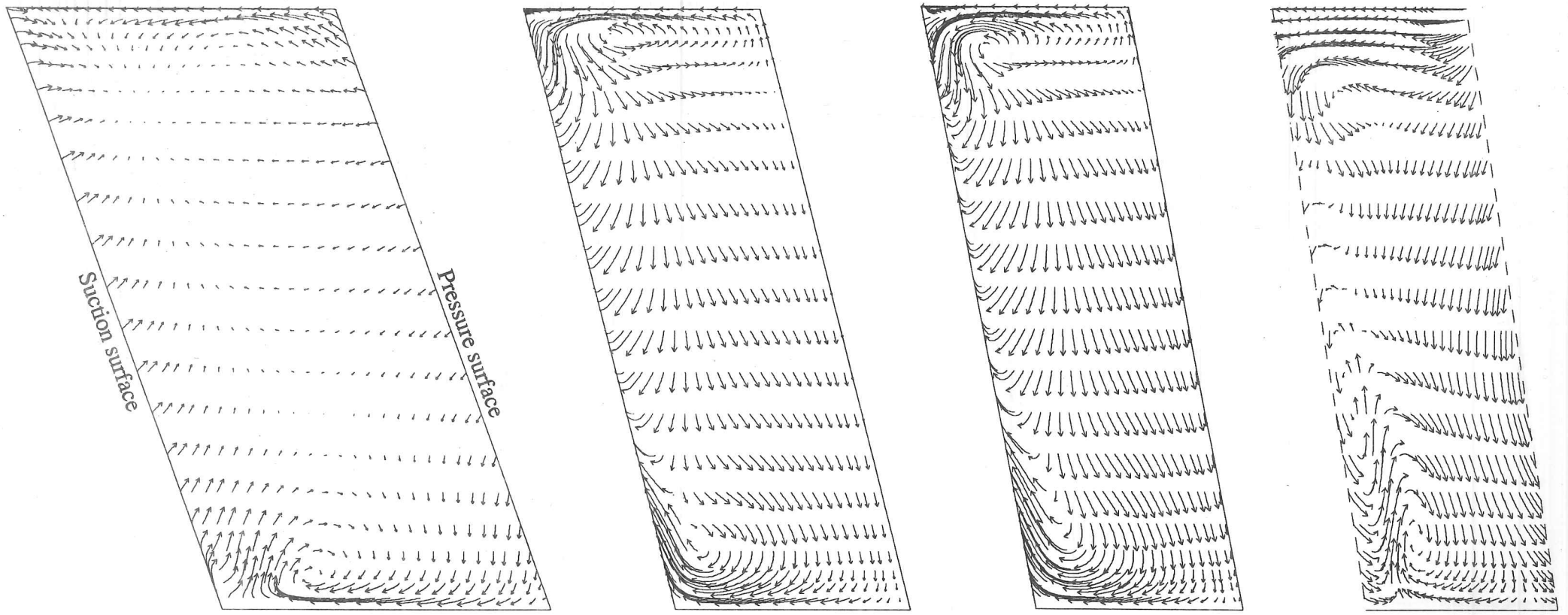

Fig.5.16 Set 2 secondary velocities (viscous prediction) (cf. fig.3.10)

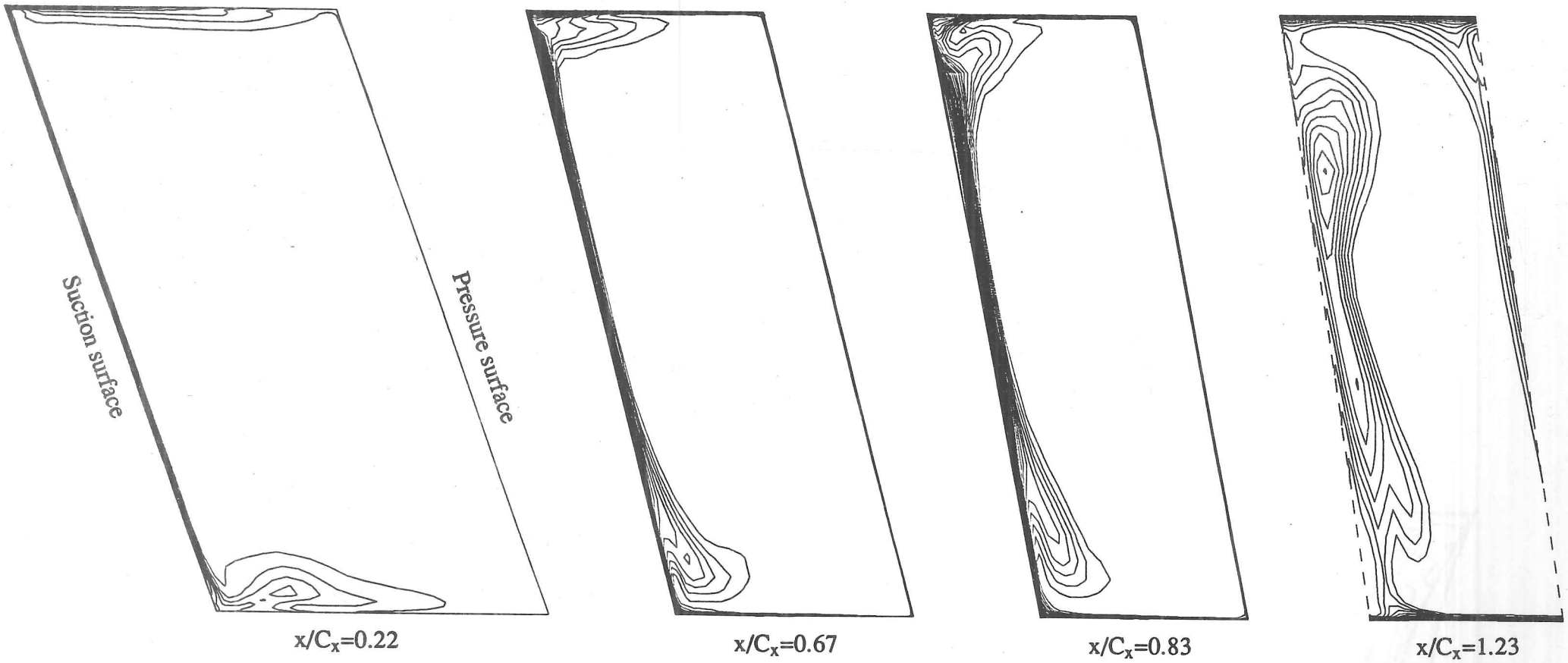

Contour interval $0.05(p_{01}-p_2)$ Zero and negative contours not plotted

Fig.5.17 Set 2 stagnation pressure loss (viscous prediction) (cf. fig.3.13)

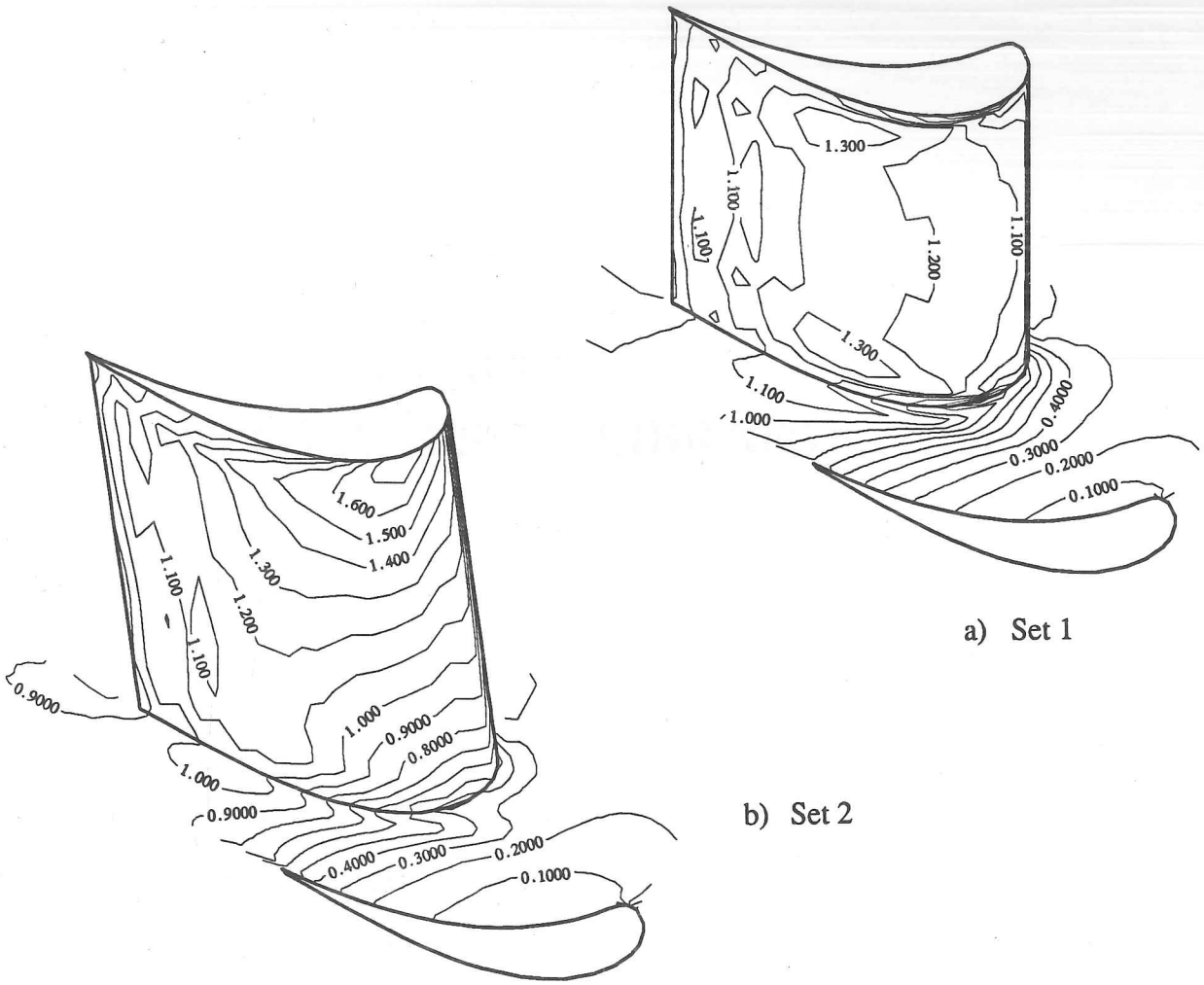

a) Set 1

b) Set 2

c) Set 3

Pressures are expressed as $\left(\frac{p_{01}-p}{p_{01}-p_2}\right)$

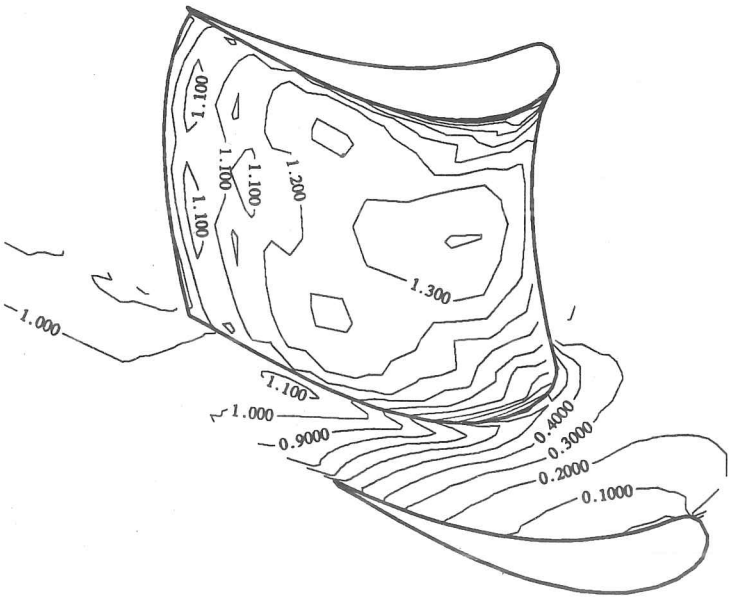

Fig.5.18 Surface static pressures (viscous prediction) (cf. fig.3.17)